UNIVERSIDAD DE CHILE
FACULTAD DE CIENCIAS FÍSICAS Y MATEMÁTICAS
ESCUELA DE POSTGRADO

Fluid Dynamics of heat and mass transport in porous media

Mathematical modelling, spectrally-based direct numerical simulations and laboratory experiments

TESIS PARA OPTAR AL GRADO DE DOCTOR EN CIENCIAS DE LA INGENIERÍA MENCIÓN FLUIDODINÁMICA

Juvenal Antonio Letelier Villalón

PROFESOR GUÍA:
Dr. Paulo Herrera Ricci

PROFESOR GUÍA 2:
Dr. Nicolás Mujica Fernández

PROFESOR GUÍA 3:
Dr. Jaime H. Ortega Palma

MIEMBROS DE LA COMISIÓN:
Dra. María Cristina Depassier Terán
Dr. Carlos Conca Rosende
Dr. Sergio Rica Mery
Dr. Amir Riaz

Este trabajo ha sido financiado por CONICYT Beca Doctorado Nacional #21110836 y Proyecto FONDAP-CONICYT #15090013 Centro de Excelencia en Geotermia de los Andes (CEGA).

SANTIAGO DE CHILE
2016

Resumen

En este trabajo se presenta el problema del transporte de calor y masa para un sistema compuesto de dos fases fluidas en un medio poroso, el cual puede ser relevante en el uso de CO_2 como fluido de trabajo en reservorios geotermales. El medio poroso fue modelado usando una celda Hele-Shaw, la cual es ampliamente usada para la visualización del transporte de escalares. Los objetivos de este trabajo son (a) investigar teórica y numéricamente las leyes de escalamiento que gobiernan los procesos de mezcla en un medio poroso, y (b) visualizar los procesos de transporte usando celdas Hele-Shaw y avanzadas técnicas de segmentación de imágenes. El modelo derivado es una extensión de la ecuación de Polubarinova-Kochina, la cual es válida para regímenes de flujos altos en medios porosos. El transporte de calor y masa en un medio poroso es gobernado por el número de Nusselt Nu_φ y la tasa de disipación media escalar $\langle \varepsilon_\varphi \rangle_\tau = \ell_{mix}/L$, donde ℓ_{mix} es la longitud de mezcla y L es la longitud horizontal de la celda. La principal contribución de este trabajo es la demostración de la existencia de los escalamientos $\langle Nu_\varphi \rangle_\tau \sim Ra_\varphi^{n(\epsilon)}$ y $\langle \varepsilon_\varphi \rangle_\tau \sim Ra_\varphi^{m(\epsilon)}$, respectivamente, donde Ra_φ es el número de Rayleigh sujeto a la definición del escalar φ, el cual puede ser temperatura o concentración, y ϵ es el cociente entre el espaciamiento de la celda y su altura. Ambas cantidades se relacionan a través del modelo $\langle Nu_\varphi \rangle_\tau = \Phi(\epsilon^2 Ra_\varphi, \Delta)\, Ra_\varphi \langle \varepsilon_\varphi \rangle_\tau$, donde Δ contiene información de los efectos de difusión lateral de mezcla. Esta contribución extiende los resultados más recientes publicados en la literatura.

Dada la importancia del parámetro adimensional ϵ en la escala de laboratorio, se realizó un detallado análisis lineal de la convección termal y la inestabilidad de Rayleigh-Taylor, incorporando efectos de tensión interfacial ya que el CO_2 es un fluido parcialmente miscible con el agua. Los resultados obtenidos usando métodos asintóticos corrigen los análisis descritos en la literatura, así como también entregan nuevas evidencias de que el inicio de la inestabilidad de Rayleigh-Taylor depende completamente de los efectos interfaciales de la mezcla.

Finalmente, para visualizar el transporte escalar, se realizaron experimentos de convección termal y mezcla por contraste de densidad. Se usaron técnicas de atenuación de luz y Schlieren sintético, además de métodos de segmentación de imágenes basados en principios variacionales, los cuales permitieron obtener interesantes resultados visuales del proceso de transporte. Se demostró que la aplicación del método optical flow permite reconstruir el mapa de temperaturas en celdas Hele-Shaw con una mejor resolución de imagen que el algoritmo PIV digital, obteniendo resultados acordes a lo esperando en sistemas geotermales sedimentarios. Además, se muestra experimentalmente que el uso de segmentación multifase es ideal para calcular propiedades físicas del proceso de mezcla, además de cantidades relacionadas con el transporte escalar, sin conocer *a priori* los valores de cantidades físicas tales como la densidad y velocidad de flujo.

Abstract

We study heat and mass transport for two-phase fluids in a porous medium, which has applications for the use of supercritical CO_2 in geothermal reservoirs. Commonly, the porous medium is modeled using a Hele-Shaw cell, which has been used for the visualization of scalar transport. The main objectives of this work are (a) to investigate, theoretically and numerically, the scaling laws that governs mixing processes in a porous medium, and (b) visualize the scalar transport processes using Hele-Shaw cells and advanced techniques for image segmentation. The mathematical model derived is an extension of the known Polubarinova-Kochina equation, which is valid for high-flux regimes in porous media. Heat and mass transfer are governed by the Nusselt number Nu_φ and the mean scalar dissipation rate $\langle \varepsilon_\varphi \rangle_\tau = \ell_{mix}/L$, where ℓ_{mix} is the mixing length and L is the width of the cell. The main contribution of this work is the demonstration of the existence of the scaling laws $\langle Nu_\varphi \rangle_\tau \sim Ra_\varphi^{n(\epsilon)}$ and $\langle \varepsilon_\varphi \rangle_\tau \sim Ra_\varphi^{m(\epsilon)}$, where Ra_φ is the Rayleigh number subject to the scalar φ which can be temperature or concentration, and ϵ measures the ratio between the cell gap and height. The Nusselt number and the mean scalar dissipation rate are related by the model $\langle Nu_\varphi \rangle_\tau = \Phi(\epsilon^2 Ra_\varphi, \Delta)\, Ra_\varphi \langle \varepsilon_\varphi \rangle_\tau$, where Δ has information about the effects of lateral difussion due to the mixture and mechanical dispersion. This contribution extends the more recent results published in the literature.

On the other hand, we study the importance of the parameter ϵ in the onset of convection at laboratory scale and the incorporation of effective interfacial tension to the model, motivated by the partial solubility of CO_2 in water. We perform a detailed linear analysis of thermal convection and Rayleigh-Taylor instability, where the results obtained using asymptotic methods provide a correction for the analysis reported in the literature, as well as give new evidences that the onset of Rayleigh-Taylor instability depends upon interfacial effects.

Finally, we perform experiments in thermal convection and mixing by density contrast to visualize scalar transport. We used light attenuation and quantitative Schlieren techniques, as well as image segmentation methods based on variational principles, which allow us to obtain interesting visual results of transport processes. We demonstrate that the application of the optical flow method to the synthetic Schlieren images can reconstruct the temperature map within Hele-Shaw cells with better image resolution than the known digital PIV. Furthermore, using the definition for the mean scalar dissipation, $\langle \varepsilon_\varphi \rangle_\tau = \ell_{mix}/L$, we have demonstrated experimentally that the Chan-Tai L^2-based multiphase segmentation with Isodata initialization is ideal for computing mixing properties, without knowing *a priori* the values of physical quantities such as the density and flow velocity.

Empezaré con Cervantes y su don Quijote, que desde su mente soñadora y por momentos lúcida decía:

"Como no estás experimentado en las cosas del mundo, todas las cosas que tienen algo de dificultad te parecen imposibles. Confía en el tiempo, que suele dar dulces salidas a muchas amargas dificultades"

Miguel de Cervantes en don Quijote de la Mancha

Para Dominique

Agradecimientos

Quiero expresar mi agradecimiento con el programa doctoral en Ciencias de la Ingeniería mención Fluidodinámica de la Universidad de Chile, por permitirme realizar un trabajo multidisciplinario en la cual convergieron varias disciplinas de la Facultad de Ciencias Físicas y Matemáticas de la Universidad de Chile (FCFM). En particular, quiero reconocer y agradecer a mis supervisores de tesis, profesor Paulo Herrera Ricci, profesor Nicolás Mujica Fernandez y profesor Jaime H. Ortega Palma, por confiar en mis ideas y entregarme soporte económico, académico y humano en aquellas etapas claves del trabajo.

Estoy muy agradecido con los profesionales técnicos del taller mecánico del departamento de Física, señores Ricardo Silva, Andrés Espinoza y Christopher Pinochet. En particular, agradezco especialmente a Ricardo Silva, quien preparó las piezas de acrílico con los más altos estándares de trabajo, me enseñó de forma entusiasta el uso de la instrumentación del taller y corrigió con ingenio los innumerables problemas que surgieron durante la fabricación de piezas, sin olvidar las tardes completas donde conversábamos sobre las aventuras de camping, pesca y recreación en el sur de Chile. Muchas gracias.

Esta investigación no hubiese sido posible sin la ayuda económica de CONICYT a través de la Beca de Doctorado Nacional 21110836 y el Beneficio de Gastos Operacionales año 2014 . En particular, agradezco a Nicolás Aguilar por sus consejos y ayuda en la auditoría realizada a los gastos operacionales. Además, agradezco a los profesionales que trabajan en el Laboratorio Nacional de Computación de Alto Rendimiento del Centro de Modelamiento Matemático (CMM) por su invaluable ayuda en la ejecución de simulaciones de alta resolución. Agradezco al profesor Victor Fuenzalida, académico del departamento de Física de la FCFM, por permitirme usar la cámara térmica disponible en el laboratorio de superficies para realizar mis experimentos de transporte de calor. Agradezco el apoyo económico y académico entregado por el Centro de Excelencia en Geotermia de los Andes (CEGA) para asistir a cursos de formación en geotermia en el país y en el extranjero. En particular, agradezco al profesor Diego Morata, del Departamento de Geología de la Universidad de Chile y Director del CEGA, quién a confiado enormemente en el trabajo que hemos desarrollado en el Laboratorio de Materia Fuera del Equilibrio (LMFE) y en el proyecto de investigación en ingeniería de reservorios que he propuesto para el futuro próximo.

En estos agradecimientos, no puedo olvidar a todas las personas que he conocido en

el CEGA, en el programa doctoral en Fluidodinámica, el LMFE y el laboratorio de imágenes del CMM. Agradezco especialmente a Hugo Ulloa, Sergio Palma, Anneli Gramusset, Leonardo Gordillo, Vicente Salinas, Andrea Schmessane, Carolina Espinoza, Rodrigo Lecaros, Fernando Padilla y Takeshi Asahi por su amistad, consejos e invaluables momentos de discusión que enriquecieron mi formación como investigador. Agradezco a mi amigo Felipe Ríos Luhr, cuyos consejos en electrónica fueron fundamentales en el avance experimental. No olvido de agradecer también a las secretarias Bernardette Vásquez y Jaqueline Suarez por su gran ayuda y a la periodista Sofía Otero. Agradezco a los profesores Andrés Fuentes y Rodrigo Demarco del Departamento de Industrias de la Universidad Técnica Federico Santa María (UTFSM) y a todas las personas que forman parte del Departamento de Física de la UTFSM Campus Santiago San Joaquín, en particular a los profesores Luis Rosales, Max Rivera, Sebastián Mendizabal, Pedro Orellana, Marcelo Ruiz, Paola Lazcano, David Zambrano, Belisario Gutierrez y Juan Guadalupe por sus consejos, trabajo conjunto y por haberme ofrecido la posibilidad de desarrollar la docencia de pregrado en ingeniería como parte activa de aprendizaje durante todo mi proceso de formación doctoral. En esta parte de mi formación, también quiero agradecer a la profesora María Cristina Depassier, del Instituto de Física de la Pontificia Universidad Católica de Chile, quien permitió que pudiese estar un tiempo realizado cátedra de Física para Ciencias Biológicas. Quiero agradecer también al profesor Germán Vargas y a Gabriel Ramos, del Instituto de Física de la Pontificia Universidad Católica de Valparaíso (PUCV) campus Curauma, por permitirme trabajar en la parte de imágenes en sus proyectos experimentales de sistemas granulares, lo cual diversificó enormemente mi formación multidisciplinaria. También, agradezco al profesor Juan Brunet y a Rodrigo Sánchez, del Instituto de Química de la PUCV campus Curauma, por confiar en el proyecto experimental de fluorescencia diseñado en el LMFE y permitirme realizar un trabajo conjunto con ellos usando el fluorómetro multifase *K2* .

De forma muy especial, quiero agradecer el apoyo de mis padres y hermanos, quienes son la inspiración y fortaleza que siempre necesité en todo los momentos de mi formación educacional, a mis suegros y a mi esposa Dominique Zelada, cuyo amor, apoyo, tolerancia y paciencia determinaron la culminación exitosa de este proceso. Le agradezco a Dios por haberme permitido conocerla en ese maravilloso viaje al sur de Chile y por regalarme la luz que guía mi vida y la de ella, nuestra pequeña hija Christine Isabel.

Table of Contents

List of Tables

List of Figures

Chapter 1

Introduction

... "sigan sabiendo ustedes que, mucho más temprano que tarde,
de nuevo se abrirán las grandes alamedas por donde pase el hombre libre,
para construir una sociedad mejor"

Salvador Allende Gossens, Septiembre de 1973

What is geothermal energy?

Geothermal energy is a type of renewable energy that can be obtained by the exploitation of the internal heat of the Earth. This energy produces in the earth's surface hydrothermal manifestations such as hot springs, steam vents and mud pools, which appear when there are an important heat flux through the earth crust due to a permeable rock strata or reservoir and an adequate natural and/or artificial water recharge in zones near to the hydrothermal manifestation. In fact, water is the working fluid that transport heat from the geothermal reservoir to surface in a process known as convection. These factors make a geothermal system, which can be classified in water-dominant, vapour-dominant (dry steam) or hot-dry rock systems.

In the literature, the geothermal resource is defined as the amount of geothermal energy that can be used in economic terms. Depending on the temperature of fluids within the reservoir, the geothermal resource can be classified as low, mid or high enthalpy. Due to the heat flux in the earth crust, which has been estimated in $82\,{}^{\mathrm{mW}}/_{\mathrm{m}^2}$ (Pollack et al, 1993), there is a change of the temperature of soil with deep expressed in terms of the normal geothermal gradient, whose average value fluctuates between $25\,{}^{\circ\mathrm{C}}/_{\mathrm{km}}$ to $30\,{}^{\circ\mathrm{C}}/_{\mathrm{km}}$ (Pollack et al, 1993). However, there are regions with high geothermal gradients, associated with zones of great seismic and volcanic activity. These are the regions with the best natural conditions for the geothermal development.

Chile is a seismic and volcanic country, whose geologic activity is controlled by the subduction process of the Nazca oceanic plate with the South American continental plate (Lahssen, 1986) and where about 15% of the active volcanoes of the world are on the chilean andean range. These conditions make that the country has a high potential

for geothermal power generation. Today, estimates of the geothermal potential of Chile done by the Petroleum National Company (ENAP) and the Andean Geothermal Center of Excellence (CEGA) give values that range from 3350 MW to 16000 MW, respectively. The last estimation represents more than 90% of the current installed capacity in the country and it is greater than the entire geothermal installed capacity in the world, which is about 11200 MW. However, geothermal energy is the more ignored non-conventional renewable energy and the less known in the country.

Geothermal explorations and studies in Chile

(with contributions of Sofía Otero, from CEGA)

Geological studies in northern and southern regions have allowed a preliminary assessment of the geothermal potential of Chile at about 16000 MW for at least 50 years of geothermal fluids with temperatures above 150 °C, located less than 1000 m underground. Yet, paradoxically geothermal energy in Chile has operated almost solely for recreational purposes, for example, the thermal baths (Lahssen, 1986; Lahssen et al, 2010). Only in recent years some institutional, business and individuals initiatives have appeared to exploit the dozens of uses geothermal energy provides.

Geothermal development in Chile is an urgent challenge, as the country requires local, clean, reliable and long term energy sources. Currently, the country has very limited fossil resources. Its carbon-based energy matrix depends on imported oil and gas. Also, its energy matrix is based heavily on hydropower, which has proven to be unstable sometimes. Chile has faced three periods of significant energy stress during the past decade. The last one was in 2007/2008, when the cessation of natural gas imports from Argentina was joined by a drought in the central zone, where hydropower accounts for more than half of our electricity generation. While Chile has enormous potential for the production of geothermal power, there are still many barriers to its development. Many of these limitations have been explored by Reed (2013).

The first geothermal exploration in Chile dates from $1921 - 1922$, promoted by an Italian colony in the northern city of Antofagasta, where a technical team of Larderello drilled two wells $70\,\text{m} - 80\,\text{m}$ deep. Then, between 1968 and 1976 there were a series of geological, geophysical and geochemical surveys in selected areas of the north of the country supported by a project agreement between CORFO and the United Nations Program for Development, which culminated in the exploratory drilling in the area of El Tatio (Lahssen, 1976; Lahssen et al, 2005), where the reservoir temperature was

estimated in 270°C (Lahssen and Trujillo, 1975). Currently, El Tatio is considered as the biggest geothermal field of the Southern Hemisphere (Glennon and Pfaff, 2003).

Northern Chile was selected for the first geothermal studies. From that time onwards, the University of Chile and the National Service of Geology and Mining (SERNAGEOMIN) conducted various studies, of which follows much of the current knowledge we have on the country's geothermal potential. The areas studied with geothermal activity are in the Pliocene Holocene volcanic stretch, which is extended along the andean range. So, the origins of the geothermal activity in the zone is due to magmatism. Unfortunately, the programs in pursuit of geothermal development in Chile were paralyzed by 1979, and until 1995 the University of Chile was the main institution dedicated to research in this area (Lahssen et al, 2010, 2015). Today, CEGA is the only institution entirely dedicated to study the geothermal systems in the andean zone.

In the following, we will discuss the hydrologic and energetic problems in northern Chile, which are the main motivations for this thesis.

1.1 Engineering motivation

1.1.1 Hydrologic problems in northern Chile

Northern Chile, a vast and arid place that has an important quaternary volcanism and intense seismic activity, has been for many years the principal economic zone of Chile due to the exploitation of mineral resources. Northern Chile has the largest copper mineralization around the world and also has some of the large-scale mineral deposits. Due to the desertic characteristic of its territory, big cities of this place are located in coastal zones. In geothermal terms, about 20% of the chilean hydrothermal manifestations are in the andean mountain range, which are characterized by very hot fluids. Some of these manifestations are in the Mamiña thermal baths in the Tarapacá Region, Puritama baths in the Antofagasta Region, and Juncalito thermal baths in the Atacama Region, to name a few.

In hydrologic terms, most basins of this zone are endorheic and arheic types. The only two exorheic basins of this zone are Lluta and Loa rivers, whose source of alimentation depends on snow availability. The great Tamarugal aquifer is extended practically in the entire Tarapacá Region, which is a powerful quaternary alluvial fill. Further south, between Loa and Copiapó rivers, there is the Atacama desert, the driest place on earth.

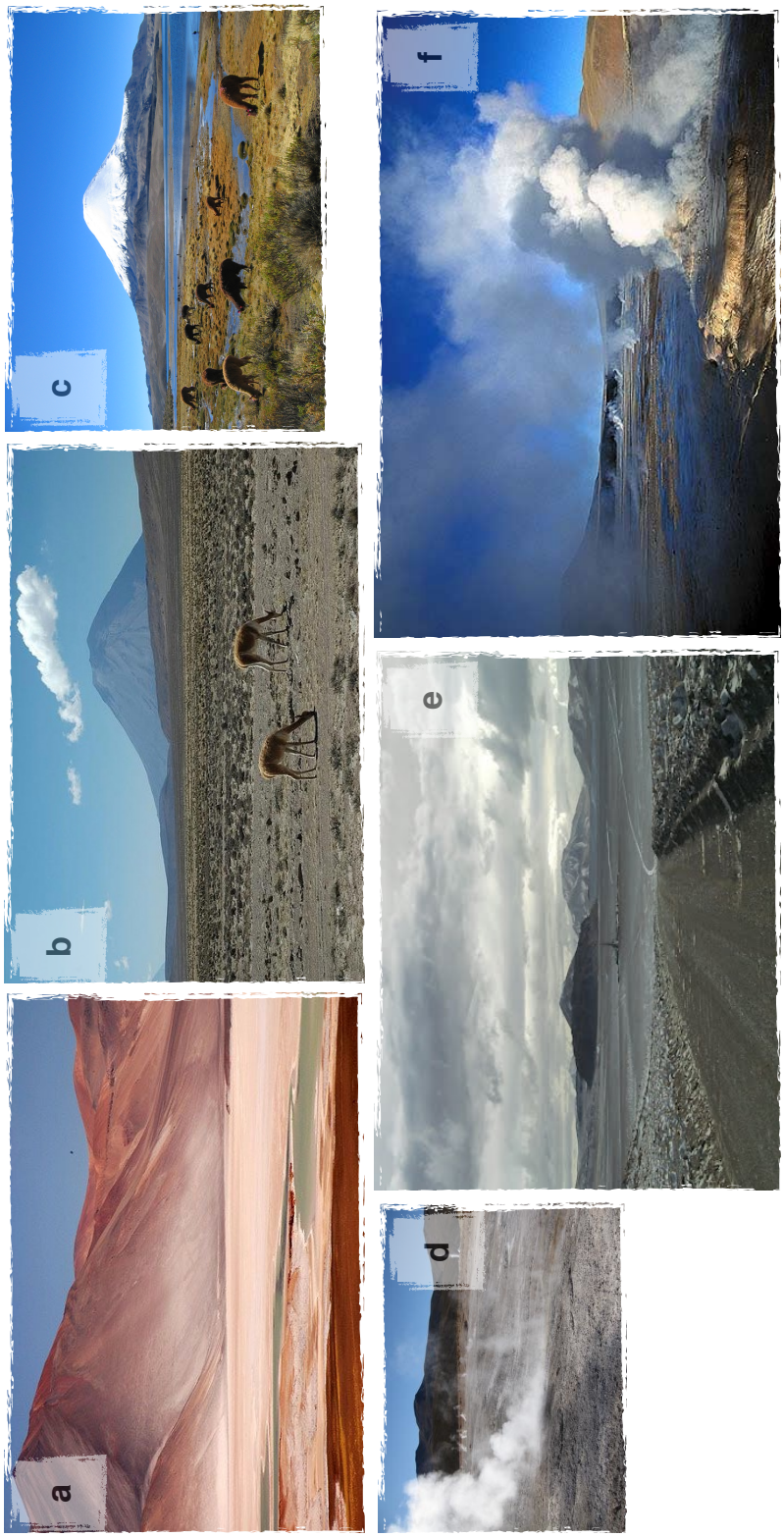

Figure 1.0.1: The northern Chile in few images. (a) Atacama desert, (b) Puchuldiza, (c) Parinacota volcano and Lauca lake, (d) Puchuldiza hydrothermal manifestation, (e) Cerro Pabellón drilling and (e) El Tatio geyser field

The aquifers of this zone are characterized by its water quality and the limited natural recharge, which are completely unfavourable for exploitation (E. Brown and J. Saldivia, 2000).

The climatic system that allows the existence of the Atacama desert and the rainy scarcity in northern Chile is the "South Pacific High", a subtropical anticyclone located in the southeast Pacific of Chile. Practically, the Tarapacá, Antofagasta and Atacama Regions are heavily influenced by this semi-permanent high pressure area in the ocean. However, in the chilean andean plateau, in each summer of the south hemisphere there is a climatic phenomenon known as the "bolivian winter". This phenomenon is characterized by orographic rainy caused by moist air masses provenients from the Amazonas, where the formation of cumuliform clouds in the andean region can generate heavy rains with a high spatial variability in endorheic high elevation basins. The amount of precipitation due to this phenomenon is about $300\,{}^{\mathrm{mm}}/_{\mathrm{year}}$ in zones close to Lauca National Park and about $150\,{}^{\mathrm{mm}}/_{\mathrm{year}}$ in San Pedro de Atacama (E. Brown and J. Saldivia, 2000; MOP-DGA, 2011).

In the endorheic high elevation basins, the aquifers are quaternary formations of volcanic rocks with a high secondary permeability. In basins at lower height, where can be observed salt flats, the aquifers are non-consolidated sediments of alluvial-fluvial origin. In general, these aquifers have a good productivity and the water quality is acceptable while fluids do not reach the salt flats (IDI-Chile, 2011). Thereby, the groundwater resources are used for domestic and mining processes, which currently have overexploitation. Considering the domestic use, in 2009 it has been estimated that water supply per person in northern Chile was 854 m^3/person/year in Tarapacá Region, 52 m^3/person/year in Antofagasta Region and 208 m^3/person/year in Atacama Region, which is undoubtedly lower than 2000 m^3/person/year requiered for human sustainable development (MOP-Chile, 2013). On the other hand, water consumption by mining in Chile represented about 9% of the national water requirements.

To maintain the energetic productivity of a geothermal reservoir for a long time, it is necessary to reinject water directly to the reservoir. This reinjection allows the control and andjusment of the pressure lost by the extraction of water within the reservoir. Due to water scarcity in northern Chile, the lack of information about groundwater amount in high elevation basins and the current and future demand of water resources, where mining can grow its demand in 200% in the next 25 years (MOP-Chile, 2013), water recharge in geothermal reservoirs can be a problem for the geothermal development in northern Chile, being an interesting topic of research for the engineering sciences.

1.1.2 CO_2 emissions in northern Chile

Due to water scarcity for energy generation in hydroelectric power plants, historically northern Chile have used the combustion of fossil resources to satisfy its energetic needs. In this zone, mining and thermoelectric power plants have an important contribution to the chilean CO_2 emissions. For example, in 2008 , mining activity emitted about 17 million ton of CO_2 to the atmosphere (Pimentel, 2009), where about 24% was due to mining operations and 76% was due to the electric energy used, which was generated from combustion of fossil resources in thermoelectric power plants in coastal zones. This amount of CO_2 emissions was about 30% of the total of greenhouse gases released by chilean industrial production during 2008 .

Currently, the energy matrix of SING is dominated by fossil combustion. In 2015 , it represented about 94% of the electric power generation of northern Chile with an installed capacity of 4390 MW and energy generation of about 16530 GWh , where about 42% was generated from carbon combustion, 44% by natural gas and 8% by diesel oil (ME-Chile, 2015). In 2010 , the chilean thermoelectric power plants that used carbon for its operations emitted between 0.95 kg to 1.40 kg of CO_2 per kWh generated, which is twice the generated emission by combustion of other sources, such as diesel and natural gas (ING-Chile, 2011). Thereby, attending to the current environmental demands for the diversification of the energy matrix, which looks to reduce the greenhouse gas emissions to the atmosphere, an interesting scientific and technological challenge is proposed, which motivates this thesis. Brown (2000) and Randolph and Saar (2011a) proposed the novel idea of use CO_2 captured from contaminant sources as working fluid in geothermal power plants, replacing water. This innovating idea can be attractive for northern Chile, where the scarcity of water and CO_2 contaminantion due to thermoelectric and mining operations threaten not only the geothermal energy development, but also the local environment.

1.2 Physical motivation

The aim of the enhanced geothermal systems is to exploit economically the geothermal resources in zones where the factors that allow the ocurrence of a geothermal system are not optimal. Brown (2000) proposed the use of supercritical CO_2 as working fluid instead of water in geothermal systems due to its physicochemical properties in reservoir conditions, which can be favourable for the operations of the geothermal power plants.

Some of these properties detailed by Brown (2000), Pruess (2006) and Magliocco et al (2011) are

- The expansivity of CO_2 can generate big differences between the cold fluid injected and the hot fluid extracted. This feature would generate strong buoyant forces which could reduce the energy consumption used in bombs for fluid circulation.
- The smaller viscosity of supercritical CO_2 , in comparison to water, would allow to inject within the reservoir greater amounts of CO_2 with less costs.
- Supercritical CO_2 would be a solvent less effective for mineralized rocks, which could eliminate some issues such as silica dissolution and precipitation in water dominated geothermal systems. The slow kinetics of mineral-fluid reactions of dry supercritical CO_2 (Oelkers et al, 2008) can reduce the failures in equipments.
- In zones with water scarcity, the hot dry rock systems can be used as enhanced geothermal systems if supercritical CO_2 is used as working fluid for hydraulic fracturing and heat transport.

In spite of these favourable features, CO_2 in reservoir conditions has a smaller specific heat than water. However, the heat transport can be compensated by the viscosity of CO_2 because the high flux amounts that would be injected and extracted from the injection/production wells could enhance the fluid displacements inside the reservoir.

The supercritical CO_2 injection has been used in the last fourty years by oil companies with the aim to enhance the oil recovery from reservoirs. Currently, the capture of CO_2 and its storage in geologic formations onshore and offshore is considered as one of the most promissing solutions to reduce the release of greenhouse gases to the atmosphere (Holloway, 1997; Benson et al, 2006; Orr, 2009). CO_2 is less dense than water, so the CO_2 stored underground tends to move upward until achieve the surface again and a possible CO_2 leakage would be dangerous for the life in near zones to the leakage. To prevent these hazards, the upward motion of CO2 can be controlled by injecting the gas in geological formations that have a caprock in its upper boundary, so the gas can be confined underground by a long time. These storage mechanism is called the stratigraphic confinement (Bachu et al, 1994). One of the most recognized projects that use the capture and storage technology is the Sleipner project in the Northern Sea in Norway, which since 1996 stores 1 Mton of CO_2 per year (Audigane et al, 2007).

Holloway (1997) identified three types of reservoirs where CO_2 can be stored in subsurface, which are: (a) empty oil and gas reservoirs, (b) unexploitable carbon reservoirs and (c) saline aquifers. From these reservoirs, the saline aquifers offer more advantages than the others because they have a greater volumetric capacity and are more abundant. After the injection, within the reservoir some physicochemical processes alter the composition of CO_2 and the underground fluids. These processes occur in different geologic time scales and they correspond to other storage mechanisms. In addition to the stratigraphic confinement, there is the solubility trapping (Teng et al, 1997; Linderberg and Wessel-Berg, 1997; Ennis-King and Paterson, 2003), where supercritical CO_2 begins to mix with the aquifer fluids, generating a vertical downward motion that enhances the mass transfer of diluted CO_2 within the reservoir. Other storage mechanisms can be seen in Fig. 1.2.1, where the spatial scale features of the different confinement options are discussed. In general, multiscale problems are a big challenge for porous media modeling.

Currently, the study of CO_2 dissolution in deep saline aquifers and its vertical transport are an interesting an active research topic (Riaz et al, 2006; Audigane et al, 2007; Neufeld et al, 2010; Golding et al, 2011; Gasda et al, 2012; Nordbotten and Celia, 2011; Gray et al, 2012; Celia et al, 2015). In relation to the Brown's proposal, Randolph and Saar (2011b) mentioned that supercritical CO_2 can be used not only as working fluid for heat transport in geothermal reservoirs, but also for solubility confinement in the same reservoir. Therefore, they proposed the carbon dioxide geothermal plume technology. Basically, the proposal indicates that CO_2 must be captured from contaminant sources and then it must be injected directly into a geothermal reservoir with a caprock in its upper boundary. CO_2 is partially miscible with reservoir fluids (Pruess and Garcia, 2002), so the principal effect is the displacement of these fluids. Finally, within the reservoir, supercritical CO_2 will be the dominant fluid-phase. A big amount of CO_2 will be stored, while in the production wells, a small amount of hot CO_2 is extracted for energy generation. This process is similar to the classical operations of geothermal power plants with water, so the remanent warm CO_2, which was used in turbines for energy extraction, is transported to the cooling towers and then the cold CO_2 is injected again to the reservoir, closing the process. Therefore, to study the factibility of this technology, it is necessary to understand the physical processes of heat and mass transport of CO_2 underground. Physically, the study of the mass transport of diluted CO_2 for different geothermal conditions, i.e., for different temperatures and heat flux conditions from boundaries, acquires real importance and it is a line of research that has

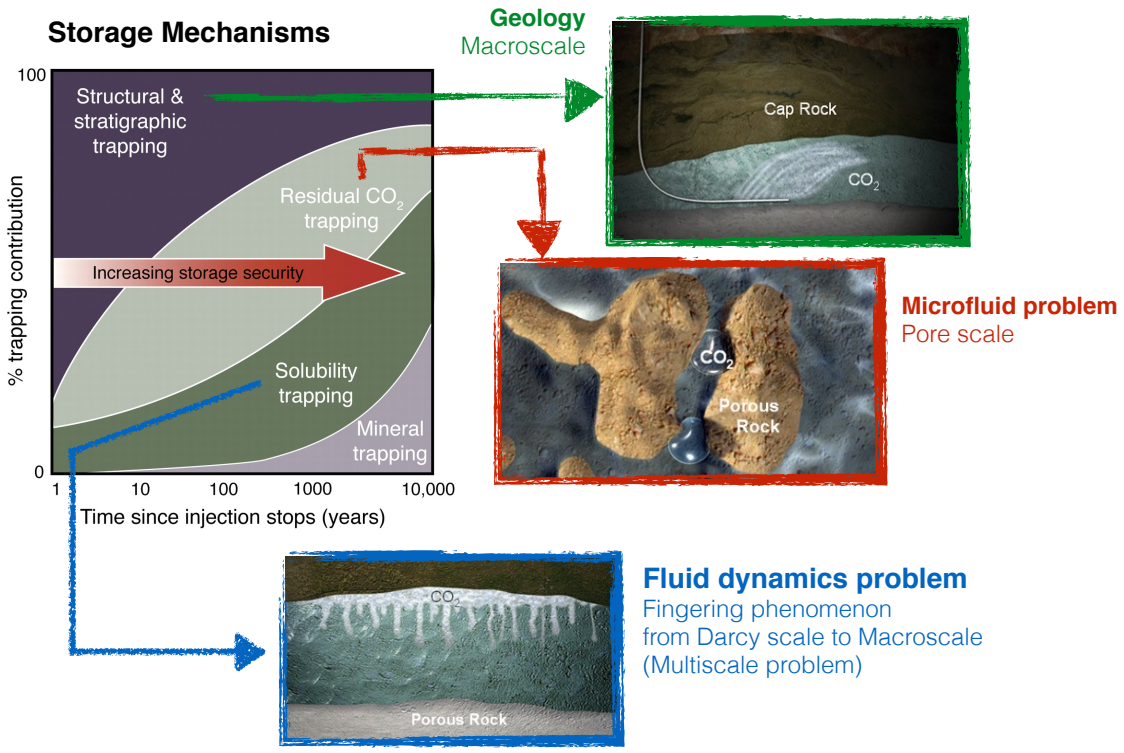

Figure 1.2.1: Storage mechanisms asociated to the injection of supercritical CO_2 in geologic formations. The first mechanism in importance is the stratigraphic confinement, which is a macroscale problem studied by geologist. The second mechanism is the solubility trapping, where CO_2 is mix with reservoir fluids, enhancing the CO_2 transport within the reservoir through multiscale fingering phenomenon. This mechanism is one of the most studied problems in porous media and fluid dynamics. The third mechanism is the residual trapping, where CO_2 is confined in the porous matrix. This phenomenon occurs at the pore scale. Finally, the mineral trapping is the last result of the physicochemical processes, where CO_2 is mineralized in the porous matrix. After many thousands of years, the product of the mineral carbonation is the caliza stone. Retrieved March 30, 2016, from http://www.co2captureproject.org/co2_trapping.html

not yet been developed. Because we are interested in study the use of CO_2 as working fluid in geothermal reservoirs instead of water, the purposes of this research are the development of a mathematical model valid in the laboratory scale, the implementation of numerical simulations to study the scaling laws of the problem and the realization of experiments at laboratory scale, with the aim to understand the physical processes that governs the fluid mixing in homogeneous porous media. This ideal model allow us to extent our model to a most realistic case in the future. We refer the work of Huppert and Neufeld (2014) for further information.

1.3 Open questions and contributions of this work

Although some advances have been achieved in the understanding of the physical processes inside a geothermal reservoir, many questions related with the mixing of two-fluid phases in porous media have not yet been solved. One of the most important questions for the carbon dioxide geothermal technology is to study how can affect the geothermal conditions in the CO_2 mass transport. This question is very complicated to answer in the mathematical physics context because fluid mixing in porous media has a multiscale nature, from pore scale to macroscale, so a theoretical understanding of the processes that governs the scalar transport is insufficient. We also need to run laboratory scale experiments, with the aim to visualize these processes, as far as possible, as well as to corroborate theoretical predictions. In particular, in this work we want to give some answers to the following scientific questions:

1. How can the Darcy model used to model the fluid dynamics be affected by inertial corrections?
2. Can heat transport be affected by the scalar mechanical dispersion?
3. Which are the physical conditions that support the nonlinear scaling between the Rayleigh number and the mean scalar dissipation rate?
4. What is the importance of boundary conditions in the onset of convection?

Thereby, the main work objectives of the research presented in this manuscript are:

- To derive from first principles, a new model consistent with the Hele-Shaw geometry, where inertial corrections and mechanical dispersion can appear naturally.
- To study using advanced mathematical tools and numerical simulations, the scaling laws from the mathematical model derived before.
- Run laboratory scale experiments using analogue fluids that represent the fluid dynamics expected in geothermal reservoirs, with the aim to visualize the scalar transport processes through advanced image analysis methods.

We hope that the reader can find all the mathematical tools, image analysis methods and experimental techniques needed for its own research interests related with fluid

mixing in porous media, as well as to enrich its knowledge from this interdisciplinary work. We have organized this manuscript in three parts, which are related with the three main work objectives that have been developed during the last three years of research.

In Part I we review the literature. Furthermore, we give some definitions for the mathematical notation used in this work. In Part II we review the theory of multiphase fluid flow and heat transport in porous media to model the fluid dynamics inside a Hele-Shaw cell. In Chapter 5, we present novel nonlinear equations for homogeneous porous medium. We derives these equations using regular perturbation theory and the Navier-Stokes model, which includes some classical nonlinear terms in porous media modeling and new destabilizing terms. Some specific discussion about the importance of inertial terms and dimensional analysis of mixing properties is also included. In this discussion and analysis, we present a new hyphotesis about the scaling laws that govern the mixing of two-fluid phases. Chapter 6 is devoted to a more mathematical problem that is the linear analysis of non-autonomous differential equations, which are very complicated to analyze using standard modal methods. We demonstrate that this drawback can be fixed using the known dominant mode method. The purpose of the application of advanced mathematical tools to the linearized equations is finding analytical solutions that capture the fluid dynamics in the onset of both thermal and density-driven convection, for the case of constant viscosity. We correct the linear analysis reported in literature for thermal convection, as well as we give new insight of the problem when including the effective interfacial tension for the Rayleigh-Taylor instability driven by density contrast, showing a notable stabilizing effect.

Part III shows the main results of numerical simulations performed for the so-called Rayleigh-Benard convection in porous media. In Chapter 7, we study the mathematical model derived in Chapter 5 for a particular case of a single fluid with constant viscosity. A total of 52 simulations were performed for two different cases of the Hele-Shaw geometry. From these results, we compute the global heat transport coefficient and the mean scalar dissipation rate as function of the Rayleigh number, obtaining new results for the scaling laws. This is the most important contribution of this work.

In Part IV, we present and discuss experimental results. About 70% of the total research time was used to design, implement and execute laboratory scale experiments that enable the visualization of transport processes within a porous medium. In Chapter 8, we present the optical density visualization methods that were used in the first stages of this research. In Chapter 9, we show the image processing methods used to

analyze quantitatively the images obtained from the experiments. An interdisciplinary approach was achieved in this chapter, because we introduce powerful mathematical techniques in image analysis as an interesting tool for experimental fluid dynamics, which is novel for both applied mathematics and experimental physics. In Chapter 10, we apply the TV-L^1 optical flow method and the Synthetic Schlieren technique to analyze thermal convection in an homogeneous porous media with applications to geothermal sedimentary basins. The main contribution of this interdisciplinary work is the enhancement of the image resolution obtained by this experimental technique, as well as the visualization of unsteady rolls which are characteristic in geothermal convection. Finally, in Chapter 11, we present a summary of the most significant results, as well a discussion of the future work.

The appendices contain additional information of the models reported in literature, computations and numerical methods used in this work. Fig. 1.3.1 shows a schematic picture that summarizes the research done. In this figure, the theoretical framework corresponds to the work presented in Part II. The governing equations are used to perform direct numerical simulations of heat transfer in porous media. The linear analysis for thermal convection confirms the numerical results obtained for the onset of convection. Nonlinear simulations corresponds to the work presented in Part III, where we obtain new scalings for the high-Ra regime. Finally, visualization and image analysis corresponds to the work presented in Part IV, where the Chan-Tai method and the TV-L^1 optical flow are applied to the experimental images. In the case of thermal convection, the results obtained from Synthetic Schlieren and the numerical simulations are compared, obtaining a good agreement between them.

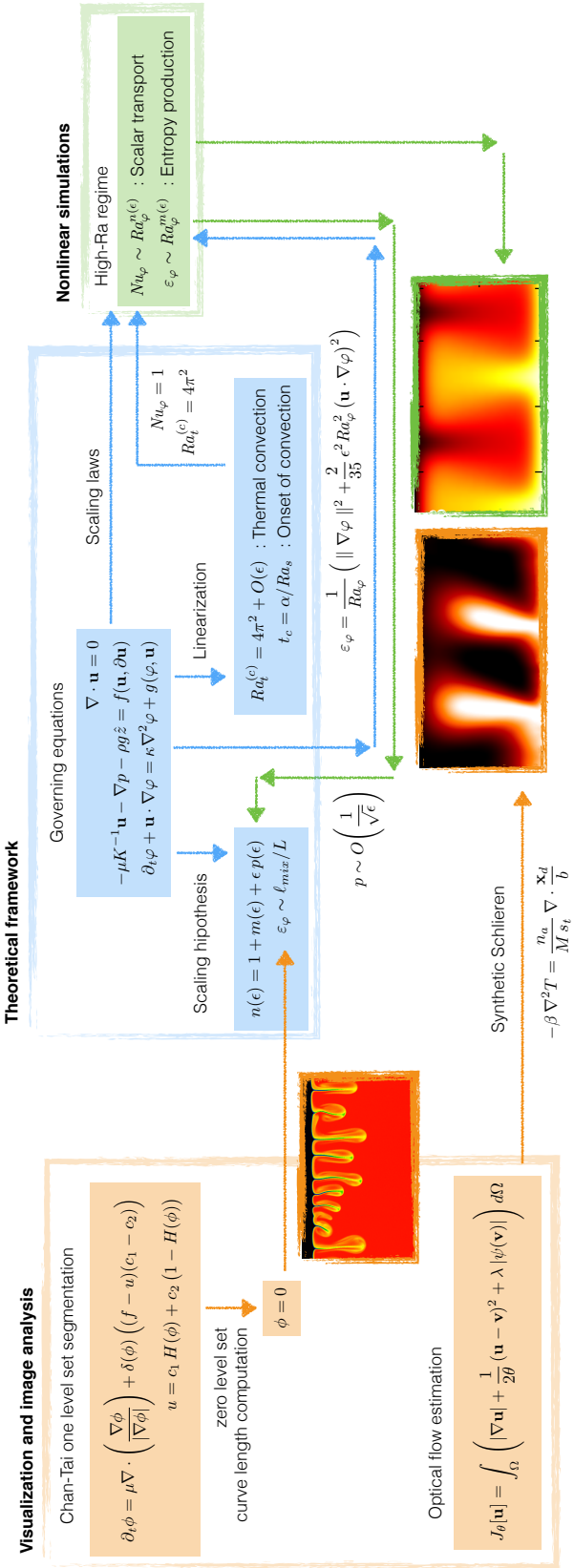

Figure 1.3.1: Summary of the research done

Part I

Literature review and previous concepts

Chapter 2

Dimensional quantities and notation

In this work, we will use the physical quantities presented in Tables 2.1 and 2.2. The definition of the dimensionless numbers used in the following chapters arise from the ratio of two or more quantities presented in these tables. With regard to the notation used in this work, a time-dependent scalar function defined by $f : \mathbb{R}^{n+1} \to \mathbb{R}$ will be denoted as $f = f(\mathbf{x}, t)$. On the other hand, a time-dependent vectorial function defined by $\mathbf{F} : \mathbb{R}^{n+1} \to \mathbb{R}^n$ will be denoted as $\mathbf{F} = \mathbf{F}(\mathbf{x}, t)$.

For time-dependent scalar functions defined by $f : [L, H] \subset \mathbb{R}^2 \to \mathbb{R}$ and denoted as $f = f(\mathbf{x}_\perp, t)$, with $\mathbf{x}_\perp = x\hat{x} + z\hat{z}$, the average in the x-direction is computed as

$$\bar{f}(z, t) = \frac{1}{L} \int_0^L f(\mathbf{x}_\perp, t)\, dx \,. \tag{2.0.1}$$

For the same scalar function, the domain average is defined as

$$\langle f \rangle(t) = \frac{1}{H} \int_0^H \bar{f}(z, t)\, dz \,. \tag{2.0.2}$$

These definitions also apply for time-dependent vectorial functions. Eqns. (2.0.1) and (2.0.2) will be useful in the derivation of global models of mixtures presented in Chapter 5, Section 5.4 on page 60 and Chapter 7, Section 7.2 on page 96.

For time-dependent scalar functions defined by $f : [L, b, H] \subset \mathbb{R}^3 \to \mathbb{R}$ and denoted as $f = f(\mathbf{x}, t)$, with $\mathbf{x} = x\hat{x} + y\hat{y} + z\hat{z}$, the average in the y-direction is computed as

$$\{f\}(\mathbf{x}_\perp, t) = \frac{1}{b} \int_0^b f(\mathbf{x}, t)\, dy \,. \tag{2.0.3}$$

Eqn. (2.0.3) will be useful in the derivation of the two-dimensional Hele-Shaw model from the Navier-Stokes equation (For further information, see Chapter 5, Section 5.2 on page 50). In this work, the subscript t is related with thermal convection, while the subscript s is related with mixing convection. For example, along the thesis, we will work with a dimensionless quantity called the Rayleigh number Ra_φ, where the scalar φ can be temperature T or concentration S_w. When $\varphi = T$, Ra_t is the thermal Rayleigh number. On the other hand, if $\varphi = S_w$, Ra_s is the solutal Rayleigh number.

A more sophisticated notation is used to compute heat and mass transfer quantiites, the Nusselt number (defined in Eqn. (4.1.10) on page 32) and the mean scalar dissipation

Table 2.1. Notation and dimensions of physical quantities used in this work

Physical quantity	**Notation**	**Dimension**
Position	$\mathbf{x}$	L
Time	t	T
Velocity	$\mathbf{u}$	LT^{-1}
Gravitational acceleration	g	LT^{-2}
Fluid density	ρ	ML^{-3}
Ambient fluid density	ρ_a	ML^{-3}
Density contrast	$\Delta\rho$	ML^{-3}
Dynamic viscosity	μ	$ML^{-1}T^{-1}$
Ambient dynamic viscosity	μ_a	$ML^{-1}T^{-1}$
Kinematic viscosity	$\nu = \mu/\rho$	L^2T^{-1}
Ambient kinematic viscosity	$\nu_a = \mu_a/\rho_a$	L^2T^{-1}
Pressure	p	$ML^{-1}T^{-2}$
Modified pressure	$\tilde{p}$	$ML^{-1}T^{-2}$
Molecular diffusivity	κ_s	L^2T^{-1}
Thermal diffusivity	κ_t	L^2T^{-1}
Water mass fraction (concentration)	S_w	1
Temperature	T	τ
Effective interfacial tension	ϕ	$M^{-1}L^7T^{-2}$
Macroscale interfacial tension	γ_ϕ	MT^{-2}
Hele-Shaw cell height	H	L
Hele-Shaw cell width	L	L
Hele-Shaw cell gap	b	L
Permeability of Hele-Shaw cells	$K = b^2/12$	L^2

Table 2.2. Scalings and dimensionless numbers used in this work

Physical quantity	**Notation**	**Dimension**
Characteristic convective velocity	$u_c = \Delta\rho\, g\, b^2/\mu_a$	LT^{-1}
Characteristic convective time	$t_c = H/u_c$	T
Characteristic pressure	$p_s = \mu_a\, u_c\, H/b^2$	$ML^{-1}T^{-2}$
Porous media convective velocity	$\bar{u}_c = \Delta\rho\, g\, K/\mu_a$	LT^{-1}
Porous media convective time	$\bar{t}_c = H/\bar{u}_c$	T
Porous media characteristic pressure	$\bar{p}_s = \mu_a\, \bar{u}_c\, H/K$	$ML^{-1}T^{-2}$
Dimensionless numbers		
Anisotrophy ratio	$\epsilon = \sqrt{K}/H$	
Prandtl number	$Pr = \nu_a/\kappa_t$	
Schmidt number (Prandtl for mass transfer)	$Sc = \nu_a/\kappa_s$	
Thermal Rayleigh number	$Ra_t = \bar{u}_c\, H/\kappa_t$	
Solutal Rayleigh number	$Ra_s = \bar{u}_c\, H/\kappa_s$	
Thermal Peclet number	$Pe_t = \epsilon\, Ra_t$	
Solutal Peclet number	$Pe_s = \epsilon\, Ra_s$	
Reynolds number	$Re = Ra_t\, Pr^{-1}$	

rate (defined in Eqn. (4.1.13) on page 33). The Nusselt number Nu_φ, where φ is either temperature or concentration, can be computed by two methods:

- The time-average method, which is used in theoretical computations

$$\langle Nu_\varphi \rangle_\tau = \frac{1}{\tau} \int_{\tau_0}^{\tau_0+\tau} Nu_\varphi(t)\, dt \quad ; \quad \tau_0 \gg 1\,. \tag{2.0.4}$$

- The geometrical method, which is used in experimental computations. We denote this quantity as $Nu_\varphi^{(g)}$.

Both definitions must satisfy the equivalence relation $Nu_\varphi^{(g)} = \langle Nu_\varphi \rangle_\tau$, which enables to compare the experimental and theoretical results. Similarly, the mean scalar dissipation rate ε_φ can also be computed by the same methods:

- The time-average method, which is used in theoretical computations. In this case,

ε_φ must be previously averaged over the domain

$$\langle \varepsilon_\varphi \rangle_\tau = \frac{1}{\tau} \int_{\tau_0}^{\tau_0+\tau} \langle \varepsilon_\varphi \rangle(t)\, dt \quad ; \quad \tau_0 \gg 1 \,. \tag{2.0.5}$$

- The geometrical method, which is used in experimental computations. We denote this quantity as $\langle \varepsilon_\varphi \rangle^{(g)}$.

As well as for the Nusselt number, both definitions must satisfy the equivalence relation $\langle \varepsilon_\varphi \rangle^{(g)} = \langle \varepsilon_\varphi \rangle_\tau$. All the physical quantities, scalings and mathematical notations showed in this chapter will be given again in each chapter and section of this work, if it so required.

Chapter 3

Physics of fluid mixtures

3.1 Dimensionless concentration quantities

Consider an ideal solution made with N different species. The basic concentration measurements used in this work are

- Mass concentration or density

$$\rho_k = \frac{m_k}{V_{total}} = \frac{\text{mass of the } k\text{th specie}}{\text{volume of solution}} \,. \tag{3.1.1}$$

- Molar concentration

$$c_k = \frac{n_k}{V_{total}} = \frac{\text{number of moles of the } k\text{th specie}}{\text{volume of solution}} \,. \tag{3.1.2}$$

The dimensionless quantities related with the definitions given in Eqns. (3.1.1) and (3.1.2) are

- Mass fraction (percentage by weight, wt%)

$$S_k = \frac{m_k}{m_{total}} = \frac{\rho_k}{\rho_{total}} \quad ; \quad m_{total} = \sum_{k=1}^{N} m_k \quad ; \quad \rho_{total} = \sum_{k=1}^{N} \rho_k \,. \tag{3.1.3}$$

- Molar fraction (percentage by moles, mol%)

$$x_k = \frac{n_k}{n_{total}} = \frac{c_k}{c_{total}} \quad ; \quad n_{total} = \sum_{k=1}^{N} n_k = c_{total}\, V_{total} \quad ; \quad c_{total} = \sum_{k=1}^{N} c_k \,. \tag{3.1.4}$$

- Volume fraction (percentage by volume, vol%)

$$\upsilon_k = \phi\, \bar{s}_k = \frac{V_k}{V_{total}} \,, \tag{3.1.5}$$

where ϕ is the porosity and $\bar{s}_k$ is the saturation of the kth specie.

From these definitions, we obtain the normalization relations $\sum_k S_k = 1$, $\sum_k x_k = 1$ and $\sum_k v_k = 1$. Also, we define the mean molar mass $\bar{M}$ as

$$\bar{M} = \frac{\rho_{total}}{c_{total}} , \tag{3.1.6}$$

and the molar mass of the kth specie as

$$M_k = \frac{m_k}{n_k} . \tag{3.1.7}$$

Using this definition, from Eqn. (3.1.7) we have $x_k M_k = m_k/n_{total}$. Next, from Eqns. (3.1.4) and (3.1.6) we obtain $n_{total} = m_{total}/\bar{M}$. Therefore, using the expressions derived before, the relation between the mass fraction S_k and the molar fraction x_k of the kth specie is

$$S_k = \frac{x_k M_k}{\bar{M}} = \frac{x_k M_k}{\sum_k x_k M_k} . \tag{3.1.8}$$

Eqn. (3.1.8) will be useful in Section 3.3.

3.2 Two-fluid miscible model

For a mixture made with two miscible fluids in isothermal conditions, the density can be written as

$$\rho(\mathbf{x}, t) = \rho_A S_A(\mathbf{x}, t) + \rho_B S_B(\mathbf{x}, t) , \tag{3.2.1}$$

where $S_A(\mathbf{x}, t)$ is the mass fraction of the fluid A as function of position $\mathbf{x}$ and time t and $S_B(\mathbf{x}, t) = 1 - S_A(\mathbf{x}, t)$ is the mass fraction of the fluid B . Moreover, ρ_A and ρ_B are the densities of fluids A and B , respectively, for a fixed temperature. The microscopic continuity equation is

$$\frac{\partial \rho}{\partial t} + \nabla \cdot (\rho \, \mathbf{u}) = 0 . \tag{3.2.2}$$

Therefore, replacing Eqn. (3.2.1) in Eqn. (3.2.2) leads to the equation

$$\frac{\partial(\rho_A S_A)}{\partial t} + \nabla \cdot (\rho_A S_A \mathbf{u}) = -\left[\frac{\partial(\rho_B S_B)}{\partial t} + \nabla \cdot (\rho_B S_B \mathbf{u}) \right] . \tag{3.2.3}$$

The introduction of diffusion is essential to relate appropiately the mixing behavior at the molecular scale between fluid A and fluid B. For fluid A, Eqn. (3.2.3) can be written as

$$\frac{\partial(\rho_A S_A)}{\partial t} + \nabla \cdot (\rho_A S_A \mathbf{u}) = \nabla \cdot \left(\kappa \, \rho_A \, \nabla S_A\right) , \tag{3.2.4}$$

where κ is the molecular diffusion between both fluids. The solution of Eqn. (3.2.4) determines the mass fraction $S_B(\mathbf{x}, t)$. In general, the density can be written as

$$\rho(\mathbf{x}, t) = \rho_0 + \bar{\rho}(z) + \rho'(\mathbf{x}, t) , \tag{3.2.5}$$

where ρ_0 is a reference density, $\bar{\rho}(z)$ is an initial vertical density distribution and ρ' is a perturbation. When $\rho' \ll \rho_0$ and $\bar{\rho} \ll \rho_0$, the Oberbeck-Boussinesq approximation can be used. For this case, Eqn. (3.2.2) is converted to the incompressibility equation

$$\nabla \cdot \mathbf{u} = 0 . \tag{3.2.6}$$

and assuming κ as constant, Eqn. (3.2.4) is converted to the scalar transport equation

$$\frac{\partial S_A}{\partial t} + \mathbf{u} \cdot \nabla S_A = \kappa \, \nabla^2 S_A . \tag{3.2.7}$$

Hereinafter, the mass fraction S_A will be called concentration. To recover the density, it is important to have a constitutive model $\rho = \rho(S_A)$. In Section 3.3, we present the model for aqueous solutions of propylene-glycol, which is used to model CO_2 dissolution in geologic reservoirs through analogue experiments in the laboratory scale.

3.3 Model for aqueous solutions of propylene-glycol

Aqueous solutions of propylene-glycol (PPG) have become in a very popular working fluid for the representation of the solubility trapping of supercritical CO_2 in saline aquifers (Backhaus et al, 2011; Ehyaei, 2014) (For further information, see Chapter 4, Section 4.2 on page 34). In this section, we present PPG+water mixture as an example of a two-fluid system where the theory presented in Section 3.1 and 3.2 can be applied. The relation between the mass fraction (concentration) and molar fraction for aqueous solutions of PPG is given by Eqn. (3.1.8)

$$S_w = \frac{x_w \, M_w}{x_w \, M_w + (1 - x_w) M_{ppg}} , \tag{3.3.1}$$

where S_w is the water concentration in the mixture, x_w is the molar fraction of water, $M_w = 18.01528\,\mathrm{g/mol}$ is the molar mass of water and $M_{ppg} = 76.09\,\mathrm{g/mol}$ is the molar mass of PPG. When $S_w = 1$ we have pure water, while for $S_w = 0$ we have PPG. Eqn. (3.3.1) is useful when mixture data is given in terms of the molar fraction.

Sun and Teja (2004) performed measurements of the density, viscosity and thermal conductivity of PPG+water at temperatures ranging from 290 K to 460 K and molar fractions ranging from 25 mol% glycol to 100 mol% glycol. The density model obtained by Sun and Teja is

$$\rho(S_w) = \sum_{i=1}^{3}\sum_{j=1}^{3} A_{ij}\,(1-S_w)^{i-1}\,T^j\,, \tag{3.3.2}$$

and the viscosity model is

$$\begin{aligned}\log\mu(x_w,T) = {} & S_{ppg}\,\log\mu_{ppg}(T) + S_w\,\log\mu_w(T) + \\ & \Big(\log\mu_{ppg}(T) - \log\mu_w(T)\Big)\,S_{ppg}\,S_w\,\Big(B_4 + B_5\,S_{ppg} + B_6\,T + B_7\,S_{ppg}^2\Big)\,,\end{aligned} \tag{3.3.3}$$

$$\log\mu_{ppg}(T) = B_1 + B_2\,T + B_3\,T^2\,, \tag{3.3.4}$$

$$\log\mu_w(T) = B_8 + \frac{B_9}{T + B_{10}}\,, \tag{3.3.5}$$

where $[\rho] = \mathrm{kg/m^3}$ and $[\mu] = \mathrm{cP}$ if $[T] = {}^\circ\mathrm{C}$. Also, $S_{ppg} + S_w = 1$. The values of A_{ij} and B_k parameters are given in Table 3.1.

On the other hand, Khattab et al (2012) reported measurements of density, viscosity, surface tension and molar volume of PPG+water mixtures at temperatures ranging from 293 K to 323 K. The Jouyban-Acree model was used for mathematical correlation of the density and viscosity, which are given by the equations

$$\begin{aligned}\log\rho(x_w,T) = {} & x_{ppg}\,\log\rho_{ppg}(T) + x_w\,\log\rho_w(T) + \\ & J_0\left[\frac{x_{ppg}\,x_w}{T}\right] + J_1\left[\frac{x_{ppg}\,x_w\,(x_{ppg}-x_w)}{T}\right] + J_2\left[\frac{x_{ppg}\,x_w\,(x_{ppg}-x_w)^2}{T}\right]\,,\end{aligned} \tag{3.3.6}$$

$$\log\rho_{ppg}(T) = J_3 + \frac{J_4}{T}\,, \tag{3.3.7}$$

$$\log \rho_w(T) = J_5 + \frac{J_6}{T} + \frac{J_7}{T^2} \,, \tag{3.3.8}$$

$$\log \mu(x_w, T) = x_{ppg}\, \log \mu_{ppg}(T) + x_w\, \log \mu_w(T) + K_0 \left[\frac{x_{ppg}\, x_w}{T}\right] + K_1 \left[\frac{x_{ppg}\, x_w\, (x_{ppg} - x_w)}{T}\right] , \tag{3.3.9}$$

where $x_{ppg} + x_w = 1$, $[\rho] = {}^{\mathrm{kg}}/_{\mathrm{m}^3}$ and $[T] = \mathrm{K}$. The values of J_i and K_i parameters are given in Table 3.1. Fig. 3.3.1(a) and Fig. 3.3.1(b) show the application of the models presented in Eqns. (3.3.2) and (3.3.6), which are compared with the experimental data.

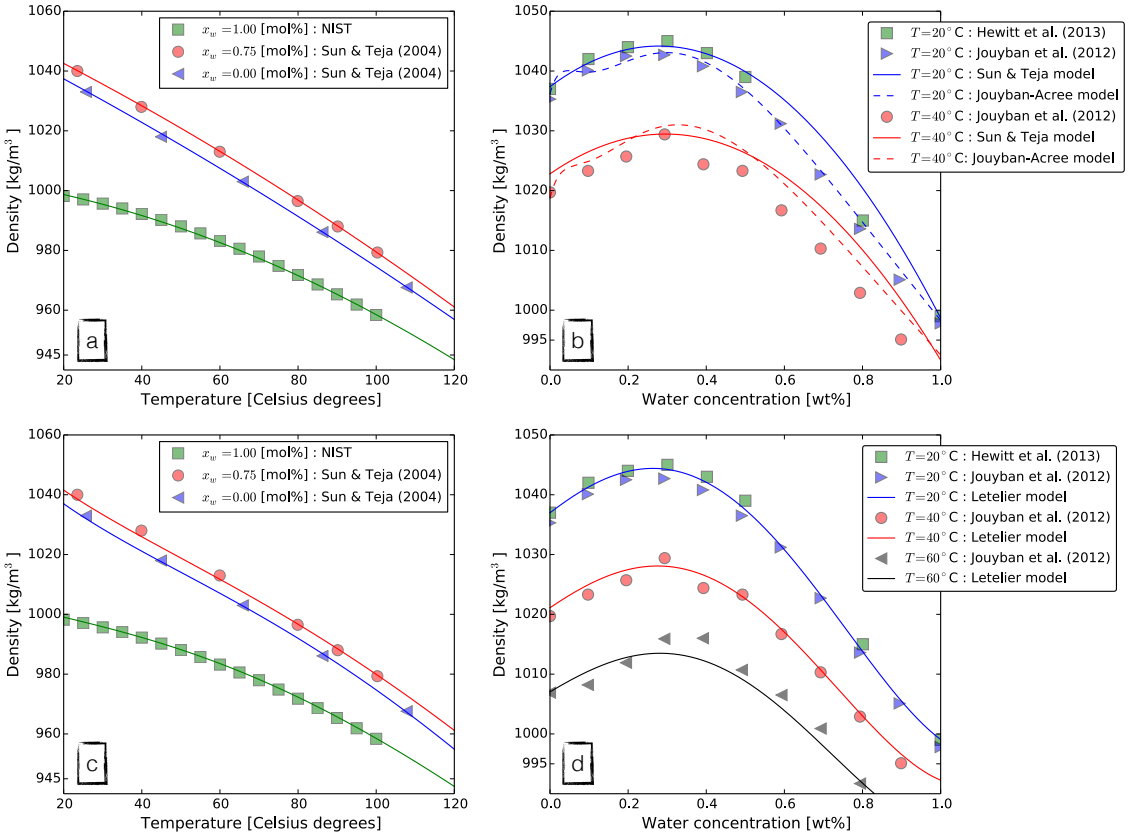

Figure 3.3.1: Models of density for aqueous solutions of PPG. Fig.(a) shows the application of the model presented in Eqn. (3.3.2) to the experimental data reported by Sun and Teja (2004), for different molar concentrations of the mixture. Fig.(b) shows the application of the model presented in Eqns. (3.3.2) and (3.3.6) to the experimental data reported by Jouyban (Khattab et al, 2012). Figs.(c) and (d) show the application of Eqn. (3.3.10) to the experimental data reported by Sun and Teja (2004) and Jouyban (Khattab et al, 2012)

Table 3.1. Model parameters for aqueous solutions of PPG

Sun and Teja (2004)		Khattab et al (2012)		Letelier model (2015)	
Density (in $^{kg}/_{m^3}$)	Viscosity (in cP)	Density (in $^{kg}/_{m^3}$)	Viscosity (in cP)	Density (in $^{kg}/_{m^3}$)	Viscosity (in cP)
$A_{11} = 1003.7$	$B_1 = -3.9701$	$J_5 = 6.243$	$K_0 = 926.206$	$p_{00} = 1023.0$	$r_{00} = 4.801$
$A_{12} = -0.20062$	$B_2 = 1000.8$	$J_6 = 373.4$	$K_1 = -606.410$	$p_{10} = 16.13$	$r_{10} = -5813$
$A_{13} = -2.5127 \times 10^{-3}$	$B_3 = -104.10$	$J_7 = -5.248 \times 10^4$	$\cdots$	$p_{01} = -15.16$	$r_{01} = 17.4$
$A_{21} = 147.12$	$\cdots$	$\cdots$	$\cdots$	$p_{20} = -0.6122$	$r_{20} = 1.634 \times 10^6$
$A_{22} = -1.1024$	$B_4 = 1.5232$	$J_3 = 6.677$	$\cdots$	$p_{11} = -2.667$	$r_{11} = -9819$
$A_{23} = 2.6902 \times 10^{-3}$	$B_5 = -5.0007$	$J_4 = 78.06$	$\cdots$	$p_{02} = -12.23$	$r_{02} = -32.84$
$A_{31} = -99.617$	$B_6 = 9.8106 \times 10^{-4}$	$\cdots$	$\cdots$	$p_{30} = 0.7005$	$r_{21} = 1.316 \times 10^6$
$A_{32} = 0.63102$	$B_7 = 3.2452$	$J_0 = 27.820$	$\cdots$	$p_{21} = -0.5813$	$r_{12} = 1.534 \times 10^4$
$A_{33} = -1.1267 \times 10^{-3}$	$\cdots$	$J_1 = -30.537$	$\cdots$	$p_{12} = -1.69$	$r_{03} = 19.1$
$\cdots$	$B_8 = -3.758023$	$J_2 = 30.476$	$\cdots$	$p_{03} = 2.869$	$r_{22} = -2.164 \times 10^6$
$\cdots$	$B_9 = 590.9808$	$\cdots$	$\cdots$	$p_{31} = -0.1454$	$r_{13} = -2768$
$\cdots$	$B_{10} = 137.2645$	$\cdots$	$\cdots$	$p_{22} = -0.2561$	$r_{04} = -7.134$
$\cdots$	$\cdots$	$\cdots$	$\cdots$	$p_{13} = 0.1065$	$r_{30} = 0$
$\cdots$	$\cdots$	$\cdots$	$\cdots$	$p_{04} = 1.82$	$r_{31} = 0$
$\cdots$	$\cdots$	$\cdots$	$\cdots$	$p_{32} = 0$	$r_{32} = 0$
$\cdots$	$\cdots$	$\cdots$	$\cdots$	$p_{23} = 0$	$r_{23} = 0$
$\cdots$	$\cdots$	$\cdots$	$\cdots$	$p_{33} = 0$	$r_{33} = 0$
$\cdots$	$\cdots$	$\cdots$	$\cdots$	$p_{14} = 0$	$r_{14} = 0$
$\cdots$	$\cdots$	$\cdots$	$\cdots$	$p_{24} = 0$	$r_{24} = 0$
$\cdots$	$\cdots$	$\cdots$	$\cdots$	$p_{34} = 0$	$r_{34} = 0$

Note. — All parameters have units (not presented here), depending on the model used. For the Sun and Teja model, the temperature must be measured in °C, while for the others it must be measured in K. If $[\rho] = {}^{kg}/_{m^3}$ and $[\mu] =$ cP, then the values of the parameters presented here are correct.

The density model of Sun and Teja fits with good agreement the experimental data presented in Fig. 3.3.1(a). However, its prediction for fixed temperature cases presented in Fig. 3.3.1(b) shows a notable departure from experimental values obtained by Khattab et al (2012). The Jouyban-Acree model given in Eqn. (3.3.6) solves this issue, but this model have a strange behavior for $S_w < 0.2$. We cannot consider the Jouyban-Acree model as a good physical model of the mixture because of this strange behavior. The physical model of $\rho(T, S_w)$ must be a monotonic curve with a unique local/global maximum when T is constant, while for S_w it must be a monotonic decreasing function with temperature.

For this reason, we model the experimental data using the following empirical expressions

$$\rho(T, S_w) = \sum_{i=0}^{3} \sum_{j=0}^{4} p_{ij} \left[\frac{1 - \mu_t T}{\sigma_t T} \right]^i \left[\frac{S_w - \mu_s}{\sigma_s} \right]^j , \tag{3.3.10}$$

$$\log \mu(T, x_w) = \sum_{i=0}^{3} \sum_{j=0}^{4} r_{ij} \frac{x_w^j}{T^i} , \tag{3.3.11}$$

where $[\rho] = {}^{\text{kg}}/_{\text{m}^3}$ and $[\mu] = \text{cP}$ if $[T] = \text{K}$. Also, $\mu_t = 3.183 \times 10^{-3}$, $\sigma_t = 2.336 \times 10^{-4}$, $\mu_s = 4.756 \times 10^{-1}$ and $\sigma_s = 3.56 \times 10^{-1}$. The values of p_{ij} and r_{ij} parameters are given in Table 3.1.

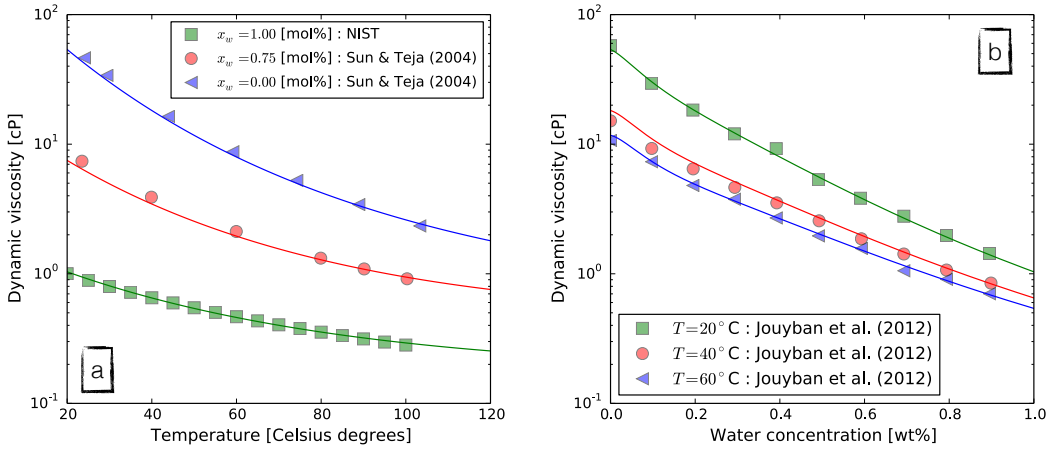

Figure 3.3.2: Model of viscosity for aqueous solutions of PPG. Figs.(a) and (b) show the application of Eqn. (3.3.11) to the experimental data reported by Sun and Teja (2004) and Jouyban (Khattab et al, 2012)

Fig. 3.3.1(c), Fig. 3.3.1(d) and Fig. 3.3.2 show the application of Eqns. (3.3.10) and (3.3.11) to the experimental data reported by Sun and Teja (2004) and Khattab et al (2012), where it is clear the good behavior of the fit in comparison with the models reported in the literature. Some important information can be obtained after the discussion of the modeling given here. In isothermal conditions (see Fig. 3.3.1(d)), it is possible to assume that Boussinesq approximation is applicable in the range $S_w \leq S_w^{(m)}$, where $\rho(S_w^{(m)}) = \rho_{max}$. If we write the density as $\rho = \rho_a + \rho'$, with $\rho_a = \rho(S_w = 0)$, we have $\rho'/\rho_a \sim 0.01$. For this case, we can approximate Eqn. (3.3.10) as

$$\rho(c) = \rho_a + \Delta\rho\, c \quad ; \quad \Delta\rho = \rho_{max} - \rho_a \quad ; \quad c = \frac{S_w}{S_w^{(m)}} \,, \tag{3.3.12}$$

where ρ_a and ρ_{max} are functions of the temperature. Eqn. (3.3.12) is widely used in fixed interface systems (Riaz et al, 2006; Pau et al, 2010) (See Chapter 4, Section 4.3 on page 43 for additional information). Anyway, in the interval $0 \leq S_w \leq 1$ the total density difference is $\Delta\rho \sim 44\,\mathrm{kg/m^3}$ and therefore $\rho'/\rho_a \sim 0.04$, so the Boussinesq approximation is still valid. For isoconcentration conditions (see Fig. 3.3.1(c)), the density can be approximated as

$$\rho(T) = \rho_a + \rho' = \rho_a + \Delta\rho \left[\frac{T - T_0}{T_f - T_0}\right] , \tag{3.3.13}$$

where $\rho'/\rho_a \sim 0.07$. For this case, the Boussinesq approximation is more discutible. Eqn. (3.3.13) is widely used in thermal convection in porous media (Otero et al, 2004; Hewitt et al, 2012).

For dynamic viscosity in isothermal conditions (see Fig. 3.3.2(b)), in the range $0.2 \leq S_w \leq 1$ we can see that the experimental data and model are practically linear in the logaritmic scale, so Eqn. (3.3.11) can be approximated as

$$\mu(c) = \mu_a \exp(R\, c) \quad ; \quad c = \frac{S_w - S_w^{(0)}}{1 - S_w^{(0)}} \quad \text{with } S_w^{(0)} = 0.2 \,, \tag{3.3.14}$$

where R is the mobility ratio. For viscous fingering phenomena in porous media, Eqn. (3.3.14) is the main model used as constitutive equation (Jha et al, 2011a,b, 2013; Pramanik and Mishra, 2015)

Chapter 4

Convective phenomena in porous media

The first experimental studies about steady and unsteady convection in homogeneous porous media were done by J. Elder (Elder, 1967a,b). In these works, thermal convection was generated by heating the below part of a Hele-Shaw cell, which represents a good approximation of an homogeneous porous medium with a permeability coefficient given by $K = b^2/12$, where b is the gap of the cell (Hele-Shaw, 1898). The topics of study addressed in these works were related with the formation of cell patterns, as well as boundary and mass discharge effects. From this pionnering studies, natural convection in homogeneous porous media has received much attention by researchers (Hartline and Lister, 1977; Caltagirone, 1980; Kvernvold and Tyvand, 1981; Simmons and Narayan, 1997; Schoofs et al, 1999; Cherkaoui and Wilcock, 2001; Nagamo et al, 2002; Otero et al, 2004; Babushkin and Demin, 2006; Nield and Bejan, 2006; Hewitt et al, 2012; Cooper et al, 2014). However, the study of the same processes in heterogeneous porous media have received little attention (Schincariol et al, 1997). These studies concluded that the results obtained in homogeneous porous media cannot be extrapolated to the heterogeneous cases. Therefore, the stability criteria found by Elder for thermal convection could not be applicable for convective geothermal systems.

In their work, Prasad and Simmons (2003) studied the Elder's problem using numerical simulations in an heterogeneous porous media, concluding that the anisotrophy of the permeability distribution has important consequences in the onset and decay of unstable patterns.

A similar problem, in the mathematical sense, is the confinement of supercritical CO_2 in geologic reservoirs which is characterized by a time dependent initial base state that governs the dynamics of the diffusive boundary layer between the CO_2 gas phase and the reservoir fluids (brine). The solubility of CO_2 in water under reservoir conditions was studied by Enick and Klara (1990), where the Krichevsfcy-llinskaya equation was used to model the system. When CO_2 is injected to deeps of about 1 km, a small amount is dissolved in brine (Van der Meer, 1992), increasing the density of the fluid mixture. One of the first studies published in literature regarding the importance of the increase of the density with applications to the geologic sequestration was done by Weir et al (1996). In this work, the simulator TOUGH2 was used to model the injection of $100\,^{kg}/_{s}$ of CO_2 for 10 years into an aquifer to 3 km deep, with the aim to evaluate

the long-term storage prospects. The main conclusions of this work were (a) some gas may escape to the surface, which depends on the permeability structure above the injection point, and (b) in the most favourable case, all CO_2 is dissolved in brine and the resulting dense fluid settles in the aquifer over severeal thousand years. In his doctoral work, J. García (Pruess and Garcia, 2002; Garcia, 2003) showed that the mixing of CO_2 with brine can increase the fluid density about 2% to 3%. He argued that the CO_2 dependency in the fluid density is often ignored, because the salinity can increase up to 20% the fluid density. However, the fluid density has a linear dependency with CO_2 concentration, which induces an instability that triggers a multiscale convective phenomenon known as solubility trapping of CO_2 in geological formations (Ennis-King and Paterson, 2003). Later, many studies reported in the literature were focused in determine the time of the onset of convection and the growth of the dominant convective modes, once that the diffusive boundary layer has achieved a critical thick (Ben et al, 2002; Ennis-King and Paterson, 2005; Riaz et al, 2006; Rapaka et al, 2008).

Another storage mechanism, the residual trapping, was modeled by Golding et al (2011), which includes the effect of capillary forces. The authors argued that the residual trapping is fundamental to sequester CO_2 permanently in geological formations and they conclude that this confinement mechanism is optimized if there are capillary bands in the formation.

In the literature, the injection of supercritical CO_2 in reservoirs at high pressures and temperatures has received little attention. In their work, Linderberg and Wessel-Berg (1997) evaluated the conditions of existence of a vertical flux in a porous medium with thermal stresses and diluted CO_2, which is important for the estimation of the total storage capacity of CO_2 in aquifers. Experimental studies of CO_2-rock interaction in geothermal conditions was reported by Ueda et al (2005), with the aim to study dissolution and precipitation phenomena, including calcite extraction from rocks that might occur during CO_2 storage into geothermal reservoirs. The study of the enhancement of CO_2 mass transfer into the reservoir brane, at high pressures and temperatures, was done by Yang and Gu (2006). To interpret their results, they introduced an effective diffusivity term, which was two times larger than the molecular diffusion coeficient of CO_2 in brine. A similar work done by Farajzadeh et al (2007) uses surfactant solutions to enhance the CO_2 mass transfer. Next, Farajzadeh et al (2009) showed experimentally that the CO_2 mass transfer rate across the interface is much faster than that predicted by Fickian diffusion. Although these efforts to understand the mass transfer processes, visualization of the mixing in such thermodynamical conditions is very difficult. In

the literature, many analogue experiments that employ working fluids that represent the fluid dynamics expected in geothermal reservoirs have been reported (Cherkaoui and Wilcock, 2001; Kneafsey and Pruess, 2009; Neufeld et al, 2010; Backhaus et al, 2011; MacMinn et al, 2012; MacMinn and Juanes, 2013; Slim et al, 2013), as well as high-resolution numerical simulations (Otero et al, 2004; Riaz et al, 2006; Pau et al, 2010; Hidalgo et al, 2012; Hewitt et al, 2012; Szulczewski et al, 2013; Hewitt et al, 2013).

In the following, we show the basic theory used in porous media and some analogue experiments implemented to visualize the convective processes.

4.1 Mathematical theory

We begin this section with the discussion of the work of Riaz et al (2006) regarding the onset of convection. They modeled the dissolution of supercritical CO_2 in brine using the Darcy equation coupled with the advection-diffusion equation for scalar transport

$$\nabla \cdot \mathbf{u} = 0 \,, \tag{4.1.1}$$

$$\mu_f \, K^{-1} \, \mathbf{u} = -\nabla p + \rho_f \, g \hat{z} \,, \tag{4.1.2}$$

$$\phi \, \frac{\partial \varphi}{\partial t} + \mathbf{u} \cdot \nabla \varphi = \phi \, \kappa_\varphi \, \nabla^2 \varphi \,, \tag{4.1.3}$$

where K is the permeability, $\mathbf{u} = u\hat{x} + w\hat{z}$ is the averaged Darcy velocity, p is the pressure, φ is the transported scalar, ϕ is the porosity, κ_φ is the molecular diffusivity, g is the gravitational acceleration, μ_f is the dynamic viscosity and $\rho_f = \rho_a + \Delta\rho \, \varphi$ is the density, with ρ_a the density reference and $\Delta\rho$ the maximum density contrast. In their work, Riaz et al used the variables $\varphi = S_c$ and $\mu_f = \mu_a$, where S_c is the concentration of CO_2 in the fluid and μ_a is a constant viscosity reference.

The initial conditions of the problem are $\mathbf{u}(\mathbf{x}, t = 0) = 0$ and $S_c(\mathbf{x}, t = 0) = 0$, while the boundary conditions are $w = 0$ in $z = 0$ and $z = H$, $S_c = 1$ in $z = 0$ and $\hat{z} \cdot \nabla S_c = 0$ in $z = H$, where H is the height of the domain shown in Fig. 4.1.1. To nondimensionalize Eqns. (4.1.1) to (4.1.3), Riaz et al used the transformations $\mathbf{x}' = \mathbf{x}/H$, $\mathbf{u}' = \mathbf{u}/u_c$, $p' = p/p_c$ and $t' = t/t_c$, where

$$u_c = \frac{\Delta\rho g K}{\mu_a} \quad ; \quad p_c = \Delta\rho g H \quad ; \quad t_c = \frac{\phi H}{u_c} \quad ; \quad t_d = \frac{H^2}{\kappa_s} \quad ; \quad Ra_s = \frac{t_d}{t_c} = \frac{\Delta\rho g K H}{\phi \mu_a \kappa_s} \,.$$

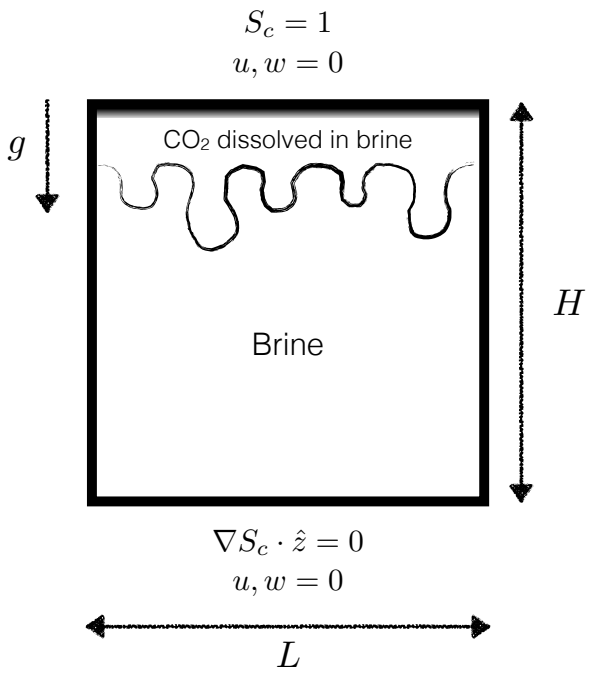

Figure 4.1.1: Schematic picture that shows the solubility confinement of CO_2 in a simple geometry. The CO_2 gas-phase begins to accumulate along the interface. Next, it is dissolved slowly in brine and creates a boundary layer more dense than brine. The unstable fluid configuration produces a vertical convection process, which enhance CO_2 mass transport within the domain (Riaz et al, 2006). This figure is an example of the canonical model presented in Chapter 5, Section 5.4 on page 61

Here, the important parameter is the Rayleigh number Ra_s. Finally, the dimensionless porous media equations given by Eqns. (4.1.1) to (4.1.3) are written as

$$\nabla' \cdot \mathbf{u}' = 0 \,, \tag{4.1.4}$$

$$\mathbf{u}' = -\nabla p' + S_c \, \hat{z} \,, \tag{4.1.5}$$

$$\frac{\partial S_c}{\partial t'} + \mathbf{u}' \cdot \nabla' S_c = \frac{1}{Ra_s} \nabla'^2 S_c \,, \tag{4.1.6}$$

with boundary conditions $w = 0$ in $z = 0$ and $z = 1$. As we shown in Chapter 5, Section 5.4 on page 58, Eqns. (4.1.4) to (4.1.6) are special cases of the Hele-Shaw model derived in this work.

Next, using perturbative methods and extending the vertical dimension $H \to \infty$, Riaz et al proposed the following expansions for the transverse velocity and concentration

$$w'(\mathbf{x}', t') = 0 + \hat{w}(\xi, t') e^{ikx'} \quad ; \quad S_c(\mathbf{x}', t') = s_0(\xi) + \hat{s}(\xi, t') e^{ikx'} \,,$$

where $s_0(\xi) = 1 - \mathrm{erf}(\xi)$ is the base state, with $\xi = z' \sqrt{Ra_s / 4t'}$ the autosimilar variable of the problem. The base state is obtained solving the equation $\partial s_0 / \partial t' = \kappa_s \, \nabla'^2 s_0$ with boundary conditions $s_0(z' = 0) = 1$ and $s_0(z \to \infty) = 0$. The linearized Eqns. (4.1.4) to (4.1.6) are written as

$$\left(\frac{Ra_s}{4t'}\frac{\partial^2}{\partial\xi^2} - k^2\right)\hat{w} = -k^2\hat{s}\,, \tag{4.1.7}$$

$$\frac{\partial\hat{s}}{\partial t'} - \frac{1}{t'}\left(\frac{1}{4}\frac{\partial^2}{\partial\xi^2} + \frac{\xi}{2}\frac{\partial}{\partial\xi} - \frac{k^2\,t'}{Ra_s}\right)\hat{s} = \sqrt{\frac{Ra_s}{\pi t'}}\,e^{-\xi^2}\,\hat{w}\,, \tag{4.1.8}$$

with boundary conditions $\hat{w} = 0$ and $\hat{s} = 0$ in $\xi = 0$ and $\xi \to \infty$. Riaz et al proposed a modal expansion of the type $\hat{s}(\xi, t') = \sum_{n=1}^{\infty} A_n(t')\,\psi_n(\xi)$, where the eigenfunctions $\psi_n(\xi)$ satisfy the equation $\mathcal{L}\psi_n = \lambda_n\psi_n = -n\,e^{-\xi^2}\,\mathcal{H}_n(\xi)$, being $\mathcal{L} = 1/4\,\partial_{\xi\xi} + \xi/2\,\partial_\xi$ the differential operator which eigenfunctions are the Hermite polynomials $\mathcal{H}_n$ with weight function $e^{-\xi^2}$ (Robinson, 1976). Considering only the term $n = 1$ in the modal expansion, the solution of Eqns. (4.1.4) to (4.1.6) allow us to obtain the growth rate by solving the non-autonomous equation

$$\frac{dA_1}{dt'} = \sigma(t', k)\,A_1 \quad ; \quad \sigma = -\frac{1}{t'} - \frac{k^2}{Ra_s} + \frac{k}{\sqrt{\pi}}\,F(t', k)\,, \tag{4.1.9}$$

where $F(t', k)$ is a function solved numerically. This methodology is known as the dominant mode solution. In Chapter 6, Section 6.3 on page 79, we have used this method to determine the effects of include both inertial and dispersive effects in the governing equations.

The comparison between the growth rate σ and the growth of the diffusive layer σ_{dif} is also important. Historically, the first approach to this type of problems was given by the quasi-steady-state approximation (QSSA), which is valid when $\sigma \gg \sigma_{dif}$. However, Riaz et al showed that QSSA is not valid when the diffusive boundary layer grows fast, but it gives accurate results for long times, when the base state changes slowly (Riaz and Meiburg, 2003). Furthermore, in the onset of convection, QSSA is no longer valid (Gresho and Sani, 1971). Riaz et al defined the critical time τ_c and the critical wavenumber k_c as the solutions of the system of equations $\sigma = 0$ and $\partial\sigma/\partial k = 0$. This procedure allows to find the scaling law $\tau_c = 146\,Ra_s^{-1}$, which is valid when $\sqrt{4t'/Ra_s} \ll 1$.

The numerical works done by Otero et al (2004) and Hewitt et al (2012) are also interesting to discusse. Both works are related with the known Elder's problem or Rayleigh-Benard convection in porous media. To model the problem, they used Eqns. (4.1.1) to (4.1.3) assuming that $\varphi = T$ and the constitutive equation for density

$\rho_f = \rho_a - (\Delta\rho/\Delta T)\,(T - T_a)$. The main objective of these works is to compute the heat transport through the Nusselt number Nu, defined as

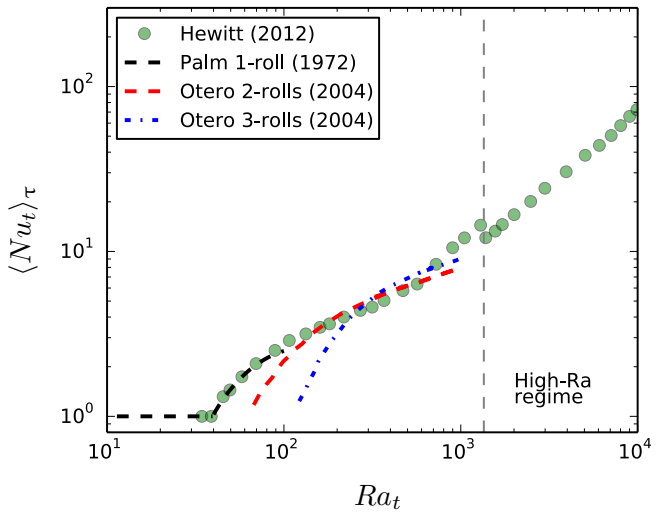

Figure 4.1.2: Scaling behaviour of $\langle Nu_t \rangle_\tau = \langle Nu_t \rangle_\tau(Ra_t)$ (Hewitt et al, 2012), which is compared with heat transport of some stable rolls reported in literature (Palm et al, 1972; Otero et al, 2004)

$$Nu_t = -\frac{\partial \bar{T}}{\partial z'}\bigg|_{z'=0} \quad ; \quad \bar{T}(z') = \frac{1}{L'}\int_0^{L'} T(\mathbf{x}')\,dx' \quad ; \quad L' = \frac{L}{H}\,. \tag{4.1.10}$$

To compute the scaling law for heat transport, they performed a temporal average of Nu_t values, which will be denoted as $\langle Nu_t \rangle_\tau$ (See Eqn. (2.0.4) on page 17 for additional information). In the high-Rayleigh regime $Ra_t > 1350$, where $Ra_t = u_c H/\kappa_t = \Delta\rho\, g\, K\, H/\mu_a\, \kappa_t$ is the thermal Rayleigh number, Hewitt et al show that the system exhibits a predominantly vertical exchange flow, where $\langle Nu_t \rangle_\tau \sim Ra_t$ asymptotically. In particular, for the values of Ra_t considered, they proposed a nonlinear scaling law of the form $\langle Nu_t \rangle_\tau \sim Ra_t^{0.95\pm0.01}$. Fig. 4.1.2 shows the scaling behaviour of $\langle Nu_t \rangle_\tau$ obtained by Hewitt et al, which is compared with heat transport of some stable rolls reported in the literature. In Chapter 7, Section 7.2 on page 96, we show that heat transport scaling has an important dependency with the Hele-Shaw geometry through the relation $\langle Nu_t \rangle_\tau \sim Ra_t^{n(\epsilon)}$, where $n \sim 0.95$ when $\epsilon \ll 1$.

The origin of the relation $\langle Nu_t \rangle_\tau \sim Ra_t$ can be obtained from the scaling analysis of the convective cell pattern shown in Fig. 4.1.3. From Eqn. (4.1.2), que can define the Darcian velocity scale as $\bar{u}_c = \Delta\rho\, g\, K/\mu_a$. From Eqn. (4.1.3), comparing the scales of the vertical gradient of the enthalpy and the lateral thermal diffusion between the two branches in the bulk, we can obtain the expression

$$w\,\frac{\partial T}{\partial z} \sim \kappa_t\,\frac{\partial^2 T}{\partial x^2} \Longrightarrow \frac{\bar{u}_c \Delta T}{H} = \frac{\kappa_t \Delta T}{L_c^2}\,. \tag{4.1.11}$$

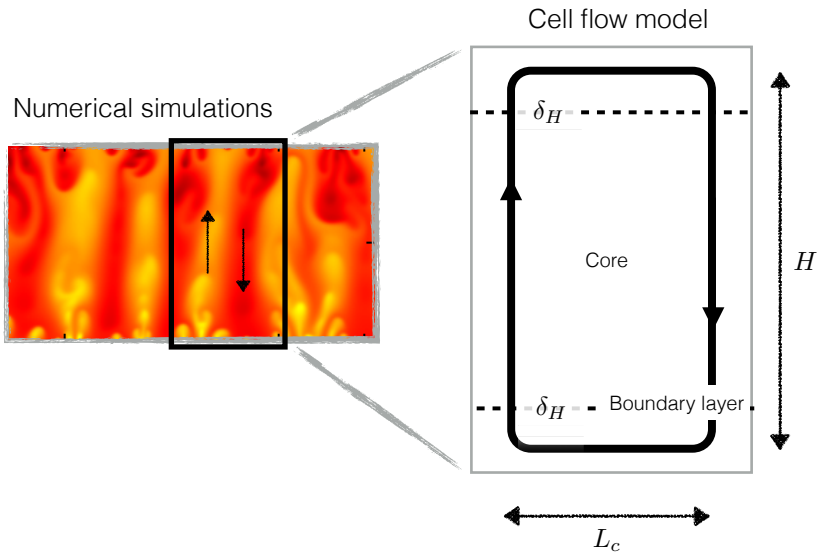

Figure 4.1.3: The origin of the geometrical relation $Nu_t^{(g)} \sim Ra_t$ from the scaling analysis of the convective cell pattern

On the other hand, from Eqn. (4.1.3) the comparison between the vertical enthalpy flux through the core and the vertical thermal conductive flux through the boundary layer allow us to compute the scale of the thermal boundary layer δ_H

$$\int_\Omega w \frac{\partial T}{\partial z}\, dV \sim \int_\Omega \frac{\partial^2 T}{\partial z^2}\, dV \Longrightarrow \bar{u}_c\, L_c\, \Delta T \sim \kappa_t\, L_c\, \frac{\Delta T}{\delta_H}\,. \tag{4.1.12}$$

The geometrical Nusselt number can be defined as $Nu_t^{(g)} = H/\delta_H$. Using the scaling relations defined before, we obtain $Nu_t^{(g)} = \bar{u}_c H/\kappa_t = Ra_t$. In Chapter 5, Section 5.4 on page 60, we show that the Hele-Shaw geometry affects this scaling relation by means of the introduction of the geometrical mean scalar dissipation rate $\langle \varepsilon_t \rangle^{(g)}$. Using dimensional analysis, we noted that the scaling law can be written as $Nu_t^{(g)} = \langle Nu_t \rangle_\tau \sim \Phi\, Ra_t\, \langle \varepsilon_t \rangle^{(g)}$, where Φ is a function to be determined experimentally.

Regarding the problem of density-driven convection by fluid mixtures, in the literature (Pope, 2011; Jha et al, 2011a; Hidalgo et al, 2012; Pramanik and Mishra, 2015) the mean scalar dissipation rate is obtained from Eqn. (4.1.6) and it is defined as

$$\langle \varepsilon_s \rangle = \frac{1}{Ra_s} \langle ||\nabla S_c||^2 \rangle \quad ; \quad \langle f \rangle = \frac{1}{L'} \int_0^1 \int_0^{L'} f(\mathbf{x}')\, dx'\, dz' \tag{4.1.13}$$

However, the works of Hidalgo et al (2012) and Jenny et al (2014) show that the time-averaged mean scalar dissipation rate $\langle \varepsilon_s \rangle_\tau$ is independent of Ra_s (See Eqn. (2.0.5) on page 18 for additional information). For thermal convection, this result also applies. In Section 5.4 on page 60, we show that the mean scalar dissipation has a correction

of the type $\langle \varepsilon_\varphi^{(\epsilon)} \rangle = \langle \varepsilon_\varphi \rangle + O(\epsilon^2)$, where ϵ is a measure of the geometry features of the Hele-Shaw model and φ is either temperature or concentration. Therefore, we obtain the relation $\langle \varepsilon_\varphi^{(\epsilon)} \rangle_\tau \sim Ra_\varphi^{m(\epsilon)}$, in contrast with the results reported in the literature.

4.2 Laboratory experiments

From the experimental physics, in the literature there are interesting results of the visualization of fluid mixing using Hele-Shaw cells. In their work, Kneafsey and Pruess (2009) obtained images of CO_2 dissolution process in water under standard conditions of temperature and pressure. Fig. 4.2.1 shows the results obtained in these experiments.

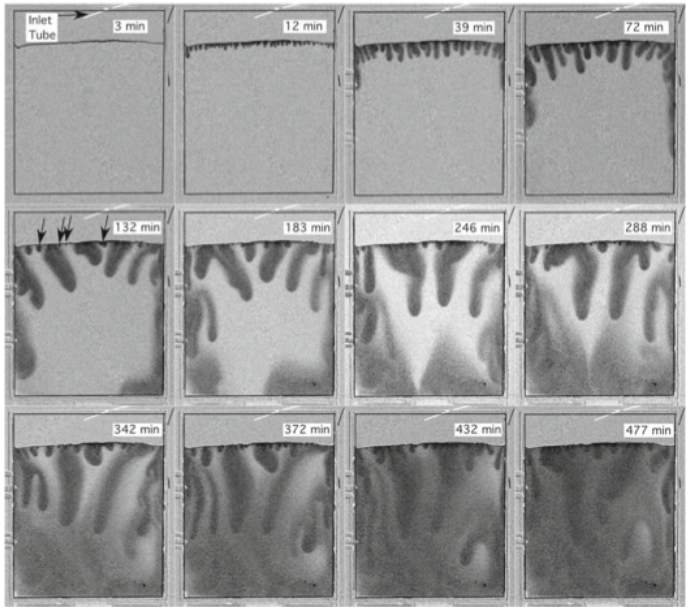

Figure 4.2.1: Images of the convection of CO_2 dissolved in deionized water under standard conditions of temperature and pressure. In $t = 12\,\text{min}$, we observe the onset of convection in the diffusive boundary layer, while in $t = 72\,\text{min}$ the convective process is fully developed. Figure from Kneafsey and Pruess (2009)

The experimental setup used by Kneafsey and Pruess (2009) consisted in the building of Hele-Shaw cells using thin glass plates, which were separated by graphite shims of thickness similar to a paper sheet. The authors noted that pure water has a pH of about 5.6, while pure water in equilibrium with CO_2 to 1 atm has a pH of about 3.8. To visualize the concentration of dissolved CO_2 in water, they used the acid-base colour indicator bromocresol green, which changes with pH from blue (pH > 5.6) to yellow (pH < 3.8). The bromocresol was diluted with water, in a ratio of $1:30$, which later was introduced in the Hele-Shaw cell through a long and thin stainless pipe. CO_2 gas-phase was introduced using a thin stainless pipe between the glass plates of the cell with a flux of tens of milliliters per minute, enough to produce small burbles when pipe is

introduced in water. Kneafsey and Pruess (2009) noted that CO_2 gas-phase is more dense than air, so air is displaced when CO_2 is injected in the upper boundary of the cell[1] . Then, CO_2 is dissolved in water by molecular diffusion and later it is transported within the cell by convection.

In their procedure, Kneafsey and Pruess (2009) noted that the cell was illuminated behind using a light table, obtaining digital 8-bit RGB images. To quantify their results, the authors computed the mixing area, which was defined as the ratio between the obscure area of the images (see Fig. 4.2.1) and the total area of the cell, assuming that the mixing area is saturated with CO_2 .

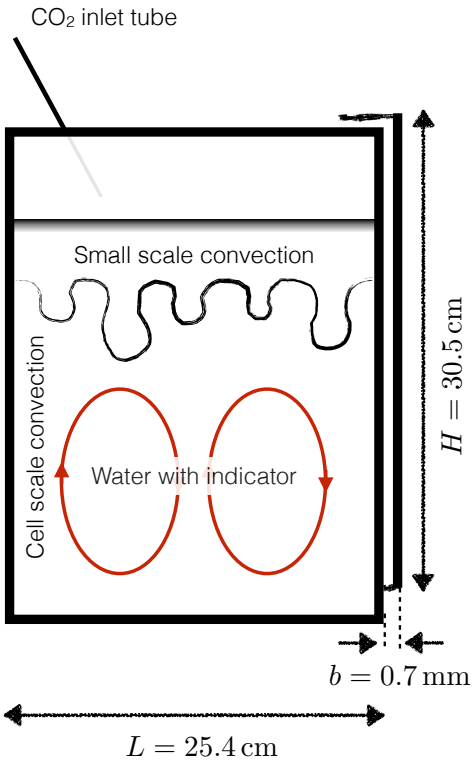

Figure 4.2.2: Experimental setup used by Kneafsey and Pruess (Kneafsey and Pruess, 2009)

The authors observed that for different setups and experimental runs, density-driven convection enhance CO_2 mass transport in comparison with pure diffusion. They noted that these results are expected for cases where the solutal Rayleigh number Ra_s is high ($Ra_s > 10^4$). Some undesirable effects, which corresponds to systematic failures in the experimental setup, were discussed. In particular, large-scale cell convection was observed due to cell heating by illumination (see Fig. 4.2.2).

[1] The molar mass of CO_2 is $44\,\mathrm{g/mol}$, while the molar mass of air is $29\,\mathrm{g/mol}$

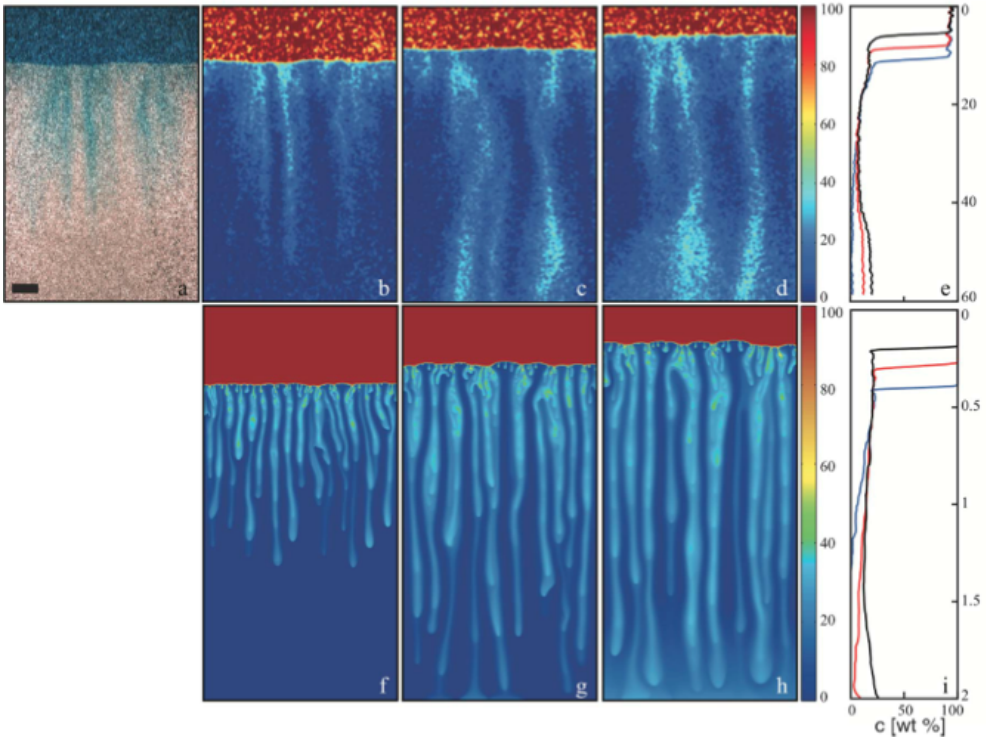

Figure 4.2.3: Experimental images of CO_2/MEG dissolution in a saturated porous medium and numerical simulations obtained by Neufeld et al. Fig.(a) is a non processed experimental image, which shows the convection of MEG with $63\,\mathrm{wt}\%$ of ethylene-glycol (blue color) in a porous medium of $1.4\,\mathrm{cm}\times 40\,\mathrm{cm}\times 80\,\mathrm{cm}$ with $Ra_s = 5.9\times 10^5$. The intensity of the tracer allows to make a concentration map (Fig.(b)). Figs. (b), (c) and (d) show concentration maps taken at $10\,\mathrm{min}$, $40\,\mathrm{min}$ and $70\,\mathrm{min}$. Figs.(f), (g) and (h) shows the concentration maps obtained from numerical simulations with $Ra_s = 2.0\times 10^4$. Finally, Figs.(e) and (i) are the average of concentration maps in the horizontal direction. Figure from Neufeld et al (2010)

On the other hand, Neufeld et al (2010) presented an analogue experiment, which models the convection of CO_2 in a reservoir using methanol and ethylene-glycol (MEG) solutions with pure water in cells filled with sand of different permeabilities and porosities. The dimensions of the cell were $1.4\,\mathrm{cm}\times 40\,\mathrm{cm}\times 80\,\mathrm{cm}$. Fig. 4.2.3 shows experimental images obtained in the experiment and some numerical simulations done for comparison. Neufeld et al (2010) observed that the interfacial vertical motion can give a direct measurement of the convective flux $F_c = \phi u_i \Delta c$, where ϕ is the porosity, u_i is the vertical interfacial velocity and Δc is the difference of concentration by weight of MEG in pure water. The left image of Fig. 4.2.5 shows the constitutive relation between the density and MEG concentration, where Δc and $\Delta\rho$ are defined graphically. In their experiments, u_i was constant and independent of finger positions. This observation indicates that F_c is constant and therefore it only depends on $Ra_s = \bar{u}_c\, H/\phi\,\kappa_s$, where H is the deep of the reservoir, κ_s is the molecular diffusivity and $\bar{u}_c = \Delta\rho g K/\mu$ is

the Darcy velocity defined in terms of the permeability K, maximum density contrast $\Delta\rho$, gravitational acceleration g and dynamic viscosity μ. These experiments allowed to obtain correlations between the geometrical Nusselt number for mass transfer $Nu_s^{(g)}$ (or Sherwood number) and Ra_s in the high-Rayleigh regime. For the low-Rayleigh regime, the authors have used numerical simulations of Eqns. (4.1.4) to (4.1.6), which supports the experimental observation of vertical motion of the interface, as we can see in Fig. 4.2.3. The Nusselt number for mass transfer $Nu_s^{(g)} = F_c/(\phi\,\kappa_s\,\Delta c/H)$ is the ratio between the convective and diffusive mass fluxes. Therefore, the scaling law $Nu_s^{(g)} \sim Ra_s^{0.84\pm0.02}$ was found by Neufeld et al (2010) (see Fig. 4.2.4).

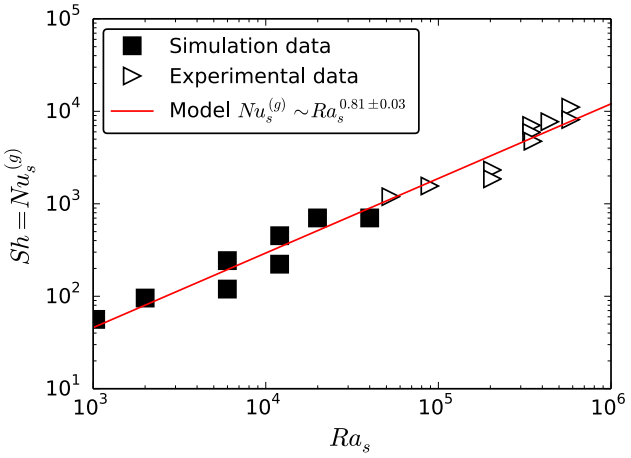

Figure 4.2.4: Sherwood number *Sh* (Nusselt for mass transfer) as function of Ra_s. The results from numerical simulations are shown in black, while experimental results are shown in white (Neufeld et al, 2010). The model $Nu_s^{(g)} \sim Ra_s^{0.81\pm0.03}$ is obtained correlating both numerical and experimental data with Ra_s

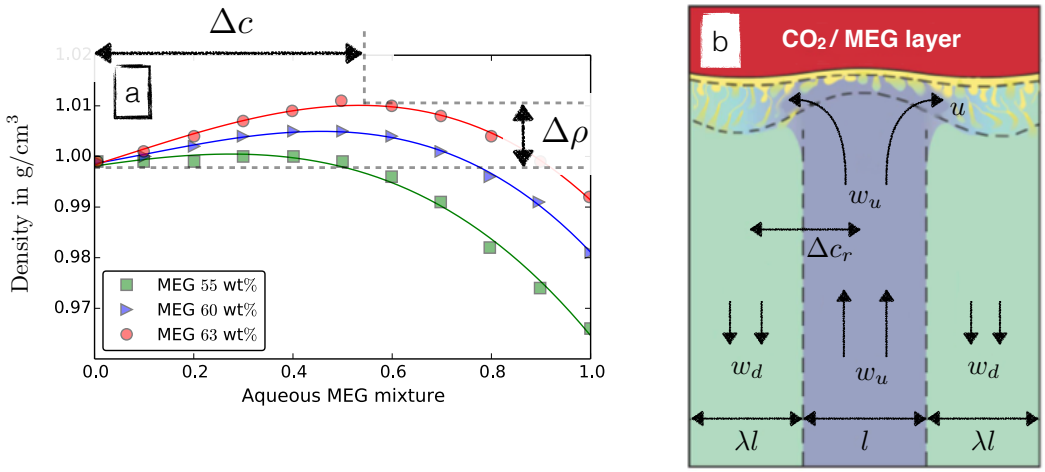

Figure 4.2.5: Fig.(a) shows the constitutive relation between the density and MEG concentration. Fig.(b) shows a schematic physical picture of the far field approximation, where long-lived plumes are developed. Figure from Neufeld et al (2010)

For high-Rayleigh convection in porous media, Howard (1964) proposed the linear scaling $Nu_s^{(g)} \sim Ra_s$, which is based on the assumption that the convective flux is independent of the deep of the reservoir and therefore it is determined only by the stability of the diffusive boundary layer in the interface. However, Neufeld et al (2010) noted that for thermal convection in porous media there are also nonlinear scalings. To explain the physical origins of the scaling $Nu_s^{(g)} \sim Ra_s^{0.84\pm0.02}$, the authors used the right image of Fig. 4.2.5 and a dimensional analysis similiar to those presented in Eqns. (4.1.11) and (4.1.12). In Fig. 4.2.5(b) there are five physical quantities of interest, which are the velocity of upwelling plumes $w_u \sim \bar{u}_c$, the velocity of downwelling plumes w_d, the width of fresh upwelling plumes l, the lateral velocity in the diffusive boundary layer u, the lateral concentration gradient scale Δc_r and the ratio $\lambda = \Delta c/\Delta c_r > 1$ which scales nonlinearly with Ra_s. In the far field approximation, where we have long-lived plumes, the effect of Δc_r in plumes is the decrease of the velocity $w_d \sim \bar{u}_c/\lambda$. Also, as the upwelling fluid approaches the interface, the relation $u \sim w_u$ is attained. Therefore, comparing the scales of the upwelling enthalpy gradient and the lateral thermal diffusion between the two branches, we can obtain the expression

$$w\,\frac{\partial c}{\partial z} \sim \kappa_s\,\frac{\partial^2 c}{\partial x^2} \Longrightarrow w_u\frac{\Delta c}{H} = \kappa_s\frac{\Delta c_r}{l^2}\,. \tag{4.2.1}$$

On the other hand, from Eqn. (4.1.3) the comparison between the vertical enthalpy flux through the core and the vertical thermal conductive flux through the boundary layer of height δ allow us to obtain the expression

$$\int_\Omega w\,\frac{\partial T}{\partial z}\,dV \sim \int_\Omega \frac{\partial^2 T}{\partial z^2}\,dV \Longrightarrow w_d\,l\,\Delta c \sim \kappa_s\,l\,\frac{\Delta c}{\delta}\,. \tag{4.2.2}$$

Inside the diffusive boundary layer, the height δ can be estimated using the relation $l \sim u\,\tau_d$, where $\tau_d = \delta^2/\kappa_s$ is the diffusive time scale. Therefore, we obtain the expression

$$\delta^2 \sim \kappa_s\,l/u \sim \kappa_s\,l/w_u\,. \tag{4.2.3}$$

Combining Eqns. (4.2.1) to (4.2.3), Neufeld et al (2010) obtained the scaling relation $\lambda \sim Ra_s^{1/5}$. Finally, the convective flux is estimated as $F_c = w_d\,\Delta c \sim u_c\,\Delta c/\lambda$ and therefore the Nusselt number is $Nu_s^{(g)} = Ra_s/\lambda \sim Ra_s^{0.8}$. The lateral diffusion explains with good agreement the nonlinear scaling observed for the Nusselt number, so an interesting problem is to show if this relation is an universal law for mass transfer scaling in the Darcian regime. It is worth noting again that Hidalgo et al (2012) show that the

nonlinear scaling of mass transfer displayed in Fig. 4.2.4 must be reflected in the mean scalar dissipation defined in Eqn. (4.1.13). However, in the Darcian high-Ra_s regime, Hidalgo et al (2012) and Jenny et al (2014) show that the mean scalar dissipation rate does not depend of Ra_s and therefore the dissolution flux (and subsequent mixing) is constant and independent of the Rayleigh number, i.e., $\langle Nu_s \rangle_\tau \sim Ra_s$, which is also a result obtained by earlier works that forcing a fixed flat dissolution interface known as the canonical model (Pau et al, 2010; Hewitt et al, 2013). Therefore, there is a clear contradiction between Neufeld's experiment and theory that motivates the theoretical framework of this thesis. Hereinafter, this problem of two-fluid mixing will be called the analogue model.

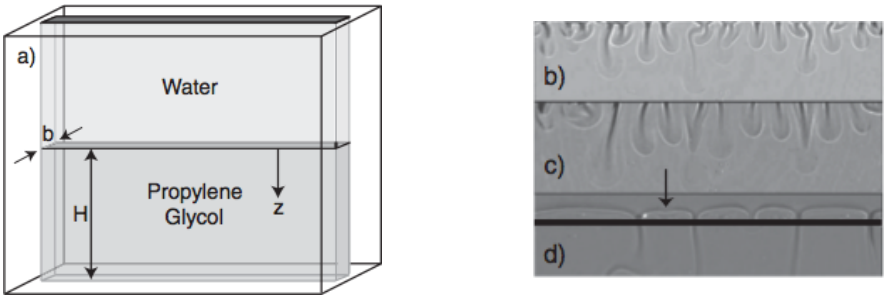

Figure 4.2.6: Experimental studies of Backhaus et al (2011). Fig.(a) shows the experimental setup. Figs.(b) to (d) show an image sequence of mixing convection obtained by optical shadowgraphy. Figure from Backhaus et al (2011)

Backhaus et al (2011) studied experimentally the same mixing problem using deionized water with propylene-glycol (PPG). They used an experimental setup based on a Hele-Shaw cell made with two acrylic plates of thickness $L_p = 1.2\,\text{cm}$, which were separated by stainless shims of thickness that varies from $b = 0.25\,\text{mm}$ to $b = 0.48\,\text{mm}$. The width available for the fluid was $L = 7.6\,\text{cm}$ and the initial height of the denser fluid had a variation from $H = 1.25\,\text{cm}$ to $H = 5.0\,\text{cm}$. The cell was divided in an upper and lower parts through an aluminium shim of thickness $7.6\,\mu\text{m}$ which was retired horizontally to allow the mixing. They noted that the small perturbations that arises when the aluminium shim is retired do not affect the onset and growth of plumes. Water ($\rho_w \sim 1.0\,\text{g/cm}^3$) is less dense than PPG ($\rho_{ppg} \sim 1.035\,\text{g/cm}^3$), but the mixing of both fluids has a density greater than PPG for some values of the water concentration S_w. For example, for $S_w = 0.3$ we have $\rho = 1.044\,\text{g/cm}^3$ and $\Delta\rho = 0.009\,\text{g/cm}^3$ relative to PPG (For further information, see Chapter 3, Section 3.3 on page 21). This is enough to trigger a Rayleigh-Taylor instability in the two-fluid system.

Backhaus et al (2011) visualized the mixing convection using optical shadowgraphy. Fig. 4.2.6 shows the evolution of plumes in time. The authors explained that the diffusive boundary layer becomes dense and the vertical convection overcomes the lateral diffusion, triggering an instability in the interface of both fluids. Also, they justified the use of the two dimensional Darcy model for their dimensional analysis because the Reynolds number of experiments was very small. The amount of water mixed was determined from the measurement of the mixing area A between the initial interface and the mid part of the subsequent diffusive interface. The results show that after an initial time, the mixing area increases linearly with time, which indicates a constant mass transfer. This observation was also obtained by Neufeld et al (2010). The Nusselt number for mass transfer was defined by Backhaus et al (2011) as

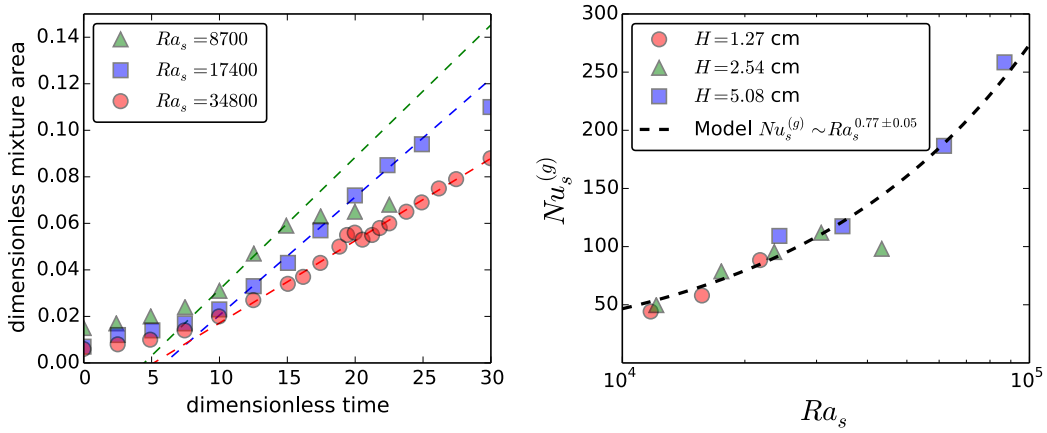

Figure 4.2.7: Experimental results of the work of Backhaus et al (2011). The left image shows the dimensionless mixture area A/LH as function of the dimensionless time t^* (triangles for $K = 0.77 \times 10^{-4}\,\mathrm{cm}^2$ and $Ra_s = 8700$, squares for $Ra_s = 17400$ and circles for $Ra_s = 34800$). The right image shows the correlation between the Nusselt and Rayleigh numbers for different values of H (circles for $H = 1.27\,\mathrm{cm}$, triangles for $H = 2.54\,\mathrm{cm}$ and squares for $H = 5.08\,\mathrm{cm}$) (Backhaus et al, 2011)

$$Nu_s^{(g)} = \frac{\dot{m}}{\rho\,(\kappa_s/H)\,bL} = Ra_s\,\frac{d}{dt^*}\left(\frac{A}{LH}\right) \quad ; \quad Ra_s = \frac{\Delta\rho\,g\,K\,H}{\mu\,\kappa_s} \quad ; \quad K = \frac{b^2}{12}\,, \tag{4.2.4}$$

where $\dot{m}$ is the convective mass transfer, L is the width and H is the height. The molecular diffusion κ_s, density ρ and dynamic viscosity μ were determined from the properties of mixture at $S_w = 0.3$.

From the right image of Fig. 4.2.7, Backhaus et al (2011) obtained the scaling law $Nu_s^{(g)} \sim Ra_s^{0.76\pm0.06}$, which is different of the scaling obtained by Neufeld et al (2010) but

close to the theoretical prediction $Nu_s^{(g)} \sim Ra_s^{0.8}$. It is worth noting that the experiments of Neufeld et al and Backhaus et al were performed in different geometries. Neufeld's experiment used a saturated porous matrix of low porosity ϕ and permeability K, so dispersion effects can be negligible, but the experiment of Backhaus was performed in a Hele-Shaw cell, where the porosity $\phi = 1$, the permeability is very high compared with a real porous medium and the ratio $\epsilon = \sqrt{K}/H$ fluctuates from 1×10^{-3} to 6×10^{-3}, so dispersion could be relevant. In Chapter 5, Section 5.4 on page 57, we show that ϵ is an important parameter in Hele-Shaw models. Therefore, Howard's scaling assumption is invalid for the analogue model, which is a more realistic representation of the convective dissolution of CO_2 in geologic formations.

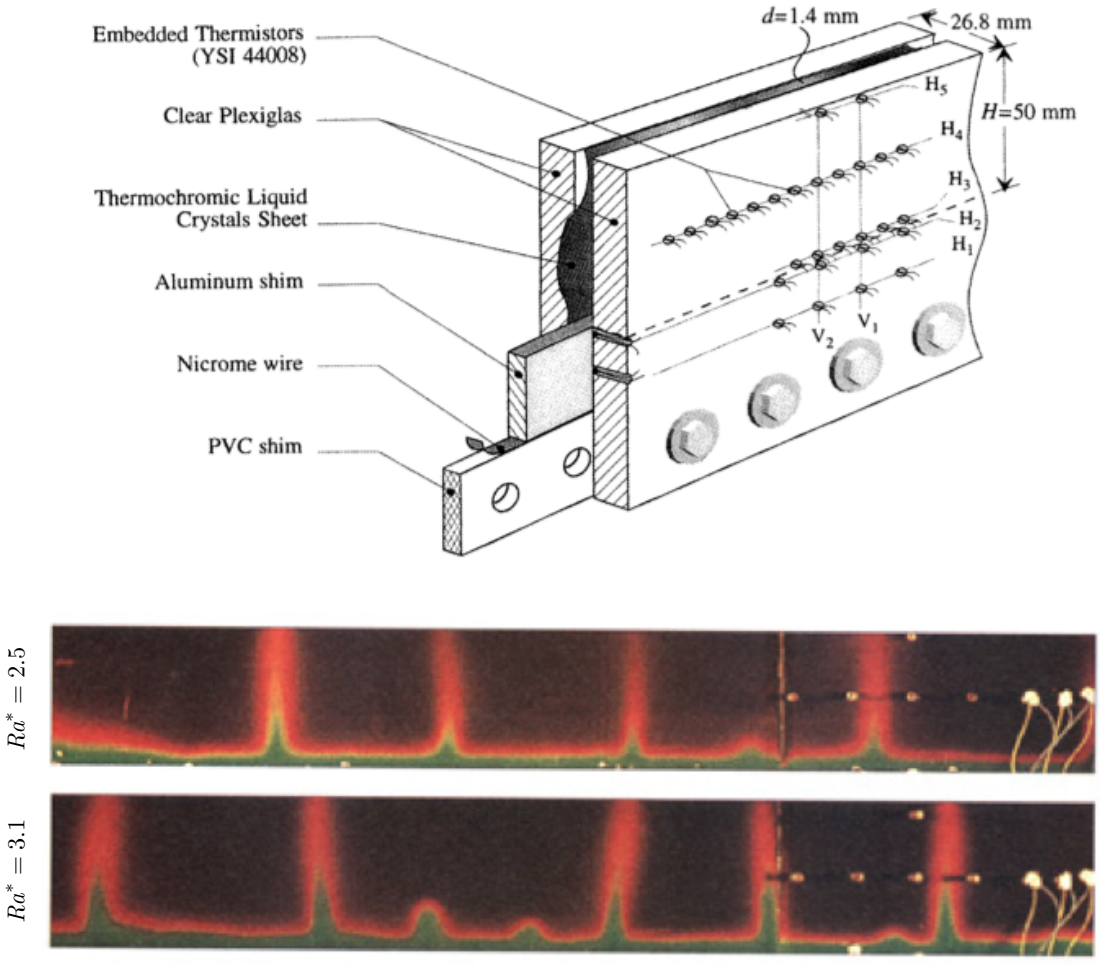

Figure 4.2.8: Experimental setup used by Cherkaoui and Wilcock and experimental images obtained for different Rayleigh numbers, where $Ra^* = Ra_t/Ra_{cr}$ with $Ra_{cr} = 29.7$. Figure from Cherkaoui and Wilcock (2001)

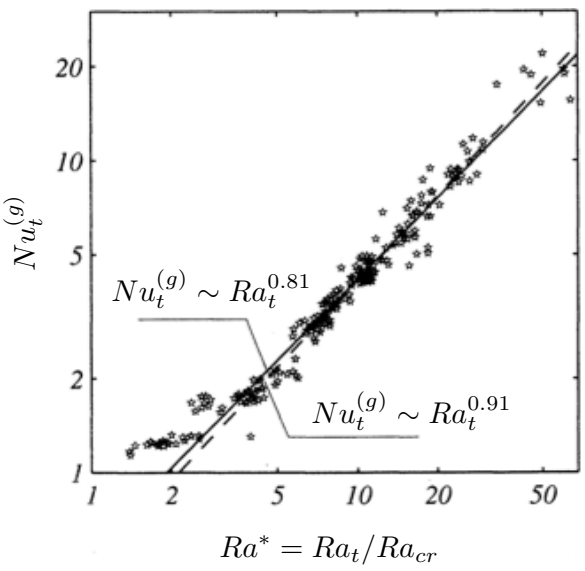

Figure 4.2.9: Nusselt number as function of the Rayleigh number. Data interpolation from the onset of convection gives the scaling law $Nu_t^{(g)} \sim Ra_t^{0.81}$. Above $Ra_t \sim 200$, the scaling law obtained is $Nu_t^{(g)} \sim Ra_t^{0.91}$. For this case, $Ra_{cr} \sim 29.7$. Figure from Cherkaoui and Wilcock (2001)

On the other hand, Cherkaoui and Wilcock (2001) performed thermal convection experiments in an Hele-Shaw cell, which consisted in two acrylic plates of thickness $L_p = 12.7\,\text{mm}$, height $H = 50\,\text{mm}$ and width $L = 800\,\text{mm}$, separated by an aluminium shim of thickness $b = 1.4\,\text{mm}$. A thin nichrome wire, connected to the electric power, gave a constant heat flux to the aluminium shim, which was the bottom base of the cell. The upper part of the cell was open to the atmosphere (see Fig. 4.2.8). A thin layer of thermocromic crystals of thickness $d_a = 125\,\mu\text{m}$ was used to visualize the convection. These crystals are sensible with temperature changes in the range of $20\,^\circ\text{C}$ to $25\,^\circ\text{C}$, so its use was only for visualization purposes. The measurement of temperature was done using thermistors. Unlike mixing convection, in thermal convection the observed exponent in the scaling $\langle Nu_t \rangle_\tau \sim Ra_t^\gamma$ is somewhat lower than the predicted by Howard (Elder, 1967a; Koster and Muller, 1982; Graham and Steen, 1994; Otero et al, 2004; Hewitt et al, 2012), where $Ra_t = \beta\,\Delta T\,g\,K\,H/\mu_a\,\kappa_t$ is the Rayleigh number. In this definition, β is the thermal expansion coefficient and ΔT is the temperature difference between the upper and lower parts of the cell. The experimental results obtained by Cherkaoui and Wilcock show that $Nu_t^{(g)} \sim Ra_t^{0.91}$ in the range $Ra_t \sim 200$ to $Ra_t \sim 1500$. Fig. 4.2.9 shows the experimental data obtained by Cherkaoui and Wilcock.

4.3 Analogue model and long-term CO_2 solubility trapping

Hewitt et al (2013) studied the problem of mixing convection using a fixed-interface system (canonical model) and two different free-interface systems, inmiscible and miscible fluids (analogue model). Fig. 4.3.1 shows a schematic picture of the three physical systems studied by Hewitt et al in terms of the equations of state. The authors solved numerically Eqns. (4.1.4) to (4.1.6) using spectrally based methods (Lele, 1992), flux-conservative techniques and an alternating-direction implicit method, obtaining an interesting behaviour for the convective flux in density-driven convection, the so-called shutdown regime, which was not observed by earlier experimental works (Neufeld et al, 2010; Backhaus et al, 2011). This regime is characterized by a decrease in time of the convective flux due to the return of plumes that have reached the base of the domain (see Fig. 4.3.2). For the miscible case, this observation was confirmed by long term experiments using deionized water and PPG (Backhaus et al, 2011).

The physical explanation given by Hewitt et al for the shutdown regime was the following. Initially, a stable diffusive boundary layer grows below the interface. After the critical time $t_0 \sim 1/Ra_s$, the Rayleigh-Taylor instability appears, leading a downward convection. Therefore, the convective dynamics is independent of the location of the bottom boundary and the flux remains constant, so the height of the interface is a monotonic function that grows linearly with time. At time $t \sim t_1$, some of these plumes reaches the base of the domain, while at time $t \sim t_2$ the return flow reaches the interface, marking the onset of the shutdown regime. For $t > t_2$, the convective flux decreases nonlinearly with time.

Hewitt et al developed a theoretical model that explains appropiately the problem. In this model, the convective flux and height of the interface can be predicted for inmiscible and miscible fluids, showing a very similar behaviour for flux over time between the inmiscible and miscible systems. However, the evolution of the interfacial height h_{int} is qualitatively different for long times because for the inmiscible case the height increases for all time, while for the miscible case it eventually decreases nonlinearly. Fig. 4.3.2 shows a schematic behaviour observed by the authors.

The constant flux regime and the linear growth of the interfacial height were observed by Neufeld et al (2010). It is interesting to note that similar results were also observed by Backhaus et al (2011). Anyway, for long term analogue experiments it is important

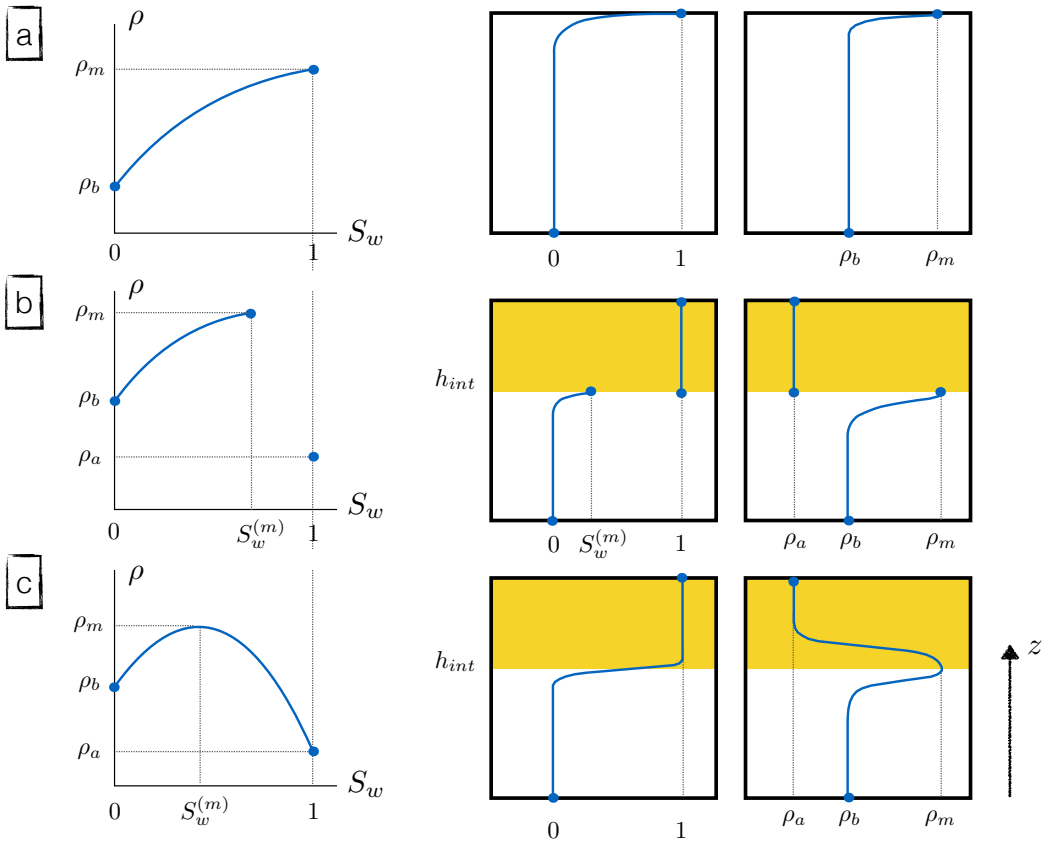

Figure 4.3.1: Schematic picture that shows typical constitutive equations $\rho(S_w)$, vertical water concentration $S_w(z)$ and vertical density profiles $\rho(z)$, for each of physical systems studied by Hewitt et al, (a) fixed-interface system, (b) inmiscible system, where h_{int} is constant, and (c) miscible system, where h_{int} is deformable and given by the maximum isopycnal (Hewitt et al, 2013)

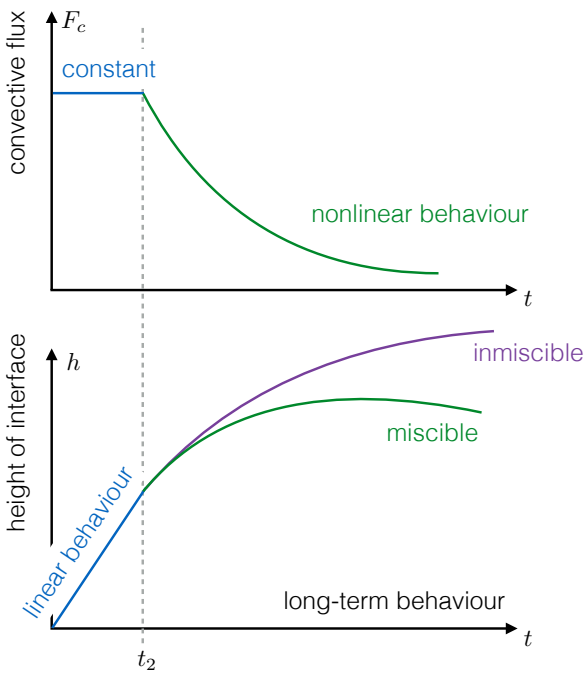

Figure 4.3.2: Schematic picture of the behaviour observed for the convective flux and interfacial height in the numerical experiments of Hewitt et al (2013), for the inmiscible and miscible cases. In both cases, the fluxes are similar, but the height has a qualitative different behaviour for long times

to remember that CO_2 is partially soluble with water, so the correlation between laboratory scale results and real CO_2 solubility trapping can be different for long times, as is suggested by Hewitt et al.

The Darcian scaling law for miscible fluids $Nu_s^{(g)} \sim Ra_s^{0.8}$ is valid in the linear regime (where the convective flux is constant). The mathematical modeling of mass transfer in the nonlinear regime observed by Hewitt et al is an open research question which seems to be more complicated to solve due to the dependency in time of the flux. Some properties of inmiscible fluids in the miscible system model, such as the incorporation of interfacial tension in the governing equations, will be interesting to study, overall if these effects can play an important role in the onset of convection. Finally, the development of new techniques of computation of the convective flux in miscible systems are crucial in the appropiate estimation of this quantity, which is very difficult to do in practice.

Part II

Theoretical background

Chapter 5

Governing equations for saturated porous media: The Hele-Shaw cell analogy

Abstract

The dissolution of supercritical CO_2 in geologic reservoirs and the geothermal convection in sedimentary basins are two problems of current interest, where the use of Hele-Shaw cells has become in a good alternative for the experimental visualization of heat and mass transfer in porous media. Commonly, the flow within the cell is modeled mathematically using the two dimensional Darcy equation. However, when the gap of the cell is increased, some three dimensional effects in the flow can appear and the Darcy equation needs corrections. In this article, we investigate the inertial contributions to Darcy equation with the application of regular asympthotic expansions to the fluid equations in a Hele-Shaw geometry of gap b and height H, where the anisotrophy parameter $\delta = b/H \ll 1$ is used as the perturbative variable. The derived momentum equation includes a viscous dissipation term $\mathbf{L}_{diss} = 6/5\,\bar{\mu}'\,\nabla'^{2}\bar{\mathbf{u}}'$, a quadratic velocity term $\mathbf{L}_{forch} = 2/35\,(\bar{\mathbf{B}}'_{\mu}\cdot\bar{\mathbf{u}}')\,\bar{\mathbf{u}}'$, a new vertical mass advection term $\mathbf{L}_{mass} = 2/35\,(\bar{\mathbf{B}}'_{\rho}\cdot\bar{\mathbf{u}}')\,\hat{z}$ and a new contribution for the Korteweg stress tensor that models interfacial effects of mixing, where $\bar{\mathbf{u}}'(\mathbf{x},t)$ is the gap-averaged velocity field and both $\bar{\mathbf{B}}'_{\mu}$ and $\bar{\mathbf{B}}'_{\rho}$ are vector-valued functions. The scalar transport equation also includes the well-known mechanical dispersion term for Hele-Shaw cells. For analogue experiments in Hele-Shaw cells that represents CO_2 dissolution in geothermal reservoirs, we show that the mechanical dispersion term cannot be neglected.

5.1 Introduction

The reduction of anthropogenic emissions to the atmosphere has been a problem of great interest in the last decade. The combustion of fossil energy sources has increased substantially the amount of CO_2 in the atmosphere, where several studies conclude a future increase in the global temperatures in the world (Hansen et al, 2010; Kirtman et al, 2013; Collins et al, 2013). Today, some effects began to be visible in polar regions and ancient glaciers in the principal mountain ranges (Vaughan et al, 2013). Therefore, mitigation strategies about greenhouse gas emissions and a future energy conversion

are actually necessary. In this context, capture and storage of supercritical CO_2 in geological reservoirs and heat extraction from enhanced geothermal systems are two examples that can contribute to this effort. The first is one of the most promising ideas to reduce the release of greenhouse gases to the atmosphere, where CO_2 is confined inside a geological formation with an impermeable caprock for a long time (Holloway, 1997; Benson et al, 2006; Orr, 2009; Pau et al, 2010; Szulczewski et al, 2013; Hewitt et al, 2013; Hidalgo et al, 2013; Huppert and Neufeld, 2014; Emami Meybodi et al, 2015). The second enables to obtain energy from natural geothermal sources, in zones where the scarcity of water or the low permeability of rock strata can make difficult the energy extraction.

In geophysics, the carbon dioxide confinement is characterized by an initial base state that governs the dynamics of the diffusive boundary layer between CO_2 gas phase and brine, where a small fraction of the gas phase is dissolved (Van der Meer, 1992; Pruess and Garcia, 2002). This process induces an instability in a wide range of scales known as Rayleigh-Taylor (Sharp, 1984), which has consequences in many natural and artificial flow systems, such as astrophysical flows (Zingale et al, 2005; Cabot and Cook, 2006), geophysical turbulence in planetary atmospheres (Huang et al, 1993) and Non-Aqueous Phase Liquid flow (NAPLs) contamination and dissolution in soils due to anthropogenic activities such as CO_2 storage in subsurface (Caltagirone, 1980; Ben et al, 2002; Ennis-King and Paterson, 2005; Riaz et al, 2006; Rapaka et al, 2008), to name a few. Mathematically, this problem is similar to the density-driven convection induced by thermal forcing in porous media, the well-studied Elder problem (Foster, 1965; Elder, 1967c; Otero et al, 2004; Hewitt et al, 2012, 2014), which has important applications in geothermal convection in sedimentary basins (Clausnitzer et al, 2001; Simms and Garven, 2004).

Physical experiments that allow the visualization of the dissolution of CO_2 gas phase into brine in geological reservoirs and geothermal convection are difficult to perform because of the extreme thermodynamical conditions presented in the deep subsurface. For this reason, analogous experiments designed for the study of density and viscous driven convection due to the mixing of two miscible fluids (Kneafsey and Pruess, 2009; Neufeld et al, 2010; Backhaus et al, 2011; Slim et al, 2013; Szulczewski and Juanes, 2013; MacMinn and Juanes, 2013; Thomas et al, 2015) and thermal convection in a single fluid phase (Babushkin and Demin, 2006; Cherkaoui and Wilcock, 2001; Cooper et al, 2014) are made in Hele-Shaw cells, because these geometries are a good approximation of an homogeneous porous media (Nield and Bejan, 2006) and

therefore the experimental results can be compared with the numerical predictions obtained by using the Darcy-Boussinesq model. However, there are still some open issues. For example, convective dissolution in geological CO_2 reservoirs has been studied experimentally using solutions of methanol and ethylene glycol (MEG) mixing with water (Neufeld et al, 2010) and aqueous solutions of propylene glycol (PPG) (Backhaus et al, 2011), where the upper boundary of the Hele-Shaw has a constant flux. The Rayleigh number Ra is the only parameter that controls the fluid dynamics. The response of the system is studied by means of the Nusselt number Nu. When $Re \ll 1$, the experimental results show that there exists a nonlinear scaling of the form $Nu \sim Ra^{0.84\pm0.02}$ (Neufeld et al, 2010) and $Nu \sim Ra^{0.76\pm0.06}$ (Backhaus et al, 2011). However, this nonlinear scaling is in contradiction with theoretical predictions obtained from the study of the mean scalar dissipation rate ε (Hidalgo et al, 2012), where a nonlinear scaling of the form $Nu \sim Ra^n$, with $|n| > 0$, must be reflected in a scaling of the type $\varepsilon \sim Ra^m$, with $|m| > 0$. Numerical simulations using the Darcy equation done by Hidalgo et al (2012) show that $m = 0$, i.e. the convective flux does not depend upon Ra, so it is necessary to have a new model that represents this experimental observation. See Chapter 5, Section 5.4 on page 60 for further information. We refer the works of Bizon et al (1997a), Gondret and Rabaud (1997), Ruyer-Quil (2001a), Ress (2002) and Martin et al (2002), where some extensions of the Darcy model are derived.

On the other hand, the transition zone between the miscible two-fluid phases indicates the existence of a step scalar gradient in the early stages of convection, which is relaxing in time due to diffusive processes. Then, an interfacial tension appears and its effects are similiar to the surface tension forces in inmiscible fluids, inhibiting the instability and finger growth (Arendt et al, 2004; Pramanik and Mishra, 2015). These interfacial effects are important not only in density-driven instabilities, but also in viscosity-driven instabilities such that the Saffman-Taylor problem. The dynamic viscosity of supercritical CO_2 is less than the liquid water in high enthalpy geothermal conditions at 1 km of depth, where pressure is 800 atm and temperature is 200 °C, so the CO_2 gas-phase can displace the water liquid-phase not only by density driven convection but also by viscous fingering (Jha et al, 2011a,b, 2013). Therefore, the combined effect can have important consequences in the onset of convection, which has not been investigated so far. This point can be very important when CO_2 dissolution in brine is affected by thermal instabilities. In this context, a novel approach that simultaneously generates renewable energy and store carbon dioxide was proposed by Brown (2000) and

Pruess (2006) and further study by Randolph and Saar (2011a,b), which is currently known as CO_2 plume geothermal system. In comparison with standard brine geothermal reservoirs, recent studies show that this technology improves the electrical production by a factor of two (Adams et al, 2015). This proposal combines both energy generation and reduction of the release of greenhouse gases to the atmosphere, so we are interested in study mathematically this problem using a reduced physical model.

In this chapter, we present our investigation about the use of supercritical CO_2 as working fluid in geothermal reservoirs considering an analogue model based on the Hele-Shaw geometry. For this case, inertial contributions to the Darcy-Boussinesq equation were obtained applying regular perturbation theory to a full miscible two-fluid system which is governed by the Navier-Stokes equation in the Boussineq limit. The model considers interfacial effects and two scalar variables of interest in geothermal problems, concentration and temperature. By using this new model, we aim of finding scaling laws for heat transport and scalar dissipation, to conciliate the existing discrepancies between numerical and experimental observations.

5.2 Capture and storage of CO_2 in geothermal reservoirs. The Hele-Shaw cell analogy

Fig. 5.2.1 shows the analogy between the storage of CO_2 in geothermal reservoirs and analogous experiments using Hele-Shaw cells. In the left image, the industrial application considers the capture and compression of cold carbon dioxide from an emitter, which is injected into a saline aquifer. The CO_2 plume is heated and transported by convection and then it experiment buoyant forces due to density contrast, reaching the upper caprock. A small portion of hot CO_2 is extracted and used to produce electricity, which is cooled and injected again in the aquifer. The right image shows a rectangular Hele-Shaw geometry filled with a fluid A of density ρ_a and dynamic viscosity μ_a at temperature T_a. The size of the cell is $L \times H \times b$, where b is the gap of the cell in the $\hat{y}$ direction, H is the height in the $\hat{z}$ direction and L is the width in the $\hat{x}$ direction. To reproduce geothermal convection, the lower and upper boundaries are heated and cooled with constant temperatures T_h and T_c, respectively. The upper boundary acts as the caprock. Next, a fluid B of density $\rho_{in} < \rho_a$, which is fully miscible with fluid A, is injected inside the cell. The concentration S_w measures the amount of fluid B dissolved in fluid A.

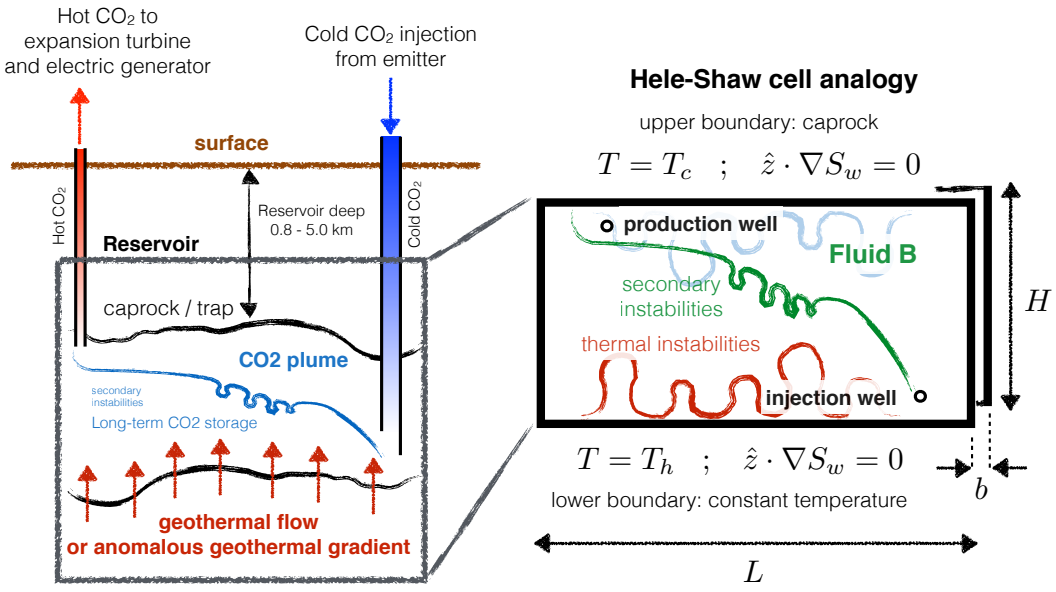

Figure 5.2.1: Capture and storage of CO_2 in geothermal reservoirs and its analogy with analogous experiments using Hele-Shaw cells

Therefore, the motion of the miscible fluid is described by the three-dimensional Navier-Stokes equations under the Boussinesq approximation (NSBE), where we consider interfacial effects due to the mixing. In cartesian tensorial form, these equations are written as

$$\nabla \cdot \mathbf{u} = 0 \tag{5.2.1}$$

$$\rho_a \frac{\mathcal{D}u_i}{\mathcal{D}t} = \partial_j \Pi^{(s)}_{ji} + \partial_j \Pi^{(k)}_{ji} - \rho g_i \tag{5.2.2}$$

$$\frac{\mathcal{D}\varphi}{\mathcal{D}t} = \kappa_\varphi \nabla^2 \varphi \tag{5.2.3}$$

$$\Pi^{(s)}_{ji} = -p\,\delta_{ji} + \mu\left[\partial_j u_i + \partial_i u_j\right] + \frac{2}{3}\lambda\,\delta_{ji}\,\nabla\cdot\mathbf{u} \tag{5.2.4}$$

$$\Pi^{(k)}_{ji} = \delta_{ji}\left[\alpha\,\nabla^2\rho + \beta\,|\nabla\rho|^2\right] - \phi\,(\partial_j\rho)(\partial_i\rho) + \gamma\,\partial_j(\partial_i\rho) \tag{5.2.5}$$

where $\mathcal{D}/\mathcal{D}t = \partial/\partial t + \mathbf{u}\cdot\nabla$, $\varphi : (T, S_w)$ is a generic scalar-valued function which can

be either the temperature T of the fluid or the concentration S_w of a secondary fluid in an ambient fluid. In Eqns. (5.2.1) to (5.2.3), κ_t is the thermal diffusivity (when $\varphi = T$), κ_s is the molecular diffusivity (when $\varphi = S_w$), $\mathbf{u} = u\hat{x} + v\hat{y} + w\hat{z}$ is the velocity field, $\mathbf{g} = g\,\hat{z}$ is the gravitational acceleration, and $\rho = \rho(S_w, T)$ is the density of the two-fluid mixing. The no-slip and no-flux boundary conditions on $\hat{y}$ direction are applied. In Eqn. (5.2.4), $\Pi_{ji}^{(s)}$ is the Stokes stress tensor, where p is the pressure, $\mu = \mu(S_w, T)$ is the dynamic viscosity of the two-fluid mixing and λ is the Stokes parameter. On the other hand, $\Pi_{ji}^{(k)}$ in Eqn. (5.2.5) is the full Korteweg tensor (Korteweg, 1901), which models the interfacial effects of fluid mixing, where α , β and γ are Lagrange multipliers and ϕ is the effective interfacial tension parameter. In this chapter, we consider that $\alpha = \beta = \gamma = 0$.

To consider the density buoyancy effects relative to the ambient fluid, we define the modified pressure $\tilde{p}$ as the scalar that satisfies the equation $\partial\tilde{p}_a/\partial z = \partial p/\partial z + \rho_a g$. Since the length scale in the $\hat{y}$ direction is much smaller than in the other directions, we introduce the following vector notation to separate these length scales: $\mathbf{x} = \mathbf{x}_\perp + \mathbf{y}$, $\mathbf{x}_\perp = x\hat{x} + z\hat{z}$, $\mathbf{y} = y\hat{y}$, $\mathbf{u} = \mathbf{u}_\perp + \mathbf{v}$, $\mathbf{u}_\perp = u\hat{x} + w\hat{z}$, $\mathbf{v} = v\hat{y}$ and

$$\nabla = \nabla_\perp + \nabla_y \,, \quad \nabla_\perp = \hat{x}\frac{\partial}{\partial x} + \hat{z}\frac{\partial}{\partial z} \,, \quad \nabla_y = \hat{y}\frac{\partial}{\partial y} \,,$$

$$\nabla^2 = \nabla_\perp^2 + \nabla_y^2 \,, \quad \nabla_\perp^2 = \frac{\partial^2}{\partial x^2} + \frac{\partial^2}{\partial z^2} \,, \quad \nabla_y^2 = \frac{\partial^2}{\partial y^2} \,.$$

To nondimensionalize the problem, we use the scalings for position $\mathbf{x}_\perp^* = \mathbf{x}_\perp/H$ and $\mathbf{y}^* = \mathbf{y}/b$, for velocity $\mathbf{u}^* = \mathbf{u}/u_c$, for time $t^* = u_c\,t/H$, for pressure $p^* = \tilde{p}_a/p_s$, for density $\rho^* = -(\rho - \rho_a)/\Delta\rho$, for viscosity $\mu^* = \mu/\mu_a$ and for temperature $T^* = (T - T_a)/\Delta T$, where $\Delta\rho = \rho_a - \rho_{in} > 0$ is the density contrast between the two fluids at temperature T_a , and $\Delta T = T_h - T_c > 0$ is the constant temperature difference between the top and bottom plates of the cell. The characteristic convective velocity scale u_c and pressure p_s are

$$u_c = \frac{\Delta\rho\, g\, b^2}{\mu_a} \,, \quad p_s = \frac{\mu_a u_c H}{b^2} \,. \tag{5.2.6}$$

The equations can be written in dimensionless form in terms of five parameters, the cell Reynolds number $Re^{(c)}$, the thermal cell Peclet number $Pe_t^{(c)}$, the solutal cell

Peclet number $Pe_s^{(c)}$, the cell capillary number $Ca^{(c)}$ and the Lewis number Le, defined as

$$Re^{(c)} = \frac{u_c\, b}{\nu_a}\,,\;\; Pe_t^{(c)} = \frac{u_c\, b}{\kappa_t}\,,\;\; Pe_s^{(c)} = \frac{u_c\, b}{\kappa_s}\,,\;\; Ca^{(c)} = \frac{u_c\, \mu_a}{\gamma_\sigma}\,,\;\; Le = \frac{\kappa_t}{\kappa_s}\,,$$

where $\nu_a = \mu_a/\rho_a$ is the momentum diffusivity of the ambient fluid and $\gamma_\phi = \phi\,(\Delta\rho)^2\, b/H^2$ is the interfacial tension, which has dimensions $[\gamma_\sigma] = MT^{-2}$. In the following sections, we assume that the cell Reynolds number is of order $Re^{(c)} = O(1)$.

5.3 Regular perturbation theory

We consider the case of a thin cell, where $b \ll H$. Following the usual procedure in regular asymptotic expansions, we introduce the small parameter $\delta = b/H$, which measures the ratio of cell spacing to height, and we introduce the following new variables $\mathbf{u}_\perp^* = \delta\,\mathbf{u}'_\perp$, $\mathbf{v}^* = \delta^2\,\mathbf{v}'$, $p^* = \delta\,p'$, $\rho^* = \delta\,\rho'$, $\mathbf{x}_\perp^* = \mathbf{x}'_\perp$, $\mathbf{y}^* = \mathbf{y}'$, $\tau = \delta\,t^*$ and $\mu^* = \mu'$. With these scalings, the NSBE are written as

$$\nabla'_\perp \cdot \mathbf{u}'_\perp = -\nabla'_y \cdot \mathbf{v}'\,, \tag{5.3.1}$$

$$\begin{aligned}\delta^2 Re^{(c)}\left[\frac{\partial \mathbf{u}'_\perp}{\partial\tau} + (\mathbf{u}'_\perp\cdot\nabla'_\perp)\mathbf{u}'_\perp + (\mathbf{v}'\cdot\nabla'_y)\mathbf{u}'_\perp\right] &= -\nabla'_\perp p' + \rho'\hat{z} + \mu'\Big[\nabla'^2_y\mathbf{u}'_\perp + \delta^2\nabla'^2_\perp\mathbf{u}'_\perp\Big]\\ &- \frac{1}{Ca^{(c)}}\left[\nabla'_\perp\rho'\Big(\delta^2\,\nabla'^2_\perp\rho' + \nabla'^2_y\rho'\Big) + \frac{1}{2}\,\nabla'_\perp\Big(\delta^2|\nabla'_\perp\rho'|^2 + |\nabla'_y\rho'|^2\Big)\right],\end{aligned} \tag{5.3.2}$$

$$\begin{aligned}\delta^4 Re^{(c)}\left[\frac{\partial \mathbf{v}'}{\partial\tau} + (\mathbf{u}'_\perp\cdot\nabla'_\perp)\mathbf{v}' + (\mathbf{v}'\cdot\nabla'_y)\mathbf{v}'\right] &= -\nabla'_y p' + \delta^2\mu'\Big[\nabla'^2_y\mathbf{v}' + \delta^2\nabla'^2_\perp\mathbf{v}'\Big]\\ &- \frac{1}{Ca^{(c)}}\left[\nabla'_y\rho'\Big(\delta^2\,\nabla'^2_\perp\rho' + \nabla'^2_y\rho'\Big) + \frac{1}{2}\,\nabla'_y\Big(\delta^2|\nabla'_\perp\rho'|^2 + |\nabla'_y\rho'|^2\Big)\right],\end{aligned} \tag{5.3.3}$$

$$\delta^2 Pe_\varphi^{(c)}\left[\frac{\partial\varphi^*}{\partial\tau} + \mathbf{u}'_\perp\cdot\nabla'_\perp\varphi^* + \mathbf{v}'\cdot\nabla'_y\varphi^*\right] = \nabla'^2_y\varphi^* + \delta^2\nabla'^2_\perp\varphi^*\,, \tag{5.3.4}$$

where $Pe_{\varphi}^{(c)}$ is the thermal or solutal cell Peclet number, depending on the definition of the generic scalar φ. The relevant parameter in Eqns. (5.3.1) to (5.3.4) is $\delta^2 = Da$, which is also known as the Darcy number (Nield and Bejan, 2006). We proceed to solve perturbatively the dimensionless form of NSBE by expanding all physical variables as $f = f^{(0)} + \delta^2 f^{(1)} + O(\delta^4)$ for $f : (\mathbf{u}'_\perp, \mathbf{v}')$ and $g = g_0 + \delta^2 g_1 + \delta^4 g_2 + O(\delta^6)$ for $g : (p', \rho', \mu', \varphi^*)$. At this stage, the only boundary conditions that we consider are $\mathbf{u}' = \mathbf{0}$ and $\hat{y} \cdot \nabla'_y \varphi^* = 0$, all of them evaluated at $y' = 0$ and $y' = 1$.

5.3.1 Leading order terms

At order $O(1)$, Eqn. (5.3.4) is $\nabla'^2_y \varphi^*_0 = 0$ subject to the boundary condition $\hat{y} \cdot \nabla'_y \varphi^*_0 = 0$ in $y' = 0$ and $y' = 1$. The solution for this equation is $\varphi^*_0 = \varphi^*_0(\mathbf{x}'_\perp, \tau)$ and, therefore, the fluid density and viscosity satisfies the variable dependency $\rho'_0 = \rho'_0(\mathbf{x}'_\perp, \tau)$ and $\mu'_0 = \mu'_0(\mathbf{x}'_\perp, \tau)$. Then, at the leading order, we must solve the Stokes equation

$$\nabla'_\perp \cdot \mathbf{u}'^{(0)}_\perp = -\nabla'_y \cdot \mathbf{v}'^{(0)} ,$$

$$-\nabla'_y p'_0 = 0 ,$$

$$-\nabla'_\perp p'_0 + \rho'_0 \hat{z} + \mu'_0 \nabla'^2_y \mathbf{u}'^{(0)}_\perp = 0 ,$$

subject to the boundary condition $\mathbf{u}'^{(0)} = \mathbf{0}$ in $y' = 0$ and $y' = 1$. The solution for the pressure is $p'_0 = p'_0(\mathbf{x}'_\perp, \tau)$, the velocity $\mathbf{u}'^{(0)}_\perp$ is the Poiseuille flow

$$\mu'_0 \, \mathbf{u}'^{(0)}_\perp = \frac{1}{2}\Big[\nabla'_\perp p'_0 - \rho'_0 \, \hat{z}\Big]\Big(y'^2 - y'\Big) , \tag{5.3.5}$$

and $\mathbf{v}'^{(0)} = \mathbf{0}$. We define the mean value of a generic variable f in the $\hat{y}$ (transverse) direction as $\{f\} = \int_0^1 f \, dy'$. Finally, we obtain the two-dimensional Darcy equation by averaging the Eqn. (5.3.5) in the transverse direction

$$\{\mu'_0\}\{\mathbf{u}'^{(0)}_\perp\} = -\frac{1}{12}\Big[\nabla'_\perp \{p'_0\} - \{\rho'_0\} \, \hat{z}\Big] . \tag{5.3.6}$$

5.3.2 $O(\delta^2)$ expansion

At order $O(\delta^2)$, the equations to be solved are

$$\nabla'_\perp \cdot \mathbf{u}'^{(1)}_\perp = -\nabla'_y \cdot \mathbf{v}'^{(1)} ,$$

$$Re^{(c)}\left[\frac{\partial \mathbf{u}'^{(0)}_\perp}{\partial \tau} + (\mathbf{u}'^{(0)}_\perp \cdot \nabla'_\perp)\mathbf{u}'^{(0)}_\perp\right] = -\nabla'_\perp p'_1 + \rho'_1 \hat{z} + \mu'_0 \nabla'^2_y \mathbf{u}'^{(1)}_\perp + \mu'_1 \nabla'^2_y \mathbf{u}'^{(0)}_\perp + \mu'_0 \nabla'^2_\perp \mathbf{u}'^{(0)}_\perp$$
$$- \frac{1}{Ca^{(c)}}\left[\nabla'_\perp \rho'_0 \left(\nabla'^2_\perp \rho'_0 + \nabla'^2_y \rho'_1\right) + \frac{1}{2}\nabla'_\perp\left(|\nabla'_\perp \rho'_0|^2 + |\nabla'_y \rho'_1|^2\right)\right] ,$$

$$-\nabla'_y p'_1 = \frac{1}{Ca^{(c)}}\left[\frac{1}{2}\nabla'_y\left(|\nabla'_y \rho'_1|^2\right)\right] ,$$

$$Pe^{(c)}_\varphi\left[\frac{\partial \varphi^*_0}{\partial \tau} + \mathbf{u}'^{(0)}_\perp \cdot \nabla'_\perp \varphi^*_0\right] = \nabla'^2_y \varphi^*_1 + \nabla'^2_\perp \varphi^*_0 , \tag{5.3.7}$$

subject to the boundary conditions $\mathbf{u}'^{(1)} = \mathbf{0}$ and $\hat{y}\cdot\nabla'_y\varphi^*_1 = 0$ in $y' = 0$ and $y' = 1$. From these boundary conditions, we obtain $\{\nabla^2_y \varphi^*_1\} = 0$, so by averaging the Eqn. (5.3.7) we obtain the solubility condition

$$\frac{\partial\{\varphi^*_0\}}{\partial \tau} + \{\mathbf{u}'^{(0)}_\perp\} \cdot \nabla'_\perp\{\varphi^*_0\} = \frac{1}{Pe^{(c)}_\varphi}\nabla'^2_\perp\{\varphi^*_0\} . \tag{5.3.8}$$

Omiting the details in the mathematical procedure, which is lengthy but straightforward, we find that the solution for φ^*_1 in Eqn. (5.3.7) is

$$\varphi^*_1 = \{\varphi^*_1\} - Pe^{(c)}_\varphi \{\mathbf{u}'^{(0)}_\perp\} \cdot \nabla_\perp\{\varphi^*_0\} f(y) , \quad f(y) = \frac{y^4}{2} - y^3 + \frac{y^2}{2} - \frac{1}{60} . \tag{5.3.9}$$

At this order, the density and viscosity satisfy the variable dependency $\rho'_1 = \rho'_1(\mathbf{x}', \tau)$ and $\mu'_1 = \mu'_1(\mathbf{x}', \tau)$. Finally, the averaged solutions of $O(\delta^2)$ equations are $\{\mathbf{v}'^{(1)}\} = \mathbf{0}$ and the two-dimensional Darcy's law extension

$$\frac{6}{5}\,Re^{(c)}\,\frac{\tilde{\mathcal{D}}_\perp\{\mathbf{u}_\perp'^{(0)}\}}{\tilde{\mathcal{D}}\tau} = -\nabla'_\perp\{p'_1\} + \{\rho'_1\}\,\hat{z} - 12\left(\{\mu'_0\}\{\mathbf{u}_\perp'^{(1)}\} + \{\mu'_1\}\{\mathbf{u}_\perp'^{(0)}\}\right) + \frac{6}{5}\,\{\mu'_0\}\nabla'^2_\perp\{\mathbf{u}_\perp'^{(0)}\}$$
$$- \frac{1}{210}\,\{\mathbf{u}_\perp'^{(0)}\}\cdot\mathbf{B}_\rho\,\hat{z} + \frac{2}{35}\left(\{\mathbf{u}_\perp'^{(0)}\}\cdot\mathbf{B}_\mu\right)\{\mathbf{u}_\perp'^{(0)}\} \tag{5.3.10}$$
$$- \frac{1}{Ca^{(c)}}\left[\nabla'_\perp\{\rho'_0\}\,\nabla'^2_\perp\{\rho'_0\} + \frac{1}{2}\,\nabla'_\perp\left(|\nabla'_\perp\{\rho'_0\}|^2 + \frac{1}{210}\left[\{\mathbf{u}_\perp'^{(0)}\}\cdot\mathbf{B}_\rho\right]^2\right)\right]$$

The modified material derivative $\tilde{\mathcal{D}}_\perp/\tilde{\mathcal{D}}\tau$ and the auxiliar vector functions $\mathbf{B}_\rho$ and $\mathbf{B}_\mu$ are defined as

$$\frac{\tilde{\mathcal{D}}_\perp}{\tilde{\mathcal{D}}\tau} = \frac{\partial}{\partial\tau} + \frac{9}{7}\left(\{\mathbf{u}_\perp'^{(0)}\}\cdot\nabla'_\perp\right),\quad \mathbf{B}_h = -\left[Pe_s^{(c)}\,\frac{\partial h'}{\partial S_w}\bigg|_0\,\nabla'_\perp\{S_w^{(0)}\} + Pe_t^{(c)}\,\frac{\partial h'}{\partial T*}\bigg|_0\,\nabla'_\perp\{T_0^*\}\right],$$

where $h:(\rho,\mu)$ and the derivatives are valued at $(S_w^{(0)},T_0^*)$.

5.3.3 $O(\delta^4)$ expansion

At order $O(\delta^4)$, the solubility condition is obtained applying $\{\nabla'^2_y\varphi_2\}=0$ to the Eqn. (5.3.4)

$$Pe_\varphi^{(c)}\left[\frac{\partial\{\varphi_1^*\}}{\partial\tau} + \{\mathbf{u}_\perp'^{(1)}\}\cdot\nabla'_\perp\{\varphi_0^*\} + \{\mathbf{u}_\perp'^{(0)}\cdot\nabla'_\perp\varphi_1^*\}\right] = \nabla'^2_\perp\{\varphi_1^*\}\,. \tag{5.3.11}$$

Using the Eqns. (5.3.5) and (5.3.9), we obtain the scalar transport equation

$$\frac{\partial\{\varphi_1^*\}}{\partial\tau} + \{\mathbf{u}_\perp'^{(0)}\}\cdot\nabla'_\perp\{\varphi_1^*\} + \{\mathbf{u}_\perp'^{(1)}\}\cdot\nabla'_\perp\{\varphi_0^*\}$$
$$= \frac{1}{Pe_\varphi^{(c)}}\,\nabla'^2_\perp\{\varphi_1^*\} + \frac{Pe_\varphi^{(c)}}{210}\,\nabla'_\perp\cdot\left[\left(\{\mathbf{u}_\perp'^{(0)}\}\cdot\nabla'_\perp\{\varphi_0^*\}\right)\{\mathbf{u}_\perp'^{(0)}\}\right] \tag{5.3.12}$$

The perturbative procedure is halted at this stage, where a general equation is constructed for $\{\mathbf{u}'_\perp\} = \{\mathbf{u}_\perp'^{(0)}\} + \delta^2\{\mathbf{u}_\perp'^{(1)}\} + O(\delta^4)$ and $\{g\} = \{g_0\} + \delta^2\{g_1\} + O(\delta^4)$, with $g:(p',\rho',\mu',\varphi^*)$. The reconstructed momentum equation is

$$\frac{6}{5}\,\delta^2 Re^{(c)}\,\frac{\tilde{\mathcal{D}}_\perp\{\mathbf{u}'_\perp\}}{\tilde{\mathcal{D}}\tau} = -\nabla'_\perp\{p'\} + \{\rho'\}\,\hat{z} - 12\,\{\mu'\}\{\mathbf{u}'_\perp\} + \frac{6}{5}\,\delta^2\{\mu'\}\nabla'^2_\perp\{\mathbf{u}'_\perp\}$$
$$- \frac{1}{210}\,\delta^2\{\mathbf{u}'_\perp\}\cdot\mathbf{B}_{\{\rho\}}\,\hat{z} + \frac{2}{35}\,\delta^2\Big(\mathbf{B}_{\{\mu\}}\cdot\{\mathbf{u}'_\perp\}\Big)\,\{\mathbf{u}'_\perp\} \qquad (5.3.13)$$
$$- \frac{\delta^2}{Ca^{(c)}}\left[\nabla'_\perp\{\rho'\}\,\nabla'^2_\perp\{\rho'\} + \frac{1}{2}\,\nabla'_\perp\left(|\nabla'_\perp\{\rho'\}|^2 + \frac{1}{210}\left[\{\mathbf{u}'_\perp\}\cdot\mathbf{B}_{\{\rho\}}\right]^2\right)\right] + O(\delta^4)$$

where the vector-valued functions $\mathbf{B}_{\{\rho\}}$ and $\mathbf{B}_{\{\mu\}}$ are aproximated as

$$\mathbf{B}_{\{h\}} = Pe_s^{(c)}\,\frac{\partial\{h'\}}{\partial\{S_w\}}\,\nabla'_\perp\{S_w\} + Pe_t^{(c)}\,\frac{\partial\{h'\}}{\partial\{T^*\}}\,\nabla'_\perp\{T^*\}\,,$$

Finally, the scalar transport equation is reconstructed as

$$\frac{\partial\{\varphi^*\}}{\partial\tau} + \{\mathbf{u}'_\perp\}\cdot\nabla'_\perp\{\varphi^*\} = \frac{1}{Pe_\varphi^{(c)}}\,\nabla'^2_\perp\{\varphi^*\} + \delta^2\,\frac{Pe_\varphi^{(c)}}{210}\,\nabla'_\perp\cdot\left[\Big(\{\mathbf{u}'_\perp\}\cdot\nabla'_\perp\{\varphi^*\}\Big)\,\{\mathbf{u}'_\perp\}\right]$$

$$= \partial_\alpha\Big(\mathcal{D}_{\alpha\beta}\,\partial_\beta\{\varphi^*\}\Big)\,, \qquad (5.3.14)$$

where we can identify the hydrodynamic dispersion $\mathcal{D}_{\alpha\beta}$ as the cartesian tensor (Aris, 1956; Ippolito et al, 1994; Oltean et al, 2004, 2008; Mainhagu et al, 2012)

$$\mathcal{D}_{\alpha\beta} = \frac{1}{Pe_\varphi^{(c)}}\,\delta_{\alpha\beta} + \delta^2\,\frac{Pe_\varphi^{(c)}}{210}\,\{u'_\perp\}_\alpha\,\{u'_\perp\}_\beta\,,$$

which is according with the Scheidegger's law (Scheidegger, 1974) $D_{\alpha\beta} = \delta_{\alpha\beta}(\psi_1 + |\mathbf{u}|\psi_2) + (\psi_3 - \psi_2)u_\alpha u_\beta/|\mathbf{u}|$, where $\psi_1 = 1/Pe_\varphi^{(c)}$, $\psi_2 = 0$ and $\psi_3 = (1/210)\,\delta^2\,Pe_\varphi^{(c)}\,|\mathbf{u}|$. In the following, we present the results of the reconstruction of the solutions obtained using asymptotic expansions.

5.4 Hele-Shaw model

To derive the dimensionless Hele-Shaw model, we introduce the appropiate new scalings for velocity $\bar{\mathbf{u}}' = 12\,\delta\,\{\mathbf{u}'_\perp\}$, pressure $\bar{p}' = \delta\,\{p'\}$, density $\bar{\rho}' = -\delta\,\{\rho'\}$, time $\tau = 12\,\delta\,t'$ and anisotrophy ratio $\epsilon = \delta/\sqrt{12} = \sqrt{K}/H$, where $K = b^2/12$ is the permeability of

the cell. Furthermore, the convective velocity u_c is scaled as $\bar{u}_c = u_c/12 = \Delta\,\rho\,g\,K/\mu_a$ and the scale of pressure is now $\bar{p}_s = \mu_a\,\bar{u}_c\,H/K$. The dimensionless dynamic viscosity is denoted by $\bar{\mu}' = \{\mu'\}$, the temperature is $T' = \{T^*\}$ and the solutal concentration is $S_w = \{S_w\}$.

The set of dimensionless parameters that will be used in the following sections are: the Prandtl number $Pr = \nu_a/\kappa_t$, the Schmidt number $Sc = \nu_a/\kappa_s$, the thermal Rayleigh number $Ra_t = \bar{u}_c\,H/\kappa_t$, the solutal Rayleigh number $Ra_s = \bar{u}_c\,H/\kappa_s$, the thermal Peclet number $Pe_t = \epsilon\,Ra_t$, the solutal Peclet number $Pe_s = \epsilon\,Ra_s$ and the Reynolds number $Re = Ra_t\,Pr^{-1}$. Therefore, by using these definitions we have that $Re^{(c)} = 12\,\delta\,Re$, $Pe_s^{(c)} = 12\,\delta\,Ra_s$, $Pe_t^{(c)} = 12\,\delta\,Ra_t$ and $Ca = \delta/12\;Ca^{(c)} = \mu_a\bar{u}_c/\bar{\gamma}_\phi$, where $\bar{\gamma}_\phi = \phi\,(\Delta\rho)^2/H$ is the macroscale interfacial tension. Then, the dimensionless Hele-Shaw model with interfacial effects is

$$\nabla' \cdot \bar{\mathbf{u}}' = 0\,, \tag{5.4.1}$$

$$\frac{6}{5}\,\epsilon^2\,Re\,\frac{\tilde{\mathcal{D}}\bar{\mathbf{u}}'}{\tilde{\mathcal{D}}t'} = \mathbf{L}_{darcy} + \epsilon^2\left(\mathbf{L}_{diss} + \mathbf{L}_{forch} + \mathbf{L}_{mass} + \mathbf{L}_{int}\right), \tag{5.4.2}$$

$$\frac{\mathcal{D}\varphi}{\mathcal{D}t'} = F_{diss} + \epsilon^2\,F_{mech}\,, \tag{5.4.3}$$

where

$$\mathbf{L}_{darcy} = -\nabla'\bar{p}' - \bar{\rho}'\hat{z} - \bar{\mu}'\,\bar{\mathbf{u}}'\,,$$

$$\mathbf{L}_{diss} = \frac{6}{5}\,\bar{\mu}'\,\nabla'^2\bar{\mathbf{u}}' \quad,\quad \mathbf{L}_{forch} = \frac{2}{35}\,(\bar{\mathbf{B}}'_\mu\cdot\bar{\mathbf{u}}')\,\bar{\mathbf{u}}' \quad,\quad \mathbf{L}_{mass} = \frac{2}{35}\,(\bar{\mathbf{B}}'_\rho\cdot\bar{\mathbf{u}}')\,\hat{z}\,,$$

$$\mathbf{L}_{int} = -\frac{1}{Ca}\left[\nabla'\bar{\rho}'\,\nabla'^2\bar{\rho}' + \frac{1}{2}\,\nabla'\left(|\nabla'\bar{\rho}'|^2 + \frac{1}{210}\left[\bar{\mathbf{u}}'\cdot\bar{\mathbf{B}}'_\rho\right]^2\right)\right],$$

$$F_{diss} = \frac{1}{Ra_\varphi}\,\nabla'^2\varphi \quad,\quad F_{mech} = \frac{2}{35}\,Ra_\varphi\,\nabla'\cdot\left[(\bar{\mathbf{u}}'\cdot\nabla'\varphi)\,\bar{\mathbf{u}}'\right],$$

$$\frac{\tilde{\mathcal{D}}}{\tilde{\mathcal{D}}t'} = \frac{\partial}{\partial t'} + \frac{9}{7}\,\bar{\mathbf{u}}'\cdot\nabla' \quad , \quad \frac{\mathcal{D}}{\mathcal{D}t'} = \frac{\partial}{\partial t'} + \bar{\mathbf{u}}'\cdot\nabla' \,,$$

$$\bar{\mathbf{B}}_h = Ra_s\,\frac{\partial \bar{h}'}{\partial S_w}\,\nabla' S_w + Ra_t\,\frac{\partial \bar{h}'}{\partial T'}\,\nabla' T' \,,$$

with $\varphi : (T', S_w)$. In particular, Eqn. (5.4.2) introduces unsteady effects in porous media and it is a generalization of the Polubarinova-Kochina model (Polubarinova-Kochina, 1952). In the following, we will call $\mathbf{L}_{diss}$ as the Brinkmann's viscous dissipative term, $\mathbf{L}_{forch}$ as the Forchheimer's term, $\mathbf{L}_{mass}$ as the vertical mass transport term and $\mathbf{L}_{int}$ as the interfacial term. We suposse that $Ca = O(1)$. Furthermore, we drop the subscript $\perp$ in ∇-operators because of the Hele-Shaw model is quasi two-dimensional. On the other hand, Ra_φ is defined as thermal or solutal Rayleigh number, which depends on the definition of variable φ. When $\epsilon \to 0$, we obtain the two dimensional Darcy equation

$$\mathbf{L}_{darcy} = \mathbf{0} \quad \Longrightarrow \quad \bar{\mathbf{u}}' = -\frac{1}{\bar{\mu}'}\left[\nabla'\bar{p}' + \bar{\rho}'\hat{z}\right] ,$$

and the classical advection-diffusion equation

$$\frac{\mathcal{D}\varphi}{\mathcal{D}t'} = F_{diss} \quad \Longrightarrow \quad \frac{\partial \varphi}{\partial t'} + \bar{\mathbf{u}}'\cdot\nabla'\varphi = \frac{1}{Ra_\varphi}\,\nabla'^2\varphi \,,$$

in the slow difussion approximation $\nabla'\cdot\bar{\mathbf{u}}' = 0$. This model will be refered hereafter as the Darcy-Boussinesq model.

5.4.1 Importance of mechanical dispersion

The right hand side of Eqn. (5.4.3) is identified as the hydrodynamic dispersion, which is the sum of both the diffusive term F_{diss} and the mechanical dispersion term F_{mech}. With these definitions, we notice that the Peclet number $Pe_\varphi = \epsilon\, Ra_\varphi$ can be written as

$$Pe_\varphi = \frac{\text{advective transport rate given by } F_{mec}}{\text{diffusive transport rate given by } F_{diss}} = \frac{\tau_{K,\varphi}^{diss}}{\tau_K^{conv}} \,,$$

where $\tau_{K,\varphi}^{diss} = K/\kappa_\varphi$ is the cell diffusive time and $\tau_K^{conv} = \sqrt{K}/\bar{u}_c$ is the cell convective time. Therefore, there are two distinct regimes for the scalar transport in the Hele-Shaw model, which depend of the characteristic values of both time scales defined before:

(a) a diffusion-dominated dynamics when $Pe_\varphi \ll 1$ and, (b) an advection-dominated dynamics when $Pe_\varphi \gg 1$. In this context, the study of heat transport in geothermal reservoirs using supercritical CO_2 as working fluid is a good example to discuss the influence of Peclet number in the scalar transport regime. A laboratory scale experiment can be performed using analogue fluids in a Hele-Shaw cell, which mimics the expected behavior in a geothermal reservoir. The cell is filled with propylene-glycol (PPG) as brine and deionized water as CO_2 gas phase (Backhaus et al, 2011; Ehyaei, 2014) (See Chapter 3, Section 3.3 on page 21 for additional information). Our hypothetical experimental design considers the following parameters: $b = 1\,\mathrm{mm}$, $H = 10\,\mathrm{cm}$, $\rho_a = 1.035\,\mathrm{g/cm^3}$, $\nu_a = 1 \times 10^{-1}\,\mathrm{cm^2/s}$, $\kappa_s = 1 \times 10^{-6}\,\mathrm{cm^2/s}$, $\kappa_t = 1 \times 10^{-4}\,\mathrm{cm^2/s}$, $T_a = 30\,^\circ\mathrm{C}$, $T_f = 70\,^\circ\mathrm{C}$, a maximum density difference due to the mixing $\Delta\rho = 0.01\,\mathrm{g/cm^3}$ and viscous difference $\Delta\mu = 10\,\mathrm{cP}$. Then, the dimensionless numbers are the following, $\epsilon = 3 \times 10^{-3}$, $Pr = 1 \times 10^3$, $Sc = 1 \times 10^5$, $Ra_t = 8 \times 10^3$ and $Ra_s = 8 \times 10^5$, which demonstrate that the phenomena is at high Rayleigh numbers. On the other hand, the hydrodynamic dispersion in thermal convection is weakly dominated by advection because $Pe_t = 3 \times 10^1 \sim O(1)$. However, in the solutal case, dispersion is strongly dominated by advection because $Pe_s = 3 \times 10^3 \sim O(1/\epsilon^2)$. In other words, both fluids can mix more efficiently by mass transfer effects rather than thermal effects and, therefore, mechanical dispersion cannot be neglected in scalar transport equations.

5.4.2 Model for the mean scalar dissipation rate

To derive the mean scalar dissipation rate, we multiply both sides of Eqn. (5.4.3) by φ. Then, using Eqn. (5.4.1) and the identities

$$\varphi \frac{\partial \varphi}{\partial t'} = \frac{1}{2} \frac{\partial}{\partial t'} \varphi^2 \,,$$

$$\varphi \nabla' \cdot (\varphi \bar{\mathbf{u}}') = \frac{1}{2} \nabla' \cdot (\varphi^2 \bar{\mathbf{u}}') \,,$$

$$\varphi \nabla'^2 \varphi = \nabla' \cdot (\varphi \nabla' \varphi) - \|\nabla' \varphi\|^2 \,,$$

$$\varphi \nabla' \cdot \left[\Big(\nabla' \cdot (\varphi \bar{\mathbf{u}}') \Big) \bar{\mathbf{u}}' \right] = \nabla' \cdot \left[\Big(\nabla' \cdot (\varphi \bar{\mathbf{u}}') \Big) \varphi \bar{\mathbf{u}}' \right] - \Big[\nabla' \cdot (\varphi \bar{\mathbf{u}}') \Big]^2 \,,$$

we obtain (Pope, 2011)

$$\frac{1}{2}\frac{\partial}{\partial t'}\varphi^2 + \nabla' \cdot \mathcal{T}_\varphi = -\varepsilon_\varphi^{(\epsilon)}\,, \tag{5.4.4}$$

where $\mathcal{T}_\varphi$ is the variance flux and $\varepsilon_\varphi^{(\epsilon)}$ is the scalar dissipation rate, both defined as

$$\mathcal{T}_\varphi = \frac{1}{2}\varphi^2\,\bar{\mathbf{u}}' - \frac{1}{Ra_\varphi}\varphi\,\nabla'\varphi - \frac{2}{35}\epsilon^2\,Ra_\varphi\left[\Big(\nabla' \cdot (\varphi\,\bar{\mathbf{u}}')\Big)\,\varphi\,\bar{\mathbf{u}}'\right], \tag{5.4.5}$$

$$\varepsilon_\varphi^{(\epsilon)} = \frac{1}{Ra_\varphi}\|\nabla'\varphi\|^2 + \frac{2}{35}\epsilon^2\,Ra_\varphi\left[\nabla' \cdot (\varphi\,\bar{\mathbf{u}}')\right]^2. \tag{5.4.6}$$

In the following, we will use the average in the horizontal direction and the domain average of a function $f = f(\mathbf{x}')$, which are defined as $\bar{f}(z') = 1/L' \int_0^{L'} f(\mathbf{x}')dx'$ and $\langle f\rangle = \int_0^1 \bar{f}(z')dz'$, respectively, where $L' = L/H$ is the aspect ratio of the cell. To understand the physical meaning of Eqn. (5.4.4), we will study the following two cases shown in Fig. 5.4.1

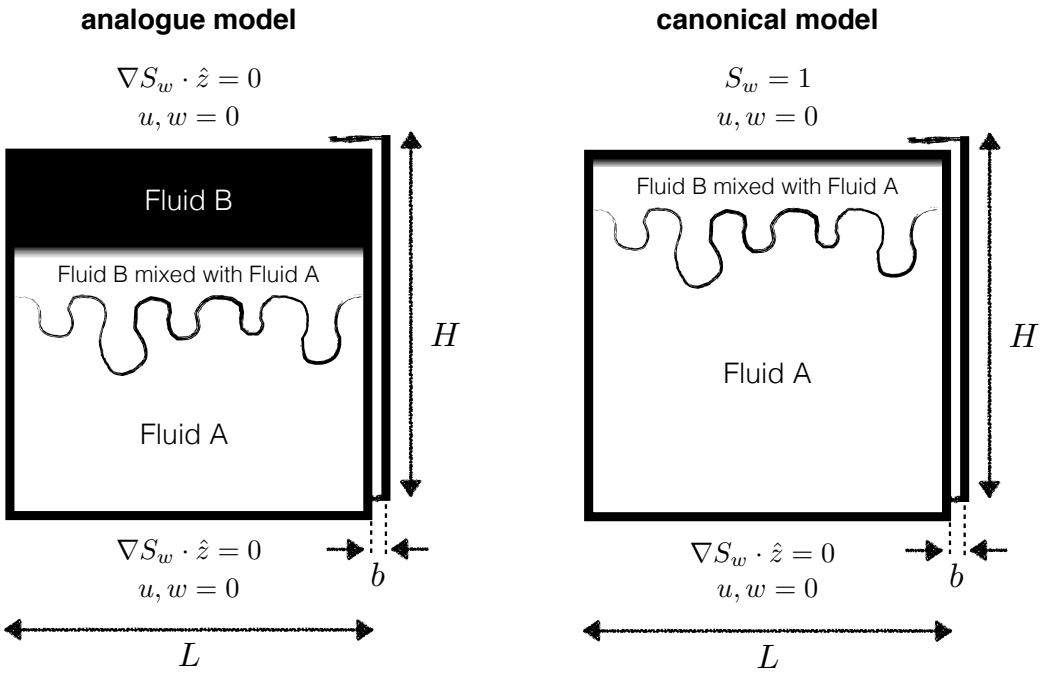

Figure 5.4.1: Analogue and canonical models of convection inside a Hele-Shaw geometry

- The canonical Rayleigh-Benard-Darcy model, which considers periodic boundary conditions in the x-direction, while in the z-direction $w' = 0$ in $z' = 0$ and $z' = 1$, $\varphi = 1$ in $z' = 1$ and $\partial\varphi/\partial z' = 0$ in $z' = 0$.
- The analogue model, with periodic boundary conditions in the x-direction, while in the z-direction $w' = 0$ and $\partial\varphi/\partial z' = 0$ in $z' = 0$ and $z' = 1$.

In the canonical model, the domain average of Eqn. (5.4.4) is written as

$$\frac{1}{2}\frac{\partial}{\partial t'}\langle\varphi^2\rangle - \mathcal{F} = -\langle\varepsilon_\varphi^{(\epsilon)}\rangle \quad ; \quad \mathcal{F} = \frac{1}{Ra_\varphi}\frac{\partial\bar{\varphi}}{\partial z'}\bigg|_{z'=1} , \tag{5.4.7}$$

where $\mathcal{F}$ is the flux and $\langle\varepsilon_\varphi^{(\epsilon)}\rangle$ is the mean scalar dissipation rate. Then, it is clear that any power-law dependency of $\mathcal{F}$ with Ra_φ must be reflected in $\langle\varepsilon_\varphi^{(\epsilon)}\rangle$ (Hidalgo et al, 2012). It is important to recall that the mean scalar dissipation rate has the contribution of the mechanical dispersion term. On the other hand, considering the analogue model, we can obtain the mean scalar variance equation

$$\frac{1}{2}\frac{\partial}{\partial t'}\langle\varphi^2\rangle = -\langle\varepsilon_\varphi^{(\epsilon)}\rangle , \tag{5.4.8}$$

where it is clear that $\langle\varepsilon_\varphi^{(\epsilon)}\rangle$ measures the rate of destruction of scalar fluctuations (Pope, 2011; Jha et al, 2011a). When $\epsilon \to 0$, we obtain the equation

$$\langle\varepsilon_\varphi^{(0)}\rangle = \frac{1}{Ra_\varphi}\langle\|\nabla'\varphi\|^2\rangle ,$$

which has been studied in previous works (Hidalgo et al, 2012; Jha et al, 2011a; Pramanik and Mishra, 2015). Eqn (5.4.8) does not show any scaling relation between the flux and the mean scalar dissipation rate. However, we can obtain a power-law dependence between both quantities using dimensional analysis. To derive that, we can approximate the interfacial convective flux F_c as

$$F_c = \int_{\partial\Omega_{mix}} \left[\varphi - \frac{K}{\kappa_\varphi}\Big(\nabla\cdot(\varphi\,\mathbf{u})\Big)\right]\mathbf{u}\cdot\hat{n}\,dS \sim f_1\Big(\varphi_m, \Delta\varphi, \mathbf{u}, K, \kappa_\varphi, H\Big)\,u_c\,b\,\ell_{mix} , \tag{5.4.9}$$

where $\partial\Omega_{mix}$ is the mixing or interfacial surface, u_c is the convective velocity scale defined in Section 5.2, φ_m is the scalar value where density is maximum, $\Delta\varphi$ is the scalar

gradient scale and ℓ_{mix} is the mixing or interfacial length, which contains information about the importance of dispersion in the interfacial convective flux. The diffusive flux F_d is approximated as the classical expression

$$F_d = \int_\Omega \kappa_\varphi \, \nabla\varphi \cdot \hat{n} \, dS \sim \kappa_\varphi \, \frac{\Delta\varphi}{H} \, b \, L \, . \tag{5.4.10}$$

Combining these approximations, the Nusselt number $Nu_\varphi^{(g)}$ and the flux $\mathcal{F}_\varphi$ are defined as

$$Nu_\varphi^{(g)} = \frac{F_c}{F_d} = \Phi\left(\epsilon^2 Ra_\varphi \, , \frac{\Delta\varphi}{\varphi_m}\right) Ra_\varphi \, \langle\varepsilon_\varphi\rangle^{(g)} \quad ; \quad \mathcal{F}_\varphi = \frac{Nu_\varphi^{(g)}}{Ra_\varphi} = \Phi\left(\epsilon^2 Ra_\varphi \, , \frac{\Delta\varphi}{\varphi_m}\right) \langle\varepsilon_\varphi\rangle^{(g)} \, , \tag{5.4.11}$$

where we define the mean scalar dissipation rate as the dimensionless interfacial length $\langle\varepsilon_\varphi\rangle^{(g)} \sim \ell_{mix}/L$ (Hidalgo et al, 2012; Pramanik and Mishra, 2015). Therefore, if $\langle\varepsilon_\varphi\rangle^{(g)} \sim Ra_\varphi^{m(\epsilon)}$ due to the contribution of the mechanical dispersion term, then we obtain the scaling law $Nu_\varphi^{(g)} \sim \Phi(\epsilon^2 Ra_\varphi, \Delta\varphi/\varphi_m) \, Ra_\varphi^{1+m(\epsilon)}$. To recover the prediction of Howard for thermal convection in porous media $Nu_t^{(g)} \sim Ra_t$, in the limit $\epsilon \to 0$ the scalings must satisfy $m(0) = 0$ and $\Phi(0) = f(\Delta T/T_m)$ does not scale with Ra_t. In this case, the mean scalar dissipation will be independent of the Rayleigh number, as suggested by Jenny et al (2014).

Thereby, if we suppose that $\Phi \sim f(\Delta T/T_m) \, Ra_t^{\epsilon\, p(\epsilon)}$ and $Nu_t^{(g)} \sim Ra_t^n$, then we obtain a scaling law where the exponents must satisfy the identity

$$n(\epsilon) = 1 + m(\epsilon) + \epsilon \, p(\epsilon) \, . \tag{5.4.12}$$

In Chapter 7, Section 7.2 on page 94, new results from nonlinear simulations of a similar problem, which is thermal convection in porous media, show that for $\epsilon = 0.001$, we have $n = 0.90 \pm 0.03$ and $m = -0.09 \pm 0.01$. On the other hand, for $\epsilon = 0.01$, we have $n = 0.40 \pm 0.03$ and $m = -0.59 \pm 0.03$. If $p(\epsilon) \sim 0$, these preliminary results support our scaling assumptions, which is demostrated in this work.

On the other hand, considering the mixing convection problem in the porous medium limit $\epsilon \to 0$, we have $m = 0$ and $\Phi(0) = f(\Delta S_w/S_w^{(m)}) \sim Ra_s^{-1/5}$, so that $Nu_s^{(g)} \sim Ra_s^{4/5}$ and $\mathcal{F}_s \sim Ra_s^{-1/5}$ (Neufeld et al, 2010). Therefore, a scaling law of the type $\Phi \sim f(\Delta S_w/S_w^{(m)}) \, Ra_s^{\epsilon\, p(\epsilon)} \sim Ra_s^{r(\epsilon)} \, Ra_s^{\epsilon\, p(\epsilon)}$ is proposed and the test of these assumptions will be an important challenge for future studies.

Chapter 6

Linear stability analysis of density-driven convection in porous media

Abstract

We have studied the linear stability of two interesting problems related with density driven convection in porous media, thermal convection and Rayleigh-Taylor instability. For both problems, we have used the Hele-Shaw model, which incorporates new terms in the momentum equation and the known mechanical dispersion in the scalar transport equation. For thermal convection, we have extended the results reported in the literature consistently with our new model, obtaining the correction $Ra_t^{(c)} = 4\pi^2 + 8\pi^2\sqrt{\gamma}\,\epsilon + [8\pi^4\chi^{\bar{\vartheta}} + 12\pi^2\gamma + 4\pi^3\gamma\sqrt{3}\tanh(\sqrt{3}\pi/2)]\,\epsilon^2 + O(\epsilon^3)$, where $\gamma = 6/5$ is a parameter related with viscous dissipation and $\chi^{\bar{\vartheta}} = 8/7 + \bar{\vartheta}$ contains the contribution of the effective interfacial tension. On the other hand, for the Rayleigh-Taylor instability, we have used the dominant-mode solution to analyze the effects of the geometry and interfacial tension in the onset of convection. In the limit of porous media, we have recovered the results reported in literature. For other cases, we show that the inertial terms of momentum equation deviate weakly the Darcian prediction but maintaining the scaling law of the type $\tau_c = a\,Ra_s^{-1}$, while interfacial tension tends to stabilize the diffusive boundary layer in time, retarding considerably the onset of convection for high-Ra_s scenarios.

6.1 Introduction

In this chapter, we study the effects of the Brinkmann's viscous dissipative term $\mathbf{L}_{diss}$, the vertical mass transport term $\mathbf{L}_{mass}$ and the interfacial term $\mathbf{L}_{int}$ in the onset of convection for two different problems: thermal convection in porous media and density-driven convection through mass transfer between two miscible fluids. We will show the linearized model for each case and the strategy to solve these equations applying the matching asymptotic methodology, with the aim to evaluate the conditions that trigger the onset of convection in terms of the model parameters and boundary conditions.

6.2 Thermal convection in porous media

Thermal convection in homogeneous porous media is a benchmark problem which has been extensively studied in the last fifty years. Experimental data recopilation done by Nield and Bejan (2006) suggest that convection occurs when $Ra_t \geq 40$. The Darcy-Boussinesq model with free slip boundary conditions predicts that the onset of thermal convection occurs when the critical Rayleigh number is

$$Ra_{t,darcy}^{(c)} = 4\pi^2 \,. \tag{6.2.1}$$

However, the Hele-Shaw geometry can affect weakly this prediction. Therefore, we are interested in computing the perturbative corrections to the critical Rayleigh number due to the geometry, which is given by the formula

$$Ra_t^{(c)} = Ra_{t,darcy}^{(c)} + \epsilon\, R_1 + \epsilon^2\, R_2 + O(\epsilon^3) \,, \tag{6.2.2}$$

where R_1 and R_2 are coefficients that depend on the boundary conditions impossed. This work has been performed firstly by Ress (2002), who has studied the following dimensional set of semi-empirical equations used to model convective flows in porous media

$$\nabla \cdot \mathbf{u} = 0 \quad ; \quad \frac{\partial T}{\partial t} + \mathbf{u} \cdot \nabla T = \kappa_t \nabla^2 T \;\; ,$$

$$\frac{\rho_a}{\phi_p}\frac{\partial \mathbf{u}}{\partial t} + \frac{\rho_a}{\phi_p^2}(\mathbf{u}\cdot\nabla)\mathbf{u} = -\nabla p + \mu_e \nabla^2 \mathbf{u} - \mu\, K^{-1}\,\mathbf{u} + \rho_a \beta_T (T - T_a) g \hat{z} - C_f \frac{\rho_a}{\sqrt{K}}\,\mathbf{u}|\mathbf{u}| \,,$$

In these equations, ϕ_p is the porosity, μ_e is the Brinkmann's effective viscosity, β_T is the coefficient of thermal volumetric expansion and C_f is the Ergun coefficient, which is strongly dependent on the flow regime. Using no slip boundary conditions, Ress (2002) has obtained the critical Rayleigh number

$$Ra_{t,rees}^{(c)} = Ra_{t,darcy}^{(c)} + \left[8\pi^2\right] Da^{1/2} + \left[8\pi^4 + 12\pi^2 + 4\pi^3\sqrt{3}\,\tanh\left(\frac{\pi\sqrt{3}}{2}\right)\right] Da + \ldots \,. \tag{6.2.3}$$

where $Da = (\mu_e/\mu)(K/H^2)$ is the Darcy number. The model proposed by Ress (2002) has some differences with the Hele-Shaw model given in Eqns. (5.4.1) to (5.4.3), which appear in Chapter 5, Section 5.4 on page 57. For example, the porosity in Hele-Shaw cells is $\phi_p = 1$ because the cell volume is filled with fluid. Then, the numerical coefficients that appear in the convective acceleration term (left side of Eqn. (5.4.2)) cannot be derived in the semi-empirical model from a particular value of the porosity. These values appear due to averaging in the confined cell direction. On the other hand, we can define without loss of generality the Brinkmann's effective viscosity in Hele-Shaw cells as $\mu_e = \mu$, so the Darcy number is $Da = \epsilon^2$. Defining the constitutive equation for density as $(\rho - \rho_a)/\Delta\rho = -(T - T_a)/\Delta T$, the buoyancy term in both models is the same, but the Forchheimer drag term is completely different. In the Hele-Shaw model, the existence of a quadratic velocity term in the right side of Eqn. (5.4.2) is due to the variations of the viscosity. However, in porous media models, the C_f coefficient is in general independent of the viscosity. Finally, the mass transport term $\mathbf{L}_{mass}$, which appears in Eqn. (5.4.2), is new for porous media models.

To study the linear stability of thermal convection using the Hele-Shaw model, we consider a single fluid phase with constant dimensionless viscosity $\bar{\mu} = 1$. The dimensionless fluid density, temperature and pressure can be written as

$$\bar{\rho}'(\mathbf{x}', t') = \bar{\rho}'_s(z') + \tilde{\rho}'(\mathbf{x}', t') \,, \tag{6.2.4}$$

$$T'(\mathbf{x}', t') = \bar{T}'_s(z') + \theta'(\mathbf{x}', t') \,, \tag{6.2.5}$$

$$\bar{p}'(\mathbf{x}', t') = \bar{p}'_s(z') + \tilde{p}'(\mathbf{x}', t') \,, \tag{6.2.6}$$

where $\bar{T}'_s(z') = 1 - z'$ is the conductive regime solution (when $\bar{\mathbf{u}}' = \mathbf{0}$) and $d\bar{p}'_s/dz = -\bar{\rho}'_s(z)$. Furthermore, the constitutive equation is defined as $\tilde{\rho}' = -\theta'$. The boundary conditions for the perturbed temperature are $\theta' = 0$ in $z' = 0$ and $z' = 1$. Then, with the aim to compare the effects of boundaries in the onset of convection, we analize the neutral marginal stability using both free slip and no slip boundary conditions.

6.2.1 Free slip boundary conditions without interfacial effects

From the perturbation of the conductive regime given by Eqns. (6.2.4) to (6.2.6), the linearized model of Eqns. (5.4.1) and (5.4.3) with $Ca \to \infty$ (no interfacial effects) is written as

$$\nabla' \cdot \bar{\mathbf{u}}' = 0 \,, \tag{6.2.7}$$

$$\epsilon^2 \, \gamma \, Re \, \frac{\partial \bar{\mathbf{u}}'}{\partial t'} = -\nabla' \bar{p}' + \theta' \hat{z} - \bar{\mathbf{u}}' + \epsilon^2 \, \gamma \, \nabla'^2 \bar{\mathbf{u}}' + \epsilon^2 Ra_t \, \beta \, \bar{w}' \, \hat{z} \tag{6.2.8}$$

$$\frac{\partial \theta'}{\partial t'} - \bar{w}' = \frac{1}{Ra_t} \, \nabla'^2 \theta' \,. \tag{6.2.9}$$

where $\gamma = 6/5$ and $\beta = 2/35$. We are interested in studying both the contribution of the vertical advection term (represented by parameter β) and the importance of the boundary conditions in the onset of thermal convection in a single fluid phase. The linear solutions of Eqns. (6.2.7) to (6.2.9) are $f(\mathbf{x}', \tau) = \hat{f}(z') \exp(s\tau) \exp(-ikx')$, with $f : (\bar{u}', \bar{w}', \tilde{p}', \theta')$. Therefore, in the marginal stability condition $s = 0$, we obtain the equations

$$ik\hat{u} - \frac{d\hat{w}}{dz'} = 0 \,, \tag{6.2.10}$$

$$\gamma\epsilon^2 \frac{d^2\hat{u}}{dz'^2} - \eta_\epsilon \hat{u} + ik\hat{p} = 0 \,, \tag{6.2.11}$$

$$\gamma\epsilon^2 \frac{d^2\hat{w}}{dz'^2} - \eta_\epsilon \hat{w} - \frac{d\hat{p}}{dz'} + \hat{\theta} + \beta\epsilon^2 Ra_t \hat{w} = 0 \,, \tag{6.2.12}$$

$$\frac{d^2\hat{\theta}}{dz'^2} - k^2\hat{\theta} + Ra_t \hat{w} = 0 \,, \tag{6.2.13}$$

where $\eta_\epsilon = 1 + \gamma\epsilon^2 k^2$. Combining the variables $\hat{p}$, $\hat{u}$ and $\hat{\theta}$ from Eqns. (6.2.10) to (6.2.13), we obtain a unique equation that solves the eigenfunction problem

$$\gamma \, \epsilon^2 \, \frac{d^6\hat{w}}{dz'^6} - \left[\eta_\epsilon + 2\gamma\epsilon^2 k^2\right] \frac{d^4\hat{w}}{dz'^4} + \left[2\eta_\epsilon k^2 + \gamma\epsilon^2 k^4\right] \frac{d^2\hat{w}}{dz'^2} - \beta\epsilon^2 k^2 \, Ra_t \, \frac{d^2\hat{w}}{dz'^2}$$

$$- k^4 \eta_\epsilon \hat{w} + \left[1 + \beta\epsilon^2 k^2\right] k^2 \, Ra_t \hat{w} = 0 \,. \tag{6.2.14}$$

Eqn. (6.2.14) represents a singular perturbation problem whose nature resides in the order of magnitude of $\mathbf{L}_{diss}$ in comparison with $\mathbf{L}_{darcy}$ (For further information, see Chapter 5, Section 5.4 on page 57). Applying free slip boundary conditions, where $\hat{w} = 0$, $d\hat{u}/dz' = 0$ and $\hat{\theta} = 0$ in $z' = 0$ and $z' = 1$, we obtain the following six boundary conditions for Eqn. (6.2.14), $\hat{w} = 0$, $d^2\hat{w}/dz'^2 = 0$ and $d^4\hat{w}/dz'^4 = 0$ at upper and lower vertical boundaries. The eigenfunction that solves this problem is $\hat{w}(z') = \sin(\pi z')$. As a consequence, the dispersion relation obtained from Eqn. (6.2.14) is

$$Ra_t(k,\epsilon) = \frac{(k^2+\pi^2)^2}{k^2} + \chi\,\epsilon^2\,\frac{(k^2+\pi^2)^3}{k^2} + O(\epsilon^4) \quad ; \quad \chi = \gamma - \beta = \frac{8}{7}\,. \tag{6.2.15}$$

This result shows that $\mathbf{L}_{diss}$ (represented by parameter γ) is linearly stable, while $\mathbf{L}_{mass}$ (represented by parameter β) is linearly unstable, as we expected. The onset of convection occurs when $dRa_t/dk = 0$. Hence, we obtain the critical thermal Rayleigh number and the most unstable wavenumber, which are

$$Ra_t^{(c)} = 4\pi^2 + 8\,\chi\,\epsilon^2\,\pi^4 + O(\epsilon^4)\,, \tag{6.2.16}$$

$$k_c = \pi - \chi\,\pi^3\,\epsilon^2 + O(\epsilon^4)\,. \tag{6.2.17}$$

When $\epsilon \to 0$, we recover the known solution $Ra_t^{(c)} = Ra_{t,darcy}^{(c)} = 4\pi^2$.

6.2.2 No slip boundary conditions without interfacial effects

On the other hand, using no-slip/Dirichlet boundary conditions $\hat{w} = 0$, $\hat{u} = 0$ and $\hat{\theta} = 0$ in $z' = 0$ and $z' = 1$, we obtain the following six boundary conditions for Eqn. (6.2.14), $\hat{w} = 0$, $D\hat{w} = 0$ and $(D^2 - k^2)\,(D^2 - k^2 - 1/(\gamma\epsilon^2))\hat{w} = (\beta/\gamma)\,k^2 Ra_t\hat{w}$ at upper and lower vertical boundaries, where $D = d/dz'$. Following the work of Bizon et al (1997a), the proposed eigenfunction that solves Eqn. (6.2.14) is $\hat{w} \sim \exp(\lambda z')$. Therefore, the dispersion relation obtained from Eqn. (6.2.14) is

$$\gamma\epsilon^2\,x^3 - x^2 - \beta\mu^2\epsilon^2\,x + \mu^2 = 0\,, \tag{6.2.18}$$

where $x = \lambda^2 - k^2$ and $\mu^2 = k^2 Ra_t$. The cubic Eqn. (6.2.18) is singular and one of the three solutions will be of order $O(1/\epsilon^2)$. Using the change of variables $x = \epsilon^2 y$ and expanding in power series $y = y_0 + \epsilon^2 y_1 + \epsilon^2 y_2 + \epsilon^6 y_3 + O(\epsilon^8)$, the solutions of Eqn. (6.2.18) obtained by singular perturbation theory are

$$x_1 = \frac{1}{\gamma\epsilon^2} - \epsilon^2\sigma\mu^2 + O(\epsilon^4)\,, \tag{6.2.19}$$

$$x_2 = \mu - \frac{1}{2}\,\beta\mu^2\epsilon^2 + O(\epsilon^4)\,, \tag{6.2.20}$$

$$x_3 = -\mu - \frac{1}{2}\,\beta\mu^2\epsilon^2 + O(\epsilon^4)\,. \tag{6.2.21}$$

Finally, the six parameters λ that build the solution of the problem are $\lambda_1 = \pm\vartheta_1$, $\lambda_2 = \pm\vartheta_2$ and $\lambda_3 = \pm\vartheta_3$, where

$$\vartheta_1 = \frac{1}{\epsilon}\,\frac{1}{\sqrt{\gamma}} + \frac{1}{2}\,\sqrt{\gamma}\,k^2\epsilon + O(\epsilon^3)\,, \tag{6.2.22}$$

$$\vartheta_2 = \sqrt{k^2+\mu} - \frac{1}{4}\,\frac{\beta\mu^2}{\sqrt{k^2+\mu}}\,\epsilon^2 + O(\epsilon^4)\,, \tag{6.2.23}$$

$$\vartheta_3 = \sqrt{\mu-k^2} + \frac{1}{4}\,\frac{\beta\mu^2}{\sqrt{\mu-k^2}}\,\epsilon^2 + O(\epsilon^4)\,. \tag{6.2.24}$$

Using symmetry arguments, we write the eigenfunction $\hat{w}$ as

$$\hat{w}(z') = A\sinh\left[\vartheta_1\left(z'-\frac{1}{2}\right)\right] + B\cosh\left[\vartheta_1\left(z'-\frac{1}{2}\right)\right] + C\sinh\left[\vartheta_2\left(z'-\frac{1}{2}\right)\right] \tag{6.2.25}$$

$$+\,E\cosh\left[\vartheta_2\left(z'-\frac{1}{2}\right)\right] + F\sin\left[\vartheta_3\left(z'-\frac{1}{2}\right)\right] + G\cos\left[\vartheta_3\left(z'-\frac{1}{2}\right)\right].$$

Applying the no slip boundary conditions to Eqn. (6.2.25) and considering the even part of the eigenfunction, we obtain the matricial equation $\mathbf{Ma} = 0$, where

$$\mathbf{M} = \begin{bmatrix} 1 & 1 & 1 \\ \vartheta_1\tanh(\vartheta_1/2) & \vartheta_2\tanh(\vartheta_2/2) & -\vartheta_3\tan(\vartheta_3/2) \\ -\mu^2 + O(\epsilon^2) & -\frac{\mu}{\gamma\epsilon^2} + \mu^2 - \frac{1}{2}\frac{\beta}{\gamma}\mu^2 + O(\epsilon^2) & \frac{\mu}{\gamma\epsilon^2} + \mu^2 - \frac{1}{2}\frac{\beta}{\gamma}\mu^2 + O(\epsilon^2) \end{bmatrix}$$

$$\mathbf{a} = \begin{bmatrix} B\cosh(\vartheta_1/2) \\ \\ E\cosh(\vartheta_2/2) \\ \\ G\cos(\vartheta_3/2) \end{bmatrix}$$

The dispersion relation is obtained solving $det(\mathbf{M}) = 0$. Since that $\vartheta_1 = O(1/\epsilon)$ and $\vartheta_2 = O(1)$, we can approximate $det(\mathbf{M}) = 0$ as

$$-\frac{2\mu}{\gamma\epsilon^2}\,\vartheta_1\tanh(\vartheta_1/2) + \left[\frac{\mu}{\gamma\epsilon^2} + \frac{1}{2}\frac{\beta}{\gamma}\,\mu^2\right]\vartheta_3\tan(\vartheta_3/2) = 0\,. \tag{6.2.26}$$

Finally, in the porous media limit $\epsilon \to 0$, we have $\tanh(\vartheta_1/2) \to 1$. Accordingly, Eqn. (6.2.26) is written as

$$-\frac{2}{\sqrt{\gamma}\epsilon} + \vartheta_3\tan(\vartheta_3/2) + O(\epsilon^2) = 0\,, \tag{6.2.27}$$

where the solution found using perturbation theory is $\vartheta_3 = \pi(1+\sqrt{\gamma}\epsilon) + O(\epsilon^2)$. The dispersion relation is obtained matching Eqns. (6.2.24) and (6.2.27). The final result is

$$Ra_t(k,\epsilon) = \frac{(k^2+\pi^2)^2}{k^2} + \frac{4\pi^2\sqrt{\gamma}}{k^2}\,(k^2+\pi^2)\,\epsilon + O(\epsilon^2)\,, \tag{6.2.28}$$

The onset of convection occurs when $dRa_t/dk = 0$. Hence, we obtain the critical thermal Rayleigh number and the most unstable wavenumber, which are

$$Ra_t^{(c)} = 4\pi^2 + \left[8\pi^2\sqrt{\gamma}\right]\epsilon + O(\epsilon^2)\,, \tag{6.2.29}$$

$$k_c = \pi(1+\sqrt{\gamma}\,\epsilon) + O(\epsilon^2)\,. \tag{6.2.30}$$

For the case $\gamma = 1$, we recover the $O(\epsilon)$ correction obtained by Ress (2002) given by Eqn. (6.2.3). Therefore, for a sufficiently small ϵ parameter in laboratory experiments using Hele-Shaw cells, we will observe the onset of convection at $Ra_t \sim 4\pi^2$. The question is how big must the ϵ parameter be in order to reproduce experimentally this result. A simple comparison between formulas Eqns. (6.2.16) and (6.2.29) helps to understand physically the porous media limit, which is shown in Fig. 6.2.1. Using this figure, we define three regions of importance

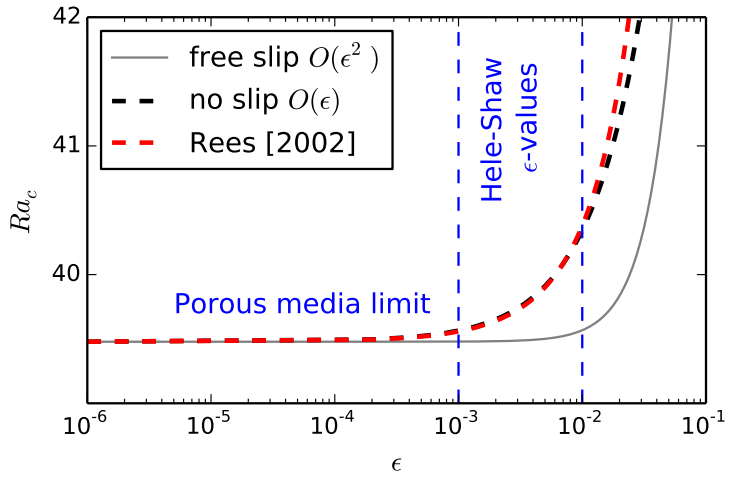

Figure 6.2.1: The porous media limit in the onset of thermal convection. For both free slip and no slip boundary conditions, we obtain the same critical Rayleigh number Ra_c when $\epsilon < 10^{-4}$. For comparise, the result obtained by Ress (2002) is presented.

- The macroscale or free-fluid regime, where $O(\epsilon) \sim 1$.
- The porous media mesoscale or Hele-Shaw regime, where $10^{-4} \leq \epsilon \leq 10^{-1}$ and the inertial corrections of Darcy equation governs the fluid dynamics.
- the microscale or Darcy regime, where $\epsilon < 10^{-4}$ and the Darcy equation governs the problem.

In the free-fluid regime, the inertial corrections of Darcy equation are invalid and the Navier-Stokes equation must be applied. Mathematically, there is no continuous connection between the free-fluid and the Hele-Shaw regimes presented in Chapter 5, Section 5.4 on page 57, because of the dimensionality of the governing equations, but there is a natural connection between the Hele-Shaw and the Darcy regimes through the porous media limit, which is defined in this chapter as the maximum ϵ for which the onset of convection is independent of the boundary conditions. There are a great number of experiments of convection using Hele-Shaw cells that have been reported in literature within the interval $10^{-3} < \epsilon < 10^{-2}$ (see Fig. 6.2.1). Data recopilation done by Nield and Bejan (2006) for thermal convection experiments suggest that the onset of convection is at $Ra_c \sim 40$, which coincides with our linear stability analysis using both free slip and no slip boundary conditions. However, accurate measurements of the onset of convection in Hele-Shaw cells are difficult to perform and it is not trivial to demonstrate the effects of no slip boundary conditions in such measurements. For instance, using a Hele-Shaw cell of gap $b = 1$ mm and height $H = 10$ cm, we obtain $\epsilon = 10^{-2}$, so the difference between the critical Rayleigh number obtained using both free-slip and no-slip boundary conditions is approximately 2%. This small difference

is due to the existence of a thin viscous boundary layer whose spatial scale is of the order of the gap of the cell. In laboratory experiments using Hele-Shaw cells, the model proposed and the experimental results presented in the literature suggest that the boundary conditions for the velocity do not impact substantially in the onset of convection. In developed thermal convection scenarios, we refer the work of Bizon et al (1997a) for a more complete lecture about the convective behavior in the cell and the influence of boundary conditions in the dynamics.

6.2.3 Perturbative solutions for velocity and temperature. $O(\epsilon^2)$ correction considering weak interfacial effects

We consider the case of weak interfacial effects $Ca = O(1)$, where for convenience we write the capillary number as $Ca = 1/\bar{\vartheta}$ with $\bar{\vartheta} > 0$. The linearized model from the perturbation of the conductive regime is

$$\gamma\epsilon^2\frac{d^4\hat{w}}{dz'^4} - \left[\eta_\epsilon + 2\gamma\epsilon^2 k^2\right]\frac{d^2\hat{w}}{dz'^2} + \eta_\epsilon\, k^2\,\hat{w} - \beta\epsilon^2\, Ra_t\, k^2\,\hat{w} - k^2\,\epsilon^2\,\bar{\vartheta}\,\frac{d^2\hat{\theta}}{dz'^2} - k^2\left[1 - k^2\epsilon^2\,\bar{\vartheta}\right]\hat{\theta} = 0\,, \tag{6.2.31}$$

$$\frac{d^2\hat{\theta}}{dz'^2} - k^2\,\hat{\theta} + Ra_t\,\hat{w} = 0\,, \tag{6.2.32}$$

with boundary conditions $\hat{w} = d\hat{w}/dz' = \hat{\theta} = 0$ on $z' = 0$ and $z' = 1$. Following the work of Ress (2002), we use matching asymptotic expansions to solve Eqns. (6.2.31) and (6.2.32). In the outer region, we have

$$\hat{w} = f(z') = f_0(z') + \epsilon f_1(z') + \epsilon^2 f_2(z') + O(\epsilon^2)\,,$$
$$\hat{\theta} = g(z') = g_0(z') + \epsilon g_1(z') + \epsilon^2 g_2(z') + O(\epsilon^2)\,,$$

with boundary conditions $f = df/dz' = g = 0$ in $z' = 0$ and $z' = 1$. On the other hand, in the left inner region ($z' \to 0$) we use the inner variable $\zeta = z'/\epsilon$, so we have

$$\hat{w} = F_l(\zeta) = F_{0,l}(\zeta) + \epsilon F_{1,l}(\zeta) + \epsilon^2 F_{2,l}(\zeta) + O(\epsilon^3)\,,$$
$$\hat{\theta} = G_l(\zeta) = G_{0,l}(\zeta) + \epsilon G_{1,l}(\zeta) + \epsilon^2 G_{2,l}(\zeta) + O(\epsilon^3)\,,$$

with boundary conditions $F_l = dF_l/d\zeta = G_l = 0$ in $\zeta = 0$. In the right inner region ($z' \to 1$) we use the inner variable $\xi = (1 - z')/\epsilon$, so we have

$$\hat{w} = F_r(\xi) = F_{0,r}(\xi) + \epsilon F_{1,r}(\xi) + \epsilon^2 F_{2,r}(\xi) + O(\epsilon^3) ,$$
$$\hat{\theta} = G_r(\xi) = G_{0,r}(\xi) + \epsilon G_{1,r}(\xi) + \epsilon^2 G_{2,r}(\xi) + O(\epsilon^3) ,$$

with boundary conditions $F_r = dF_r/d\xi = G_r = 0$ in $\xi = 0$. The matching conditions are $F_l(\zeta \to \infty) = f(z' \to 0)$, $F_r(\xi \to \infty) = f(z' \to 1)$, $G_l(\zeta \to \infty) = g(z' \to 0)$ and $G_r(\xi \to \infty) = g(z' \to 1)$. Finally, we expand the Rayleigh number as

$$Ra_t = R_0 + \epsilon R_1 + \epsilon^2 R_2 + O(\epsilon^3) \tag{6.2.33}$$

The leading order equations to be solve in the outer region are

$$\frac{d^2 f_0}{dz'^2} - k^2 f_0 + k^2 g_0 = 0 , \tag{6.2.34}$$

$$\frac{d^2 g_0}{dz'^2} - k^2 g_0 + R_0 f_0 = 0 , \tag{6.2.35}$$

with boundary conditions $f_0(0) = 0$, $f_0(1) = 0$, $g_0(0) = 0$ and $g_0(1) = 0$. The boundary conditions for the derivative are absent at this order. Therefore, the solutions obtained are the same that for the case of free-slip boundary conditions

$$f_0 = \sin(\pi z) \ , \ g_0 = \frac{\pi^2 + k^2}{k^2} \sin(\pi z) \ , \ R_0 = \frac{(\pi^2 + k^2)^2}{k^2} . \tag{6.2.36}$$

In the limit $z \to 0$, $\sin(\pi z) \sim \pi z \sim \pi \epsilon \zeta$. For $z \to 1$, $\sin(\pi z) \sim \pi (1 - z) \sim \pi \epsilon \xi$. Then, due to matching asymptotic conditions, we have the solutions $F_0 = G_0 = 0$. When we reconstruct the velocity $\hat{w}(z')$, the inclusion of the inner solutions of order $O(\epsilon)$ can correct the Neumann boundary condition $d\hat{w}/dz'$ in $z' = 0$ and $z' = 1$, missing in the outer solution at the leading order. However, this procedure does not satisfy at the same time the Dirichlet boundary condition $\hat{w} = 0$ in $z' = 0$ and $z' = 1$. Therefore, it is necessary to find the outer solution of order $O(\epsilon)$ to correct the Dirichlet boundary condition of the velocity, but losing the Neumann boundary condition once again, which can be corrected by introducing the inner solutions of order $O(\epsilon^2)$ and so on. We call

it relaxation of no-slip boundary conditions to this form of solving the problem using inner and outer expansions.

Therefore, the $O(\epsilon)$ equations in the left inner region are

$$\gamma \frac{d^4 F_{1,l}}{d\zeta^4} - \frac{d^2 F_{1,l}}{d\zeta^2} = 0 \,, \tag{6.2.37}$$

$$\frac{d^2 G_{1,l}}{d\zeta^2} = 0 \,, \tag{6.2.38}$$

with boundary conditions $F_{1,l} = dF_{1,l}/dz' = G_{1,l} = 0$ on $\zeta = 0$. The solutions are the following

$$F_{1,l} = A_1 \left(\frac{1}{\sqrt{\gamma}} \zeta - 1 + \exp\left[- \frac{\zeta}{\sqrt{\gamma}} \right] \right) \;,\; G_{1,l} = A_2 \, \zeta \,. \tag{6.2.39}$$

By using the matching conditions, we have $A_1 = \pi \sqrt{\gamma}$ and $A_2 = \pi \, (\pi^2 + k^2)/k^2$. By symmetry arguments, the solutions of the $O(\epsilon)$ equations in the right inner region are

$$F_{1,r} = A_1 \left(\frac{1}{\sqrt{\gamma}} \xi - 1 + \exp\left[- \frac{\xi}{\sqrt{\gamma}} \right] \right) \;,\; G_{1,r} = A_2 \, \xi \,. \tag{6.2.40}$$

Therefore, the physical solutions can be written using composite expansions as

$$\hat{w}(z) = f_0(z') + \epsilon \left[f_1(z') + F_{1,l}(z'/\epsilon) + F_{1,r}(z'/\epsilon) \right] - f_{int}^{(l)}(z') - f_{int}^{(r)}(z') + O(\epsilon^2) \,,$$

$$\hat{\theta}(z) = g_0(z') + \epsilon \left[g_1(z') + G_{1,l}(z'/\epsilon) + G_{1,r}(z'/\epsilon) \right] - g_{int}^{(l)}(z') - g_{int}^{(r)}(z') + O(\epsilon^2) \,,$$

where $f_{int}^{(l)}(z') = \pi \, z' - \epsilon \, \pi \, \sqrt{\gamma}$, $f_{int}^{(r)}(z') = \pi \, (1 - z') - \epsilon \, \pi \, \sqrt{\gamma}$, $g_{int}^{(l)}(z') = (\pi \, (\pi^2 + k^2)/k^2) \, z'$ and $g_{int}^{(r)}(z') = (\pi \, (\pi^2 + k^2)/k^2) \, (1 - z')$ are the common solutions between the outer and inner regions. Finally, we have $\hat{w} = \hat{w}_0 + \epsilon f_1 + O(\epsilon^2)$ and $\hat{\theta} = g_0 + \epsilon g_1 + O(\epsilon^2)$, where

$$\hat{w}_0(z') = \sin(\pi \, z') + \pi \, \sqrt{\gamma} \, \epsilon \left\{ \exp\left[- \frac{z'}{\epsilon \, \sqrt{\gamma}} \right] + \exp\left[\frac{(z' - 1)}{\epsilon \, \sqrt{\gamma}} \right] \right\} . \tag{6.2.41}$$

As we can see, the velocity solution Eqn. (6.2.41) satisfies the Neumann boundary conditions but does not satisfy the Dirichlet conditions. To find the functions f_1 and g_1, we must solve the $O(\epsilon)$ equations in the outer region, which are

$$-\frac{d^2 f_1}{dz'^2} + k^2 f_1 - k^2 g_1 = 0 \,, \tag{6.2.42}$$

$$\frac{d^2 g_1}{dz'^2} - k^2 g_1 + R_0 f_1 = -R_1 f_0 \,, \tag{6.2.43}$$

with boundary conditions $f_1(z' = 0) = f_1(z' = 1) = -\pi\sqrt{\gamma}$, which are given by Eqn. (6.2.41) and $g_1(z' = 0) = g_1(z' = 1) = 0$. Eqns. (6.2.34), (6.2.35), (6.2.42) and (6.2.43), can be combined into a unique equation written as

$$R_0 \left[f_0 \frac{d^2 f_1}{dz'^2} - f_1 \frac{d^2 f_0}{dz'^2} \right] + k^2 \left[g_0 \frac{d^2 g_1}{dz'^2} - g_1 \frac{d^2 g_0}{dz'^2} \right] = -k^2 R_1 f_0 g_0 \,. \tag{6.2.44}$$

It is very easy to show that $\int_0^1 (f_0 f_1'' - f_1 f_0'')\, dz' = f_0'(0) f_1(0) - f_0'(1) f_1(1)$ and $\int_0^1 (g_0 g_1'' - g_1 g_0'')\, dz' = 0$. Therefore, by integrating Eqn. (6.2.44) we obtain

$$R_1 = 4\pi^2 \sqrt{\gamma}\, \frac{(\pi^2 + k^2)}{k^2} \,. \tag{6.2.45}$$

The solutions of Eqns. (6.2.42) and (6.2.43) are

$$f_1 = \frac{\pi\sqrt{\gamma}}{2} \left\{ 2\left(z' - \frac{1}{2}\right) \cos(\pi z') - \operatorname{sech}\left(\frac{\lambda}{2}\right) \cosh\left[\lambda\left(z' - \frac{1}{2}\right)\right] \right\} , \tag{6.2.46}$$

$$\begin{aligned} g_1 = {} & \frac{2\pi^2\sqrt{\gamma}}{k^2} \sin(\pi z') \\ & + \frac{\pi\sqrt{\gamma}}{2} \frac{(\pi^2 + k^2)}{k^2} \left\{ 2\left(z' - \frac{1}{2}\right) \cos(\pi z') + \operatorname{sech}\left(\frac{\lambda}{2}\right) \cosh\left[\lambda\left(z' - \frac{1}{2}\right)\right] \right\} , \end{aligned} \tag{6.2.47}$$

where $\lambda = \sqrt{\pi^2 + 2k^2}$. The reconstructed Rayleigh number $Ra_t = R_0 + \epsilon R_1 + O(\epsilon^2)$ obtained by the matching asymptotic method coincides with the result given by Eqn. (6.2.28). To extend this result, we must solve the $O(\epsilon^2)$ equations in the left inner region, which are the following

$$\gamma \frac{d^4 F_{2,l}}{d\zeta^4} - \frac{d^2 F_{2,l}}{d\zeta^2} = 0 \,, \tag{6.2.48}$$

$$\frac{d^2 G_{2,l}}{d\zeta^2} = 0 \,, \tag{6.2.49}$$

with boundary conditions $F_{2,l} = dF_{2,l}/dz' = G_{2,l} = 0$ on $\zeta = 0$. By using the intermediate variable method, the solutions of these equations are

$$F_{2,l} = \pi\,\gamma \left[1 + \frac{\lambda}{2}\,\tanh\left(\frac{\lambda}{2}\right)\right]\left(\frac{1}{\sqrt{\gamma}}\,\zeta - 1 + \exp\left[-\frac{\zeta}{\sqrt{\gamma}}\right]\right),$$

$$G_{2,l} = \left[\frac{2\pi^2\sqrt{\gamma}}{k^2} + \pi\sqrt{\gamma}\,\frac{(\pi^2+k^2)}{k^2}\left(1 - \frac{\lambda}{2}\,\tanh\left(\frac{\lambda}{2}\right)\right)\right]\zeta \,.$$

On the other hand, by using symmetry arguments, the solutions of the $O(\epsilon)$ equations in the right inner region are

$$F_{2,r} = \pi\,\gamma \left[1 + \frac{\lambda}{2}\,\tanh\left(\frac{\lambda}{2}\right)\right]\left(\frac{1}{\sqrt{\gamma}}\,\xi - 1 + \exp\left[-\frac{\xi}{\sqrt{\gamma}}\right]\right),$$

$$G_{2,r} = \left[\frac{2\pi^2\sqrt{\gamma}}{k^2} + \pi\sqrt{\gamma}\,\frac{(\pi^2+k^2)}{k^2}\left(1 - \frac{\lambda}{2}\,\tanh\left(\frac{\lambda}{2}\right)\right)\right]\xi \,.$$

Therefore, by using composite expansions, the physical solutions of the problem are $\hat{w} = \hat{w}_0 + \epsilon\,\hat{w}_1 + \epsilon^2 f_2 + O(\epsilon^3)$ and $\hat{\theta} = g_0 + \epsilon\,g_1 + \epsilon^2 g_2 + O(\epsilon^3)$, where

$$\hat{w}_1(z') = f_1(z') + \epsilon\,\pi\,\gamma\left(1 + \frac{\lambda}{2}\,\tanh\left(\frac{\lambda}{2}\right)\right)\left\{\exp\left[-\frac{z'}{\epsilon\sqrt{\gamma}}\right] + \exp\left[\frac{(z'-1)}{\epsilon\sqrt{\gamma}}\right]\right\}. \tag{6.2.50}$$

The dependence of $\hat{w}$ with ϵ is shown in Fig. 6.2.2. This figure shows that the influence of the boundary layer in the dynamics is negiglible for $\epsilon \ll 1$. From Eqn. (6.2.50),

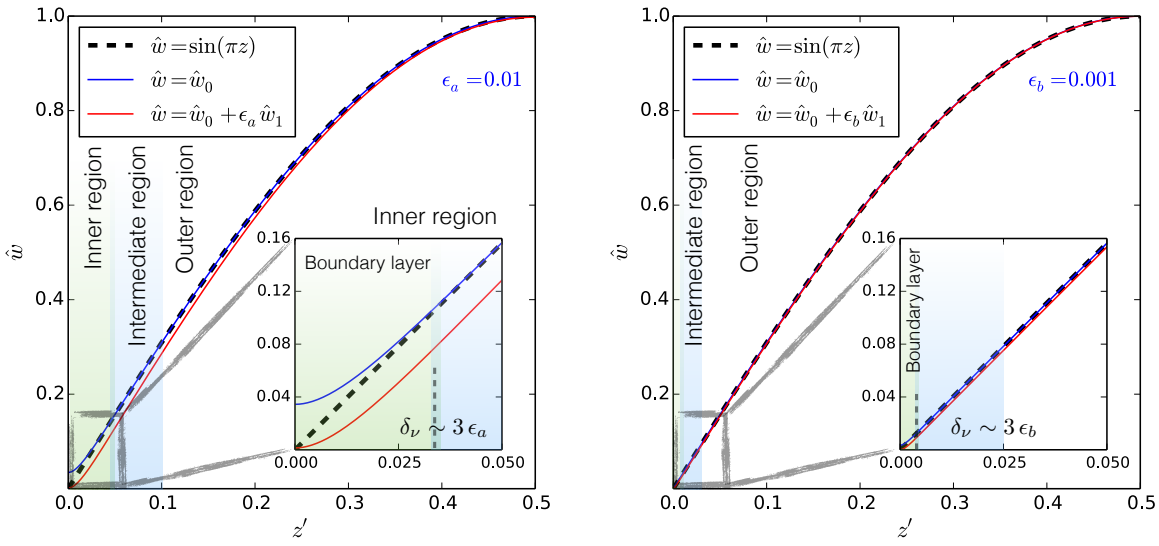

Figure 6.2.2: Vertical velocity profiles for different values of ϵ. The left image shows $\hat{w}$ for $\epsilon = 0.01$, while the right image shows $\hat{w}$ for $\epsilon = 0.001$. Both profiles are compared with the solution obtained using free-slip boundary conditions $\hat{w} = \sin(\pi z')$. The thickness of boundary layer estimated is $\delta_\nu \sim \epsilon$, which is shown in the inset plots. We can see that the influence of the boundary layer in the dynamics is negiglible for $\epsilon \ll 1$

we obtain the following boundary conditions, $f_2(z'=0) = f_2(z'=1) = -\pi\gamma(1 + \lambda/2\,\tanh(\lambda/2))$ and $g_2(z'=0) = g_2(z'=1) = 0$. Then, the $O(\epsilon^2)$ equations in the outer region are the following

$$-\frac{d^2 f_2}{dz'^2} + k^2 f_2 - k^2 g_2 = -\gamma\left[\frac{d^4 f_0}{dz'^4} - 2k^2\frac{d^2 f_0}{dz'^2} + k^4 f_0\right] + \beta R_0\, k^2 f_0$$

$$+ k^2\,\bar{\vartheta}\left[\frac{d^2 g_0}{dz'^2} - k^2\, g_0\right], \tag{6.2.51}$$

$$\frac{d^2 g_2}{dz'^2} + R_0\, f_2 - k^2\, g_2 = -R_1\, f_1 - R_2\, f_0\,. \tag{6.2.52}$$

Eqns. (6.2.34), (6.2.35), (6.2.51) and (6.2.52) can be combined into a unique equation, obtaining the following

$$R_0\left[f_0\,\frac{d^2f_2}{dz'^2}-f_2\,\frac{d^2f_0}{dz'^2}\right]+k^2\left[g_0\,\frac{d^2g'^2}{dz^2}-g_2\,\frac{d^2g_0}{dz'^2}\right]=-R_1\,k^2\,g_0f_1-R_2\,k^2\,f_0g_0 \qquad (6.2.53)$$

$$+\,\gamma\,R_0\left[f_0\,\frac{d^4f_0}{dz'^4}-2k^2\,f_0\,\frac{d^2f_0}{dz'^2}+k^4\,f_0^2\right]-\beta\,R_0^2\,k^2\,f_0^2-k^2\,\bar{\vartheta}\,R_0\left[f_0\,\frac{d^2g_0}{dz'^2}-k^2\,f_0g_0\right].$$

Using the relations $\int_0^1(f_0\,f_2''-f_2\,f_0'')\,dz'=f_0'(0)\,f_2(0)-f_0'(1)\,f_2(1)$, $\int_0^1(g_0\,g_2''-g_2\,g_0'')\,dz'=0$ and $f_2(0)=f_2(1)$, we can integrate the Eqn. (6.2.53), obtaining

$$R_2=\chi^{(\bar{\vartheta})}\,\frac{(\pi^2+k^2)^3}{k^2}+\frac{4\pi^2\gamma}{k^2}\,(\pi^2+k^2)\left[1+\frac{\lambda}{2}\,\tanh\left(\frac{\lambda}{2}\right)\right]+\frac{2\pi^2\gamma}{k^2}\,(3\pi^2+k^2)\,, \qquad (6.2.54)$$

where $\chi^{(\bar{\vartheta})}=\gamma-\beta+\bar{\vartheta}$. The introduction of $\bar{\vartheta}>0$ in the equations shows that the interfacial effects stabilize linearly the system at order $O(\epsilon^2)$, as we expected. Therefore, the reconstructed Rayleigh number is

$$Ra_t(k,\epsilon)=\frac{(\pi^2+k^2)^2}{k^2}+\epsilon\left\{4\pi^2\sqrt{\gamma}\,\frac{(\pi^2+k^2)}{k^2}\right\} \qquad (6.2.55)$$

$$+\,\epsilon^2\left\{\chi^{(\bar{\vartheta})}\,\frac{(\pi^2+k^2)^3}{k^2}+\frac{4\pi^2\gamma}{k^2}\,(\pi^2+k^2)\left[1+\frac{\lambda}{2}\,\tanh\left(\frac{\lambda}{2}\right)\right]+\frac{2\pi^2\gamma}{k^2}\,(3\pi^2+k^2)\right\}+O(\epsilon^3)\,.$$

Minimizing Ra_t with respect to k and applying the perturbative expansion $k=k_0+\epsilon k_1+\epsilon^2k_2+O(\epsilon^3)$, we obtain the following solutions of the critical wavenumber by solving the minimization problem order by order

$$\begin{aligned}
k_0&=\pi\,,\\
k_1&=\pi\sqrt{\gamma}\,,\\
k_2&=\pi\gamma-\pi^3\chi^{(\bar{\vartheta})}+\frac{\pi^2\gamma\sqrt{3}}{6}\,\tanh\left(\frac{\pi\sqrt{3}}{2}\right)-\frac{\pi^3\gamma}{2}\,\mathrm{sech}^2\left(\frac{\pi\sqrt{3}}{2}\right).
\end{aligned}$$

Finally, the critical thermal Rayleigh number obtained using matching asymptotic expansions is

$$Ra_t^{(c)} = 4\pi^2 + \left[8\pi^2\sqrt{\gamma}\right]\epsilon + \left[8\pi^4\chi^{(\bar{\vartheta})} + 12\pi^2\gamma + 4\pi^3\gamma\sqrt{3}\,\tanh\left(\frac{\pi\sqrt{3}}{2}\right)\right]\epsilon^2 + O(\epsilon^3)\,. \tag{6.2.56}$$

which is a generalized result of the critical Rayleigh number given by Ress (2002). Eqn. (6.2.56) shows that the geometry (inertial) effects appear at order $O(\epsilon)$ due to the viscous dissipation, while the interfacial effects appear at order $O(\epsilon^2)$. Furthermore, in Eqn. (6.2.56), we can see that $Ra_t^{(c)} > Ra_{t,darcy}^{(c)}$, so geometry effects also contributes to the weak stabilization of the system.

6.3 Long-wave instability dynamics in Rayleigh-Taylor convection

The solubility trapping of supercritical CO_2 in saturated geologic reservoirs is an interesting problem where the stability of the two-fluid system depends on an unsteady base-state. The dissolution of CO_2 into brine forms a diffusive layer which becomes unstable due to the increase of the density of the fluid inside of a thin interfacial region between the gas (CO_2) and fluid (brine) phases. This mechanism of instability is called Rayleigh-Taylor (Sharp, 1984). When the time is greater than the critical time of the onset of convection, the fingering phenomenon starts to dominate the dynamics, enhancing the mass transport of the dissolved CO_2 into the reservoir. In this chapter, we study the consequences of inertial terms and weak capillary effects in the stability of the problem, which have not been addressed until now.

Fig. 6.3.1 shows the analogy between the onset of instability in the mixing of two-fluid phases in Hele-Shaw cells (the analogue system) and the approximation proposed when $t' \ll 1$, using a semi-infinite domain in the self-similarity system reference (the canonical system). The analogue system represents a physical laboratory picture of the dissolution of CO_2 into brine in geologic reservoirs, while the canonical system is adequate to determine the critical time of the onset of instability. Following the work of Riaz et al (2006), from Eqns. (5.4.1) to (5.4.3) and using the constitutive equation $\bar{\rho}' = S_w$, the base scalar solution of the canonical system is given by a pure diffusion process, where $\bar{\mathbf{u}}' = \mathbf{0}$ and $S_w = s_0$ must satisfy the equation

$$\frac{\partial s_0}{\partial t'} = \frac{1}{Ra_s}\,\frac{\partial^2 s_0}{dz'^2}\,,$$

with boundary conditions $s_0 = 1$ at $z' = 0$ and $\partial s_0/\partial z' = 0$ at $z' = \infty$. The base pressure is the solution of the equation

$$\nabla' \bar{p}'_s = -s_0\, g\, \hat{z} - \vartheta \left[\nabla' s_0\, \nabla'^2 s_0 + \frac{1}{2}\,\nabla'\Big(|\nabla' s_0|^2\Big) \right].$$

By using the self-similar variable $\xi = z'\sqrt{Ra_s/4t'}$, the base scalar solution is $s_0 = 1 - \mathrm{erf}(\xi)$, which is time independent in the (ξ, t') reference system. This solution is valid when the penetration deep $\delta(t') = \sqrt{4t'/Ra_s} \ll 1$. Next, we perturbe the base-state solution as follows

$$S_w = s_0(\xi) + \check{s}(\xi, t')\, e^{-ikx'}\,, \tag{6.3.1}$$

$$\bar{u}' = 0 + \check{u}(\xi, t')\, e^{-ikx'}\,, \tag{6.3.2}$$

$$\bar{w}' = 0 + \check{w}(\xi, t')\, e^{-ikx'}\,, \tag{6.3.3}$$

$$\bar{p}' = \bar{p}'_s(\xi) + \check{p}(\xi, t')\, e^{-ikx'}\,. \tag{6.3.4}$$

Using the notation $\partial f/\partial \xi = f_\xi$ for spatial derivatives and $Ca = 1/\bar{\vartheta}$ for the capillary number, the linearized perturbed equations can then be expressed as

$$ik\check{u} = \frac{1}{2}\,\eta_{t'}\,\check{w}_\xi\,, \tag{6.3.5}$$

$$\gamma\,\epsilon^2\,Re\,\frac{\partial \check{u}}{\partial t'} = \frac{1}{2t'}\,\gamma\,\epsilon^2\,Re\,\xi\,\check{u}_\xi + i\,k\,\check{p} - \bar{\mu}\,\check{u} + \gamma\,\epsilon^2\,\bar{\mu}\left[-k^2\,\check{u} + \frac{1}{4}\,\eta_{t'}^2\,\check{u}_{\xi\xi} \right] \tag{6.3.6}$$

$$- \frac{i\,k}{\sqrt{\pi}}\,\epsilon^2\,\bar{\vartheta}\,\eta_{t'}^2\,e^{-\xi^2}\left[\frac{1}{2}\,\check{s}_\xi - \xi\,\check{s} \right],$$

$$\gamma\,\epsilon^2\,Re\,\frac{\partial \check{w}}{\partial t'} = \frac{1}{2t'}\,\gamma\,\epsilon^2\,Re\,\xi\,\check{w}_\xi - \frac{1}{2}\,\eta_{t'}\,\check{p}_\xi + \check{s} - \bar{\mu}\,\check{w} + \frac{1}{\sqrt{\pi}}\,\eta_{t'}\,\beta\,\epsilon^2\,Ra_s\,e^{-\xi^2}\,\check{w} \tag{6.3.7}$$

$$+ \gamma\,\epsilon^2\,\bar{\mu}\left[-k^2\,\check{w} + \frac{1}{4}\,\eta_{t'}^2\,\check{w}_{\xi\xi} \right] - \frac{1}{\sqrt{\pi}}\,\epsilon^2\,\bar{\vartheta}\,\eta_{t'}^3\,e^{-\xi^2}\left[\xi\,\check{s}_\xi - \frac{1}{2}\,\check{s}_{\xi\xi} + \frac{k^2\,t'}{Ra_s}\,\check{s} \right],$$

$$\frac{\partial \check{s}}{\partial t'} - \frac{1}{t'}\left[\frac{1}{4}\,\check{s}_{\xi\xi} + \frac{1}{2}\,\xi\,\check{s}_{\xi} - \frac{k^2\,t'}{Ra_s}\,\check{s}\right] = \frac{1}{\sqrt{\pi}}\,\eta_{t'}\,e^{-\xi^2}\,\check{w}\,, \tag{6.3.8}$$

where $\eta_{t'} = \sqrt{Ra_s/t'}$, $\gamma = 6/5$ and $\beta = 2/35$. The boundary conditions are $\check{s} = \check{u} = \check{w} = 0$ in $\xi = 0$, and $\check{s}_{\xi} = \check{u} = \check{w} = 0$ in $\xi = \infty$. For $\epsilon \to 0$, we obtain the same linear equations studied by Riaz et al (2006). Eqns. (6.3.6) to (6.3.8) represent a linear system of non-autonomous equations which cannot be solved analytically. Unfortunately, the non-autonomous nature of equations prohibits the use of classical disturbances of the type $e^{\sigma t'}$ in Eqns. (6.3.1) to (6.3.4), where σ is the growth rate (Farrel and Ioannou, 1996).

In their work, Riaz et al (2006) show that the modal expansion of $\check{s}$ given by the expression

$$\check{s}(\xi, t') = \sum_{n=1}^{\infty} a_n(t')\,\psi_n(\xi)\,, \tag{6.3.9}$$

and applied to the nonlinear streamwise operator

$$\mathcal{L} = \frac{1}{4}\,\check{s}_{\xi\xi} + \frac{1}{2}\,\xi\,\check{s}_{\xi}\,, \tag{6.3.10}$$

leads to the eigenvalue problem $\mathcal{L}\psi_n = \lambda_n\,\psi_n = -n\,e^{-\xi^2}\,\mathcal{H}_n(\xi)$, where $\mathcal{H}_n(\xi)$ are the Hermite polynomials and $n = 1, 2, 3, \ldots$. These polynomials provide an optimal basis for the canonical system (see Fig. 6.3.1). In general, the modal expansion technique is not recommended for study non-autonomous systems because it does not address the interesting problem of the transient growth of small perturbations, which can be demostrated analyzing the non-orthogonality of the eigenmodes (Schmid, 2007). However, in the limit $\epsilon \to 0$, the temporal evolution of the first mode $n = 1$, in a semi-infinite domain, captures the long-wave instability dynamics with a good agreement with nonlinear simulations. For this case, the scaling law for the critical time is $\tau_c \sim 146 Ra_s^{-1}$ (Riaz et al, 2006).

For a more detailed description of the onset of convection, new techniques related with non-modal linear stability analysis have been reported in the literature, which can capture the transient growth of small perturbations. We refer the recent work of Hota et al (2015) for further details. We will apply the self-similarity quasi steady-state approximation technique (SS-QSSA) (Pramanik and Mishra, 2013) to Eqns. (6.3.5) to (6.3.8), with the aim to study the temporal evolution of the first (dominant) mode $n = 1$ in the canonical system presented in Fig. 6.3.1. Only for this case, we can use

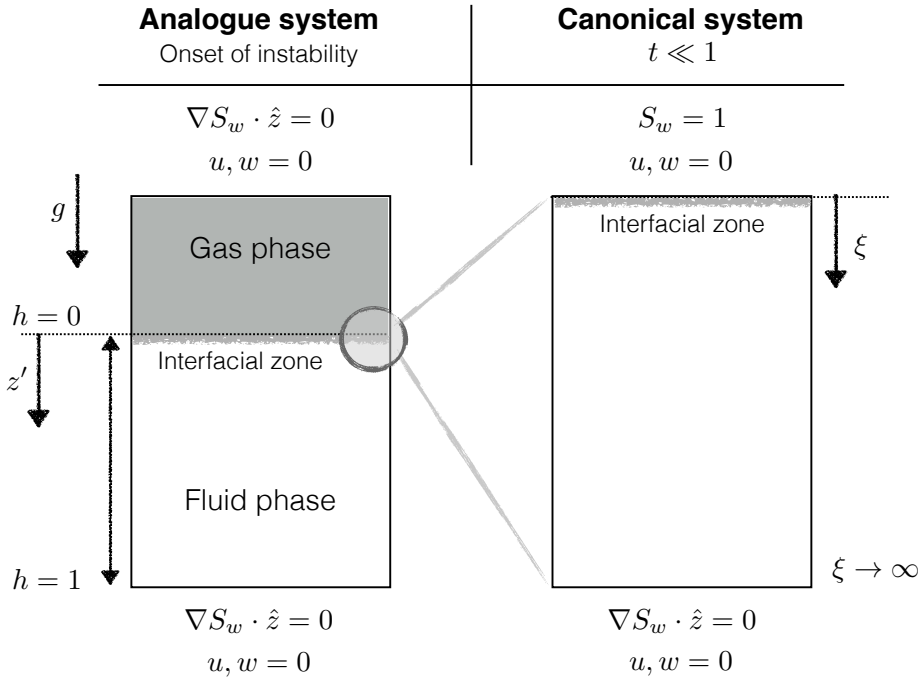

Figure 6.3.1: The analogue and canonical systems in Hele-Shaw cells. The onset of instability in the mixing of two-fluid phases in Hele-Shaw cells is represented by the analogue system, while the canonical system is the mathematical approximation when $t' \ll 1$ using a semi-infinite domain in the self-similarity system reference.

the approximation $\check{f}(\xi, t') \sim \hat{f}(\xi)\, \exp(\sigma(k, \tau_f)\, t')$, where $\sigma = \sigma(k, \tau_f)$ is the growth rate and τ_f is the frozen time (Riaz et al, 2006).

6.3.1 Dominant-mode solution using the SS-QSSA technique

The main reasons to work with the SS-QSSA using the first (dominant) mode, instead of non-modal analysis, are the following

- The solutions have a better behavior at short times when we work in the self-similarity (ξ, t') space (Riaz et al, 2006; Pramanik and Mishra, 2015).
- The non-autonomous system can be reduced for one which is autonomous and analytically soluble, by freezing the base-state at a particular time τ_f.
- When $\epsilon \ll 0$ and $k = 0$, the first mode decays as $\sigma = -1/\tau_f$, which always stabilizes the flow. Then, a long-wave cutoff exists and the fluid becomes unstable for $t' > \tau_f$.

- In the limit $\epsilon \to 0$, the critical time and the long-wave cutoff are computed exactly by the dominant-mode solution (Riaz et al, 2006) (See Chapter 4, Section 4.1 on page 29 for additional information about the long-wave cutoff). We will suppose that for $\epsilon \ll 1$, we can still obtain reliable results.

Therefore, this method allow us to use classical modal analysis to study the linearized equations. Then, introducing the frozen time τ_f in Eqns. (6.3.5) to (6.3.8) and applying only the first mode of Eqn. (6.3.9), which is $\psi_1(\xi) = \hat{s}(\xi) = \xi \exp(-\xi^2)$, we obtain the following linear system of equations

$$ik\hat{u} = \frac{1}{2}\,\eta_\tau\,\hat{w}_\xi\,, \tag{6.3.11}$$

$$\begin{aligned}\sigma(k,\tau_f)\,\gamma\,\epsilon^2\,Re\,\hat{u} = {} & \frac{1}{2\tau_f}\,\gamma\,\epsilon^2\,Re\,\xi\,\hat{u}_\xi + i\,k\,\hat{p} - \bar{\mu}\,\hat{u} + \gamma\,\epsilon^2\,\bar{\mu}\left[-k^2\,\hat{u} + \frac{1}{4}\,\eta_\tau^2\,\hat{u}_{\xi\xi}\right] \\ & - \frac{i\,k}{\sqrt{\pi}}\,\epsilon^2\,\bar{\vartheta}\,\eta_\tau^2\,e^{-\xi^2}\left[\frac{1}{2}\,\hat{s}_\xi - \xi\,\hat{s}\right],\end{aligned} \tag{6.3.12}$$

$$\begin{aligned}\sigma(k,\tau_f)\,\gamma\,\epsilon^2\,Re\,\hat{w} = {} & \frac{1}{2\tau_f}\,\gamma\,\epsilon^2\,Re\,\xi\,\hat{w}_\xi - \frac{1}{2}\,\eta_\tau\,\hat{p}_\xi + \hat{s} - \bar{\mu}\,\hat{w} + \frac{1}{\sqrt{\pi}}\,\eta_\tau\,\beta\,\epsilon^2\,Ra_s\,e^{-\xi^2}\,\hat{w} \\ & + \gamma\,\epsilon^2\,\bar{\mu}\left[-k^2\,\hat{w} + \frac{1}{4}\,\eta_\tau^2\,\hat{w}_{\xi\xi}\right] - \frac{1}{\sqrt{\pi}}\,\epsilon^2\,\bar{\vartheta}\,\eta_\tau^3\,e^{-\xi^2}\left[\xi\,\hat{s}_\xi - \frac{1}{2}\,\hat{s}_{\xi\xi} + \frac{k^2\,\tau_f}{Ra_s}\,\hat{s}\right],\end{aligned} \tag{6.3.13}$$

$$\left[\sigma(k,\tau_f) + \frac{1}{\tau_f} + \frac{k^2}{Ra_s}\right]\hat{s} = \frac{1}{\sqrt{\pi}}\,\eta_\tau\,e^{-\xi^2}\,\hat{w}\,. \tag{6.3.14}$$

After a straightforward algebraic procedure, we obtain the following general boundary layer equation (Orr-Sommerfeld model)

$$\begin{aligned}&\Big[A_0 + \epsilon^2(A_1 + \sigma\,A_2)\Big]\,\hat{w} + \Big[B_0 + \epsilon^2\,B_1\Big]\,\hat{w}_\xi + \Big[C_0 + \epsilon^2(C_1 + \sigma\,C_2)\Big]\,\hat{w}_{\xi\xi} \\ &\quad + \epsilon^2\,P_0\,\hat{w}_{\xi\xi\xi} + \epsilon^2\,R_0\,\hat{w}_{\xi\xi\xi\xi} = k^2\,\xi\,e^{-\xi^2} - \frac{1}{\sqrt{\pi}}\,k^2\,\epsilon^2\,\bar{\vartheta}\,\eta_\tau^3\left[1 + \frac{k^2\,\tau_f}{Ra_s}\right]\xi\,e^{-2\xi^2}\,,\end{aligned} \tag{6.3.15}$$

where

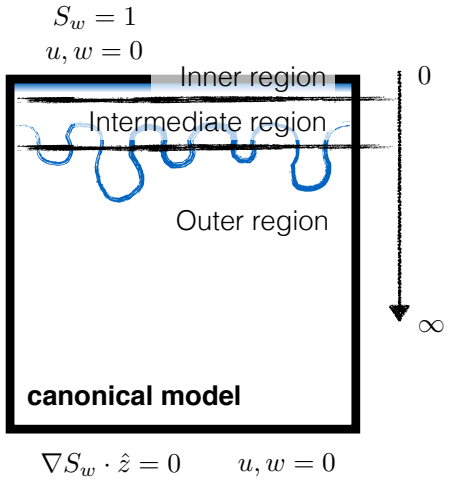

Figure 6.3.2: Asymptotic regions in the canonical model. The inner region is directly related with the diffusive boundary layer

$$A_0(\xi) = \bar{\mu}\, k^2 \quad ; \quad A_1(\xi) = \bar{\mu}\,\gamma\, k^4 - \frac{1}{\sqrt{\pi}}\, k^2\, \eta_\tau\, \beta\, Ra_s\, e^{-\xi^2} \quad ; \quad A_2 = \gamma\, Re\, k^2 \,,$$

$$B_0(\xi) = -\frac{1}{4}\,\eta_\tau^2\,\bar{\mu}_\xi \quad ; \quad B_1(\xi) = -\frac{1}{2\tau_f}\,\gamma\, Re\, k^2\,\xi - \frac{1}{4}\,\bar{\mu}_\xi\, k^2\,\eta_\tau^2\,\gamma \,,$$

$$C_0(\xi) = -\frac{1}{4}\,\eta_\tau^2\,\bar{\mu} \quad ; \quad C_1(\xi) = \frac{1}{8\tau_f}\,\gamma\, Re\,\eta_\tau^2 - \frac{1}{2}\,\bar{\mu}\, k^2\,\eta_\tau^2\,\gamma \quad ; \quad C_2 = -\frac{1}{4}\,\eta_\tau^2\,\gamma\, Re \,,$$

$$P_0(\xi) = \frac{1}{8\tau_f}\,\gamma\, Re\,\eta_\tau^2\,\xi + \frac{1}{16}\,\eta_\tau^4\,\gamma\,\bar{\mu}_\xi \quad ; \quad R_0(\xi) = \frac{1}{16}\,\eta_\tau^4\,\gamma\,\bar{\mu} \,.$$

Eqn. (6.3.15) can be solved analytically by means of matching asymptotic methods (see Fig. 6.3.2). Since the interfacial tension term $\bar{\vartheta}$ appears at order $O(\epsilon^2)$, we incorporate it in the solution of Eqn. (6.3.15) by introducing the term $\bar{\delta} = \epsilon^2\,\bar{\vartheta}$. In the following, we assume that $\bar{\mu} = 1$ and the boundary conditions are $\hat{w} = 0$ and $\hat{w}_\xi = 0$, both evaluated at $\xi = 0$ and $\xi \to \infty$.

In the outer region, we have the expansion in power series

$$\hat{w} = f(\xi) = f_0(\xi) + \epsilon f_1(\xi) + \epsilon^2 f_2(\xi) + O(\epsilon^2) \,,$$

with boundary conditions $f = f_\xi = 0$ in $\xi = 0$ and $\xi \to \infty$. On the other hand, in the upper inner region ($\xi \to 0$), we use the inner variable $\zeta = \xi/\epsilon$, so we have

$$\hat{w} = F(\zeta) = F_0(\zeta) + \epsilon F_1(\zeta) + \epsilon^2 F_2(\zeta) + O(\epsilon^3) \,,$$

with boundary conditions $F = F_\zeta = 0$ in $\zeta = 0$.

6.3.2 $O(1)$ outer solution

At order $O(1)$, Eqn. (6.3.15) in the outer region is written as

$$\frac{\partial^2 f_0}{\partial \xi^2} - \bar{\alpha}_1^2 f_0 = -\bar{\alpha}_1^2 \left[\xi\, e^{-\xi^2} - \bar{\alpha}_2\, \xi\, e^{-2\xi^2} \right], \tag{6.3.16}$$

$$\bar{\alpha}_1 = \frac{2k}{\eta_\tau} \quad ; \quad \bar{\alpha}_2 = \frac{1}{\sqrt{\pi}}\, \bar{\delta}\, \eta_\tau^3 \left[1 + \frac{k^2\, \tau_f}{Ra_s} \right],$$

with boundary conditions $f_0 = 0$ in $\xi = 0$ and $\xi \to \infty$. The homogeneous solution of Eqn. (6.3.16) is $f_0^{(h)} = \theta_1(\xi) \exp(\bar{\alpha}_1 \xi) + \theta_2(\xi) \exp(-\bar{\alpha}_1 \xi)$, while the particular solution is obtained by means of the method of variation of parameters

$$\frac{\partial \theta_1}{\partial \xi} = -\frac{\bar{\alpha}_1}{2} \left[\xi\, e^{-\xi^2} - \bar{\alpha}_2\, \xi\, e^{-2\xi^2} \right] e^{-\bar{\alpha}_1 \xi} \quad ; \quad \frac{\partial \theta_2}{\partial \xi} = \frac{\bar{\alpha}_1}{2} \left[\xi\, e^{-\xi^2} - \bar{\alpha}_2\, \xi\, e^{-2\xi^2} \right] e^{\bar{\alpha}_1 \xi}.$$

Thereby, the general solution of Eqn. (6.3.16) is

$$\begin{aligned} f_0 = {} & e^{\bar{\alpha}_1 \xi} \left[K_1 + K_2\, e^{-\bar{\alpha}_1 \xi - \xi^2} + K_3\, \mathrm{erf}\!\left(\xi + \frac{1}{2}\, \bar{\alpha}_1 \right) - K_4\, e^{-\bar{\alpha}_1 \xi - 2\xi^2} - K_5\, \mathrm{erf}\!\left(\sqrt{2}\xi + \frac{1}{2\sqrt{2}}\, \bar{\alpha}_1 \right) \right] \\ & + e^{-\bar{\alpha}_1 \xi} \left[- K_1 - K_2\, e^{\bar{\alpha}_1 \xi - \xi^2} + K_3\, \mathrm{erf}\!\left(\xi - \frac{1}{2}\, \bar{\alpha}_1 \right) + K_4\, e^{\bar{\alpha}_1 \xi - 2\xi^2} - K_5\, \mathrm{erf}\!\left(\sqrt{2}\xi - \frac{1}{2\sqrt{2}}\, \bar{\alpha}_1 \right) \right], \end{aligned} \tag{6.3.17}$$

where the K_i parameters are the following

$$K_1 = \frac{1}{8}\, \bar{\alpha}_1^2\, \sqrt{\pi}\, e^{\bar{\alpha}_1^2/4} \left[\frac{1}{2\sqrt{2}}\, \bar{\alpha}_2 - 1 \right] \quad ; \quad K_2 = \frac{1}{4}\, \bar{\alpha}_1 \quad ; \quad K_3 = \frac{1}{8}\, \bar{\alpha}_1^2\, \sqrt{\pi}\, e^{\bar{\alpha}_1^2/4},$$

$$K_4 = \frac{1}{4\sqrt{2}}\, \bar{\alpha}_1\, \bar{\alpha}_2 \quad ; \quad K_5 = \frac{1}{16\sqrt{2}}\, \bar{\alpha}_1^2\, \bar{\alpha}_2\, \sqrt{\pi}\, e^{\bar{\alpha}_1^2/4}.$$

6.3.3 $O(\epsilon)$ inner solution

From Eqn. (6.3.17), we can see that in the limit $\xi \to 0$ we obtain $f_0 \sim 2(K_4 - K_2)\,\bar{\alpha}_1\,\xi$. Therefore, replacing $\xi = \epsilon\,\zeta$ in the expression given before, we obtain $f_0 \sim \epsilon\,F_1$ with $F_1(\zeta) = 2(K_4 - K_2)\,\bar{\alpha}_1\,\zeta$, which is the matching condition between the inner and outer solutions. In other words, in the power series expansion of $\hat{w}$ given for the inner region, we obtain the solution $F_0 = 0$. Thereby, at order $O(\epsilon)$, Eqn. (6.3.15) in the inner region is written as

$$\bar{\omega}\,\frac{\partial^4 F_1}{\partial \zeta^4} - \frac{\partial^2 F_1}{\partial \zeta^2} = 0 \quad ; \quad \bar{\omega} = \frac{1}{4}\,\eta_\tau^2\,\gamma\,, \tag{6.3.18}$$

with boundary conditions $F_1 = F_{1,\zeta} = 0$ in $\zeta = 0$. The solution of Eqn. (6.3.18) is

$$F_1 = \frac{1}{2}\,\bar{\alpha}_1^2\,\sqrt{\bar{\omega}}\left(\frac{1}{\sqrt{2}}\,\bar{\alpha}_2 - 1\right)\left[\frac{1}{\sqrt{\bar{\omega}}}\,\zeta - 1 + \exp\left(-\frac{\zeta}{\sqrt{\bar{\omega}}}\right)\right]. \tag{6.3.19}$$

Therefore, using composite expansions, the solution of $\hat{w}$ can be written as

$$\hat{w} = f_0 + \frac{1}{2}\,\epsilon\,\bar{\alpha}_1^2\,\sqrt{\bar{\omega}}\left(\frac{1}{\sqrt{2}}\,\bar{\alpha}_2 - 1\right)\exp\left(-\frac{\xi}{\epsilon\,\sqrt{\bar{\omega}}}\right) + \epsilon\,f_1 + O(\epsilon^2)\,. \tag{6.3.20}$$

To find the function f_1, we use the methodology of relaxation of no-slip boundary conditions presented in Section 6.2 on page 72.

6.3.4 $O(\epsilon)$ outer solution and velocity reconstruction

At order $O(\epsilon)$, Eqn. (6.3.15) in the outer region is written as

$$\frac{\partial^2 f_1}{\partial \xi^2} - \bar{\alpha}_1^2\,f_1 = 0\,, \tag{6.3.21}$$

with boundary conditions $f_1 = -(1/2)\,\bar{\alpha}_1^2\,\sqrt{\bar{\omega}}\left(\bar{\alpha}_2/\sqrt{2} - 1\right)$ in $\xi = 0$ and $f_1 = 0$ in $\xi \to \infty$. The solution of Eqn. 6.3.21 is

$$f_1 = -\frac{1}{2}\,\bar{\alpha}_1^2\,\sqrt{\bar{\omega}}\left[\frac{1}{\sqrt{2}}\,\bar{\alpha}_2 - 1\right]e^{-\bar{\alpha}_1\xi}\,. \tag{6.3.22}$$

Finally, the solution of $\hat{w}$ at order $O(\epsilon^2)$ is

$$\hat{w} = f_0 + \frac{1}{2}\,\epsilon\,\bar{\alpha}_1^2\,\sqrt{\bar{\omega}}\left(\frac{1}{\sqrt{2}}\,\bar{\alpha}_2 - 1\right)\left[\exp\left(-\frac{\xi}{\epsilon\,\sqrt{\bar{\omega}}}\right) - \exp(-\bar{\alpha}_1\,\xi)\right] + O(\epsilon^2)\,. \quad (6.3.23)$$

Eqn. (6.3.23) has a dependency with parameters ϵ and $\bar{\delta} = \epsilon^2\,\bar{\vartheta}$ and therefore can be used to find the growth rate $\sigma = \sigma(k, \tau_f)$.

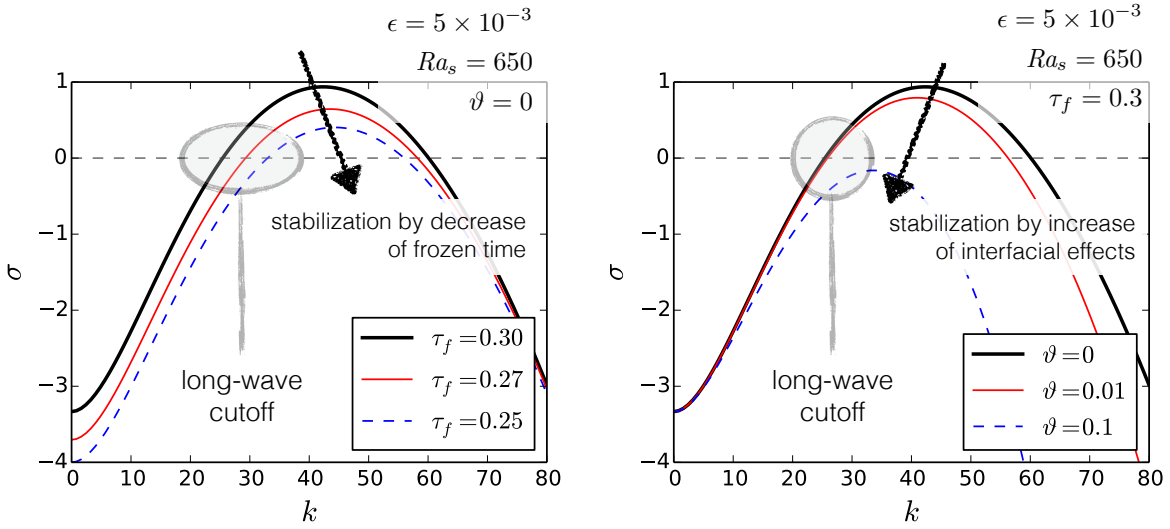

Figure 6.3.3: The growth rate σ in function of some values of ϵ, τ_f and $\bar{\vartheta}$. The left image shows artificial stabilization effects due to the decrease of the values of the frozen time. On the other hand, for fixed values of Ra_s, ϵ and τ_f, the right image also shows stabilization effects but due to the increase of interfacial tension. For both cases, the long-wave cutoff is marked appropiately

6.3.5 Critical time and wavenumber scalings

Integrating Eqn. (6.3.14) over the whole ξ-domain, we obtain the equation

$$\sigma(k, \tau_f) = -\frac{1}{\tau_f} - \frac{k^2}{Ra_s} + \frac{1}{\sqrt{\pi}}\,\eta_\tau\,\frac{\langle e^{-\xi^2}\,\hat{w}\rangle}{\langle \xi\,e^{-\xi^2}\rangle} \quad ; \quad \langle f\rangle = \int_0^\infty f(\xi)\,d\xi\,, \quad (6.3.24)$$

where the first two terms of the right hand side of Eqn. (6.3.24) are stabilizers. The last term of the same equation is a nonlinear destabilizer which must be evaluated numerically using Eqns. (6.3.17) and (6.3.23). Fig. 6.3.3 shows the growth rate in function of some values of ϵ, τ_f and $\bar{\vartheta}$. The left image shows artificial stabilization

effects due to the decrease of the values of the frozen time. In particular, for fixed values of Ra_s, ϵ and $\bar{\vartheta}$, the left image shows that there is a time τ_c such that $\sigma = 0$ and $\partial\sigma/\partial k = 0$. On the other hand, for fixed values of Ra_s, ϵ and τ_f, the right image also shows stabilization effects but due to the increase of interfacial tension, which is an expected result.

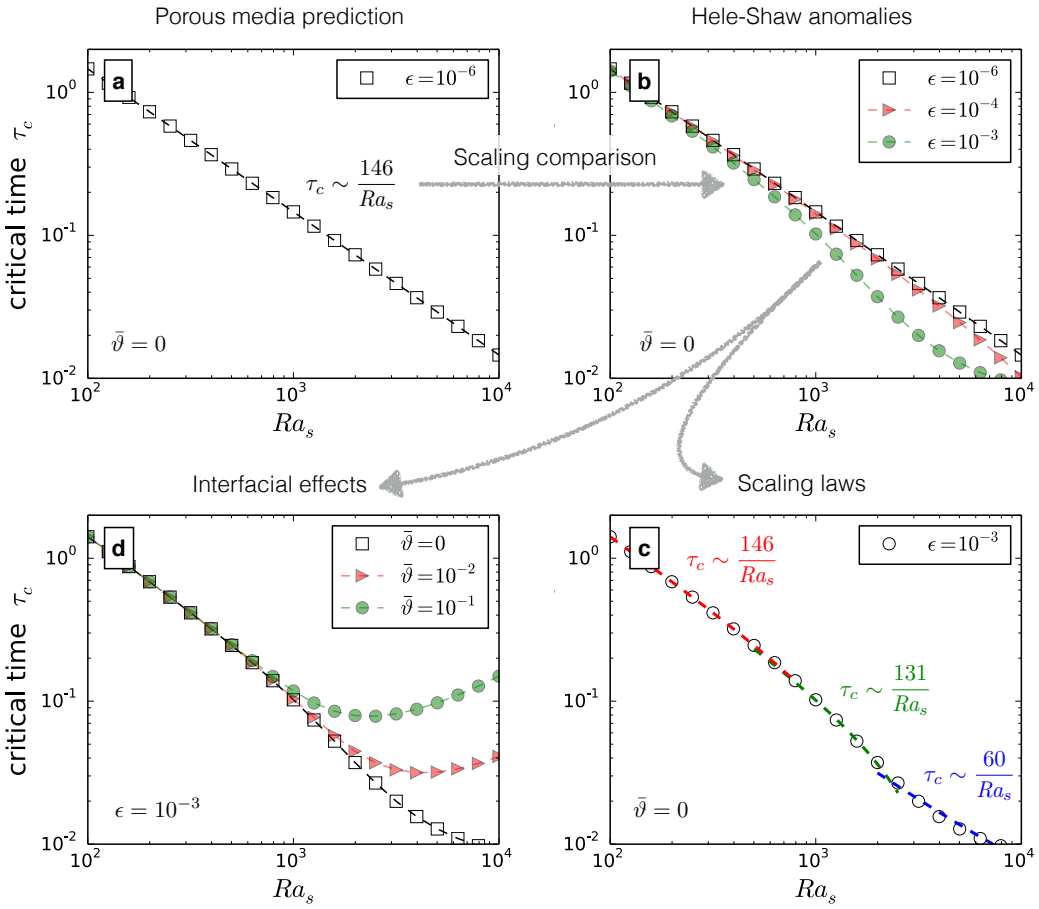

Figure 6.3.4: Critical time τ_c in function of the Rayleigh number Ra_s, for different values of ϵ and $\bar{\vartheta}$. Fig.(a) shows the porous media prediction for $\epsilon = 1 \times 10^{-6}$. Fig.(b) shows the effects of inertial terms. Considering $\epsilon = 1 \times 10^{-3}$, Fig.(c) shows the different scaling laws, depending on the Ra_s values. Finally, Fig.(d) shows the effects of considering interfacial tension.

To find the critical time τ_c and the most unstable wavenumber k_c in the onset of convection, we must solve numerically the following equations

$$\sigma = 0 \quad \Longrightarrow \quad \check{F}(k, \tau_f) = -\frac{1}{\tau_f} - \frac{k^2}{Ra_s} + \frac{1}{\sqrt{\pi}}\,\eta_\tau\,\frac{\langle e^{-\xi^2}\,\hat{w}\rangle}{\langle \xi\, e^{-\xi^2}\rangle} = 0\,, \tag{6.3.25}$$

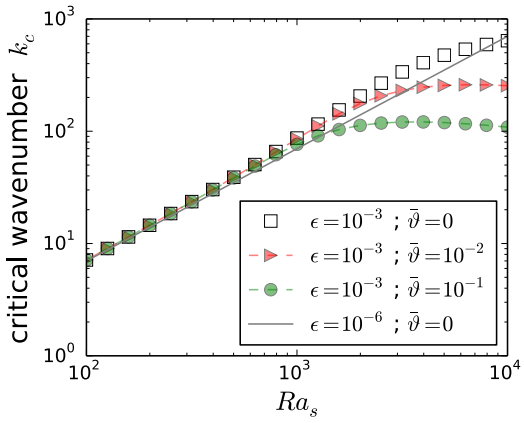

Figure 6.3.5: Critical wavenumber k_c in function of the Rayleigh number Ra_s, for different values of ϵ and $\bar{\vartheta}$

$$\frac{\partial\sigma}{\partial k}=0 \quad\Longrightarrow\quad \check{G}(k,\tau_f)=-\frac{2k}{Ra_s}+\frac{1}{\sqrt{\pi}}\,\eta_\tau\,\frac{\langle e^{-\xi^2}\,(\partial\hat{w}/\partial k)\rangle}{\langle \xi\, e^{-\xi^2}\rangle}=0\,, \tag{6.3.26}$$

Fig. 6.3.4 shows the critical time τ_c in function of the Rayleigh number Ra_s, for different values of ϵ and $\bar{\vartheta}$. In Fig. (a), for $\epsilon=1\times10^{-6}$, we obtain the same scaling prediction reported by Riaz et al (2006), which is $\tau_c\sim 146\,Ra_s^{-1}$. This result is not surprinsingly because $\epsilon\ll 1$. However, in Fig.(b), for $\bar{\vartheta}=0$ we obtain a weak nonlinear deviation of the porous media prediction when we increase ϵ. We will call this deviation the Hele-Shaw anomaly. Thereby, in comparison with predictions based on the traditional Darcy model, the geometry (inertial) effects of the cell tends to destabilize weakly the system in less time. Fig.(c) shows the scalings obtained for $\epsilon=1\times10^{-3}$ and $\bar{\vartheta}=0$, which are modeled as the piecewise function $\tau_c=a\,Ra_s^{-1}$, with a a constant depending on the interval of Ra_s considered. Finally, Fig. (d) shows dramatic changes in the τ_c-Ra_s curve due to interfacial effects, which has not been reported in the literature. Physically, fluid structures with small wavelength λ in the diffusive boundary layer are more susceptible to stabilization in time than large λ, due to the accion of effective interfacial tension which retards considerably the onset of convection. When Ra_s grows, the critical wavenumber k_c so does, as shown in Fig. 6.3.5. Thereby, for $Ra_s<1\times10^3$, the critical time is not affected by the interfacial tension due to the fluid structures of large λ can break the action of Korteweg stresses. However, for $Ra_s>1\times10^3$, the changes observed in the τ_c-Ra_s curve can be explained by means of the stabilization in time of structures with small λ. This observation has been obtained using the dominant-mode solution. However, with the aim to capture the contribution of the short-wave cutoff, it would be important to make a non modal analysis.

Part III

Nonlinear simulations

Chapter 7

Heat transport at high Rayleigh number regime in porous media

This chapter has been submitted as research paper called **"Heat transport at high Rayleigh number regime using a solenoidal Hele-Shaw model"**, authored by Juvenal A. Letelier, Paulo Herrera, Nicolás Mujica and Jaime H. Ortega, in Physical Review Letters **(May 2016)**.

Abstract

In this chapter, we investigate the effect of considering inertial terms in a Darcy model derived from the Navier-Stokes equations assuming slow diffusion and using regular perturbation theory for Hele-Shaw geometries. This geometry has been used as an analogue for two-dimensional homogeneous porous media in laboratory-scale experiments. The proposed model allows computing the nonlinear hydrodynamic dispersion tensor for Hele-Shaw cells, as well as the Brikmann dissipative term and the nonlinear Forchheimer drag term. The application of the model to thermal convection in a Hele-Shaw geometry, when viscosity is constant and applying periodic boundary conditions in the horizontal direction, gives new nonlinear scalings for both the Nusselt number and thermal dissipation rate. We demonstrate that the time-averaged Nusselt number $\langle Nu \rangle_\tau$ and mean scalar dissipation rate $\langle \varepsilon \rangle_\tau$ depend upon the anisotropy ratio $\epsilon = \sqrt{K}/H$, where $K = b^2/12$ is the cell permeability, b is the cell gap and H is the cell height. For $\epsilon = 0.01$, we obtain $\langle Nu \rangle_\tau \sim Ra^{0.40\pm0.03}$ and $\langle \varepsilon \rangle_\tau \sim Ra^{-0.59\pm0.03}$, whereas for $\epsilon = 0.001$ the scalings are $\langle Nu \rangle_\tau \sim Ra^{0.90\pm0.03}$ and $\langle \varepsilon \rangle_\tau \sim Ra^{-0.09\pm0.01}$. The result of $\langle Nu \rangle_\tau$ for $\epsilon = 0.001$ is in agreement with the scalings found by using the standard Darcy model. Our numerical results satisfy the expression $\langle Nu \rangle_\tau = Ra_t \langle \varepsilon \rangle_\tau$, which is derived from the proposed model.

7.1 Introduction

Thermal convection appears in a wide range of problems of interest in physics and geosciences, such as chaotic dynamics and bifurcations (Bizon et al, 1997b; Sheu et al,

2008), emerging patterns (Schoofs et al, 1999), scaling unifying theories of the thermal convection (Grassmann and Lohse, 2011), saturated porous media (Foster, 1965; Elder, 1967c; Otero et al, 2004; Hewitt et al, 2012) and geodynamics in the earth's mantle (Davies, 1999), as well as in industrial applications such as geothermal reservoir engineering. In particular, it has important implications for the study of the feasibility and implementation of novel technologies for the mitigation of anthropogenic gas emissions due to energy generation such as the use of carbon dioxide as working fluid in geothermal reservoirs (Brown, 2000; Benson et al, 2006; Randolph and Saar, 2011b; Adams et al, 2014), which are complex porous media systems whose modeling must be done through numerical computation (Pruess, 1991; Battistelli et al, 1997; Croucher and O'Sullivan, 2008).

In porous media, traditionally the transport of a passive scalar is modeled by simultaneously solving Darcy equation with the scalar advection-diffusion equation in the slow diffusion regime (incompressibility equation) (Joseph et al, 1996)

$$\mu K^{-1}\mathbf{u} = -\nabla p + \rho\, g\, \hat{z} \quad ; \quad \frac{\partial T}{\partial t} + \mathbf{u}\cdot\nabla T = \kappa_t\, \nabla^2 T \quad ; \quad \nabla\cdot\mathbf{u} = 0\,,$$

where $\mathbf{u}$ is the Darcy-scale average velocity field, g is the gravitational acceleration, ρ is the fluid density, μ is the dynamic viscosity, φ is the passive scalar and κ_φ is the scalar diffusivity. This system of partial differential equations will be referred hereafter as the standard Darcy model. In this model, the Rayleigh number $Ra_\varphi = \bar{u}_c H/\kappa_\varphi$ is the only parameter that controls the fluid-dynamics, where $\bar{u}_c$ is the characteristic convective velocity and H is the height of the cell. The response of the system is studied by means of the Nusselt number Nu_φ (Otero et al, 2004; Neufeld et al, 2010; Backhaus et al, 2011; Hidalgo et al, 2012) [1] . When the scalar is the mass fraction of a mixture, *i.e.*, $\varphi = S_w$, a nonlinear scaling of the form $Nu_s \sim Ra_s^\gamma$, with $0 \leq \gamma \leq 1$, must be reflected in the mean scalar dissipation rate $\langle\varepsilon_s\rangle \sim Ra_s^\beta$ (Hidalgo et al, 2012). If $Nu_s \sim Ra_s$, *i.e.*, the dissolution flux is independent of the Rayleigh number [2] , then $\langle\varepsilon_s\rangle$ also is independent of Ra_s , which has been demostrated using dimensional analysis (Jenny et al, 2014). However, empirical results of mixtures of two miscible fluids in porous media systems with no-flux boundaries (Neufeld et al, 2010; Backhaus et al, 2011) report a scaling of the form $Nu_s \sim Ra_s^{4/5}$, whereas numerical studies show that $\langle\varepsilon_s\rangle$ seems to be constant for a wide range of Ra_s in the same type of systems. The physical origins of this

[1] In mass transport, where φ is the mass fraction of a mixture, the Nusselt number Nu_φ is also known as the Sherwood number

[2] Valid for times less than the shutdown time (Hewitt et al, 2013), where the dissolution flux decreases notably. In thermal convection, the dissolution flux is called the convective flux

behaviour remains unexplained. The standard Darcy model for mixing convection and heat transport are mathematically similar, so we are interested in studying theoretical connections between these results with thermal convection in porous media [3] .

Previous studies on thermal convection, *i.e.*, $\varphi = T$, based on numerical simulations of the standard Darcy model with periodic boundary conditions in the horizontal direction and free-slip in the vertical direction (Otero et al, 2004; Hewitt et al, 2012), demonstrated that for $Ra_t > 4\pi^2$ the system is unstable and large-scale stable convective rolls appear, enhancing heat transport. The linear stability analysis of density-driven convection phenomena in porous media is shown in Chapter 6, Section 6.2 on page 65. However, for $1350 < Ra_t < 10000$ the quasi-steady convective rolls are not supported by the system and unsteady columnar plumes dominate the dynamics, which marks a transition to an out-of-equilibrium state known as the high-Ra_t regime, where nonlinear scalings between the Nusselt and Rayleigh number given by the expressions $Nu \sim Ra_t^{0.90}$ and $Nu \sim Ra_t^{0.95}$ have been obtained numerically (Otero et al, 2004; Hewitt et al, 2012). For $Ra_t \gtrsim 10^4$, the system exhibits a predominantly vertical exchange flow, where the scaling $Nu \sim Ra_t$ was observed asymptotically (Hewitt et al, 2012). Therefore, we expect that the mean scalar dissipation rate for heat transport $\langle \varepsilon \rangle$ be independent of Ra_t . For this type of systems, it is clear that the standard Darcy model applied to heat transport gives the same conclusions obtained for mixing convection, so we need to consider other porous media model to find a nonlinear scaling of the form $Nu \sim Ra_t^{\gamma}$, with $0 \leq \gamma \leq 1$.

Some studies that analyzed generalized porous media models have shown that mechanical dispersion plays a predominant role in certain regimes (Riaz et al, 2004; Oltean et al, 2004, 2008). Unfortunately, mechanical dispersion is not usually considered within porous media models that describe thermal convection at high-Ra_t regime, therefore its consequences over heat transport under these conditions has received little attention [4] . The Hele-Shaw cells have been used to visualize heat transport in porous media (Cherkaoui and Wilcock, 2001; Babushkin and Demin, 2006; Cooper et al, 2014; Letelier et al, 2016) and their mechanical dispersion tensor is well-known (Oltean et al, 2004, 2008), so it offers a good alternative to generalize the standard Darcy model. Many efforts to derive inertial corrections of the Darcy equation have been reported

[3] In thermal convection, convective flux fluctuates around a mean value when convection reaches a statistical steady regime. There is no the shutdown behaviour observed in mixing convection (Hewitt et al, 2013)

[4] In generalized porous media models, mechanical dispersion appears as a response of the detours due to tortuosity and variable routes of the flow in the porous matrix

in the literature during the last thirty years (Vafai and Tien, 1981; Whitaker, 1986; Auriault, 1987; Rubinstein and Torquato, 1989; Gondret and Rabaud, 1997; Bizon et al, 1997b; Ruyer-Quil, 2001b; Bratsun and Wit, 2004; Oltean et al, 2004), where different governing equations are presented in Appendix A.

In this chapter, we study through numerical simulations a new model which is derived by using regular perturbation theory to Navier-Stokes equations in the slow diffusion approximation, to model Rayleigh-Benard convection in Hele-Shaw geometries. The proposed model allows us to recover asymptotically the standard Darcy model. The main contributions of this article are (a) to derive and present the Hele-Shaw model which naturally incorporates mechanical dispersion and nonlinearities related with the Brinkmann and Forchheimer terms, which appear in extended porous media models, and (b) to show that the incorporation of the mechanical dispersion in Hele-Shaw geometries has important consequences for heat transport at high-Ra_t that are not predicted by the standard Darcy model in the slow diffusion approximation.

7.2 Mathematical model and scalings

We consider a rectangular Hele-Shaw cell filled with an incompresible ambient fluid, which in absence of forcing has density ρ_a and viscosity μ_a at temperature T_a. We assume that the viscosity is constant. The volume of the cell is $L \times H \times b$, where b is the gap of the cell in the $\hat{y}$ direction, H is the height in the $\hat{z}$ direction and L is the width in the $\hat{x}$ direction. The cell is heated from the bottom with constant temperature T_h and cooled from above with constant temperature T_c. When $b \ll H$, the motion of the fluid is described by the two-dimensional gap-averaged equations for the Hele-Shaw model (For further information, see Chapter 5 on page 47)

$$\nabla \cdot \mathbf{u} = 0 \,, \tag{7.2.1}$$

$$\frac{6}{5}\,\rho_a\,\frac{\tilde{\mathcal{D}}\mathbf{u}}{\tilde{\mathcal{D}}t} = -\nabla p - \rho\, g\, \hat{z} - \mu_a\, K^{-1}\mathbf{u} + \frac{6}{5}\,\mu_a\,\nabla^2\mathbf{u} + \frac{2}{35}\frac{K}{\kappa_t}\,(\mathbf{u}\cdot\nabla\rho)\, g\, \hat{z}\,, \tag{7.2.2}$$

$$\frac{\mathcal{D}T}{\mathcal{D}t} = \kappa_t\,\nabla^2 T + \frac{2}{35}\frac{K}{\kappa_t}\,\nabla\cdot\Big[(\mathbf{u}\cdot\nabla T)\,\mathbf{u}\Big]\,, \tag{7.2.3}$$

where $\mathbf{u} = u\hat{x} + w\hat{z}$ is the velocity vector, g is the gravitational acceleration, T is the temperature, $\rho = \rho(T)$ is the density, μ_a is the dynamic viscosity and κ_t is the thermal diffusivity of the fluid. Here, $K = b^2/12$ is the permeability, $\tilde{\mathcal{D}}/\tilde{\mathcal{D}}t = \partial/\partial t + 9/7\,\mathbf{u}\cdot\nabla$ and $\mathcal{D}/\mathcal{D}t = \partial/\partial t + \mathbf{u}\cdot\nabla$. The derivation of this model is discussed in Chapter 5 on page 47. The right hand side of Eqn. (7.2.2) contains the Brinkmann viscous dissipative term $6/5\,\mu\,\nabla^2\mathbf{u}$ (Nield and Bejan, 2006; Breugem and Rees, 2006) and a new scalar buoyant term proportional to $(\mathbf{u}\cdot\nabla\rho)\,g\hat{z}$, which can be important in zones with high density contrast. On the other hand, the right side of Eqn. (7.2.3) is the hydrodynamic dispersion which can be separated in two terms, the diffusive term, $\kappa_t\,\nabla^2 T$, and the mechanical dispersion term, $(2/35)\,(K/\kappa_t)\,\nabla\cdot\left[(\mathbf{u}\cdot\nabla T)\,\mathbf{u}\right]$. The general tensorial form of the hydrodynamic dispersion, according to the Scheidegger's law, is $D_{sr} = \delta_{sr}(\alpha + |\mathbf{u}|\beta) + (\gamma - \beta)\,u_s u_r/|\mathbf{u}|$ (Taylor, 1953; Aris, 1956; Kvernvold and Tyvand, 1981; Ippolito et al, 1994; Riaz et al, 2004; Meybodi and Hassanzadeh, 2011), where $\alpha = \kappa_t$, $\beta = 0$ and $\gamma = (2/35)\,(K/\kappa_t)\,|\mathbf{u}|$.

From Eqns. (7.2.1) to (7.2.3), we define the following appropiate scales for velocity $\bar{u}_c = \Delta\rho\, g\, K/\mu_a$, pressure $p_s = \mu_a\,\bar{u}_c\,H/K$ and time $\tau = H/\bar{u}_c$, which are used commonly in the literature. In addition, we define the following set of dimensionless parameters: the anisotropy ratio $\epsilon = \sqrt{K}/H$, the Prandtl number $Pr = \nu_a/\kappa_t$, the Rayleigh number $Ra_t = \bar{u}_c H/\kappa_t$ and the Peclet number $Pe_t = \epsilon\, Ra_t$. In the literature, $\epsilon^2 = Da$ is also known as the Darcy number and it is a relevant parameter in studies of non-Darcian effects (Nield and Bejan, 2006). When $\epsilon \to 0$, the system of Eqns. (7.2.1) to (7.2.3) is reduced to the standard Darcy model. To make the scalar transport equations dimensionless, we use the following scalings for position $\mathbf{x}' = \mathbf{x}/H$, velocity $\mathbf{u}' = \mathbf{u}/\bar{u}_c$, time $t' = t/\tau$ and temperature $T' = (T - T_a)/\Delta T$, where $\Delta T = T_h - T_c$ is the constant temperature difference between the top and bottom plates.

Since we are interested in analyzing the effects of inertial corrections in the development of convection, we compare heat transport properties of the proposed Hele-Shaw model with published results in the literature (Otero et al, 2004; Hewitt et al, 2012). We study the problem using a numerical code based on spectral methods (*flow_solve*, Winters and de la Fuente (2012)), considering a single fluid phase with constant viscosity and $Pr = 7$, similar to water [5]. In the simulations, we consider ϵ and the aspect ratio of the cell $L' = L/H$ as constant values. Furthermore, we consider periodic boundary conditions in the horizontal direction for all variables and we perturbe the initial

[5] Evidently, for high-Pr numbers, the left hand side of Eqn. (7.2.2) can be neglected in comparison to the Darcy drag term proportional to $\mathbf{u}$

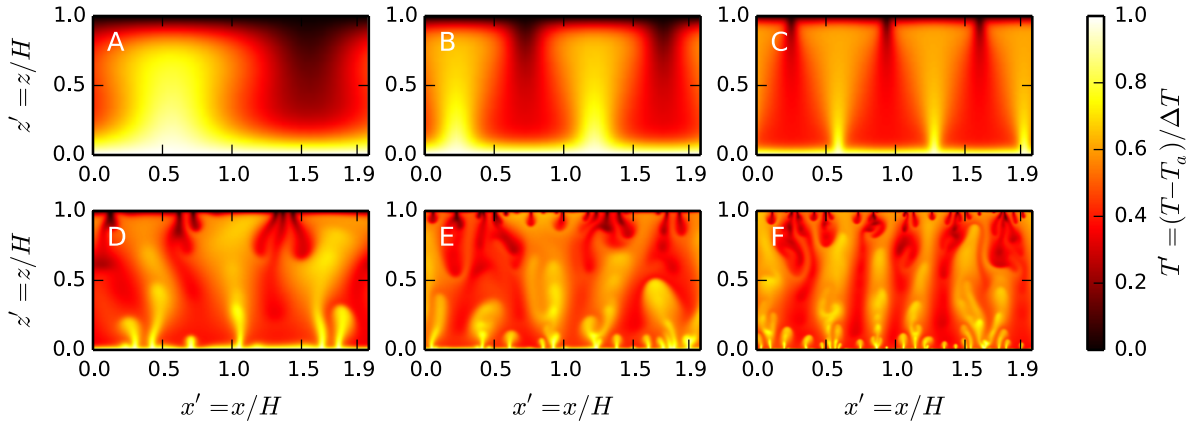

Figure 7.2.1: Numerical simulations of thermal convection using the Hele-Shaw model with cell aspect ratio $L' = L/H = 2$, for $Pr = 7$ and $Pe_t = \sqrt{35/2}$, in order to show the dynamics when $O(\kappa_t \nabla^2 T) \sim O((2/35)(K/\kappa_t)\nabla \cdot [(\mathbf{u} \cdot \nabla T)\mathbf{u}])$, for different ϵ and Ra_t values. (A) unicellular steady convection for $\epsilon = 4.18 \times 10^{-2}$ and $Ra_t = 100$, (B) bicellular steady convection for $\epsilon = 1.32 \times 10^{-2}$ and $Ra_t = 316$, (C) tricellular steady convection for $\epsilon = 4.18 \times 10^{-3}$ and $Ra_t = 1000$. The following panels show unsteady dynamics, (D) for $\epsilon = 1.67 \times 10^{-3}$ and $Ra_t = 2512$, (E) for $\epsilon = 8.35 \times 10^{-4}$ and $Ra_t = 5012$ and finally (F) for $\epsilon = 5.27 \times 10^{-4}$ and $Ra_t = 7943$.

conductive base-state $T = T_s(z) + \theta(\mathbf{x}, t)$, where $T_s(z) = T_a + \Delta T\,(1 - z/H)$ is the conductive regime solution. Moreover, we have $w = 0$, $\hat{z} \cdot \nabla \mathbf{u} = 0$ and $\theta = 0$ in $z = 0$ and $z = H$. Examples of the results from simulations using our Hele-Shaw model are presented in Fig. 7.2.1. In this figure, some features of the temperature distribution are displayed, when diffusion and mechanical dispersion terms are comparables: (A) unicellular steady convection for $\epsilon = 4.18 \times 10^{-2}$ and $Ra_t = 100$, (B) bicellular steady convection for $\epsilon = 1.32 \times 10^{-2}$ and $Ra_t = 316$, (C) tricellular steady convection for $\epsilon = 4.18 \times 10^{-3}$ and $Ra_t = 1000$. The following panels show unsteady dynamics, (D) for $\epsilon = 1.67 \times 10^{-3}$ and $Ra_t = 2512$, (E) for $\epsilon = 8.35 \times 10^{-4}$ and $Ra_t = 5012$ and finally (F) for $\epsilon = 5.27 \times 10^{-4}$ and $Ra_t = 7943$.

7.2.1 Heat transport

To compute the heat transport, we will average the equations over the entire domain. Hence, we consider that the average in the horizontal direction and the domain average of a function $f = f(\mathbf{x}')$ are defined as $\bar{f}(z') = 1/L' \int_0^{L'} f(\mathbf{x}')dx'$ and $\langle f \rangle = \int_0^1 \bar{f}(z')dz'$ respectively, where $L' = L/H$ is the aspect ratio of the cell. Then, heat transport can

be studied by means of the Nusselt number defined as

$$Nu = -\left.\frac{\partial \bar{T}'}{\partial z'}\right|_{z'=0} \tag{7.2.4}$$

The dimensionless form of Eqn. (7.2.3) is

$$\frac{\partial \theta'}{\partial t'} + \mathbf{u}' \cdot \nabla' \theta' - w' = \frac{1}{Ra_t}\left[\nabla'^2 \theta' + \frac{2}{35}\, Pe_t^2\, \nabla' \cdot \left(\left(\mathbf{u}' \cdot \nabla' T'\right) \mathbf{u}'\right)\right] . \tag{7.2.5}$$

Then, the average in the horizontal direction of Eqn. (7.2.5) is

$$\frac{\partial \theta'}{\partial t'} + \frac{\partial}{\partial z'}\left(\overline{w'T'}\right) = \frac{1}{Ra_t}\left[\frac{\partial^2 \theta'}{\partial z'^2} + \frac{2}{35}\, Pe_t^2\, \frac{\partial}{\partial z'}\left(\overline{(\mathbf{u}' \cdot \nabla' T')w'}\right)\right] . \tag{7.2.6}$$

In the steady state regime, we integrate in the vertical Eqn. (7.2.6), obtaining the formula

$$\overline{w'T'} - \langle w'T' \rangle = \frac{1}{Ra_t}\frac{\partial \bar{\theta}'}{\partial z'} + \frac{2}{35}\,\epsilon^2\, Ra_t \left[\overline{w'\nabla' \cdot (T'\mathbf{u}')} - \langle w'\nabla' \cdot (T'\mathbf{u}') \rangle\right] . \tag{7.2.7}$$

Evaluating Eqn. (7.2.7) in $z' = 0$ and regarding that $\partial T'/\partial z' = -1 + \partial \theta'/\partial z'$, we obtain an expression for the Nusselt number given by the formula

$$Nu = 1 + Ra_t \langle w'T' \rangle - \frac{2}{35}\, Pe_t^2 \langle w'\nabla' \cdot (\mathbf{u}'T') \rangle , \tag{7.2.8}$$

which includes the contribution of the mechanical dispersion, relevant for Hele-Shaw geometries under regimes of high-Pe number. The time average of Eqn. (7.2.8) is defined using Eqn. (2.0.4) on page 17. Fig. 7.2.2 shows $\langle Nu \rangle_\tau$ computed using Eqns. (7.2.4) and (7.2.8), for ϵ and Ra_t fixed. Theoretically, both computations must be equal, which is corrobored numerically by this figure. The time average of Eqn. (7.2.8) is important because enables to compute heat transport using averaged global quantities, instead of derivatives evaluated in a boundary.

Fig. 7.2.3 shows the time-averaged $\langle Nu \rangle_\tau$-Ra_t scaling obtained from the numerical simulations which are compared with previously published results, for fixed ϵ, Pr and

L'. In all numerical simulations, we initialize the velocity and temperature fields with the conductive solutions. We have performed two simulation sets, for $\epsilon = 0.01$ and $\epsilon = 0.001$. These values were chosen based on that several experimental studies in Hele-Shaw cells have used ϵ-values within this interval (Elder, 1967c; Cherkaoui and Wilcock, 2001; Cooper et al, 2014; Letelier et al, 2016). For the two simulated ϵ-cases, we observe that the onset of convection is near to the standard Darcy model prediction $Ra_t^{(c)} = 4\pi^2$ (see Eqn. (6.2.56) in Chapter 6, Section 6.2 on page 79). This result is expected since the very small influence of mechanical dispersion and inertial corrections in such Ra_t regime. Furthermore, for $4\pi^2 < Ra_t < 1350$, our results are in agreement with some steady convective rolls states reported in the literature (Nield and Bejan, 2006; Otero et al, 2004; Hewitt et al, 2012). Some examples of steady convective rolls are presented in Fig. 7.2.1. However, beyond the high-Ra_t limit, there is a clear separation of the time-averaged Nu-Ra scaling, which now depends on ϵ. For $\epsilon = 0.01$, we have $\langle Nu\rangle_\tau \sim Ra_t^{0.40\pm0.03}$, so the influence of Pe_t number in the convection is much more appreciable than the case $\epsilon = 0.001$, where $\langle Nu\rangle_\tau \sim Ra_t^{0.90\pm0.03}$. For this last case, the time-averaged $\langle Nu\rangle_\tau$-Ra_t scaling at the high-Ra_t regime is similar to the standard Darcy model prediction, *i.e.*, $\langle Nu\rangle_\tau \sim Ra_t$ (Otero et al, 2004). Evidently, mechanical dispersion effects reduce heat transport, because it tends to homogenize the temperature field.

7.2.2 The role of mechanical dispersion

If $i = x, z$ and $j = x, z$, Eqn. (7.2.3) can be written as

$$\frac{\partial T'}{\partial t'} + \partial_j \Pi_j = \partial_i \Big[\mathcal{D}_{ij}\, \partial_j T' \Big] \quad ; \quad \mathcal{D}_{ij} = \frac{1}{Ra_t}\,\delta_{ij} + \frac{2}{35}\,\epsilon^2 Ra_t\, \bar{u}_i'\, \bar{u}_j' \,, \tag{7.2.9}$$

where $\Pi_j = \bar{u}_j' T'$ is the convective heat flux in j-direction, $\partial_j \Pi_j$ is the convective heat flux density (scalar) and $\mathcal{D}_{ij}$ is the hydrodynamic dispersion tensor. Now, consider the term $\Phi_i = \bar{u}_i'\, \bar{u}_j'\, \partial_j T'$. Using the equation $\partial_i\, \bar{u}_i' = 0$, we obtain $\Phi_i = \bar{u}_i'\, \partial_j (\bar{u}_j' T') = \bar{u}_i'\, \partial_j \Pi_j$, so we can see that Φ_i is also a flux in i-direction. In particular, $\Phi_z = w'\, \nabla' \cdot (\mathbf{u}' T')$ can be interpreted as the "vertical flux of the convective heat density". The Hele-Shaw cell is a 3D geometry, where heat flux can also be transported in y-direction. But, since $O(y) \ll O(z)$, we can reduce the governing equations to a quasi-2D model, where the perturbative 3D effects in the scalar transport are captured by the flux density $\partial_i \Phi_i$, *i.e.*, the mechanical dispersion, which causes additional mixing.

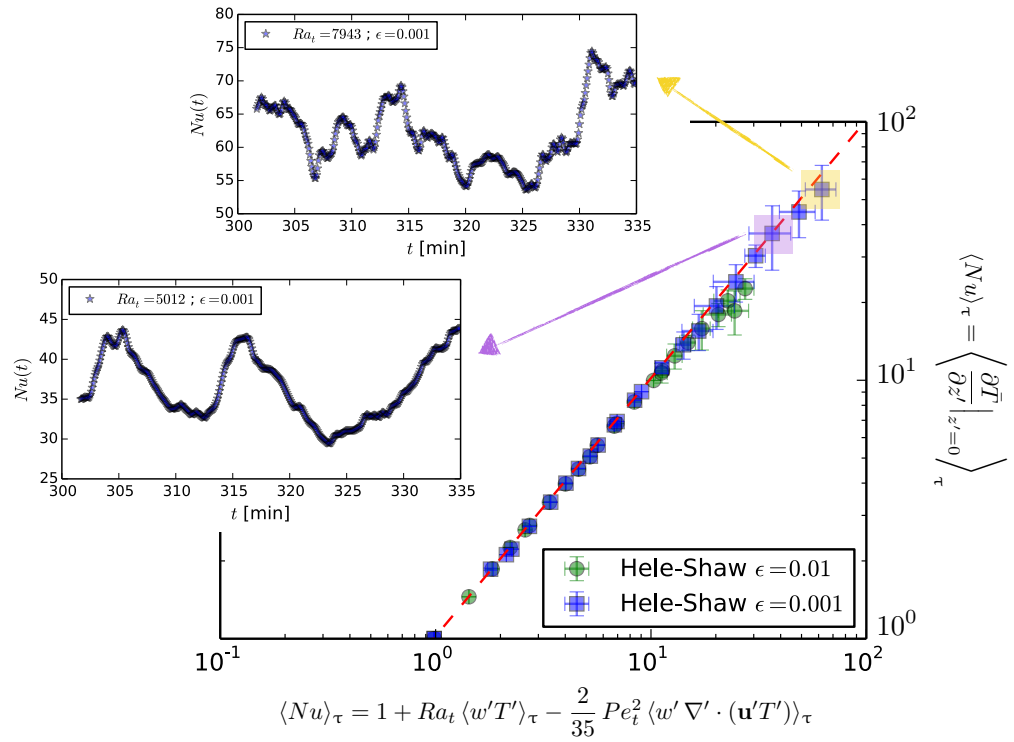

Figure 7.2.2: $\langle Nu \rangle_\tau$ computed using Eqns. (7.2.4) and (7.2.8). For each point, Ra_t has a specific value. Theoretically, global heat transport computed by these formulas must be equal, which is demonstrated in this figure. The dashed red straigh line has a slope equal to one. The inset plots show Nu as function of time for two different points with specific Ra_t and ϵ values

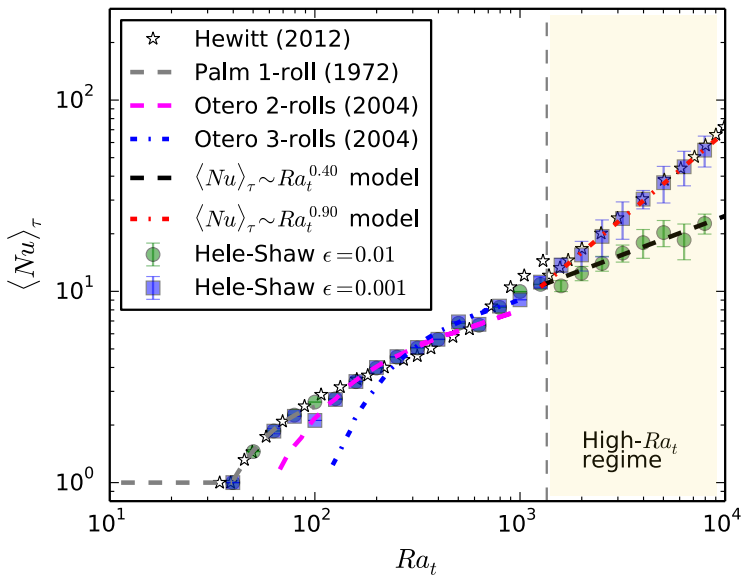

Figure 7.2.3: Time-averaged $\langle Nu \rangle_\tau$ as function of Ra, for $Pr = 7$ and $L' = 2$. For $Ra_t \leq 1350$, the Hele-Shaw simulations are consistent with previously published results. However, for $Ra > 1350$, there is a deviation from the Darcy high-Ra_t regime which depends on $\epsilon = \sqrt{K}/H$. It is clear that when ϵ is very small, the simulations of the Hele-Shaw model give similar results to the predictions of the standard Darcy model at high-Ra_t regime. The error bars are amplified by a factor two, for visualization purposes

In porous media, it is well known that mechanical dispersion appears as a response of the detours due to tortuosity and variable routes of the flow in the porous matrix, as example. In our case, mechanical dispersion appears due to the existence of a third confined spatial dimension. Therefore, the importance of $\Phi_z = w' \nabla' \cdot (\mathbf{u}' T')$ is focused on the capturing of the effects of the gap of the cell in scalar transport.

Eqn. (7.2.9) can be written as

$$\frac{\partial T'}{\partial t'} + \partial_i \left(\Pi_i - \frac{2}{35} \epsilon^2 Ra_t \, \Phi_i \right) = \frac{1}{Ra_t} \nabla'^2 T' \,, \tag{7.2.10}$$

where we can define a net heat flux Ψ_i in i-direction as

$$\Psi_i = \Pi_i - \frac{2}{35} \epsilon^2 Ra_t \, \Phi_i \,. \tag{7.2.11}$$

Eqn. (7.2.9) represents the competition of two process, heat transport and mixing. In particular, Π_z represents the vertical heat flux, which can be interpreted as the advection of a fluid parcel with constant temperature T', but Φ_z can be interpreted as the advection of a fluid parcel that continuosly exchange heat with the surrounding fluid, so the fluid parcel is mixing with other parcels, reaching intermediate temperatures. The net effect of that is the decrease of global heat transport, due to the minus sign in Ψ_z. It is important to note that the domain average of Ψ_z is equal to the convective flux $\mathcal{F}$.

7.2.3 Scalar dissipation rate

Fluid mixing can be studied by observing the temporal evolution of the mean scalar dissipation rate, denoted as $\langle \varepsilon \rangle_\tau$ (Jha et al, 2011b; Hidalgo et al, 2012; Jha et al, 2013; Pramanik and Mishra, 2015). In the context of mixing convection, *i.e.*, $\varphi = S_w$, dimensional analysis and direct numerical simulations show that the standard Darcy model lead to mean scalar dissipation rates that are independent of Ra_s (Hidalgo et al, 2012; Jenny et al, 2014), which is in agreement with the hypotheses of constant dissolution flux in porous media at high-Ra_s regime. However, experimental results of mixing convection using Hele-Shaw cells report that there exists a nonlinear scaling of Nu_s with Ra_s (Neufeld et al, 2010; Hidalgo et al, 2012). Therefore, to study the same

problem in heat transport, we define the mean thermal (scalar) dissipation rate as (see Eqn. (5.4.6) in Chapter 5, Section 5.4 on page 61)

$$\langle \varepsilon_t \rangle = \frac{1}{Ra_t} \left[\langle ||\nabla' \theta'||^2 \rangle + \frac{2}{35} Pe_t^2 \langle (\nabla' \cdot (\mathbf{u}' \theta'))^2 \rangle \right], \tag{7.2.12}$$

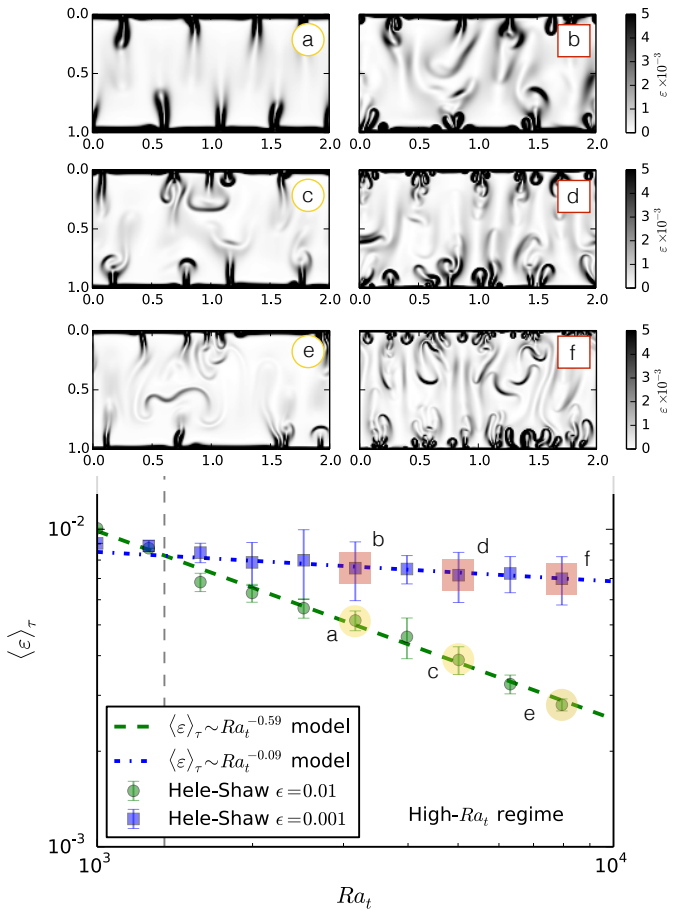

Figure 7.2.4: Time-averaged mean thermal dissipation rate $\langle \varepsilon \rangle_\tau$ as function of Ra_t in the high-Ra_t number regime, for $Pr = 7$ and $L' = 2$. While the classical Darcy-Boussinesq model predicts that $\langle \varepsilon \rangle_\tau$ is independent of Ra_t, our model shows that $\langle \varepsilon \rangle_\tau$ exhibits a nonlinear scaling with Ra_t that depends on ϵ values. For $\epsilon = 0.01$, we have $\langle \varepsilon \rangle_\tau \sim Ra_t^{-0.59 \pm 0.03}$, while for $\epsilon = 0.001$ we have $\langle \varepsilon \rangle_\tau \sim Ra_t^{-0.09 \pm 0.01}$. Inset plots (a), (c) and (e) show $\varepsilon(\mathbf{x})$ for $\epsilon = 0.01$ and $Ra_t = 3162$, $Ra_t = 5012$ and $Ra_t = 7943$, respectively, while inset plots (b), (d) and (f) show $\varepsilon(\mathbf{x})$ for $\epsilon = 0.001$ and $Ra_t = 3162$, $Ra_t = 5012$ and $Ra_t = 7943$, respectively. In comparison with the inset plots (a), (c) and (e), it is clear that in the inset plots (b), (d) and (f) there are more regions that are actively mixed, which coincides with the visualization of more edges. This behaviour observed in the inset plots (b), (d) and (f) is due to the influence of the porous media drag term $\mu_a K^{-1} \mathbf{u}$ when $\epsilon \ll 1$, which increases shear effects. The error bars are amplified by a factor two, for visualization purposes

The physical meaning of Eqn. (7.2.12) is the quantification of the evolution in time of the mixing lenght of the flow in homogeneous (Hidalgo et al, 2012; Pramanik and Mishra, 2015) and heterogeneous porous media (Le Borgne et al, 2011). If $\epsilon \to 0$, we have $Pe_t \to 0$ and therefore we obtain $\langle \varepsilon \rangle = (1/Ra_t) \langle ||\nabla' \theta'||^2 \rangle$, which has been studied in previous works (Hidalgo et al, 2012; Pramanik and Mishra, 2015). Because energy is constantly injected through the boundaries and dissipated by the flow, the analysis of the time-averaged mean thermal dissipation rate gives more evidence of the importance of dispersion for convection. Any power-law dependence of $\langle Nu \rangle_\tau$ with Ra_t will be

reflected also in this quantity (Hidalgo et al, 2012). Fig. 7.2.4 shows the time-averaged $\langle\varepsilon\rangle_\tau$-$Ra_t$ scaling at high-Ra_t number regime. In situations where dispersion is dominant, thermal dissipation can be unfavoured due to the homogenization of the temperature. This situation is displayed in the inset plots of Fig. 7.2.4, which show regions that are actively mixed. These regions are effective shear zones identified as edges of thermal plumes. The inset plots (a), (c) and (e) show cases where dispersion is dominant, presenting a low density of edges in contrast with inset plots (b), (d) and (f), where dispersion is negligible and the Darcy drag term $\mu_a K^{-1}\mathbf{u}$ is dominant. For $\epsilon = 0.001$ we have $\langle\varepsilon\rangle_\tau \sim Ra_t^{-0.09\pm0.01}$, which is not surprinsing since this case is similar to the standard Darcy model prediction for mixing convection. In the asympthotic case $\langle Nu\rangle_\tau \sim Ra_t$, the time-averaged $\langle\varepsilon\rangle_\tau$ is independent of Ra_t. However, a new result is obtained for $\epsilon = 0.01$, where we have $\langle\varepsilon\rangle_\tau \sim Ra_t^{-0.59\pm0.03}$. In this case, the dispersive effects have consequences in the flow, allowing a better thermal homogenization of the fluid. This result provides more conclusive evidence of the importance of the mechanical dispersion in thermal convection in porous media.

From Eqn. (7.2.3), in the steady state regime and applying the boundary conditions used in this letter, it is easy to show that the global heat transport and mean scalar dissipation rate are related by the expression $\langle Nu\rangle_\tau = Ra_t\,\langle\varepsilon\rangle_\tau$. Fig. 7.2.5 shows that our numerical results are in good agreement with the theoretical prediction, in contrast to previous results reported for mixing convection (Hidalgo et al, 2012).

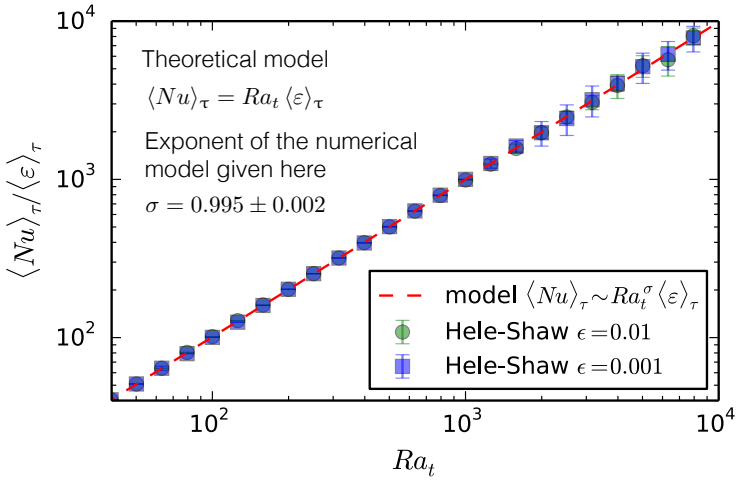

Figure 7.2.5: Relation between $\langle Nu\rangle_\tau$ and $\langle\varepsilon\rangle_\tau$. Our numerical results satisfies the theoretical relation $\langle Nu\rangle_\tau = Ra_t\,\langle\varepsilon\rangle_\tau$. The error bars are amplified by a factor two, for visualization purposes

In summary, by using asymptotic regular expansions to the Navier-Stokes equations to model the dynamics of flow in a Hele-Shaw cell, we present a two-dimensional Hele-Shaw model and the hydrodynamic dispersion for this type of confined geometry.

This model considers the Brinkmann term, proportional to $\mu\,\nabla^2\mathbf{u}$, and a new buoyant term, proportional to $(\nabla\rho\cdot\mathbf{u})\,g\hat{z}$, which has not been incorporated in previous works. The application of the model for the case studied in this letter shows new scalings for the time-averaged Nusselt number and mean thermal dissipation rate. In Darcian regimes, we show based on numerical simulations that $\langle\varepsilon\rangle_\tau$ is independent of Ra_t, as we expected, while for regimes dominated by mechanical dispersion, we obtain a scaling of the form $\langle Nu\rangle_\tau \sim Ra_t^\gamma$, with $0 \leq \gamma \leq 1$, which is reflected in the mean thermal dissipation rate $\langle\varepsilon\rangle_\tau \sim Ra_t^{\gamma-1}$. The exponent γ depend on the values of ϵ.

An interesting future work, which is in progress, is related with the relation $\langle Nu\rangle_\tau = Ra_t\,\langle\varepsilon\rangle_\tau$ and its application to mixing convection, *i.e.*, $\varphi = S_w$. If φ is a generic scalar, then we want to demonstrate that the expression $\langle Nu_\varphi\rangle_\tau = \Phi(\epsilon, Ra_\varphi)\,Ra_\varphi\,\langle\varepsilon_\varphi\rangle_\tau$ is valid for scalar transport in homogeneous porous media, where Φ is a function that contains information about boundary conditions, mixture dynamics and geometry (See Eqn. (5.4.11) on page 63 for additional information). When $\varphi = T$, with periodic boundary conditions in the horizontal direction, then $\Phi = 1$.

Part IV

Visualization and image analysis

Chapter 8

Optical density visualization methods

As part of this thesis, we conducted two experiments to illustrate the main features of scalar transport processes in Hele-Shaw cells. We used analogue fluids that reasonably represent the processes that happen within a geothermal reservoir. These experiments were

- Thermal convection in porous media (Chapter 10 on page 127)
- Mass transport by fluid mixing (Chapter 11, Section 11.1 on page 145)

Next, we discuss briefly the Hele-Shaw geometry and the optical techniques used in these experiments.

8.1 The Hele-Shaw geometry

Hele-Shaw cells are a fairly good representation of an homogeneous porous media. As is discussed in Chapter 5 on page 47, Hele-Shaw cells allow us to visualize scalar transport phenomena which would be difficult to observe using a real porous matrix. However, its quasi-2D geometry strongly restricts the applicability to real cases, limiting its use only for academic purposes related with the physical understanding of diverse porous media phenomena.

The Hele-Shaw geometry notation used in the experiments is shown in Fig. 8.1.1. We have defined two important regions, the cell gap or confined z-direction and the $x - y$ Hele-Shaw plane.

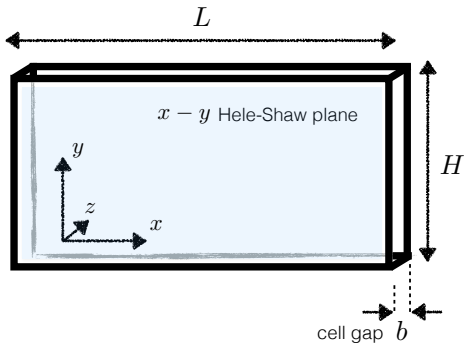

Figure 8.1.1: The Hele-Shaw geometry used in the experiments

All the illustrations and equations used for data treatment follows the geometry defined in Fig. 8.1.1. Mass transport and thermal convection are visualized by means of light attenuation and quantitative Schlieren techniques, respectively, which are discussed on next.

8.2 Visualization by light attenuation

Light attenuation is a very useful method for the visualization of scalar transport in Hele-Shaw cells. The method is based in the absorption of light intensity due to a dye dissolved in the working fluid. The most simple model that explains the absorption features is the Lambert-Beer law

$$-\log\frac{B_r}{B_i} = \bar{\varepsilon}\, b\, \bar{c} \quad ; \quad \bar{c}(\mathbf{x},t) = \frac{1}{b}\int_0^b c(\mathbf{x},z,t)\, dz\ , \tag{8.2.1}$$

where B_r is the total intensity received in the sensor, B_i is the initial total intensity from the light source, $\bar{\varepsilon}$ is a global property of the absorption, b is the path length along the cell gap and $\bar{c}$ is the dimensionless averaged concentration of solution along the path, with $\mathbf{x}$ the position in the Hele-Shaw cell plane and t the time (in many cases, related with the camera time exposure). However, a more complete model of light attenuation applied to Hele-Shaw cells must consider light transmission properties of each physical medium where light can travel, including the CMOS Bayer filter transmission (for coloured images). Such model is written as (**?**)

$$B_r = \int_0^\infty I_r(\lambda)\, d\lambda = \int_0^\infty \mathcal{T}_g^2(\lambda)\, \mathcal{T}_l(\lambda)\, \mathcal{T}_{sf}(\lambda)\, I_i(\lambda)\, e^{-\varepsilon(\lambda)\, b\, \bar{c}(\mathbf{x},t)}\, d\lambda\ . \tag{8.2.2}$$

The total intensity detected by CMOS sensor can be written as $L_r = B_r^\alpha$, where α is a parameter that considers the nonlinear response of CMOS sensors and, therefore, must be determined experimentally. Furthermore, in Eqn. (8.2.2) we have that $\mathcal{T}_g$, $\mathcal{T}_l$ and $\mathcal{T}_{sf}$ are the transmissivity of optical acrilic, camera lens and CMOS Bayer filter, respectively. Fig. 8.2.1 shows a schematic picture of a light attenuation experiment using both Hele-Shaw cells and the application of the Lambert-Beer law.

A useful hypothesis for the evaluation of Eqn. (8.2.2) is that the transmissivities of acrilic and lens are independent of wavelenght. Then, Eqn. (8.2.2) can be written as

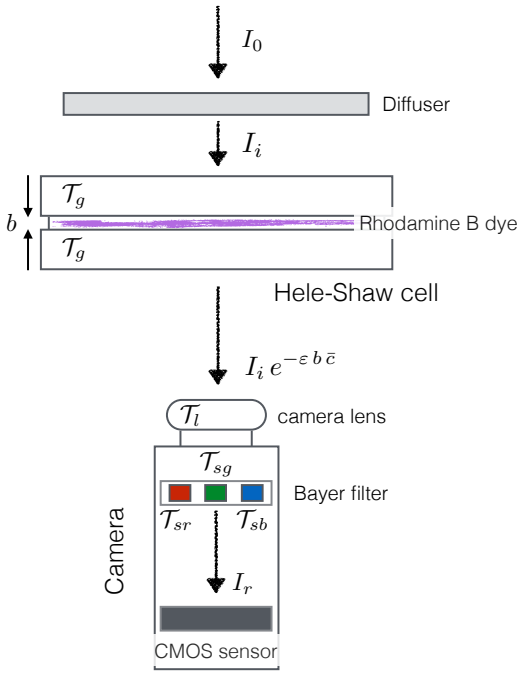

Figure 8.2.1: Hele-Shaw experimental setup for scalar transport visualization using light attenuation. An incoming light of intensity $I_0(\lambda)$ is initially diffused, obtaining light of intensity $I_i(\lambda)$. Light rays travel across the cell gap, where there is Rhodamine B dissolved in the fluid ambient with a concentration of the order of 1×10^{-5} g/cm^3. Due to attenuation, light rays leave the cell with intensity $\mathcal{T}_g^2(\lambda)\, I_i(\lambda)\, f(\lambda)$, where f is the attenuation function. Finally, light comes to CMOS sensor after having crossed the camera lens and the Bayer filter, so the final light intensity is $I_r(\lambda) = \mathcal{T}_g^2(\lambda)\, \mathcal{T}_l(\lambda)\, \mathcal{T}_{sf}(\lambda)\, I_i(\lambda)\, f(\lambda)$

$$\frac{B_r}{B_{r,0}} = \left[\int_0^\infty \mathcal{T}_{sf}(\lambda)\, I_i(\lambda)\, e^{-\varepsilon(\lambda)\, b\, \bar{c}(\mathbf{x},t)}\, d\lambda \right] \Big/ \left[\int_0^\infty \mathcal{T}_{sf}(\lambda)\, I_i(\lambda)\, d\lambda \right], \tag{8.2.3}$$

where $B_{r,0}$ is the total intensity received when $\bar{c} = 0$. Therefore, the aplicability of Eqn. (8.2.3) is restricted to previously known spectral characteristics of $\mathcal{T}_{sf}(\lambda)$, $I_i(\lambda)$ and the attenuation function $f(\lambda) = \exp\left[-\varepsilon(\lambda)\, b\, \bar{c}\right]$, measured using a spectrophotometer.

Eqn. (8.2.3) is a generalized version of Lambert-Beer law given in Eqn. (8.2.1). To illustrate that, we will present an academic case following the work done by Oltean et al (2004). Suposse that the diffused light I_i is red and dye is blue. Then, to obtain a high image contrast, we select the red channel of the Bayer filter. The spectral features will be modeled as follows

$$I_i = \exp\left[-\frac{\left(\lambda - \mu_\lambda^{(1)}\right)^2}{2\sigma_1^2} \right] \quad ; \quad f = 1 - \mathcal{A}\, \exp\left[-\frac{\left(\lambda - \mu_\lambda^{(2)}\right)^2}{2\sigma_2^2} \right], \tag{8.2.4}$$

$$\mathcal{T}_{sr} = \frac{1}{2}\, \exp\left[-\frac{\left(\lambda - \mu_\lambda^{(3)}\right)^2}{2\sigma_3^2} \right] \Big(1 + \tanh(\lambda_3 - \lambda)\Big) + \frac{1}{2}\left[\frac{5}{2} - \frac{1}{400}\, \lambda \right] \Big(1 + \tanh(\lambda - \lambda_3)\Big), \tag{8.2.5}$$

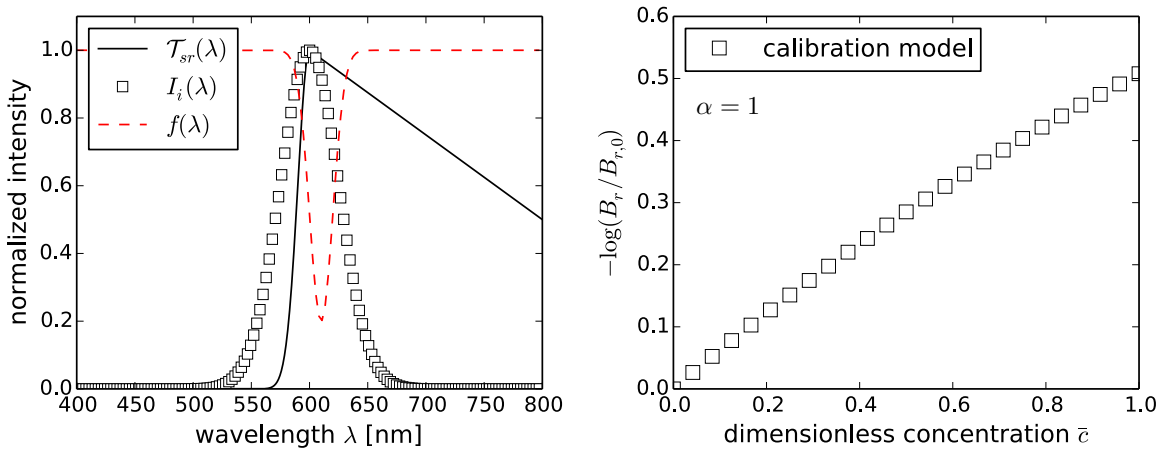

Figure 8.2.2: Spectral characteristics of $\mathcal{T}_{sf}(\lambda)$, $I_i(\lambda)$ and $f(\lambda)$ functions, modeled by Eqns. (8.2.4) and (8.2.5), and the application of Eqn. (8.2.3) for different values of $\bar{c}$. The right image is the Lambert-Beer law for $\alpha = 1$

where $\mu_\lambda^{(1)} = \mu_\lambda^{(3)} = \lambda_3 = 600$ nm, $\mu_\lambda^{(2)} = 610$ nm, $\sigma_1 = 25$ nm, $\sigma_2 = 10$ nm and $\mathcal{A} = 0.8$. The left image of Fig. 8.2.2 shows the result of the spectral modeling. Using these models in Eqn. (8.2.3), for $\alpha = 1$ we obtain the calibration curve shown in the right image of Fig. 8.2.2, which is the Lambert-Beer law. This curve allow us to obtain the physical picture of the scalar transport in terms of the dimensionless concentration only comparing each colored pixel with the corresponding $\bar{c}$ value. For visualization purposes, it is enough to take photographs of solutions and then compute the ratio $B_r/B_{r,0}$.

8.3 Synthetic Schlieren

The Synthetic Schlieren (SS) method is a non-intrusive, optical density visualization technique in fluid mechanics that measures the optical refractive index gradients of a test fluid by means of the quantification of the deflections of the light rays that come from a background image (Dalziel et al, 2000).

The SS equation, in the simplified one-dimensional problem, can be obtained minimizing the optical length functional (Kumar and Muralidhar, 2012)

$$F[y] = \int_0^L n(y)\sqrt{1+\left(\frac{dy}{dz}\right)^2}\,dz\,, \tag{8.3.1}$$

where $y = y(z)$ is the vertical deflection of the light ray in function of the horizontal

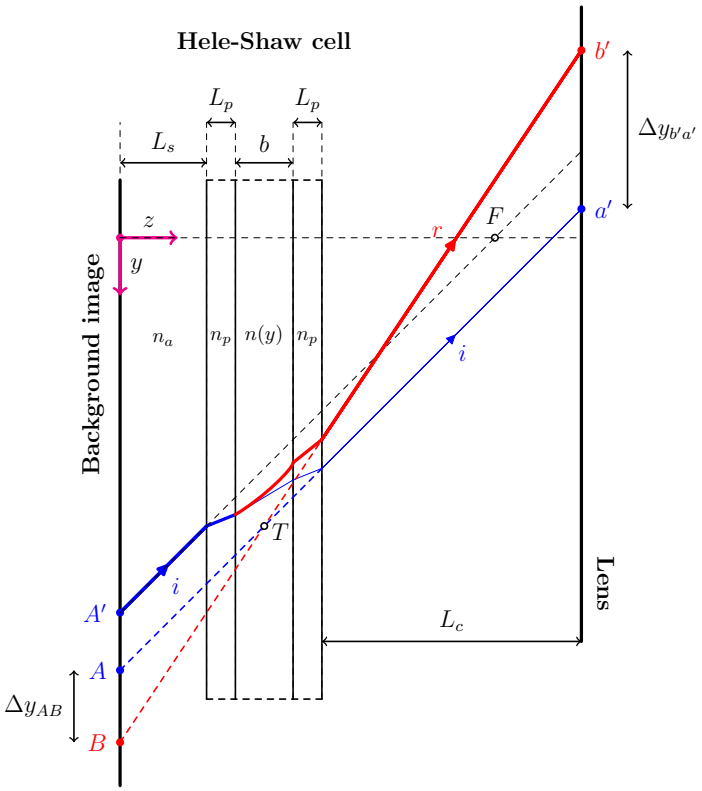

Figure 8.3.1: Light ray deflection due to a variable optical refractive index $n(y)$. The optical system is a Hele-Shaw cell made of acrylic. There are three physical media where light rays can travel, air, acrylic and the test fluid, with optical refractive index n_a, n_p and $n(y)$ respectively. The points F and T are the focal length of the lens and the intersection of the apparent (incident, dashed blue line) and refracted (dashed red line) light rays

variable z, as shown in Fig. 8.3.1, and $n = n[y(z)]$ is the optical refractive index of the fluid, which depends on space. The Euler-Lagrange equation associated with Eqn. (8.3.1) is

$$n(y)\,\frac{d^2y}{dz^2} = \left[1 + \left(\frac{dy}{dz}\right)^2\right]\frac{dn}{dy}\,, \tag{8.3.2}$$

which boundary conditions are associated with the physical problem to be solved. We assume that the optical system satisfies the paraxial approximation $dy/dz \ll 1$. If n is constant, the solution of Eqn. (8.3.2) is a straigh line $y(z) = y_i - z\,\tan\phi_i$, where $\tan\phi_i$ is the angle of the incident light ray. In a more general case, assuming that $n[y(z)] = n_f - n'[y(z)]$, where n_f is the reference refractive index of the fluid at temperature T_0, $n' \ll n_f$ and dn'/dy varies slowly with coordinate y, the solution of Eqn. (8.3.2) is

$$y(z) = y_i - z\,\tan\phi_i - \frac{1}{2n_f}\,\frac{dn'}{dy}\,z^2\,. \tag{8.3.3}$$

The paraxial approximation is satisfied when $\phi_i \leq 10°$. In such case, $\tan\phi_i \sim \phi_i$ is valid within an accuracy of 1%. From Fig. 8.3.1, reconstructing the light ray trajectory

from A' to a', we have

$$y_{a'} = y_{A'} - L_s\,\alpha - 2\,L_p\,\frac{n_a}{n_p}\,\alpha - b\,\frac{n_a}{n_f}\,\alpha - L_c\,\alpha\,, \tag{8.3.4}$$

where n_a, n_p and n_f are the optical refractive index for air, acrylic and the test fluid reference, respectively, and α is the incident paraxial angle in the position A'. This result is satisfied by a light ray that comes from the background image, when the system is unperturbed. Finally, reconstructing the light ray trajectory from A' to b' and defining the apparent displacement on the lens position $\Delta y_{a'b'} = y_{a'} - y_{b'}$, we obtain the well-known SS formula (Dalziel et al, 2000)

$$\Delta y_{a'b'} = \frac{b}{n_f}\,\frac{dn'}{dy}\left[\frac{1}{2}\,b + \frac{n_f}{n_p}\,L_p + \frac{n_f}{n_a}\,L_c\right], \tag{8.3.5}$$

where the angle of deflection ε, formed by the incident and the refracted light rays (see Fig. 8.3.2), is defined as

$$\varepsilon = \frac{b}{n_a}\,\frac{dn'}{dy}\,. \tag{8.3.6}$$

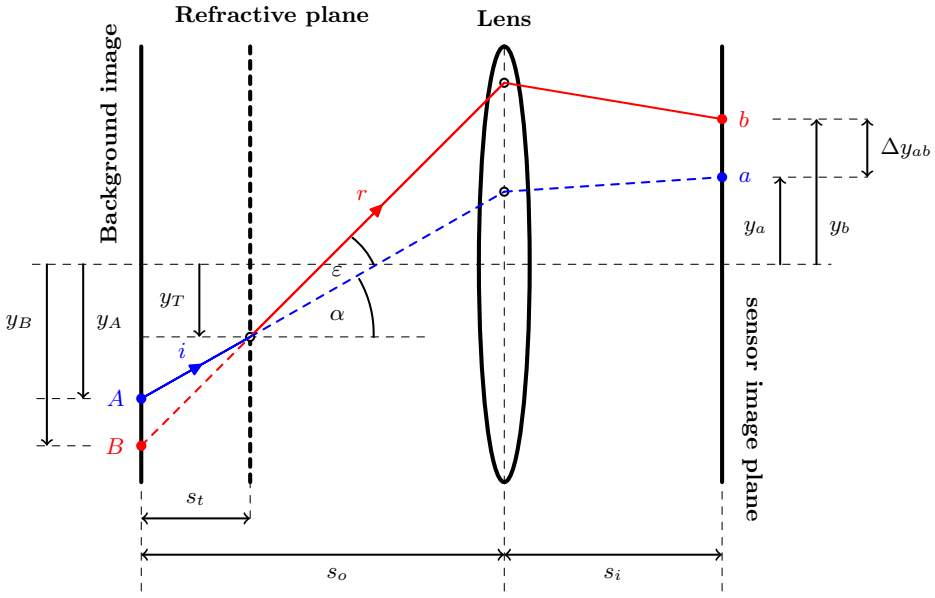

Figure 8.3.2: Synthetic Schlieren experiment setup. The image is a one dimensional representation, where $\Delta y_{ba} = (\Delta x, \Delta y)$. The deflection angle ε is the angle between the refracted and the incident light rays (Gojani et al, 2013)

Finally, using geometric operations, we obtain the apparent displacement on the background image $\Delta y_{AB} = y_B - y_A = s_t\,\varepsilon$, where s_t is the parallel distance to the optical axis between the background image and the intersection point of the light rays perturbed and unperturbed, as shown in Fig. 8.3.2, which is defined as

$$s_t = \frac{n_a}{n_f}\left[\frac{1}{2}\left(\frac{2n_f}{n_a} - 1\right) b + \frac{n_f}{n_p}\left(\frac{2n_p}{n_a} - 1\right) L_p + \frac{n_f}{n_a} L_s\right] .$$

This distance defines an effective refractive plane where light rays are deflected by local changes of the optical refractive index.

Let $M = s_i/s_o$ be the lens magnification. Using the thin lenses law, we have $M = f/(s_o - f)$, where f is the focal length and s_o is the distance between the background image and camera, so the apparent displacement measured in the plane of the image sensor is $\Delta y_{ab} = M\Delta y_{AB}$. Replacing these relations in the definition of Δy_{AB}, we obtain

$$\varepsilon = \frac{\Delta y_{ab}}{M s_t} , \tag{8.3.7}$$

recovering the definition of the angle of deflection ε proposed by Gojani et al (2013), in the context of image recording using the Background-Oriented Schlieren (BOS) technique. In general, the SS and BOS techniques quantify a scalar property of the fluid, such as the density ρ, which depends of the thermodynamic variables through a constitutive equation. For example, if the fluid is air, then the Gladstone-Dale model and the ideal gas equation are applied successfully when BOS is used (Richard and Raffel, 2001). In our experiments, a Hele-Shaw cell filled with pure PPG is heated from below and cooled from above with constant temperature difference $\Delta T = T_{bot} - T_{top}$. Then, a constitutive equation $n = n(T)$ is necessary to reconstruct the thermal dynamics, so the equation to solve is

$$\frac{dn'}{dy} = \frac{n_a}{b}\,\varepsilon(y) , \tag{8.3.8}$$

which constitutes the mathematical formulation for the simplified one-dimensional model. If the deflection of the light ray has two-dimensional components, given by $\vec{\varepsilon} = \varepsilon_x\,\hat{x} + \varepsilon_y\,\hat{y}$, the equations for the angles of deflection are

$$\varepsilon_x = \frac{\Delta x\,(s_0 - f)}{f\,s_t} \quad , \quad \varepsilon_y = \frac{\Delta y\,(s_0 - f)}{f\,s_t} , \tag{8.3.9}$$

where Δx and Δy are the spatial deflections in the plane of the image sensor. Traditionally, these deflections are estimated from classical PIV algorithms (Tokgoz et al, 2012) or optical flow estimation, where the Lucas-Kanade (Lucas and Kanade, 1981), Horn-Shunck (Horn and Schunck, 1981) and Brox (Brox et al, 2004) algorithms have been applied to experimental images giving satisfactory results (Atchenson et al, 2009). Here, we show that it is possible to enhace the detection of deflections by using OpFlow. Finally, Eqn. (8.3.8) is extended to the vector model $\nabla n' = n_a \vec{\varepsilon}(\mathbf{x})/b$, where taking the divergence on both sides of equation, we obtain the Poisson equation for SS-BOS techniques

$$\nabla^2 n' = \frac{n_a}{b} \nabla \cdot \vec{\varepsilon}(\mathbf{x}) \,, \tag{8.3.10}$$

with Neumann boundary conditions $\hat{x} \cdot \nabla n' = 0$ in $x = 0$ and $x = L$, in addition to the Dirichlet boundary conditions which are $n'(y = 0) = n'_{bot}$ and $n'(y = H) = n'_{top}$. Eqn. (8.3.10) will be used to reconstruct the temperature inside a Hele-Shaw cell for $Ra = 680$, which is presented in Chapter 10, Section 10.5 on page 138. To solve Eqn. (8.3.10), we implement the Red-Black SOR-Chebyshev method (Press et al, 2007) using OpenMP libraries.

Chapter 9

Image processing methods

The aim of this chapter is to present an image segmentation method that can be able to compute the perimeter and area of mixing as function of time, as well as a variational technique that detects small displacements of fluid parcels due to convective phenomena. The measurement of the area is useful to determine the mass transfer, while the perimeter quantification is ideal to determine the interfacial dynamics. On the other hand, the detection of small displacements of fluid parcels is essential to compute dynamic quantities such as velocity or scalar concentration as functions of time. Next, we present two image methods used widely in applied mathematics, but unfortunately have received little attention in physical aplications.

9.1 Multiphase image segmentation

Image segmentation means to split a digital image in many meaningful parts or objects. Therefore, the detection of edges is the most important problem in segmentation. Motivated by the quantification of mixing properties of density-driven convection from our experiments, we are interested in apply active contours to find some geometric properties of these edges and the regions that are defined by them. Fig. 9.1.1 shows an illustrative result of a density-driven convection experiment using the light attenuation technique.

The basic idea of active contours is following the evolution in time of a mathematical curve until detecting meaningful objects within an image f. To do this, classical models of active contours use edge detection methods based on the computation of the gradient of the image, which controls the evolution of the curve. Let Ω be an open bounded subset in $\mathbf{R}^2$, with boundary $\partial\Omega$. Let $f : \bar{\Omega} \to \mathbf{R}$ be an image and $\psi : [0,1] \to \mathbf{R}^2$ be a parametrized curve. Classical models minimize functionals of the type (Kass et al, 1988)

$$J[\psi] = \alpha \int_0^1 |\psi'(s)|\, ds + \beta \int_0^1 |\psi''(s)|^2\, ds - \lambda \int_0^1 |\nabla f(\psi(s))|\, ds\,, \tag{9.1.1}$$

where α, β and λ are positive parameters. The first two parameters of Eqn. (9.1.1) control the smoothness of the contour, while the third term attracs the contour towards

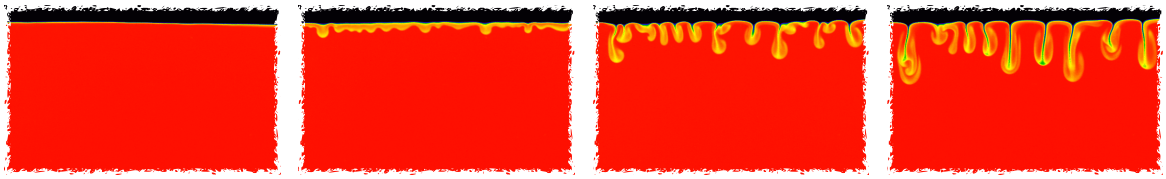

Figure 9.1.1: Dynamics observed in a density-driven convection experiment, where a fluid A (black) is mixed with a fluid B (red). The computation of the mixing length gives important information about the fluid dynamics in a porous medium.

the boundary of objects in the image. The minimization of Eqn. (9.1.1) implies that the segmentation contour must be in zones where $|\nabla f|$ is maximum.

9.1.1 Chan-Vese model

Since that active contours are not accurate when the image f is noisy, Chan and Vese (2001) proposed a model of active contours that is not based on the image gradient as the methodology to detect edges. They studied a particular case of the known Mumford-Shah segmentation model (Mumford and Shah, 1989). The Mumford-Shah functional is given by the expression

$$J_{MS}[u,\psi] = \mu\,\mathcal{L}(\psi) + \lambda \int_{\Omega} |f(\mathbf{x}) - u(\mathbf{x})|^2\, dA + \int_{\Omega\backslash\psi} |\nabla u(\mathbf{x})|^2\, dA\,, \tag{9.1.2}$$

where $\mu, \lambda > 0$, $\mathbf{x} = x\,\hat{x} + y\,\hat{y}$ and $dA = dx\,dy$. The function $u(\mathbf{x})$ is an approximation of the image $f(\mathbf{x})$, which is obtained minimizing Eqn. (9.1.2) with $\psi(\mathbf{x})$ a set of curves where $u(\mathbf{x})$ can be discontinuous. The first term of the right hand side of Eqn. (9.1.2) ensures the regularity of $\psi(\mathbf{x})$ through the definition of the curve length $\mathcal{L}(\psi)$ using the Haussdorf measure, while the second term represents the accuracy of the approximation. Finally, the third term ensures that $u(\mathbf{x})$ be differentiable inside the region $\Omega\backslash\psi$. In general, the algorithms that solve Eqn. (9.1.2) are complicated and costly in computational resources.

The simplification proposed by Chan y Vese to the Mumford-Shah model consists in restricting the functional $J_{MS}[u,\psi]$ to a set of functions $u(\mathbf{x})$ that are constant and continuous by parts. Thereby, we define an open subset $\omega \subset \Omega$ and its boundary

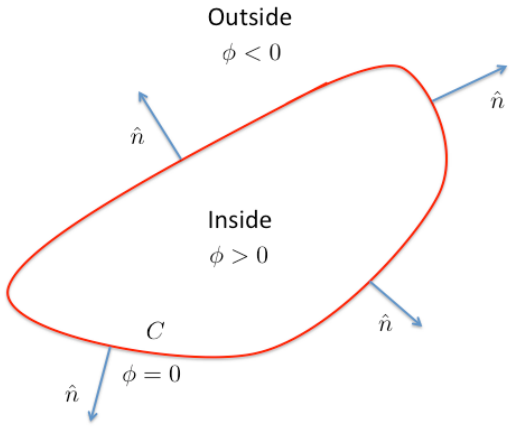

Figure 9.1.2: Contour $\psi = \{\mathbf{x} \in \Omega : \phi(\mathbf{x}) = 0\}$ propagating in normal direction

$\psi = \partial\omega$, which can evolve iteratively, and we also define the function $u(\mathbf{x})$ as

$$u(\mathbf{x}) = \begin{cases} c_1\,, & \text{for } \mathbf{x} \in \omega \\ c_2\,, & \text{for } \mathbf{x} \in \Omega\backslash\bar{\omega} \end{cases} \tag{9.1.3}$$

which removes the contribution of the image gradient $|\nabla \mathbf{u}|$ in Eqn. 9.1.2. Thereby, Chan and Vese introduce the following functional

$$J_{CV}[u,\psi] = \mu\,\mathcal{L}(\psi) + \nu\,\mathcal{A}(\omega) + \lambda_1 \int_{\omega} |f(\mathbf{x}) - c_1|^2\,dA + \lambda_2 \int_{\Omega\backslash\bar{\omega}} |f(\mathbf{x}) - c_2|^2\,dA\,, \tag{9.1.4}$$

as a particular case of Eqn. (9.1.2), extending the regularization of the edge detection by means of the incorporation of the area $\mathcal{A}(\omega)$ of the detected object. In Eqn. (9.1.4), all parameters are constant and positive. To minimize Eqn. (9.1.4), we use the level set method (Osher and Sethian, 1988; Getreuer, 2012)

9.1.2 Level-set formulation

In the level set formulation, the contour $\psi(\mathbf{x})$ is represented by a Lipschitz function $\phi : \Omega \to \mathbf{R}$, such that

$$\begin{aligned} \psi = \partial\omega &= \{\mathbf{x} \in \Omega \,:\, \phi(\mathbf{x}) = 0\} \\ inside(\psi) = \omega &= \{\mathbf{x} \in \Omega \,:\, \phi(\mathbf{x}) > 0\} \\ outside(\psi) = \Omega\backslash\bar{\omega} &= \{\mathbf{x} \in \Omega \,:\, \phi(\mathbf{x}) < 0\} \end{aligned}$$

Fig. 9.1.2 shows the definition of the level set function. Using the function $\phi(\mathbf{x})$, the regularizer terms $\mathcal{L}(\psi)$ and $\mathcal{A}(\psi)$ are written as (Zhao et al, 1996)

$$\mathcal{L}(\psi) = \text{Length}\{\phi = 0\} = \int_\Omega |\nabla H(\phi(\mathbf{x}))|\, dA = \int_\Omega \delta(\phi(\mathbf{x}))\, |\nabla \phi(\mathbf{x})|\, dA\,,$$

$$\mathcal{A}(\psi) = \text{Area}\{\phi \geq 0\} = \int_\Omega H(\phi(\mathbf{x}))\, dA\,,$$

where $H(x)$ is the Heaviside function and $\delta(x) = dH(x)/dx$ is the delta distribution. To numerically regularize the model, Chan and Vese used the following definition for the Heaviside function

$$H_\epsilon(x) = \frac{1}{2}\left[1 + \frac{2}{\pi}\arctan\left(\frac{x}{\epsilon}\right)\right] \quad ; \quad \delta_\epsilon(x) = \frac{d}{dx}\, H(x) = \frac{\epsilon^2}{\pi(\epsilon^2 + x^2)}\,. \tag{9.1.5}$$

Finally, Eqn. (9.1.4) is written in terms of the level set function $\phi(\mathbf{x})$ and Eqn. (9.1.5) as

$$\begin{aligned} J_\epsilon[c_1, c_2, \phi] = \mu \int_\Omega \delta_\epsilon(\phi(\mathbf{x}))\, |\nabla \phi(\mathbf{x})|\, dA + \nu \int_\Omega H_\epsilon(\phi(\mathbf{x}))\, dA \\ + \lambda_1 \int_\Omega |f(\mathbf{x}) - c_1|^2\, H_\epsilon(\phi(\mathbf{x}))\, dA + \lambda_2 \int_\Omega |f(\mathbf{x}) - c_2|^2 \left(1 - H_\epsilon(\phi(\mathbf{x}))\right) dA\,, \end{aligned} \tag{9.1.6}$$

where the image approximation $u(\mathbf{x})$ defined in Eqn. (9.1.3) can be written in terms of the level set function as

$$u(\mathbf{x}) = c_1\, H_\epsilon(\phi(\mathbf{x})) + c_2 \left(1 - H_\epsilon(\phi(\mathbf{x}))\right) \quad ; \quad \mathbf{x} \in \bar{\Omega}\,. \tag{9.1.7}$$

9.1.3 Differential equations for Chan-Vese model

Using the Gâteaux derivative defined in Appendix B, we minimize the functional given in Eqn. (9.1.6) with regard to the constants c_1 and c_2, keeping ϕ fixed. Then, we obtain the expressions

$$c_1 = \frac{\int_\Omega f(\mathbf{x})\, H_\epsilon(\phi(\mathbf{x}))\, dA}{\int_\Omega H_\epsilon(\phi(\mathbf{x}))\, dA} \quad ; \quad c_2 = \frac{\int_\Omega f(\mathbf{x}) \left(1 - H_\epsilon(\phi(\mathbf{x}))\right) dA}{\int_\Omega \left(1 - H_\epsilon(\phi(\mathbf{x}))\right) dA}\,. \tag{9.1.8}$$

Now, keeping c_1 and c_2 fixed, the minimization of Eqn. (9.1.6) with regard to ϕ, using the steepest descent method, gives the equation

$$\frac{\partial \phi}{\partial t} = \delta_\epsilon(\phi)\left[\mu\,\nabla\cdot\left(\frac{\nabla\phi}{|\nabla\phi|}\right) - \nu - \lambda_1\left(f(\mathbf{x})-c_1\right)^2 + \lambda_2\left(f(\mathbf{x})-c_2\right)^2\right] = 0 \quad ; \quad \text{in } \Omega\,,$$

$$\phi(\mathbf{x}, t=0) = \phi_0(\mathbf{x}) \quad ; \quad \text{in } \Omega\,, \tag{9.1.9}$$

$$\frac{\delta_\epsilon(\phi)}{|\nabla\phi|}\frac{\partial\phi}{\partial n} = 0 \quad ; \quad \text{in } \partial\Omega\,,$$

which is the Euler-Lagrange model that solves the minimization problem, where $\hat{n}$ is the normal of $\partial\Omega$ and $\partial\phi/\partial n$ is the normal derivative of ϕ at the boundaries. Eqn. 9.1.9 is also called Morphological Active Contours without Edges (MorphACWE) (Marquez-Neila et al, 2014). Fig. 9.1.3 shows an example of the application of Chan-Vese model in an experimental image. The initial level set $\phi_0(\mathbf{x})$ was computed using the Isodata algorithm (Hodneland, 2003) (see Appendix C). Unfortunately, Chan-Vese model is sensitive to the initial level set because of the non-convexity nature of Eqn. (9.1.4). The left image shows in red color the active contour detected, while the right image shows the image reconstruction using Eqn. (9.1.7). The parameters used were $\lambda_1 = \lambda_2 = 1$, $\mu = 0.3$, $\nu = 0$ and $\epsilon = 1$.

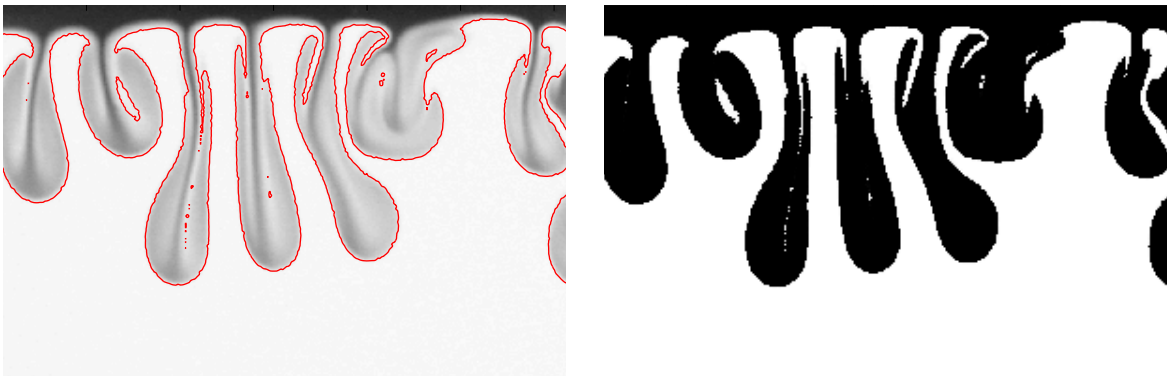

Figure 9.1.3: Example of Chan-Vese segmentation in an experimental image. We have lost much information about the mixing dynamics, if we only use one level set function. However, the edges are correctly segmented

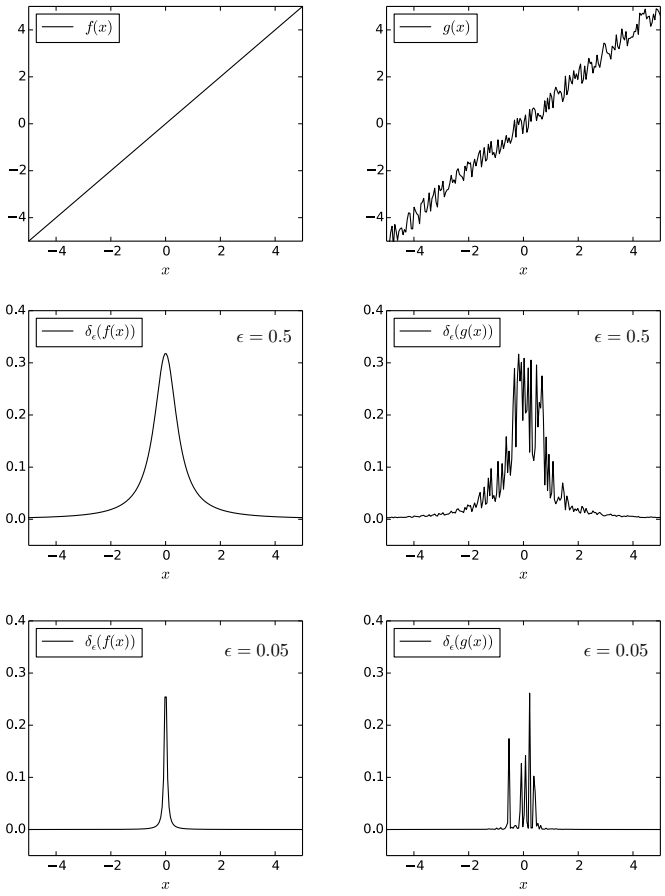

Figure 9.1.4: Spurious oscillations of δ_ϵ-distribution. The left column shows the function $f(x) = x$ and $\delta_\epsilon(f(x))$ for some ϵ values, while the right column shows $g(x) = f(x) + \text{rand}(x)$ and $\delta_\epsilon(g(x))$. The random nature of $g(x)$ is absorbed and amplified by $\delta_\epsilon(g(x))$, so the δ_ϵ-distribution seems to be a poor tool to detect edges.

9.1.4 δ_ϵ-distribution problems in length computation

In numerical computation, unfortunately the δ_ϵ-distribution tends to create spurious oscillations if the parameter ϵ is too small. Otherwise, the accuracy is lost if ϵ is too large. If the level set function ϕ is not smooth enough, then $\delta_\epsilon(\phi)$ is not appropiate to compute the curve length

$$\mathcal{L} = \int_\Omega \delta_\epsilon(\phi(\mathbf{x}))\, |\nabla\phi(\mathbf{x})|\, dA\,, \tag{9.1.10}$$

due to spurious oscillations. To show this issue, Fig. 9.1.4 shows the linear function $f(x) = x$ and the same function with the addition of noise, $g(x) = x + \text{rand}(x)$. The application of the δ_ϵ-distribution to both functions shows important differences, which depend on noise and ϵ values. When ϵ is too small, we can see that $\delta_\epsilon(g(x))$ is even worse, so the application of δ_ϵ-distribution in the length curve formula is difficult in practice.

9.1.5 TV-L^2 multiphase Chan-Tai model

Fig. 9.1.3 shows that the Chan-Vese segmentation is good to obtain a binary separation between regions with a clear interface between them. However, when we apply Chan-Vese segmentation, we can lose much information about the mixing dynamics. This motivates the development of multiphase segmentation techniques to detect more regions of interest.

An interesting approach to build a multiphase segmentation model is the extension to two or more level sets. We can extend the functional of Eqn. (9.1.6) to two level sets, namely $\psi_1 = \{\mathbf{x} \in \Omega \,:\, \phi_1(\mathbf{x}) = 0\}$ and $\psi_2 = \{\mathbf{x} \in \Omega \,:\, \phi_2(\mathbf{x}) = 0\}$. Therefore, we can detect four regions or phases, where each pixel in the domain will belong to one and only one phase. These phases are the following

$$
\begin{aligned}
\omega_1 &= \{\mathbf{x} \in \Omega \,:\, \phi_1(\mathbf{x}) \geq 0 \text{ and } \phi_2(\mathbf{x}) \geq 0\}\,, \\
\omega_2 &= \{\mathbf{x} \in \Omega \,:\, \phi_1(\mathbf{x}) \geq 0 \text{ and } \phi_2(\mathbf{x}) < 0\}\,, \\
\omega_3 &= \{\mathbf{x} \in \Omega \,:\, \phi_1(\mathbf{x}) < 0 \text{ and } \phi_2(\mathbf{x}) \geq 0\}\,, \\
\omega_4 &= \{\mathbf{x} \in \Omega \,:\, \phi_1(\mathbf{x}) < 0 \text{ and } \phi_2(\mathbf{x}) < 0\}\,.
\end{aligned}
$$

Finally, the image approximation $u(\mathbf{x})$ can be written in terms of the level set functions as

$$
\begin{aligned}
u(\mathbf{x}) = {} & c_{11}\, H_\epsilon(\phi_1(\mathbf{x}))H_\epsilon(\phi_2(\mathbf{x})) + c_{12}\, H_\epsilon(\phi_1(\mathbf{x}))\Big(1 - H_\epsilon(\phi_2(\mathbf{x}))\Big) \\
& + c_{21}\, \Big(1 - H_\epsilon(\phi_1(\mathbf{x}))\Big)H_\epsilon(\phi_2(\mathbf{x})) + c_{22}\, \Big(1 - H_\epsilon(\phi_1(\mathbf{x}))\Big)\Big(1 - H_\epsilon(\phi_2(\mathbf{x}))\Big) \quad ; \quad \mathbf{x} \in \bar{\Omega}\,.
\end{aligned}
\tag{9.1.11}
$$

However, the Chan-Vese multiphase segmentation with two level sets is not capable to detect all phases correctly (Hodneland, 2003). To avoid this problem, we change Eqn. (9.1.6) to the following functional with two level sets

$$
F_\epsilon[c_{ij}, \phi_1, \phi_2] = \mu \int_\Omega \Big(|\nabla\phi_1(\mathbf{x})| + |\nabla\phi_2(\mathbf{x})|\Big)\, dA + \frac{1}{2}\int_\Omega \Big(f(\mathbf{x}) - u(\mathbf{x})\Big)^2\, dA\,, \tag{9.1.12}
$$

where $u(\mathbf{x})$ is defined in Eqn. (9.1.11). Eqn. (9.1.12) was proposed by Chan and Tai (2004) within the context of elliptic inverse problems with piecewise constant coefficients. The first term of the right hand side of Eqn. (9.1.12) is the length term

with $\delta_\epsilon = 1$ and also corresponds to a total variation L^2-regularity term, which has denoising capabilities (Rudin et al, 1992). On the other hand, the second term of the right hand side of Eqn. (9.1.12) has cross terms that are not present in the Chan-Vese model.

The application of the Gâteaux derivative and the steepest descent method to Eqn. (9.1.12) gives the following nonlinear system of differential equations

$$\frac{\partial \phi_1}{\partial t} = \mu \nabla \cdot \left(\frac{\nabla \phi_1}{|\nabla \phi_1|} \right) + \delta_\epsilon(\phi_1) \left[(f-u) \left(H_\epsilon(\phi_2) (c_{11} - c_{21}) + \left(1 - H_\epsilon(\phi_2)\right) (c_{12} - c_{22}) \right) \right] = 0 \,, \tag{9.1.13}$$

$$\frac{\partial \phi_2}{\partial t} = \mu \nabla \cdot \left(\frac{\nabla \phi_2}{|\nabla \phi_2|} \right) + \delta_\epsilon(\phi_2) \left[(f-u) \left(H_\epsilon(\phi_1) (c_{11} - c_{12}) + \left(1 - H_\epsilon(\phi_1)\right) (c_{21} - c_{22}) \right) \right] = 0 \,, \tag{9.1.14}$$

where the c_{ij} constants are defined as

$$c_{11} = \frac{\int_\Omega f(\mathbf{x})\, H_\epsilon(\phi_1) H_\epsilon(\phi_2)\, dA}{\int_\Omega H_\epsilon(\phi_1) H_\epsilon(\phi_2)\, dA} \quad ; \quad c_{12} = \frac{\int_\Omega f(\mathbf{x})\, H_\epsilon(\phi_1)(1 - H_\epsilon(\phi_2))\, dA}{\int_\Omega H_\epsilon(\phi_1)(1 - H_\epsilon(\phi_2))\, dA} \,, \tag{9.1.15}$$

$$c_{21} = \frac{\int_\Omega f(\mathbf{x})\, (1 - H_\epsilon(\phi_1)) H_\epsilon(\phi_2)\, dA}{\int_\Omega (1 - H_\epsilon(\phi_1)) H_\epsilon(\phi_2)\, dA} \quad ; \quad c_{22} = \frac{\int_\Omega f(\mathbf{x})\, (1 - H_\epsilon(\phi_1))(1 - H_\epsilon(\phi_2))\, dA}{\int_\Omega (1 - H_\epsilon(\phi_1))(1 - H_\epsilon(\phi_2))\, dA} \,.$$

Unfortunately, as in Chan-Vese segmentation, the Chan-Tai model is also sensitive to the initial level set because of the non-convexity nature of Eqn. (9.1.12). Then, to compute the initial level set $\phi_0(\mathbf{x})$ for a given image $f(\mathbf{x})$, we use again the Isodata algorithm. Fig. 9.1.5 shows an example of the application of multiphase Chan-Tai model to the same experimental image segmented in Fig. 9.1.3. Next, Fig. 9.1.6 shows the segmentation of four different fluid phases, which have an interesting physical meaning. Because the experimental images shown in Fig. 9.1.1 represent the mixing between two miscible fluids A and B, in Fig. 9.1.6 the fluid A and fluid B are correctly segmented, while the convective penetration of fluid A into fluid B and the mixing zone are new visualizations which have not been reported in literature. These images allow us to study independently the mixing dynamics, the evolution of the length curve and the grow of the total mixing area, for example.

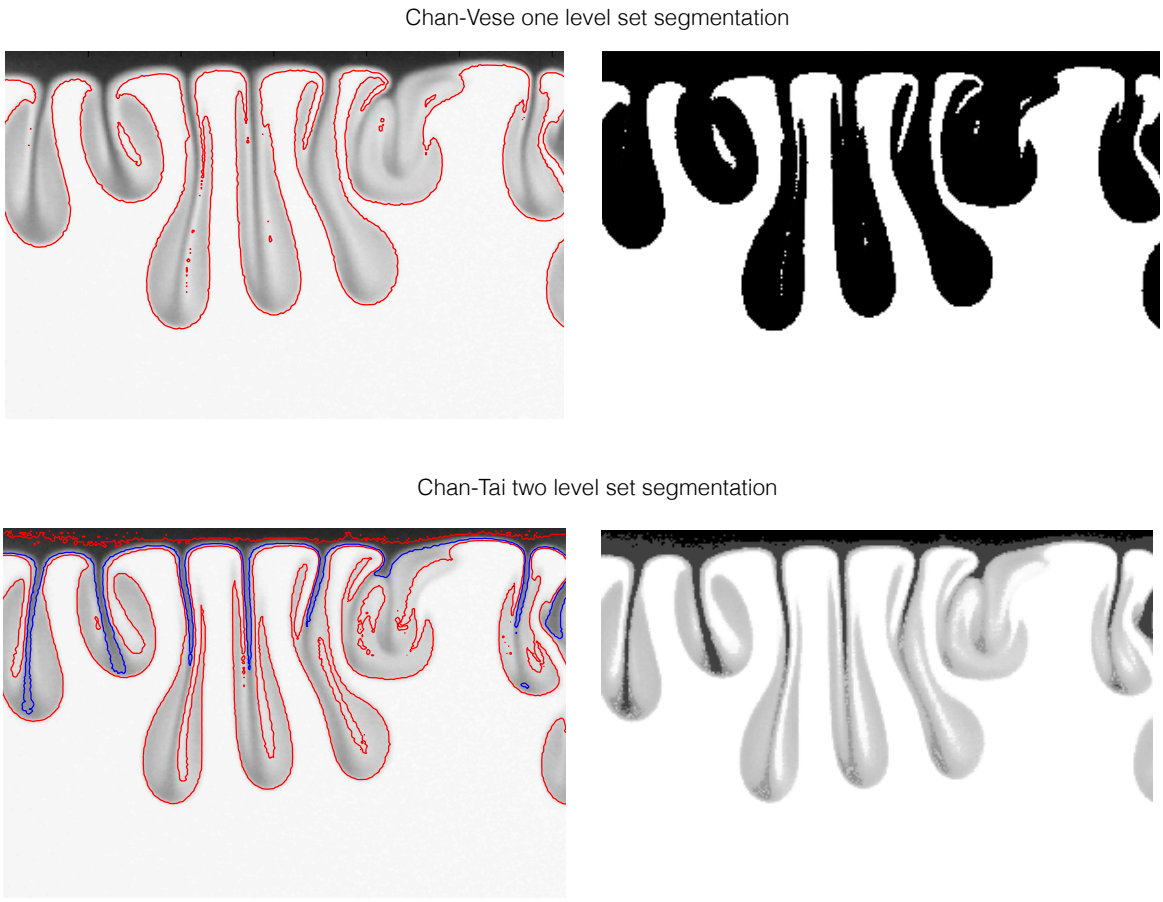

Figure 9.1.5: Example of Chan-Tai segmentation in an experimental image. The use of two level set functions allows us to detect more mixing structures

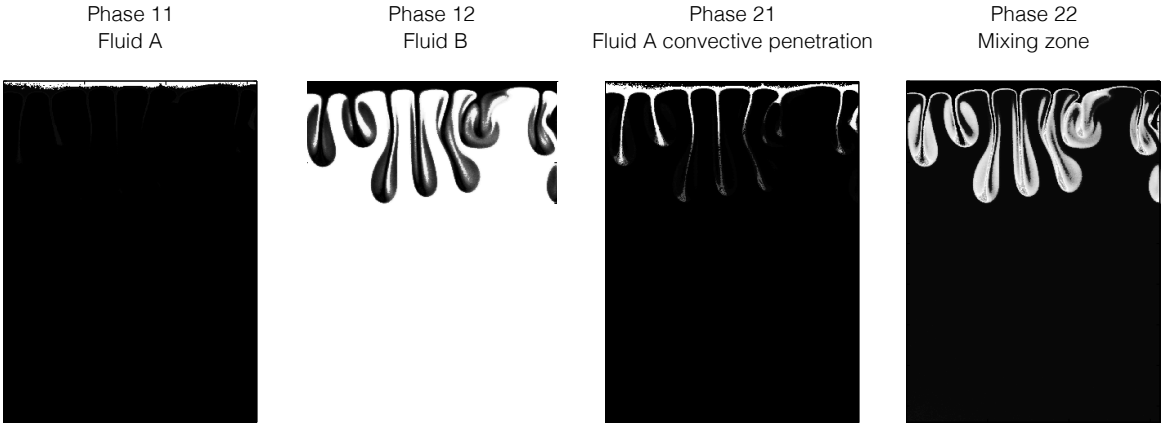

Figure 9.1.6: Phase segmentation using the Chan-Tai two level set model. The different fluid phases, which are produced by the mixing dynamics, are identified by white color

9.2 Video motion by TV-L^1 optical flow

Optical flow is a mathematical method that quantifies the apparent motion of objects in space caused by the relative motion between a physical observer and the scene or by physical phenomena, such as particle motion or thermal convection (Baker et al, 2011). This idea was introduced by J.J. Gibson during the Second World War, and played a key role in the development of the ecological approach to visual perception, an approach that emphasizes studying human perception in the natural environment. He defined optical flow as information carried by light resulting from environmental structure and the animal's path through the environment (Gibson, 1950, 1966).

All optical flow methods have an issue known as the aperture problem, which arises when a moving object is viewed through an aperture without the information of some structural properties such as edges, corners and texture data (Wedel and Cremers, 2011). Fig. 9.2.1 shows an example of the aperture problem in optical flow, where the image (b) is a rotation of image (a). With this information, we do not know if the rotation is clockwise or counterclockwise, so optical flow loses physical meaning. If the rotation is clockwise, then optical flow can be applied, obtaining the image (c).

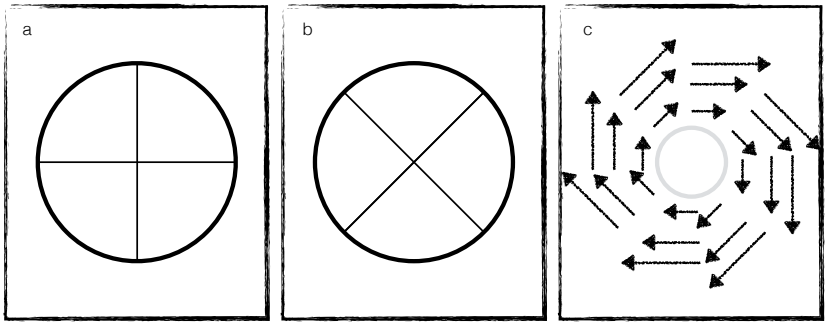

Figure 9.2.1: The aperture problem and the optical flow solution when some structural information is known

9.2.1 L^2 Horn-Schunck model

Let $I(\mathbf{x}, t_0)$ be the intensity of a fluid parcel in the location $\mathbf{x}$ at time t_0, and $I(\mathbf{x} + \mathbf{u}(\mathbf{x}), t_1)$ be the intensity of the same parcel at time t_1, which will have displaced in space. The quantity $\mathbf{u}(\mathbf{x}) = (u, w)$ is the two-dimensional displacement field (or optical flow field) that has to be determined. The most important assumption of optical flow is that the intensity value of the parcel $I(\mathbf{x}, t_0)$ does not change while it moves to

$I(\mathbf{x}+\mathbf{u}, t_1)$, which is known as the brightness constancy assumption (BCA), and it is represented by the equation

$$-\frac{\partial I}{\partial t} = \nabla I \cdot \mathbf{u} \tag{9.2.1}$$

which contains two unknows, u and w, that cannot be solved due to the aperture problem, thus it is necessary to introduce an additional regularity constrain. To regularize the problem, Horn and Schunck (1981) introduced a smoothness term by penalizing the derivative of the optical flow field, yielding a functional which must be minimized using a variational approach

$$F[\mathbf{u}] = \int_{\Omega} \left(|\nabla \mathbf{u}|^2 + \lambda |\vartheta(\mathbf{u})|^2 \right) d\Omega \ , \tag{9.2.2}$$

$$\vartheta(\mathbf{u}) = \frac{\partial I}{\partial t} + \nabla I \cdot \mathbf{u}$$

where $\vartheta(\mathbf{u})$ imposes the BCA constrain to Eqn. (9.2.2). The introduction of the quadratic L^2-regularizer $\varepsilon_{reg} = |\nabla \mathbf{u}|^2$, called spatial coherence, favoring flow fields which are spatially smooth, penalizing the high variations. Therefore, this quadratic regularizer does not allow the detection of discontinuities in the optical flow field (Wedel and Cremers, 2011). The quadratic L^2-regularity present in the Horn-Schunck functional might not be a regularizer based in physical approaches. A first order div-curl L^2-regularizer of the type $\varepsilon_{reg} = \alpha|\nabla \cdot \mathbf{u}|^2 + \beta|\nabla \times \mathbf{u}|^2$ was introduced by Suter (1994) and a second order div-curl L^2-regularizer $\varepsilon_{reg} = \alpha|\nabla(\nabla \cdot \mathbf{u})|^2 + \beta|\nabla(\nabla \times \mathbf{u})|^2$ has been proposed by Gupta and Prince (1996), where both have a much more physical meaning, penalizing high divergence-rotational components. However, the first and second order div-curl method are more difficult to implement computationally (Corpetti et al, 2005; Stark, 2013). A well-known limitation of the Horn-Schunck method is that can only estimate small motions. Despite of that, the method has been well evaluated (Meinhardt-Llopis et al, 2013) and the variational formulation given by Eqn. (9.2.2) allow us to compute the optical flow field for all pixels within the image, resulting in a dense flow field (one vector per pixel). This feature is attractive since it does not require subpixel algorithms to estimate the apparent displacement through the position of the maximum in the correlation plane, such as for digital PIV. Despite that the accuracy of the subpixel level in PIV is 0.1 to 0.05 pixels, the image resolution obtained in SS by using cross-correlation methods is of the order of the size of the interrogation window

scaled with the overlap used (one vector per window), which is 8×8 pixels in the most general case. Moreover, the computational costs of using OpFlow are more expensive than digital PIV.

9.2.2 *TV*-L^1 optical flow model

In general, in real-world scenes and laboratory scale experiments, there may be many objects with defined edges moving. Because of that, some authors change the quadratic L^2-regularity to a L^1-regularity which better preserve discontinuities (Wedel and Cremers, 2011). In this context, the total variation optical flow method (OpFlow) is a variational method whose formulation is based in the minimization of the functional given by Zach et al (2007)

$$J[\mathbf{u}] = \int_{\Omega} \Big(|\nabla \mathbf{u}| + \lambda |\psi(\mathbf{u})| \Big) \, d\Omega \ , \tag{9.2.3}$$

$$\psi(\mathbf{u}) = I(\mathbf{x} + \mathbf{u}_0, t_1) + \nabla I(\mathbf{x} + \mathbf{u}, t_1) \cdot (\mathbf{u} - \mathbf{u}_0) - I(\mathbf{x}, t_0) \ ,$$

which is the L^1 version of Horn-Schunck functional Eqn. (9.2.2), where $\psi(\mathbf{u})$ is called the residual (BCA data term), $\mathbf{u}_0$ is an approximation of $\mathbf{u}$ and λ is a parameter known as the attachment parameter (Sanchez et al, 2013). Despite there are many versions of L^1-regularity terms proposed in literature, we have chosen the OpFlow formulation given by Zach et al (2007) because they have proposed an exact numerical scheme to solve Eqn. (9.2.3) by using the well-known Rudin-Osher-Fatemi (ROF) model, which has denoising capabilities without blurring edges (Rudin et al, 1992). This point is important, because we want to detect not only discontinuities on the flow, but also get a smooth flow where noise is controlled. The *TV*-L^1 method, which means total variation with the L^1-norm, is used to compute the integral over the domain of the absolute values of mathematical quantities of interest. In Eqn. (9.2.3), the objective quantity to minimize is the L^1-norm of the gradient of the flow subject to the L^1-norm of the BCA data term, which is controlled by the parameter λ. An efficient method given by Zach et al (2007), which uses the duality-based method proposed by Chambolle (2004), solves Eqn. (9.2.3). The method enables one to find the minimum of the strictly

convex functional with a quadratic relaxation

$$J_\theta[\mathbf{u}] = \int_\Omega \left(|\nabla \mathbf{u}| + \frac{1}{2\theta} (\mathbf{u} - \mathbf{v})^2 + \lambda |\psi(\mathbf{v})| \right) d\Omega \ , \tag{9.2.4}$$

where $\mathbf{v}$ is an auxiliary vector (known as the dual variable) and the parameter θ is known as the tightness parameter (Sanchez et al, 2013). Setting the parameter θ to a small value, it forces J_θ to reach its minimum value when $\mathbf{u} \sim \mathbf{v}$, obtaining the TV-L^1 functional given by Eqn. (9.2.3). Although the optical flow is rigorous and accessible to further developments, there is a certain ambiguity in the correct choice of parameters λ and θ that represent the apparent motion of an experimental image pair and the computation of dense motion fields. The choice of both parameters is often a practical problem in the application of OpFlow to analize physical experiments.

If an exact representation of the flow is known (the ground truth image), some popular performance estimators such as the angular error, the average end-point error, the interpolation error and the normalized interpolation error (Barron et al, 1994; Baker et al, 2011) help to set λ and θ. However, in experimental images, this information is not known a priori and the choice by inspection of the parameters is a common practice. To solve this problem, we propose to use digital PIV as a preprocessing step. The idea is to compare the results of both techniques, digital PIV and Opflow, by using the structural similarity index metric (Wang et al, 2004; Wang and Bovik, 2009). We associate the highest value of this metric with the optimal values for λ and θ for the image in study, so that the initial image resolution obtained with digital PIV can be improved by the dense flow field given by OpFlow. As well as the Horn-Schunck optical flow, the resolution of OpFlow is equal to one pixel. As a consequence, OpFlow can detect small structures of few pixels of length with a better definition, while globally structural properties are similar to those obtained by digital PIV. Fig. 9.2.2 shows an example of the enhancement of the detection of structures using TV-L^1 optical flow, in a thermal laboratory experiment using quantitative Schlieren. For further information, we refer the Chapter 10, Section 10.4 on page 134.

The OpFlow method has been extensively evaluated against other optical flow methods (Barron et al, 1994; Baker et al, 2011) using the average end-point error over some images of the Middlebury database, obtaining better results in comparison with Lucas-Kanade, Horn-Schunck and Brox algorithms which have been used in BOS literature (Atchenson et al, 2009). In particular, an interesting extension given by Wedel et al (2008) which uses a cartoon-texture image decomposition by the TV-L^1

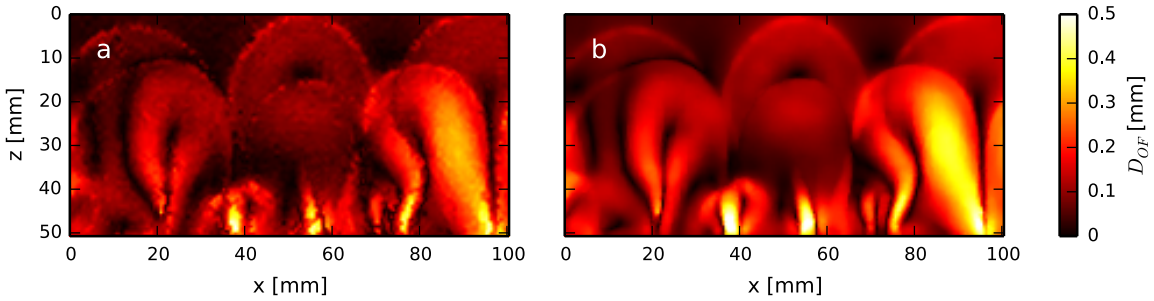

Figure 9.2.2: Enhancement of the detection of structures using *TV-L*^{1} optical flow (right image), in comparison with the known digital PIV (left image) (see figure 10.4.4)

model improves the BCA constrain and therefore the optical flow estimation. In our experimental applications, it is not neccesary to use this decomposition.

Chapter 10

Thermal experiments in porous media

This chapter has been published as research paper called **"Enhancement of synthetic schlieren image resolution using total variation optical flow: Application to thermal experiments in a Hele-Shaw cell"**, authored by Juvenal A. Letelier, Paulo Herrera, Nicolás Mujica and Jaime H. Ortega, in Experiments in Fluids **(2015)** 57:18 . doi:10.1007/s00348-015-2109-1.

Abstract

We present an improvement to the standard Synthetic Schlieren technique to obtain the temperature distribution of a fluid inside of a Hele-Shaw cell. We to use the total variation L^1-norm optical flow method to treat experimental images and to obtain quantitative results of the development of thermal convection inside a cell, by detecting the gradients of the optical refractive index. We present a simple algorithm to set the optical flow parameters, which is based on the comparison between the optical flow output and the result obtained by digital PIV using the structutal index metric. As an example of the application of the proposed method, we analyze laboratory experiments of thermal convection in porous media using a Hele-Shaw cell. We demonstrate that the application of the proposed method produces important improvements versus digital PIV, for the quantification of the gradients of the refractive index including the detection of small scale convective structures. In comparison with correlation-based digital methods, we demonstrate the advantages of the proposed method, such as denoising and edge capture. These features allow us to obtain the temperature, for this experimental setting, with better image resolution than other techniques reported in the literature.

10.1 Introduction

Over the last few decades, many visualization and image processing techniques in experimental fluid dynamics have been proposed to describe qualitatively and quantitavely the behavior of certain flow regimes. The Synthetic Schlieren technique (SS) (Dalziel et al, 1998; Sutherland et al, 1999; Dalziel et al, 2000) has been used to study interesting fluid dynamics problems such as internal waves and stratification because of its simple implementation and the quality of the results that can be obtained. This technique is

based on the detection of the apparent displacements of a synthetic background due to changes in the optical refractive index of the test fluid. Commonly, the computational method used to detect the apparent displacements is digital PIV (Raffel et al, 1998), a correlation-based image method which has subpixel accuracy but an image resolution of the order of the overlap times the interrogation window size. Moreover, some interesting mathematical techniques in image processing such as Lucas-Kanade, Horn-Schunck and Brox optical flow methods (Horn and Schunck, 1981; Lucas and Kanade, 1981; Brox et al, 2004), have been applied in images obtained with the Background Oriented Schlieren technique (BOS) (Richard and Raffel, 2001; Gojani and Obayashi, 2012; Gojani et al, 2013; Raffel, 2015), an optical visualization method similar to SS. The application of the mentioned optical flow methods improve the image resolution in comparison with digital PIV (Atchenson et al, 2009). The same conclusion has been reported when another versions of optical flow method have been applied in particle tracking and velocimetry experiments (Ruhnau et al, 2005a,b; Ruhnau and Schnorr, 2007).

All optical flow methods have an issue known as the aperture problem, which arises when a moving object is viewed through an aperture without the information of some structural properties such as edges, corners and texture data (Wedel and Cremers, 2011). Therefore, to avoid this problem, all optical flow methods require a regularization. Depending of the regularization used, optical flow can be formulated using a featured-based approach or a variational approach. In general, variational formulations have the best performance in statistical evaluations. One of these formulations, based on the introduction of a L^1-regularity term $\varepsilon_{reg} = |\nabla \mathbf{u}|$ (Rudin et al, 1992; Zach et al, 2007) and known as the TV-L^1 optical flow estimation (abbreviated as OpFlow), has shown to have interesting properties such as noise removal and the preservation of edges and contrast (Chan et al, 2001; Strong and Chan, 2003). Therefore, OpFlow (Zach et al, 2007; Sanchez et al, 2013) is promising for analysing results of physical experiments.

The Rayleigh-Benard convection (RBC) in porous media is a benchmark problem where many visualization techniques has been applied. RBC is of particular interest in research because it appears in a wide range of geophysical problems, including earth's mantle convection, geothermal energy extraction and underground energy storage systems. In the laboratory scale, some experiments about RBC in porous media using analogue working fluids in Hele-Shaw cells have been widely reported in literature (Elder, 1967a,b; Hartline and Lister, 1977; Koster and Muller, 1982; Nield and Bejan, 2006; Cooper et al,

2014). In this context, the use of passive dyes for the observation of streaklines (Horne and O'Sullivan, 1974), the pH color indicator method (Hartline and Lister, 1977), the holographic interferometry technique (Koster, 1983; Lee and Kim, 2004), thermal point measurements (Nagamo et al, 2002) and thermo-sensitive liquid-crystals (Ozawa et al, 1992; Cooper et al, 2014) have been used to show the onset and the development of vertical thermal plumes that enhance heat transport inside the cell. However, the resolution of the images obtained with existing techniques is limited and thermal details are commonly missing. Then, RBC in porous media using a Hele-Shaw cell is a good candidate to apply SS and to visualize thermal plumes.

In this chapter we propose the use of OpFlow as an image analysis method for the SS technique, which gives better image resolution. To illustrate the applicability of OpFlow in optical density visualization, we implement the SS technique to quantify the temperature field inside a Hele-Shaw cell, where the working fluid has a temperature dependent viscosity and the cell is heated from below and cooled from above. The choice of studying heat transport in such type of fluids is motivated by the growing interest in understanding the physics of the geothermal energy extraction through carbon dioxide injection (Randolph and Saar, 2011b) and supercritical CO_2 storage in geological formations (Benson et al, 2006; Emami Meybodi et al, 2015), where the viscosity is variable with the concentration of dissolved supercritical CO_2 into brine and only slightly variable with temperature.

The mathematical theory of OpFlow is discussed in Chapter 9, Section 9.2 on page 122. OpFlow depends on some non-physical free parameters which, in general, are choosen through visual inspection of the results. We determine these parameters by using a statistical methodology in which digital PIV plays a central role. The main goals and contributions are

- To use a statistical tool to define adequately the OpFlow parameters to analyze experimental images, using digital PIV as a preprocessing step.
- To quantify the refractive index gradients in the flow, in a wide range of spatial scales, using the discontinuity detection capabilities of OpFlow.
- To use OpFlow results to reconstruct the temperature map in stratified fluids in an out-of-equilibrium regime.

Using these results, we demonstrate that the horizontal average temperature as a

function of the vertical coordinate gives important information about the heat flux at the boundaries and the behavior of the convection inside the cell.

10.2 Statistical metrics

In order to compare the similitude between two images, the mean square error (MSE) has been used in signal processing applications. If f and g are two images represented as a two-dimensional array of size $N_x \times N_y$, the MSE metric between them is defined as

$$\mathrm{MSE} = \frac{1}{N_x N_y} \sum_{i=1}^{N_x} \sum_{j=1}^{N_y} \Big[f_{j,i} - g_{j,i} \Big]^2 \ . \tag{10.2.1}$$

Therefore, a minimum value of MSE means a good similarity between images. In addition, the structural similarity index metric (SSIM) is defined as

$$\mathrm{SSIM} = \frac{(2\mu_f \mu_g + C_1)(2\sigma_{fg} + C_2)}{(\mu_f^2 + \mu_g^2 + C_1)(\sigma_f^2 + \sigma_g^2 + C_2)} \ , \tag{10.2.2}$$

where, if the image is stored as a one dimensional array of size $N = N_x N_y$, the mean intensity and the standard deviation of the image f are defined as

$$\mu_f = \frac{1}{N} \sum_{s=1}^{N} f_s \ \ ; \ \ \sigma_f = \sqrt{\frac{1}{N-1} \sum_{s=1}^{N} \Big[f_s - \mu_f \Big]^2} \ .$$

In Eqn. (10.2.2), C_1 and C_2 are constants. The SSIM metric satisfies the conditions of symmetry, boundedness ($\mathrm{SSIM} \leq 1$) and unique maximum ($\mathrm{SSIM} = 1$ if and only if $f = g$). Wang and Bovik (2009) compare both metrics with a series of images distorted from an original image, concluding that the MSE values are nearly identical, even though the same images present important visual differences that are detected using SSIM. This conclusion is important in the comparison of our experimental images, so we analyse the data with the SSIM method instead of MSE.

10.3 Experimental setup

10.3.1 Working fluid properties

Analogue fluids that represent a physical phenomenon in underground systems have been used in the context of supercritical CO_2 dissolution in brine-saturated porous media (Neufeld et al, 2010). In this context, Backhaus et al (2011) used aqueous solutions of propylene-glycol (PPG) as working fluid. The PPG shows interesting thermodynamical properties with important changes in temperature (Sun and Teja, 2004). For the SS technique, the important variable to consider is the change of the optical refractive index as function of temperature. For the working fluid in consideration, this dependency is modelled as $n(T) = n_0 - \beta T$, where $n_0 = 1.4391$ and $\beta = 0.0003\,°\mathrm{C}^{-1}$ (Turan et al, 2002).

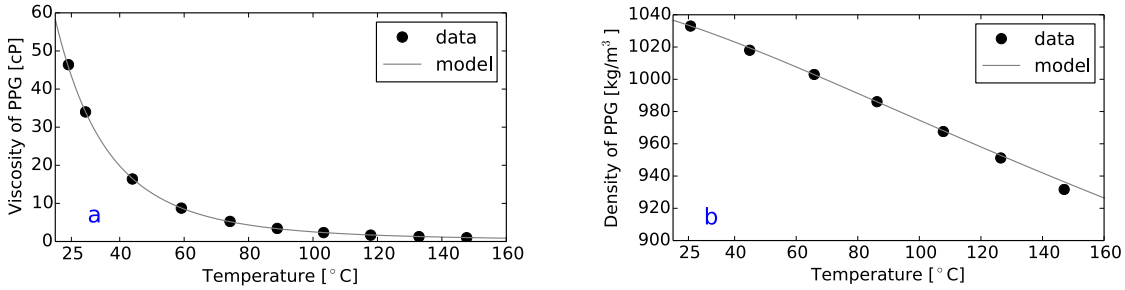

Figure 10.3.1: Figure 10.1(a). Dynamic viscosity of PPG as a function of temperature. **Figure** 10.1(b). Density of PPG as a function of temperature. Experimental data were extracted from Sun and Teja (2004)

The density and dynamic viscosity of PPG were obtained from Sun and Teja (2004). Fig. 10.3.1 shows the dependence with temperature for both fluid properties. This information will be used later to explain the results from visualization of temperature maps. For the experimental results shown in this chapter, the Prandtl number $Pr = \nu/\kappa$, where $\nu = \mu/\rho$ is the kinematic viscosity, is $Pr = 275$. Furthermore, the working temperatures were $T_{min} = 30\,°\mathrm{C}$ and $T_{max} = 45\,°\mathrm{C}$, as shown in Fig. 10.6.1.

10.3.2 Experimental setup and procedures

The experimental setup and methodology used for the adquisition of images are similiar to those described in Wildeman et al (2012) and suggested by Gojani et al (2013) (see

Fig. 8.3.2 in Chapter 8, Section 8.3 on page 110). The homogeneous porous media is represented by a Hele-Shaw cell, which is made with acrylic of height $H = 100\,\text{mm}$, width $L = 150\,\text{mm}$ and thickness $L_p = 8\,\text{mm}$. To separate the plates, we use two aluminium shims of width $\tilde{L} = 150\,\text{mm}$, height $\tilde{H} = 30\,\text{mm}$ and thickness $b = 1\,\text{mm}$, sealing the cell on the top and bottom by pressing the plates and shims with stainless steel bolts. On the sides, the cell is sealed using O-rings which are pressed by other acrylic plates using bolts of similar characteristics, creating an experimental device which is water proof (see Fig. 10.3.2).

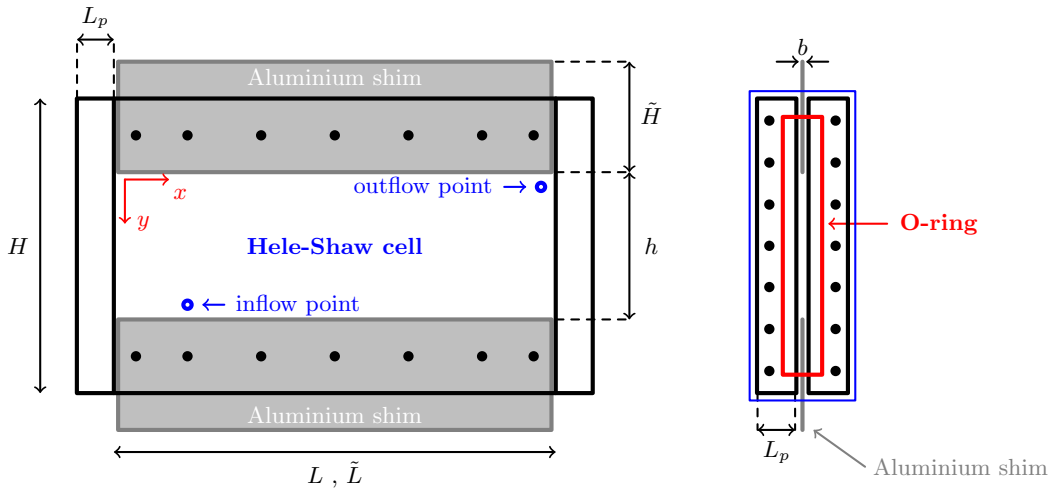

Figure 10.3.2: Schematic view of the Hele-Shaw cell. The dimensions of variables presented in this figure are the following: $L = \tilde{L} = 150\,\text{mm}$, $H = 100\,\text{mm}$, $L_p = 8\,\text{mm}$, $\tilde{H} = 30\,\text{mm}$, $h = 50\,\text{mm}$ and $b = 1\,\text{mm}$

The design of the Hele-Shaw cell leaves a free flow channel of dimensions $L \times h \times b$, with $h = 50\,\text{mm}$. The cell is filled with propylene glycol from an inflow point, saturating the flow channel, where fluid excess goes to a head tank through an outflow point. To generate the thermal convection, we add two nichrome wires on the free sides of aluminium shims, applying a constant current. The temperature on the shims are measured using both, a RTD-PT100 sensor connected to a Keithley nano-voltmeter and a thermal camera ULIRvision, which confirms that the aluminium shims are heated uniformly, so we consider that the measured temperature on shims are the boundary conditions in which thermal convection can develop inside the cell. The convective behavior is controlled by the Rayleigh number $Ra = \Delta\rho g K H/\mu\kappa$ (Otero et al, 2004), where $\Delta\rho$ is the maximum density difference, g is the gravitational acceleration, $K = b^2/12$ is the permeability of the cell, b is the gap of the cell, H is the height, μ is

the dynamic viscosity and κ is the thermal diffusivity. With this information, for the experimental results shown in Section 10.5 we have $Ra = 680$.

10.3.3 Visualization and error analysis

To mount the experiment we use an optical table and a metallic structure where the cell is inserted vertically. A white light LED panel is placed behind the cell and a white acrylic light diffusor is placed between the cell and the LED panel. At the diffusor, we add a background pattern of dots printed on a transparent slide, creating the background image shown in Fig. 10.3.3.

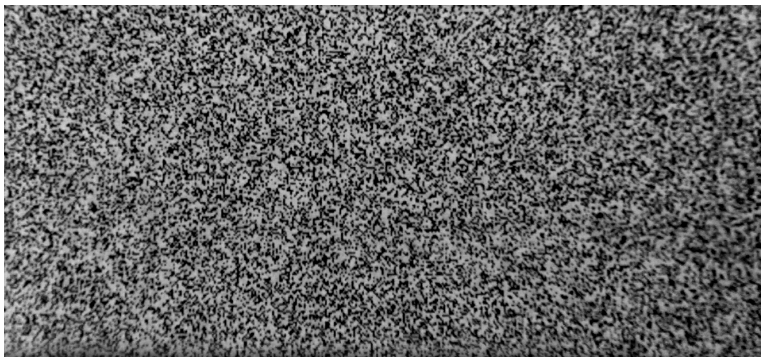

Figure 10.3.3: Background dots pattern for BOS measures. The size of the image is $10 \times 5\,\mathrm{cm}^2$

Accordingly with Fig. 8.3.2 presented in Chapter 8, Section 8.3 on page 108, the SS configuration of the experiments is given by the parameters s_t, s_o and f. For the results shown in Section 10.4 we have $L_s = 5\,\mathrm{cm}$ and $s_o = 100\,\mathrm{cm}$. A Canon Rebel T3 EOS camera was used to acquire photographs of size $5184\,\mathrm{pixel} \times 3456\,\mathrm{pixel}$. The images were saved using the 8-bit JPEG format since our main objective is to detect apparent displacements of synthetic dots of appreciable size. The 14-bit RAW format is very expensive in terms of data storage for our purposes. As we demonstrate in Section 10.4, the use of a lossy codec is adequate to accomplish our objectives.

The image focus was achieved by using a telephoto lens Canon EF $75 - 300\,\mathrm{mm}$ $f/4 - f/5.6$ and the focal lenght was set to $f = 135\,\mathrm{mm}$ with a focal ratio $f_r = 5.6$. It is important to note that any issue from the CMOS sensor of the camera such as photon shot noise, pixel vignetting and fill fraction of pixels, can be avoided by the OpFlow denoising capabilities when images are analyzed. However, non-uniform response due to the photon shot noise can impact negatively in the CMOS sensor performance and

therefore in the BCA constrain, limiting the applicability of OpFlow. In such cases, preprocessing the images using the cartoon-texture decomposition can be useful to fix this problem (Wedel et al, 2008). In this work, this preprocessing step was not used because the original images are adequate to be analyzed directly with OpFlow.

Following Gojani et al (2013), an experiment is well-suited for the application of SS when the fluid flow only deflects the light ray, but does not displace it. From Fig. 8.3.2 presented in Chapter 8, Section 8.3 on page 108, this condition is satisfied when $b/(s_o - s_t) = 1 \times 10^{-3} \ll 1$, which is fulfilled by our experimental setup. Moreover, the background image dimensions must satisfy the condition $\max\{L/2, H/2\} \leq s_o/4$ to ensure the paraxial limit asummed in Eqn. (8.3.8). In our experiments, we have $L/2 = 10\,\text{cm}$ and $H/2 = 5\,\text{cm}$.

The optical refractive index values considered in this work are $n_a = 1.00029$, $n_p = 1.49$ and $n_f = 1.4331$ at $T = 20\,^\circ\text{C}$. Considering that the cells lengths were measured using a vernier of resolution 0.01 mm and the cell gap was measured using a micrometer of resolution $0.001\,\text{mm}$, we have $s_t = 61.28 \pm 0.03\,\text{mm}$. The error in the estimation of ε can be computed using the formula $\sigma_\varepsilon = \delta/[2(s_o - f)]$, where δ is the diameter of a single dot in the background image. By construction, $\delta = 100\,\mu\text{m}$ and $\sigma_\varepsilon = 6 \times 10^{-5}\,\text{rad}$. A single pixel of the CMOS camera sensor is equivalent to $1\,\text{pixel} = 91.95 \pm 0.09\,\mu\text{m}$ of the background image, so by using the angular error σ_ε and the maximum displacement detected by OpFlow, which is $\Delta y_{ab}^{(max)} = 5.5\,\text{pixel}$, we have $\Delta y_{AB}^{(max)} = 0.506 \pm 0.004\,\text{mm}$. The error of this estimation is the spatial resolution of the optical system in our experiments. Obviously, the spatial resolution can be enhanced by two ways, reducing the dot diameter or increasing the distance s_o and magnification.

10.4 Optical flow results

10.4.1 Displacement sensibility analysis

The OpFlow algorithm and libraries given by Sanchez et al (2013), modified for automation and data storage purposes using python libraries and HDF5, was applied to the acquire images. As an example of this application, for a fixed $\lambda = 0.1$ and variable θ, we obtain the image sequence presented in Fig. 10.4.1, where the displacement $D_{OF}(\theta, \lambda) = \sqrt{\mathbf{u} \cdot \mathbf{u}}$, detected by OpFlow Eqn. (9.2.4) presented in Chapter 9, Section 9.2 on page 122,

depends on θ. For very small θ, the method does not detect changes in the pair of images, but for very large θ values, the flow is over smoothed.

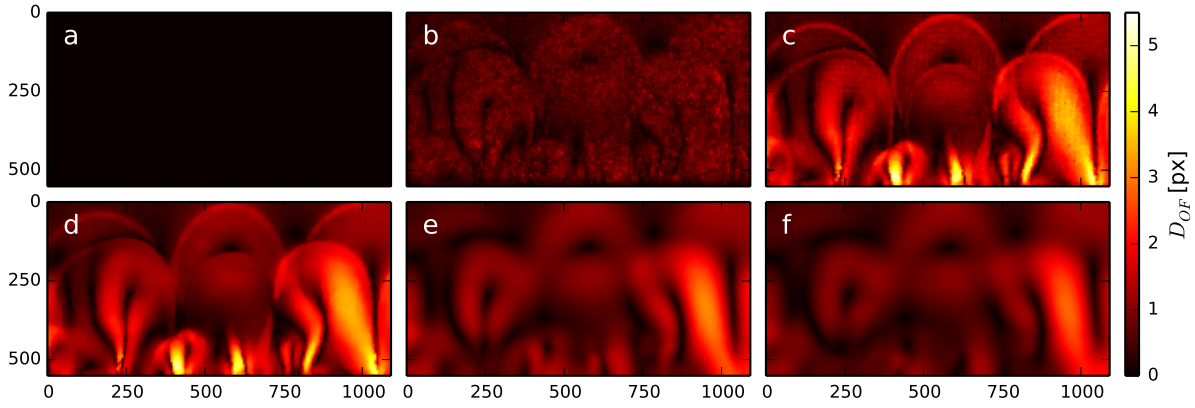

Figure 10.4.1: OpFlow results for $\lambda = 0.1$ and different values of θ : $\theta = 1 \times 10^{-4}$ (a), $\theta = 1 \times 10^{-2}$ (b), $\theta = 1 \times 10^{-1}$ (c), $\theta = 1$ (d), $\theta = 1 \times 10^{2}$ (e) and $\theta = 1 \times 10^{4}$ (f). With the objective to compare the size of the image and the maximum displacement detected by OpFlow, the vertical and horizontal coordinate values in each image are given in pixels. The conversion is $550\,\text{pixel} = 50\,\text{mm}$

By visual inspection of the sequence presented above, we conclude that the best image resolution was achieved for $O(\theta) \sim 1$. Fig. 10.4.2 shows $\max[D_{OF}]$ as function of θ, for several values of λ. It is interesting to note that $\max[D_{OF}]$ always has a local maximum for $10^{-4} < \theta < 10^{2}$ and $\lambda > 10^{-2}$. Moreover, $\max[D_{OF}]$ reaches a constant value for $\theta > 10^{2}$, which is clearly observed in Fig. 10.4.1(e) and Fig. 10.4.1(f), where the images appear diffused in comparison with others.

Considering these results for $\max[D_{OF}]$, the principal problem that arises when OpFlow is applied is the correct choice of optimal parameters. When the exact flow is not known, there is no ground truth image to compare with, so that the choice of parameters must be done by visual inspection. Physically, the method loses strength when it is compared with other techniques such as digital PIV, which detects a correct maximum displacement. Moreover, digital PIV is not adequate when cross-correlation is poor. In this sense, it is reasonable to think that there is a compromise between a good correlation of a pair images (digital PIV) and the generation of dense fields (OpFlow), which can be used to analyse image motion with high accuracy. In the following, we will explain the application of the statistical metrics defined above, to obtain an approximation of the adequate values of OpFlow parameters using a digital PIV preprocessing, where we want to compute an initial result of the apparent displacement, which is later enhanced by means of the OpFlow estimation.

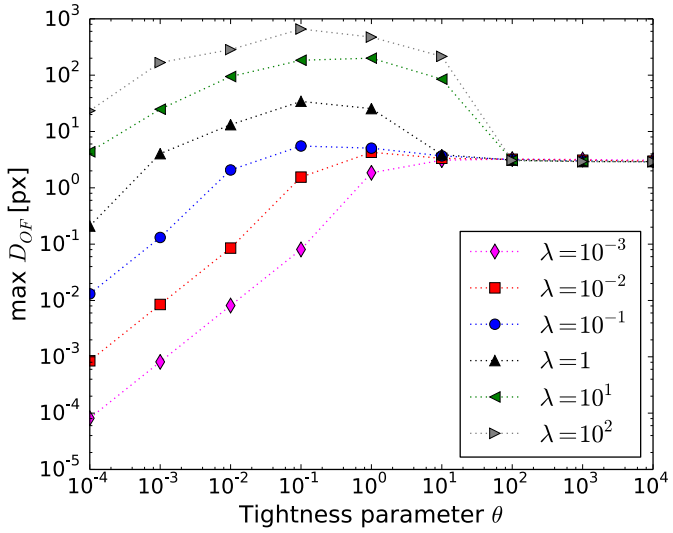

Figure 10.4.2: Sensitivity analysis of OpFlow parameters, using the maximum displacement detected as the metric. It is interesting to note that this metric reach a constant value for $\theta > 10^2$, which is independent of λ

10.4.2 Comparison between digital PIV and OpFlow

OpenPIV (Liberzon et al, 2009) is an open-source software that implements the cross correlation algorithm given in Raffel et al (1998), using Fast Fourier Transform (FFT) and standard statistical tools for vector validation. Setting the interrogation window $w = 16\,\text{pixel}$, the overlap as 50% and the well-known peak to peak as a signal to noise method with thresholding of 1.8, the maximum displacement detected by the method is $\max[D_{PIV}] = 5.4\,\text{pixel} = 0.497\,\text{mm}$. To compare the OpFlow and digital PIV results using OpenPIV, the statistical metric defined in Eqn. (10.2.2) gives the mathematical background to establish a methodology to fix the Opflow parameters. This methodology consists in finding the maximum value of the SSIM metric for several scales of λ and θ. As an example, we use the same data set used to generate the maps shown in Fig. 10.4.1 and we compute the SSIM for an array of 13×13 values of λ and θ. A quadratic bivariate spline is applied to the scatter data, generating the smoothed and continuous map shown in Fig. 10.4.3(b). The maximum value SSIM $= 0.684$ is achieved for $\lambda_c = 0.029$ and $\theta_c = 1.072$, where the position of this point is shown in Fig. 10.4.3(a).

Therefore, the λ and θ values found using SSIM are choosen as the OpFlow parameters, giving the results shown in Fig. 10.4.4, which is similar to the visual inspection parameter estimation and where a significant improvement with respect to the digital PIV result is observed. It is interesting to note that the OpFlow result is denoised, capturing the small scale displacements that are hidden in the digital PIV result. Moreover, the result of the application of the SSIM metric to both image methods gives a small θ_c, so the proposed method effectively recover an important feature of Chambolle's method

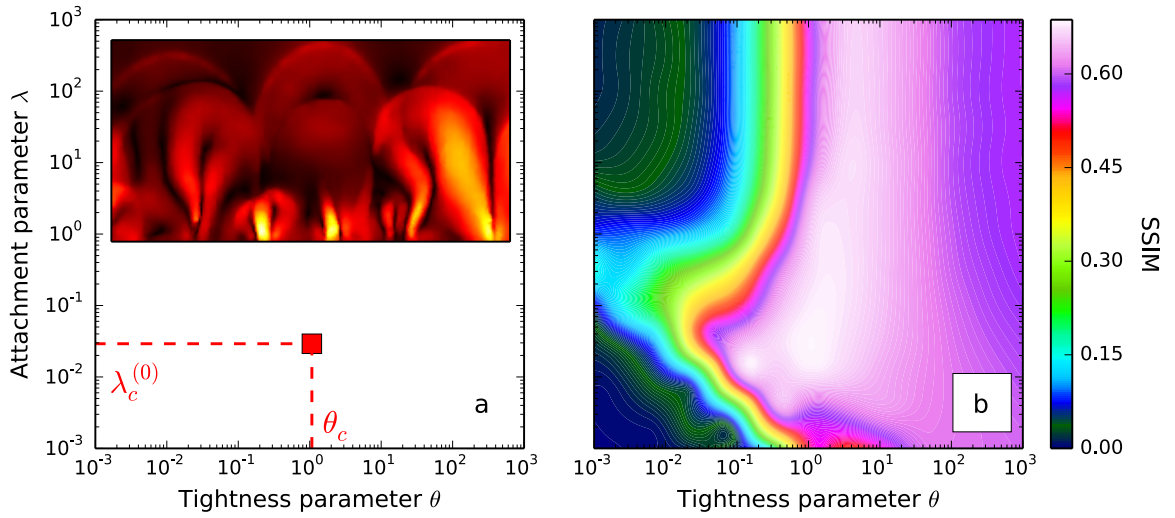

Figure 10.4.3: SSIM parameter space. The statistical strategy enables to define adequately the OpFlow parameters. The maximum value of SSIM was achieved for $\lambda_c = 0.029$ and $\theta_c = 1.072$ which is indicated by the square dot in figure (a). As result, the smooth OpFlow output using these parameter values is showed in the inset plot in figure (a). This plot is discussed in Fig. 10.4.4. Figure (b) shows the characteristic values of SSIM parameter space for the image pair analyzed. The structure of the SSIM parameter space is not universal and depends on the images

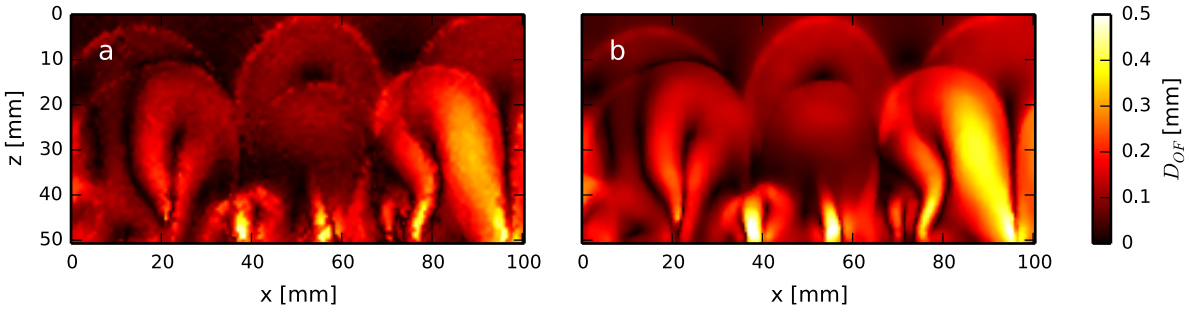

Figure 10.4.4: OpenPIV (a) compared with OpFlow result (b) for the apparent displacement of background dots pattern. The OpFlow image was generated using the parameters $\lambda = 0.029$ and $\theta = 1.072$. A significant improvement of the resolution of the displacement was achieved using OpFlow, in comparison with OpenPIV

(Chambolle, 2004) and λ is converted to the important parameter in OpFlow, because it controls the accuracy of the method. There is no theoretical method to determine the optimal values of both parameters from OpFlow equation. However, the empirical results from this kind of experiments suggest that the statistical methodology allows the definition of a good set of OpFlow parameters that ensures a good representation of the observed physical phenomena. For experimental image sequences, the methodology can be automated and the OpFlow parameters can be computed for each image. As

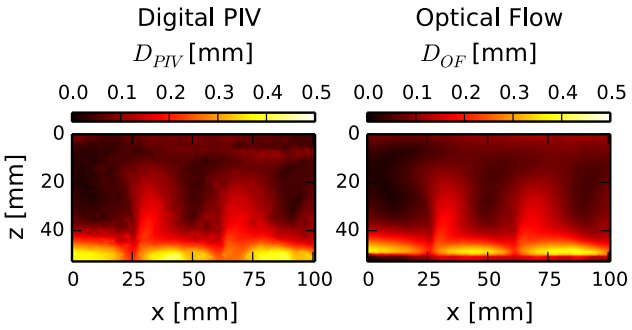

Figure 10.4.5: OpenPIV compared with OpFlow for the apparent displacement of background dots pattern, for an experiment where $f = 55\,\mathrm{mm}$, $f_r = 7.1$, $b = 1\,\mathrm{mm}$, $L_p = 8\,\mathrm{mm}$, $L_s = 100\,\mathrm{mm}$ and $s_o = 403\,\mathrm{mm}$. The OpFlow parameters are $\lambda = 0.02$ and $\theta = 2.48$

example, we observe that OpenPIV took about 30 s to analyse an image of 622 pixel × 1341 pixel in a MacBook Pro with an Intel Core i7 2.2 GHz processor, while the methodology using SSIM is a time-consuming process, taking about 15 min to analyse the same image. However, computing these parameters for a few images and calculating the mean values, we obtain a reasonable strategy to optimally set λ and θ. Once that has been done, the OpFlow parameters are set globally for each image. Using OpenMP libraries, the time execution of the OpFlow algorithm is aproximatelly 30 s.

To evidencing the capabilities of OpFlow in the edge detection and image denoising, on the right image of Fig. 10.4.5 it is possible to appreciate an horizontal boundary structure on the bottom zone of the image, which corresponds to the aluminium shim. This boundary is not detected by OpenPIV, as shown on the left image of Fig. 10.4.5. Additionally, the noise result obtained with OpenPIV is typical of cross-correlation methods applied to SS experiments and it is due to the image resolution of the method, where we use an interrogation window of $w = 16$ pixels with an overlap of 50%. On the other hand, OpFlow removes the noise, preserving the edges detected and improving the image resolution.

10.5 Thermal reconstruction

To reconstruct the thermal distribution, we use the mathematical theory presented in Chapter 8, Section 8.3 on page 108, where the temperatures at bottom and top of the cell are constants. Fig. 10.5.1 shows the result of the reconstruction of temperature from the apparent displacement on the background image shown in the right image of Fig. 10.4.5. In this figure, we observe few convective isolated plumes which are similar to the numerical results shown in Fig. 7.2.1. The conductive heat transfer is characterized by a stable temperature gradient in the whole domain, where the

temperatures at $z = 0$ and $z = H$ are the temperatures measured at the aluminium shims. The same figure shows the horizontally averaged temperature versus depth, $\bar{T}(z,t) = (1/L)\int_0^L T(\mathbf{x},t)\,dx$. $\bar{T}(z)$ has a constant value in the middle of the cell with constant standard deviation, which is a behavior observed in developed thermal convection in porous media (Otero et al, 2004).

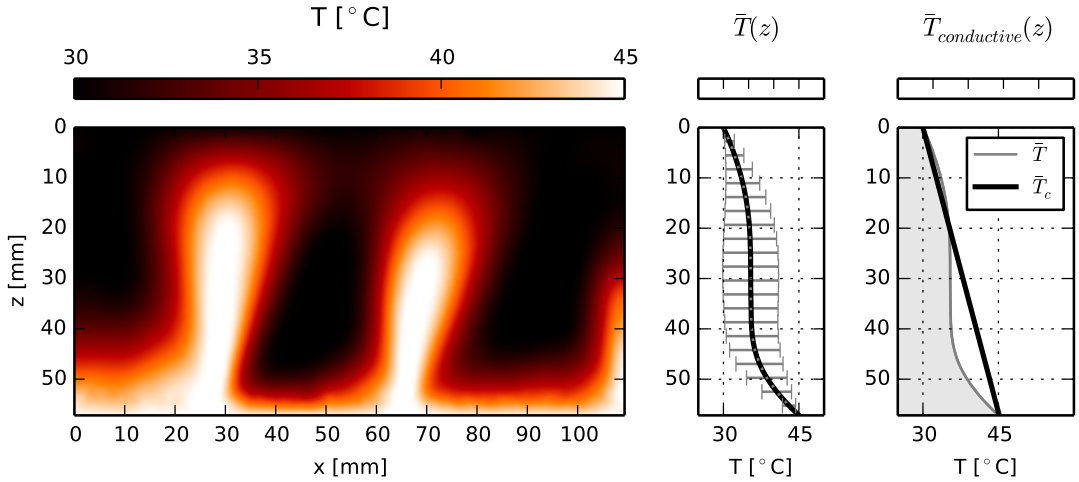

Figure 10.5.1: Thermal reconstruction of the OpFlow result presented in Fig. 10.4.5. The horizontal averaged temperature is shown with error bars, which is compared with the conductive regime. A deviation from the conductive regime is evidenced by means of the difference of the areas below the curve

However, it is interesting to note that the values of $\partial\bar{T}/\partial z$ are different at the vertical boundaries, which can be explained considering the variability of the dynamic viscosity of the fluid with temperature and the heat lost due to thermal conduction through the solid walls. In fact, the viscosity of PPG at 30 °C is 32 cP, while this value at 45 °C is 15 cP, which is an important difference compared with the viscosity of water in the same range of temperatures (See Chapter 3, Section 3.3 on page 21 for additional information). Defining the heat available per horizontal unit length as $Q_L^{(av)} = (1/L)\int_V \bar{\rho}\,c_p\,T\,dV = \bar{\rho}\,c_p\,b\int_0^H \bar{T}\,dz$, where $\bar{\rho}$ is the mean density between the range of temperatures considered, we see that the area below the curve of the observed $\bar{T}(z)$ is less than the theoretical curve for the purely conductive case. Considering $c_p = 2.51\,{}^{\mathrm{J}}/_{\mathrm{g\,K}}$ and $\bar{\rho} = 1.023 \pm 0.007\,{}^{\mathrm{g}}/_{\mathrm{cm}^3}$, where the error is related with the deviation from the mean value for a range of temperatures between 30 °C and 45 °C, we obtain $\Delta Q_L = Q_L^{(conv)} - Q_L^{(cond)} = -2.63 \pm 0.02\,{}^{\mathrm{J}}/_{\mathrm{cm}}$.

Thus, we have experimental evidence that some heat was conducted through the acrylic used to built the cell. This finding arises the question of how this heat transfer

affects the convective behavior of the fluid. This question has also been studied by Koster (1983), concluding that the acrylic affects the thermal convection, so the new question is what is the amount of heat lost by conduction and how the heat lost scales with Ra, for this kind of experiments.

The thermal conductivity of acrylic is similar to that of PPG, which is $k_{ppg} = 0.195 \pm 0.001\,{}^{\mathrm{W}}/_{\mathrm{m\,K}}$ (Sun and Teja, 2004). The error is related with the deviation from the mean value for a range of temperatures between 30 °C and 60 °C. To understand the energetic balance in thermal convection between the fluid and the acrylic, we analyse a transient convection regime for $Ra = 680$. The choice of this value is related with the observations of the geothermal convection in sedimentary basins (Clausnitzer et al, 2001).

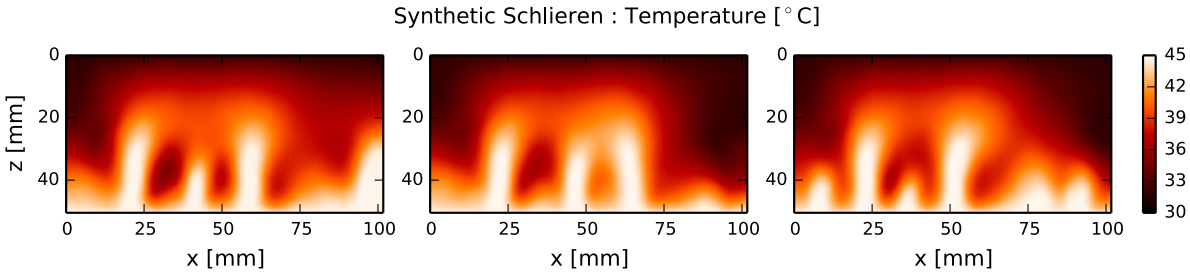

Figure 10.5.2: Thermal reconstruction for an experimental image sequence for $Ra = 680$. The time difference between images is $\Delta t = 5\,\mathrm{min}$, from left to right. Some well-known nonlinear behaviors such as coalescence and destabilization of protoplumes can be observed

Another example of thermal reconstruction is shown in Fig. 10.5.2. We can see many thermal plumes, where some nonlinear behaviors such as the coalescence and destabilization of protoplumes in the bottom boundary layer are evidenced. These processes are triggered by parcels of denser fluid that reach the lower regions of the cell and cause the convergence of parcels of less dense fluid. Due to viscosity effects, the dense fluid parcels move slowly in comparison with lighter fluid, so the observed nonlinear behavior is not only driven by density, but also by viscosity.

10.6 Transient dynamics

The transient regime is controlled by the temperature rise of the aluminium shims, which is slow. It takes about one hour to reach a constant temperature, as shown in Fig. 10.6.1. Because the top and bottom boundaries have temperatures that change

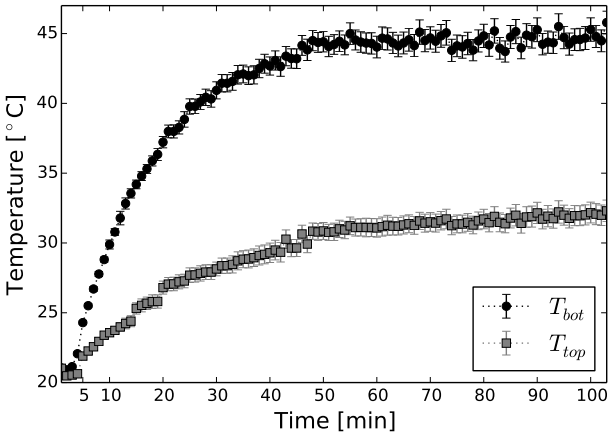

Figure 10.6.1: Temperatures of the aluminium shims, on bottom T_{bot} and top T_{top}. These measurements were used as boundary conditions for thermal reconstruction in the transient regime

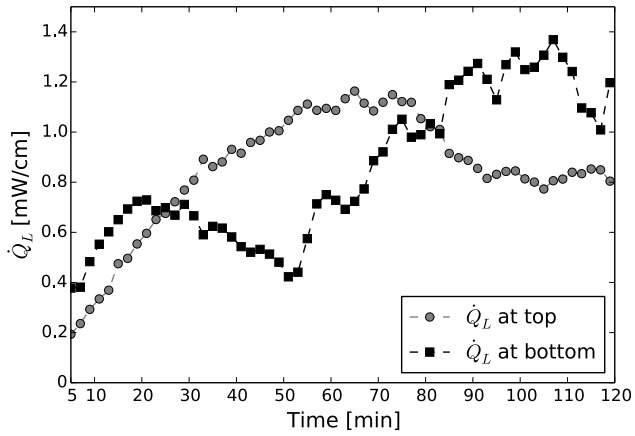

Figure 10.6.2: Conductive heat flux per unit length, at bottom and top of the cell, during the transient regime

with time, the lower zone of the cell shows the appeareance of a boundary layer that destabilizes in a few thermal fingers, as we show in Fig. 10.6.2. This result is a good example that shows the transition to a full developed convective dynamics, where the convection is driven by density and viscosity.

Fig. 10.6.2 shows the conductive flux at vertical boundaries, where the conductive flux per unit length is computed as $\dot{Q}_L = k_{ppg}\, b\, \partial\bar{T}/\partial z$, being k_{ppg} the thermal conductivity of PPG. From this figure, we can observe that the heat flux at the bottom has a local minimum at $t = 50\,\text{min}$, which coincides with the beginning of the destabilization of the thermal boundary layer. We define the mean value of a horizontal-averaged physical quantity $\bar{f}(z,t)$ as $\langle f\rangle(t) = (1/H)\int_0^H \bar{f}(z,t)\,dz$. Analysing the mean temperature evolution presented in Fig. 10.6.3, we can observe that this quantity grows monotonically in the transient regime, until reach an statistically constant value of $\langle T\rangle = 37.9 \pm 0.3\,°\text{C}$ from time $t = 80\,\text{min}$. In other words, the system reaches a steady-state regime from this time, where the amplitude and shape of thermal plumes seems to be similar.

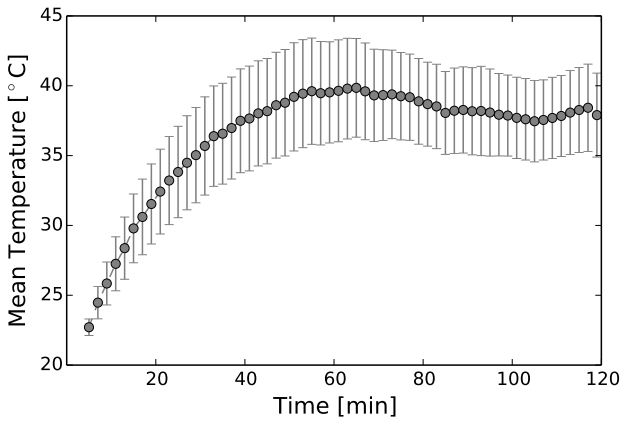

Figure 10.6.3: Mean temperature $\langle T \rangle$ as function of time. We can see that the temporal evolution of this quantity seems to have a statistically constant value from the time $t = 80\,\mathrm{min}$

Therefore, neglecting viscous dissipation and thermal dispersion, a first conclusion from the temperature reconstruction is that the difference between the conductive heat flux at top and bottom, from time $t = 80\,\mathrm{min}$ (see Fig. 10.6.2), can be explained if we take into account the energy lost by wall conduction.

The total amount of energy injected to the fluid is used mainly in two processes, (a) to locally increase the temperature of the fluid, i.e. $\partial T/\partial t \neq 0$ and (b) to exchange energy with the solid walls by conduction. The estimation of the amount of mechanical energy converted into heat is important for the correct interpretation of the energy balance of the system. The results obtained from the temperature maps, for this regime, are not sufficient to conclude any effect from the dynamic viscosity in the development of thermal fingers and more information is need to characterize the dynamics of the flow under these conditions.

Chapter 11

Conclusions and future work

In this thesis we have studied the problem of heat and mass transport for two-phase fluids in a porous medium, which has applications in the use of supercritical CO_2 in geothermal reservoirs. This work attempts to conciliate the experimental observations obtained in analogue fluid systems with a corrected theory of flow within Hele-Shaw cells, so this work can be seen as a first approach that contributes to the understanding of the physics of mass transfer in geothermal conditions at the laboratory scale. By means of theoretical modeling, numerical simulations and visualization, we have investigated the role of the perturbative corrections to the Darcy equation in heat and mass transport in an homogeneous porous medium.

Here, we have demonstrated through theory and numerical simulations that the inertial corrections to the Darcy equation are relevant for the scalings laws that governs both heat and mass transport. In Chapter 5 we derived a mathematical model for analogue experiments of CO_2 dissolution in geothermal brine using Hele-Shaw cells. The model is a generalization of the Polubarinova-Kochina equation for porous media, which contains the hydrodynamic dispersion term in the scalar transport equation, as well as the Brinkmann and Forchheimer terms. A new vertical buoyant term is obtained in the momentum equation. Interfacial tension effects is also considered in this model because CO_2 is partially miscible with water and it offers new phenomenology that can help to explain other storage mechanisms, such as residual trapping. We show that mechanical dispersion in the scalar transport equation cannot be neglected for analogue experiments, which is relevant to matching experimental and theoretical results.

We also study the mean scalar dissipation rate and how it scales with the Rayleigh number. Using dimensional analysis, we show that the scaling of the mean scalar dissipation rate for thermal convection in porous media can be written as $\langle \varepsilon_t \rangle_\tau \sim Ra_t^{m(\epsilon)}$, which is due to the contribution of the mechanical dispersion F_{mech} in the scalar transport equation. This has not been considered in previous works. Here, ϵ is the perturbative parameter. This observation offers new insight about mixing processes in porous media and its quantification. On the other hand, for mixing convection, we give a new hypothesis about the mass transfer scaling. Here, we show that $\langle Nu_t \rangle \sim \Phi\, Ra_s \langle \varepsilon_s \rangle$, where Φ contains information about mechanical dispersion and lateral diffusion. This scaling proposal is new and offers a simple physical theory

to the experimental observations reported in literature.

In Chapter 6, we studied the linear stability of two interesting problems in transport phenomena in porous media, thermal convection and Rayleigh-Taylor instability driven by density contrast. For both problems, we used the Hele-Shaw model derived in the previous chapter. We extended the results reported in the literature for thermal convection. These results have been obtained using different mathematical strategies considering free slip and no slip boundary conditions. On the other hand, for the Rayleigh-Taylor instability, we used the dominant-mode solution to analyze the effects of geometry (inertial terms) and interfacial tension in the onset of convection. In the limit of porous media, we recovered the results reported in the literature. For other cases, we show that the inertial terms of the momentum equation deviate the Darcian prediction but maintaining the scaling law of the type $\tau_c = a\, Ra_s^{-1}$, while interfacial tension stabilizes the diffusive boundary layer in time, delaying the onset of convection at least in one order of magnitude.

In the second part of this work, we implemented the mathematical model derived in Chapter 5 for the thermal convection case using spectrally-based numerical techniques. In Chapter 7, the application of the model to heat transport shows new scalings for the time-averaged Nusselt number and mean thermal dissipation rate, which depends on the perturbative parameter ϵ. For $\epsilon = 10^{-3}$, we obtain $\langle Nu \rangle_t \sim Ra_t^{0.90}$ and $\langle \varepsilon \rangle \sim Ra_t^{-0.09}$, while for $\epsilon = 10^{-2}$, we obtain $\langle Nu \rangle_t \sim Ra_t^{0.40}$ and $\langle \varepsilon \rangle \sim Ra_t^{-0.59}$. These results support our scaling hypothesis derived before and it explains some anomalous scalings observed in experiments using Hele-Shaw cells, by means of the introduction of both the mechanical dispersion term in the scalar transport equation and inertial corrections in the momentum equation.

In the third and final part of this work, in Chapter 8 we implemented two optical visualization techniques to obtain images of the convective processes, light attenuation and quantitative Schlieren. Althought both techniques are easy to implement in the laboratory, the image analysis is challenging. In Chapter 9 we introduce two image processing methods that have not been used in experimental fluid mechanics, the multiphase image segmentation and TV-L^1 optical flow, both based on variational principles. In particular, in Chapter 9 we show that the Chan-Tai method splits well four dynamic phases of the mixing process, without the need to have structural information such as the density and velocity fields. This result is fundamental for the computation of some physical measures in laboratory experiments, such as the convective flux, using only geometrical information.

In Chapter 10, we present a methodology based on the use of the TV-L^1 optical flow method (OpFlow) to analyze experimental images obtained by the SS technique. Comparing the images analyzed by digital PIV and OpFlow, we can estimate the optimal OpFlow parameters for a specific set of experimental images, to improve the image resolution. As a benchmark case study where Synthetic Schlieren can be applied succesfully in the measurement of a scalar quantity, in this case temperature, we perform laboratory experiments of thermal convection in porous media, using a Hele-Shaw cell filled with propylene-glycol as working fluid. The main advantages of the methodology to capture refractive index gradients using OpFlow are both image denoising and edge detection, which are crucial for further analysis of reconstructed temperature maps. We provide results that show the capabilities of OpFlow for the analysis of this type of experiments. These results are impossible to obtain using digital PIV, despite that the correlation methods can be enhanced using a smoothing post-processing.

Using the dense flow field given by OpFlow, we reconstruct the temperature map for an experimental transient regime and we study the conductive heat flux per unit length and the mean temperature as function of time, observing that the developed convection reaches a steady-state regime. Qualitatively, our thermal measurements show that the thermal boundary layer at the bottom destabilizes after a transient time. Above this boundary layer, heat transport is enhanced by a vertical advective flux that must be quantified. A work related with this problem is in progress. We will measure simultaneously both the temperature and velocity fields in order to better characterize the fluid dynamics of this type of systems.

In order to extend the work presented in this thesis, in the following we present some works in progress that will be completed in the present year.

11.1 Interfacial detection using image segmentation

The Chapter 9, Section 9.1, is devoted in the introduction of image segmentation methods based in variational principles as a tool to detect interfacial motion. In that section, the Chan-Tai segmentation method allow us to separate the mixing dynamics in four meaningful phases: fluid A, fluid B, convective penetration of fluid A and the mixing zone (see Fig. 9.1.6 on page 121). From all these phases, the convective penetration of fluid A has the deeper physical meaning because the boundary of this phase represents the zone of maximum isopycnal or density, which is fundamental in the computation of the convective flux (see Eqn. (5.4.9) on page 62). However, although

these interesting results, Chan-Tai multiphase model is expensive computationally and requires an initial level-set close to the final image segmentation, which is due to the non-convexity nature of its variational formulation. Remember that the term non-convex means that the minimum of a functional depends on the initial functions selected for its calculation. Therefore, for the segmentation model applied to the experimental images shown in Fig. 9.1.1 on page 114, it is essential to have a variational principle that be convex, where we have one and only one minimum in the image domain.

An interesting variational formulation that can solve the problem is the model of Cai et al (2013) given by the functional

$$J_c[u] = \int_\Omega \left(\frac{\lambda}{2} (f-u)^2 + \frac{\mu}{2} |\nabla u|^2 + |\nabla u| \right) dA \,, \tag{11.1.1}$$

where the minimization of Eqn. (11.1.1) gives one and only one solution $u(\mathbf{x})$ which can be solved using popular algorithms such as the split-Bregman (Goldstein and Osher, 2009) (see Appendix D for further information). For $\mu = 0$, Eqn. (11.1.1) is reduced to the known ROF model for image restoration (Rudin et al, 1992). Next, the function $u(\mathbf{x})$ can be easily segmented in different phases by thresholding.

The objective of the proposed work is to separate in different phases the mixture dynamics observed when deionized water is mixed with propylene-glycol (PPG) in a Hele-Shaw cell. We performed experiments using both fluids, where the experimental setup is shown in Fig. 8.2.1, page 107. The light attenuation technique discussed in Chapter 8, Section 8.2, was used. To visualize the dynamics, the passive dye used was Rhodamine B which was dissolved in deionized water in a concentration of $1\times10^{-5}\,\mathrm{g/cm^3}$. The light absorption properties of Rhodamine B in water and PPG at 20 °C are shown in Fig. 11.1.1

The transmisivity properties of the Bayer filter in a CMOS APS sensor are displayed in Fig. 11.1.2. From Figs. 11.1.1 and 11.1.2, it is clear that the green channel of a RGB image of the experiment is more sensible to detect the light absorption due to the dye dissolved in water.

After having selected the green channel of RGB images and then applying some morphological tools, we obtain images of good quality which are shown in Fig. 11.1.3. In fact, the image resolution is better than the experimental images reported in literature and discussed in Chapter 4, Section 4.2 (Kneafsey and Pruess, 2009; Neufeld et al, 2010; Backhaus et al, 2011; Hewitt et al, 2013).

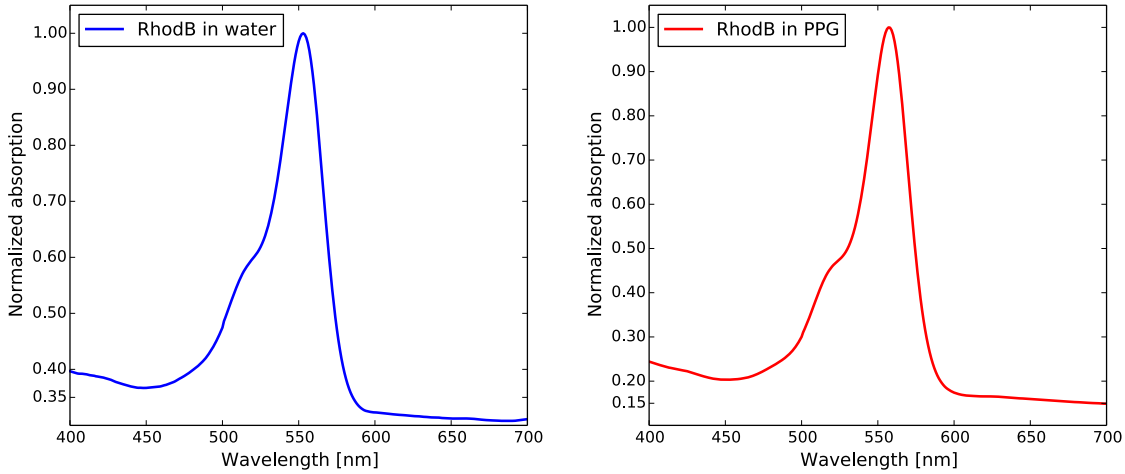

Figure 11.1.1: Light absorption properties of Rhodamine B in water and PPG. Data were obtained with the colaboration of prof. J. Brunet and R. Sánchez in the Spectroscopy and Photophysics laboratory of the Pontifical Catholic University of Valparaíso, campus Curauma.

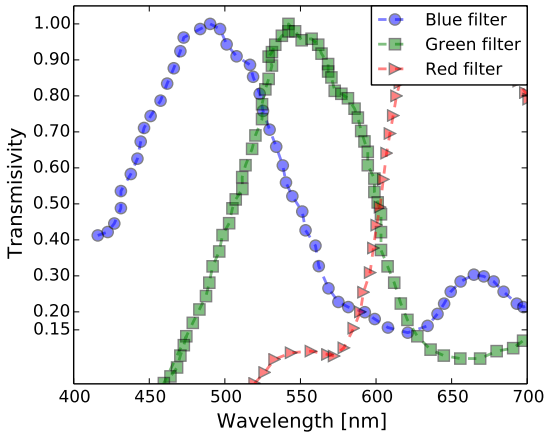

Figure 11.1.2: Normalized transmisivity properties of the Bayer filter in a CMOS APS sensor. See Fig. 8.2.2, page 108, which shows an academic example of transmisivity for the red channel

Therefore, to accomplish the objectives of the proposed work, we will apply Eqn. (11.1.1) to the images displayed in Fig. 11.1.3. After that, to find the final segmentation, we will use the known K-means algorithm for four phases. One of these phases will be the convective penetration of water in PPG, called phase $P_w^{(ppg)}$, so we will compute the boundary of $P_w^{(ppg)}$ using the classical Chan-Vese segmentation. We know that the mean scalar dissipation ratio is defined as $\langle \varepsilon \rangle = \ell_{mix}/L$ (see Chapter 5, Section 5.4.2), so the computation of the mixing length ℓ_{mix} will be counting the number of pixels of the zero level-set and dividing it by the number of pixels of the horizontal direction of the image. If $\langle \varepsilon \rangle$ is constant in time, then we expect that the flux be constant in time.

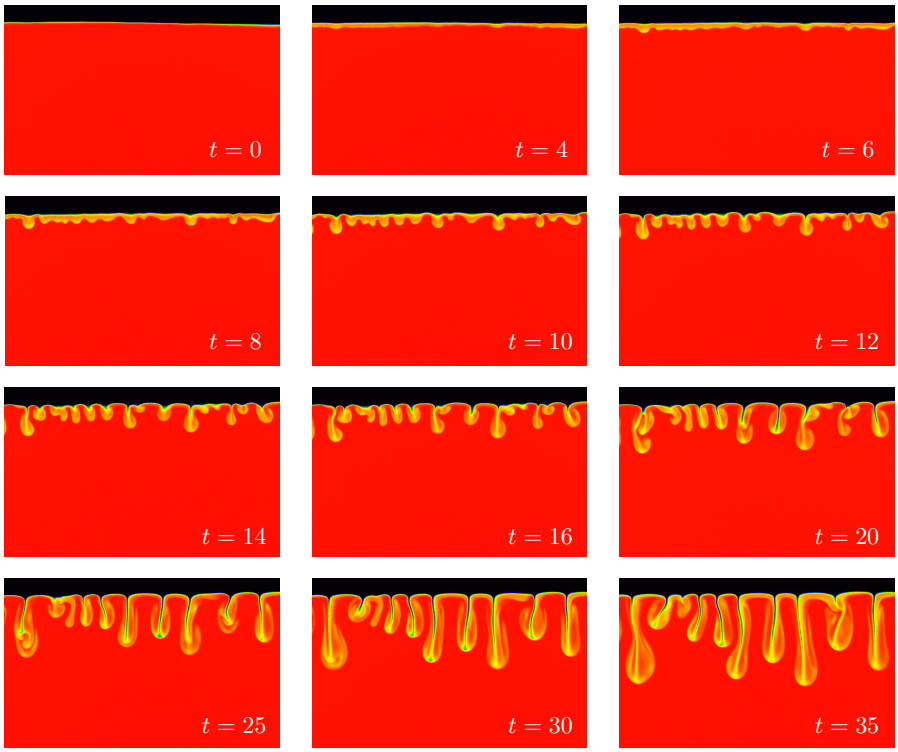

Figure 11.1.3: Results of a density-driven convection experiment, for different dimensionless times, where deionized water (black) is mixing with PPG (red). This sequence is also shown in Fig. 9.1.1, page 114, where some images were used in the application of Chan-Vese and Chan-Tai segmentation methods. These images mimic the convective dissolution of CO_2 in a geological formation

To demonstrate that, we can compute the quantity Q_c as the ratio between the area of $P_w^{(ppg)}$ and the area of the cell (Backhaus et al, 2011), which is easy to do. If Q_c is linear in time, then the flux $F_c = \dot{Q}_c$ will be constant. The originality of the proposed work is based on the inclusion of variational segmentation techniques in the detection of the interfacial zone of a mixing system, without using some structural information such as the density and velocity fields. By means of geometrical information, we want to demonstrate that segmentation can be an important tool for fluid mixing studies.

11.2 Numerical simulations

11.2.1 Thermal convection

From the results obtained in Chapter 7 and the scaling assumptions given in Chapter 5, Section 5.4.2, an interesting future work is the demonstration that the general scaling law for heat transport in porous media is given by the expression

$$\langle Nu \rangle_t = \Phi\left(\epsilon^2 Ra_t\right) Ra_t \, \langle \varepsilon_t \rangle \sim Ra_t^{1+m(\epsilon)+\sqrt{\epsilon}\, g(\epsilon)} \,, \tag{11.2.1}$$

where $\Phi \sim Ra_t^{\sqrt{\epsilon}\, g(\epsilon)}$ and $\langle \varepsilon \rangle \sim Ra_t^{m(\epsilon)}$. The methodology will be the execution of numerical simulations for several values of ϵ, which allow us to determine the scaling law for both the Nusselt number and the mean scalar dissipation rate. With this information, we will be able to compute the function $g(\epsilon)$.

11.2.2 Mixing convection

We want to study numerically the dissolution of a fluid into another in isothermal conditions. The viscosity of the fluid mixing is constant. We use the *flow_solve* software (Winters and de la Fuente, 2012) to study the effects of hydrodynamic dispersion in the dimensionless convective flux and mean scalar dissipation rate for this problem.

The study is focused in the analogue-fluid model discussed in Chapter 5, Section 5.4.2, where the density is a nonlinear function of concentration and no-flux boundary conditions are imposed in all walls. Therefore, we define the density ρ_f as

$$\rho_f(S_w) = \rho_a + \frac{2\Delta_w(\rho_a - \rho_{in})}{1 - 2\Delta_w} S_w - \frac{(\rho_a - \rho_{in})}{1 - 2\Delta_w} S_w^2 \tag{11.2.2}$$

where S_w is the concentration of a secondary fluid in the ambient fluid, ρ_a is the ambient fluid density, ρ_{in} is the secondary fluid density and Δ_w is the dimensionless concentration where fluid density is maximum. Rayleigh-Taylor instability appears when the fluid mixing is more dense than the fluid ambient, so the maximum density difference that generates the instability is defined as $\Delta\rho = \Delta_w^2(\rho_a - \rho_{in})/(1 - 2\Delta_w)$. For PPG+water solutions, where PPG is the ambient fluid, we have $\Delta\rho = 9\,{}^{\mathrm{kg}}/_{\mathrm{m}^3}$ at $\Delta_w = 0.26$ (see Chapter 3, Section 3.3 for further information). For $\Delta_w \geq 0.5$, Eqn. (11.2.2) is not valid.

The initial conditions are $\mathbf{u}(\mathbf{x}, t) = \mathbf{0}$ and $S_w(\mathbf{x}, t = 0) = S_o(z) + \delta_s(\mathbf{x})$, where

$$S_o(z) = \frac{1}{4} - \frac{2}{\pi}\sum_{n=1}^{N}\frac{1}{n}\,\sin\left[\frac{n\pi z_o}{H}\right]\cos\left[\frac{n\pi z}{H}\right]e^{-n^2\pi^2\tau}$$

$$\delta_s(\mathbf{x}) = A\ \mathrm{rand}(x)\ \exp\left[-\frac{(z-z_o)^2}{\sigma_z^2}\right]$$

with $\mathrm{rand}(x) \in [-1,1]$ the uniform distribution, $N = 1\times10^6$ is the number of modes, $\tau = 1\times10^{-5}$ is a diffusion parameter and $z_o < H$ is the height of the initial fluid interfase. Fig. 11.2.1 shows the graph of this initial condition.

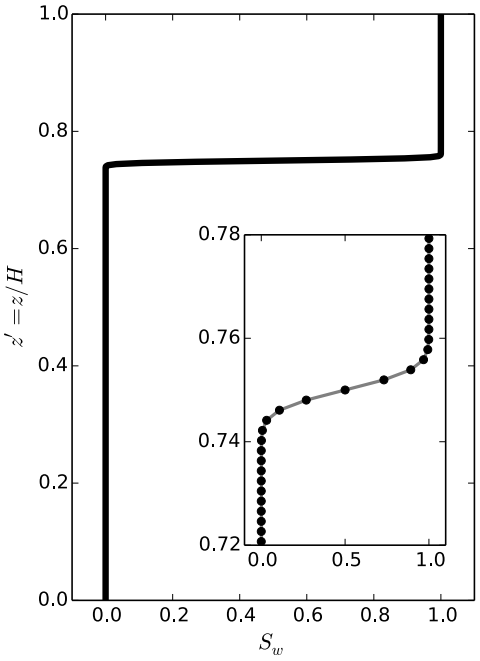

Figure 11.2.1: Initial condition for $S_w(\mathbf{x}, t = 0) = S_o(z)$ with $z_o = 3H/4$. The inset graph shows the same curve using $n_z = 513$ grid points, in the window where is the interfacial zone. See Fig. 4.3.1, page 44, which shows the miscible case discussed by Hewitt et al (2013)

In the simulations, we use the following fixed parameters, $\rho_a = 1035\,\mathrm{kg/m^3}$, $\rho_{in} = 1000\,\mathrm{kg/m^3}$ and $\Delta_w = 0.3$. With this values, $\Delta\rho = 7.875\,\mathrm{kg/m^3}$. The height H depends on Rayleigh number . Finally, for initial conditions we have $z_o = 3H/4$ and $\sigma_z = 3\Delta z$. As example, Fig. 11.2.2 shows some results of the simulations for $Pr = 10$, $Ra_s = 3981$ and $Pe_s = 4.1833$, in a box of aspect ratio $L' = L/H = 1/2$.

Some of the objectives of this future work are: (a) To demonstrate that the scaling law for mass transfer in mixing convection can be written as

$$\langle Nu\rangle_t = \Phi\left(\epsilon^2 Ra_\varphi, \Delta S_w/S_w^{(m)}\right) Ra_s\,\langle\varepsilon_s\rangle \quad ; \quad \rho(S_w^{(m)}) = \rho_{max}\ , \tag{11.2.3}$$

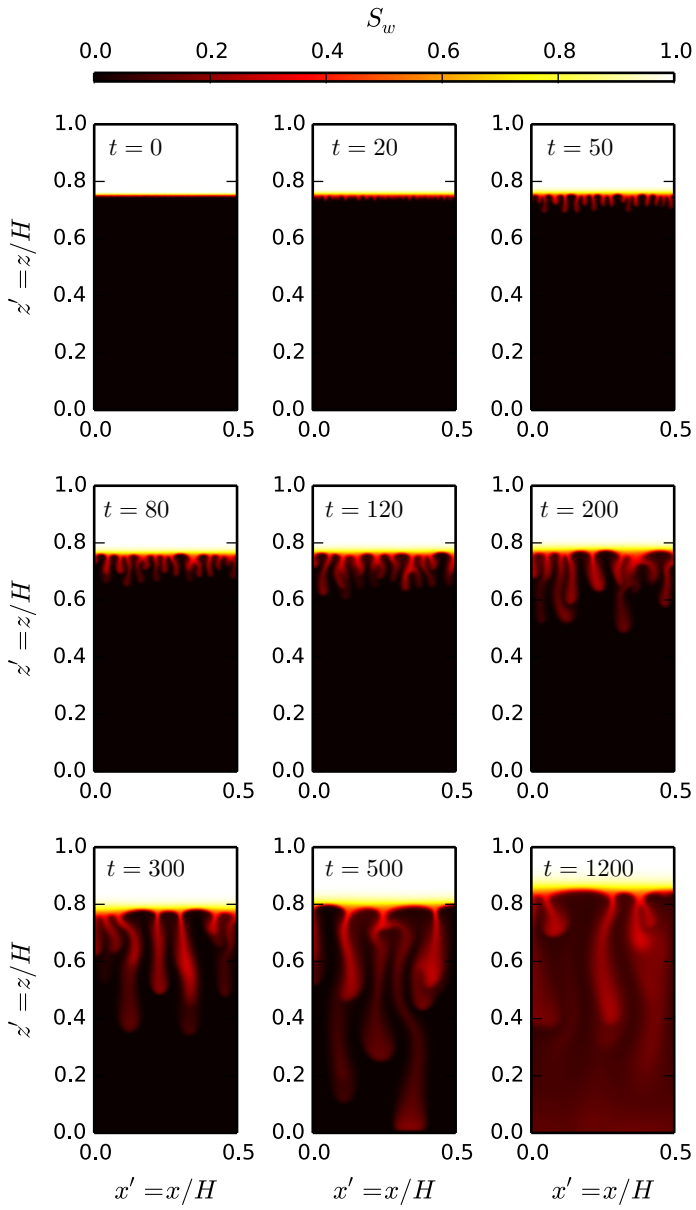

Figure 11.2.2: Results of the numerical simulations of the analogue model presented in this section, for different dimensionless times. The dimensionless parameters are $Pr = 10$, $Ra_s = 3981$ and $Pe_s = 4.1833$. It is interesting to note that the interfacial zone between both fluids moves upward from $h_{int} = 0.75$ at $t = 0$ to $h_{int} = 0.8$ at $t = 500$

and (b) to use Chan-Vese segmentation to compute the normal vector of the maximum isopycnal curve, with the aim to compute the convective flux given in Eqn. (5.4.9). This idea is original, because flux is computed using indirect information such as the upward velocity of the interface.

11.2.3 Mixing convection in geothermal conditions

This future work will be a good contribution of this thesis in the geophysical context, because it will study the fluid dynamics when a geothermal reservoir is turned off due to the injection of a cool fluid. Gravity currents, secondary instabilities and enhancement of heat transport will be the main topics of study. For its analysis, we will use the equations and tools developed in this thesis. The schematic picture of the simulations will be similar to the image displayed in Fig. 5.2.1, page 51.

Bibliography

Adams BM, Kuehn TH, Bielicki JM, Randolph JB, Saar MO (2014) On the importance of the thermosiphon effect in CPG (CO2 plume geothermal) power systems. Energy 69:409–418, doi: 10.1016/j.energy.2014.03.032

Adams BM, Kuehn TH, Bielicki JM, Randolph JB, Saar MO (2015) A comparison of electric power output of CO_2 Plume Geothermal (CPG) and brine geothermal systems for varying reservoir conditions. Applied Energy 140:365–377, doi: 10.1016/j.apenergy.2014.11.043

Arendt B, Dittmar D, Eggers R (2004) Interaction of interfacial convection and mass transfer effects in the system CO_2-water. Int J Heat Mass Tran 47:3649–3657, doi: 10.1016/j.ijheatmasstransfer.2004.04.011

Aris R (1956) On the dispersion of a solute in a fluid flowing through a tube. Proc R Soc London, Ser A 235:67, doi: 10.1098/rspa.1956.0065

Atchenson B, Heidrich W, Ihrke I (2009) An evaluation of optical flow algorithms for background oriented schlieren imaging. Exp Fluids 46:467–476, doi: 10.1007/s00348-008-0572-7

Audigane P, Gaus I, Czernichowski-Lauriol I, Pruess K, Xu T (2007) Two-dimensional reactive transport modelling of CO_2 injection in a saline aquifer at the Sleipner site. Amer J of Science 307:974–1008

Auriault J (1987) Nonsaturated deformable porous media: Quasistatics. Transp Porous Med 2:45–64, doi: 10.1007/BF00208536

Babushkin I, Demin V (2006) Experimental and theoretical investigation of transient convective regimes in a Hele-Shaw cell. Fluid Dynamics 41:323–329, doi: 10.1007/s10697-006-0047-6

Bachu S, Gunther W, Perkins E (1994) Aquifer disposal of CO_2: Hidrodynamic and mineral trapping. Energy Conserv Mgmt 35:269–279

Backhaus S, Turitsyn K, Ecke RE (2011) Convective Instability and Mass Transport of Diffusion Layers in a Hele-Shaw Geometry. Phys Rev Lett 106:104,501, doi: 10.1103/PhysRevLett.106.104501

Baker S, Scharstein D, Lewis JP, Roth S, Black MJ, Szeliski R (2011) A Database and Evaluation Methodology for Optical Flow. Int J Comput Vis 92:1–31, doi: 10.1007/s11263-010-0390-2

Barron J, Fleet D, Beauchemin S (1994) Performance of optical flow techniques. Int J Comput Vis 12:43–77

Battistelli A, Calore C, Pruess K (1997) The simulator tough2/ewasg for modelling geothermal reservoirs with brines and non-condensible gas. Geothermics 26(4):437 – 464, doi: 10.1016/S0375-6505(97)00007-2, URL http://dx.doi.org/10.1016/S0375-6505(97)00007-2

Ben Y, Demekhin EA, Chang HC (2002) A spectral theory for small-amplitude miscible fingering. Phys Fluids 14:999–1010, doi: 10.1063/1.1446885

Benson S, Cook P, et al (2006) Underground Geological Storage. In: Metz B, Davidson O, de Coninck H, Loos M, Meyer L (eds) Carbon Dioxide Capture and Storage. Special Report of the Intergovernmental Panel on Climate Change, Cambridge University Press, pp 195–276

Bizon C, Werne J, Predtechensky AA, Julien K, McCormick WD, Swift JB, Swinney HL (1997a) Plume dynamics in quasi-2D turbulent convection. Chaos 7:107, doi: 10.1063/1.166243

Bizon C, Werne J, Predtechensky AA, Julien K, McCormick WD, Swift JB, Swinney HL (1997b) Plume dynamics in quasi-2D turbulent convection. Chaos 7:107, doi: 10.1063/1.166243

Bratsun D, Wit AD (2004) On marangoni convective patterns driven by an exothermic chemical reaction in two-layer systems. Phys Fluids 16:1082–1096, doi: 10.1063/1.1648641

Breugem WP, Rees DAS (2006) A Derivation of the Volume-Averaged Boussinesq Equations for Flow in Porous Media with Viscous Dissipation. Transp Porous Med 63:1–12, doi: 10.1007/s11242-005-1289-1

Brown D (2000) A hot dry rock geothermal energy concept utilizing supercritical CO_2 instead of water. In: Proceedings of the Twenty-Fifth Workshop on Geothermal Reservoir Engineering, Stanford University, pp 233–238

Brox T, Bruhn A, Papenberg N, Weickert J (2004) High accuracy optical flow estimation based on a theory for warping. In: Pajdla T, Matas J (eds) Proc. 8th European Conference on Computer Vision, Springer-Verlag Berlin Heidelberg, Prague, 4, pp 25–36

Cabot WH, Cook AW (2006) Reynolds number effects on Rayleigh-Taylor instability with possible implications for type Ia supernovae. Nature Physics 2:562–568, doi: 10.1038/nphys361

Cai X, Chan R, Zeng T (2013) A Two-Stage Image Segmentation Method Using a Convex Variant of the Mumford-Shah Model and Thresholding. SIAM J Imaging Sci 6(1):368–390, doi: 10.1137/120867068

Caltagirone JP (1980) Stability of a saturated porous layer subject to a sudden rise in surface temperature: Comparison between the linear and energy methods. Q J Mechanics Appl Math 33(1):47–58, doi: 10.1093/qjmam/33.1.47

Celia MA, Bachu S, Nordbotten JM, Bandilla K (2015) Status of CO_2 storage in deep saline aquifers with emphasis on modeling approaches and practical simulations. Water Resour Res 51:6846–6892, doi: 10.1002/2015WR017609

Chambolle A (2004) An Algorithm for Total Variation Minimization and Applications. J Math Imaging Vis 20:89–97

Chan T, Tai X (2004) Level set and total variation regularization for elliptic inverse problems with discontinuous coefficients. J Comput Phys 193:40–66, doi: 10.1016/j.jcp.2003.08.003

Chan T, Vese L (2001) Active Contours without Edges. IEEE T Image Process 10:266–277, doi: 10.1109/83.902291

Chan TF, Osher S, Shen J (2001) The digital TV filter and nonlinear denoising. IEEE T Image Process 10:231–241, doi: 10.1109/83.902288

Cherkaoui A, Wilcock W (2001) Laboratory studies of high Rayleigh number circulation in an open-top Hele-Shaw cell: An analog to mid-ocean ridge hydrothermal systems. J Geophys Res 106:10,983, doi: 10.1029/2000JB900470

Clausnitzer V, Bayer U, Fuhrmann J (2001) Large-scale thermal convective instability in sedimentary basins. Eur Geophys Soc, Geophys Res Abstracts HS02-02

Collins M, Knutti R, Arblaster J, Dufresne JL, Fichefet T, Friedlingstein P, Gao X, Gutowski WJ, Johns T, Krinner G, Shongwe M, Tebaldi C, Weaver AJ, Wehner M (2013) Long-term Climate Change: Projections, Commitments and Irreversibility. In: Stocker TF, Qin D, Plattner GK, Tignor M, Allen S, Boschung J, Nauels A, Xia Y, Bex V, Midgley PM (eds) Climate Change 2013: The Physical Science Basis. Contribution of Working Group I to the Fifth Assessment Report of the Intergovernmental Panel on Climate Change, Cambridge University Press, Cambridge, United Kingdom and New York, NY, USA, pp 1029–1136, doi: 10.1017/CBO9781107415324.024

Cooper C, Crews J, Schumer R, Breitmeyer R, Voepel H, Decker D (2014) Experimental investigation of transient thermal convection in porous media. Transp Porous Med 104:335–347, doi: 10.1007/s11242-014-0337-0

Corpetti T, Heitz D, Arroyo G, Memin E, Santa-Cruz A (2005) Fluid experimental flow estimation based on an optical flow scheme. Exp Fluids 40:80–97, doi: 10.1007/s00348-005-0048-y

Croucher A, O'Sullivan M (2008) Application of the computer code TOUGH2 to the simulation of supercritical conditions in geothermal systems. Geothermics 37:622–634

Dalziel SB, Hughes GO, Sutherland BR (1998) Synthetic schlieren. In: Proceedings of the 8th International Symposium on Flow Visualization, Sorrento, pp 62.1–62.6

Dalziel SB, Hughes GO, Sutherland BR (2000) Whole field density measurements by synthetic schlieren. Exp Fluids 28:322–335, doi: 10.1007/s003480050391

Davies G (1999) Dynamic Earth: Plates, Plumes and Mantle Convection. Cambridge University Press, URL https://books.google.cl/books?id=t7kyQXKK6yMC

E Brown and J Saldivia (2000) Informe nacional sobre la gestión del agua en Chile. CEPAL, Naciones Unidas. http://www.cepal.org/samtac/noticias/documentosdetrabajo/8/23338/InCh01100.pdf, Online accessed 14 March 2016

Ehyaei D (2014) An Experimental Investigation on Solute Natural Convection in a Vertical Hele-Shaw cell. PhD thesis, University of Maryland, College Park

Elder J (1967a) Steady free convection in a porous medium heated from below. J Fluid Mech 27:29–48, doi: 10.1017/S0022112067000023

Elder J (1967b) Transient convection in a porous medium. J Fluid Mech 27:609–623, doi: 10.1017/S0022112067000576

Elder JW (1967c) Steady free convection in a porous medium heated from below. J Fluid Mech 27:29 – 48, doi: 10.1017/S0022112067000023

Enick R, Klara SM (1990) CO_2 solubility in water and brine under reservoir conditions. Chem Eng Commun 90:23–33, doi: 10.1080/00986449008940574

Ennis-King J, Paterson L (2003) Role of convective mixing in the long-term storage of carbon dioxide in deep saline formations. SPE J 10:349–356

Ennis-King JP, Paterson L (2005) Role of convective mixing in the long-term storage of carbon dioxide in deep saline formations. SPE Journal 10:349 – 356, doi: 10.2118/84344-PA

Farajzadeh R, Barati A, Delil HA, Bruning J, Zitha PLJ (2007) Mass Transfer of CO_2 Into Water and Surfactant Solutions. Pet Sci Technol 25(12):1493–1511, doi: 10.1080/10916460701429498

Farajzadeh R, Bruning J, Zitha PLJ (2009) Mass Transfer of CO_2 Into Water: Experiment and Modeling. Ind Eng Chem Res 48(13):6423–6431, doi: 10.1021/ie801521u

Farrel BF, Ioannou PJ (1996) Generalized Stability Theory. Part II: Nonautonomous Operators. J Atmos Sci 53:2041–2053

Foster TD (1965) Stability of a homogeneous fluid cooled uniformly from above. Phys Fluids 8:1249–1257, doi: 10.1063/1.1761393

Garcia J (2003) Fluid dynamics of carbon dioxide disposal into saline aquifers. PhD thesis, UC Berkeley, California

Gasda SE, Nordbotten JM, Celia MA (2012) Vertically averaged approaches for CO_2 migration with solubility trapping. Water Resour Res 47:W05,528, doi: 10.1029/2010WR009075

Getreuer P (2012) Chan-Vese Segmentation. Image Processing On Line 2:214–224, doi: 10.5201/ipol.2012.g-cv

Gibson J (1950) The perception of visual surfaces. The American journal of psychology 63(3):367–384

Gibson J (1966) The problem of temporal order in stimulation and perception. The Journal of psychology 62(2):141–149

Glennon JA, Pfaff RM (2003) The extraordinary thermal activity of El Tatio Geyser Field, Antofagasta Region, Chile. Geyser Observation and Study Association (GOSA) Transactions 8:31–78

Gojani AB, Obayashi S (2012) Assesment of some experimental and image analysis factors for background oriented schlieren measurements. Appl Optics 51:7554–7559, doi: 10.1364/AO.51.007554

Gojani AB, Kamishi B, Obayashi S (2013) Measurement sensitivity and resolution for background oriented schlieren during image recording. Journal of Visualization 16:201–207, doi: 10.1007/s12650-013-0170-5

Golding MJ, Neufeld JA, Hesse MA, Huppert HE (2011) Two-phase gravity currents in porous media. J Fluid Mech 678:248–270, doi: 10.1017/jfm.2011.110

Goldstein T, Osher S (2009) The split Bregman algorithm for L^1 regularized problems. SIAM J Imaging Sci 2:323–343

Gondret P, Rabaud M (1997) Shear instability of two-fluid parallel flow in a Hele-Shaw cell. Phys Fluids 9:3267, doi: 10.1063/1.869441

Graham MD, Steen P (1994) Plume formation and resonant bifurcations in porous-media convection. J Fluid Mech 272:67–90, doi: 10.1017/S0022112094004386

Grassmann S, Lohse D (2011) Multiple scaling in the ultimate regime of thermal convection. Phys Fluids 23:045,108, doi: 10.1063/1.3582362

Gray W, Herrera P, Gasda S, Dahle H (2012) Derivation of vertical equilibrium models for CO_2 migration from pore scale equations. Int J of Numer Analysis and Modelling 9(3):745–776

Gresho PM, Sani RL (1971) Stability of a fluid layer subjected to a step change in temperature: transient vs. frozen time analysis. Int J Heat Mass Transfer 14:207–221

Gupta SN, Prince JL (1996) Stochastic models for DIV-CURL optical flow methods. IEEE Signal Proc Let 3:32–34

Hansen J, Ruedy R, Sato M, Lo K (2010) Global Surface Temperature Change. Rev Geophys 48, doi: 10.1029/2010RG000345

Hartline BK, Lister RB (1977) Thermal convection in a Hele-Shaw cell. J Fluid Mech 79:379–389, doi: 10.1017/S0022112077000202

Hele-Shaw H (1898) The flow of water. Nature 58:34–36

Hewitt DR, Neufeld JA, Lister JR (2012) Ultimate Regime of High Rayleigh Number Convection in a Porous Medium. Phys Rev Lett 108:224,503, doi: 10.1103/PhysRevLett.108.224503

Hewitt DR, Neufeld JA, Lister JR (2013) Convective shutdown in a porous medium at high Rayleigh number. J Fluid Mech 719:551– 586, doi: 10.1017/jfm.2013.23

Hewitt DR, Neufeld JA, Lister JR (2014) High Rayleigh number convection in a three-dimensional porous medium. J Fluid Mech 748:879–895

Hidalgo JJ, Fe J, Cueto-Felgueroso L, Juanes R (2012) Scaling of Convective Mixing in Porous Media. Phys Rev Lett 109:264,503, doi: 10.1103/PhysRevLett.109.264503

Hidalgo JJ, MacMinnc CW, Juanes R (2013) Dynamics of convective dissolution from a migrating current of carbon dioxide. Adv Water Resour 62:511–519, doi: 10.1016/j.advwatres.2013.06.013

Hodneland E (2003) Segmentation of Digital Images. Master's thesis, University of Bergen

Holloway S (1997) An overview of the underground disposal of carbon dioxide. Energ Convers Manage 38:S193–S198

Horn B, Schunck B (1981) Determining optical flow. Artif Intell 17:185–203, doi: 10.1016/0004-3702(81)90024-2

Horne RN, O'Sullivan MJ (1974) Oscillatory convection in a porous medium heated from below. J Fluid Mech 66:339–352, doi: 10.1017/S0022112074000231

Hota TK, Pramanik S, Mishra M (2015) Non-modal linear stability analysis of miscible viscous fingering in a Hele-Shaw cell. arXiv preprint arXiv:150403734

Howard LN (1964) Convection at high Rayleigh number. In: Görtler H (ed) Applied Mechanics, Proc. 11th Intl Cong. Appl. Math., pp 1109–1115

Huang CS, Kelley MC, Hysell DL (1993) Nonlinear Rayleigh-Taylor instabilities, atmospheric gravity waves and equatorial spread F. J Geophys Res-Space 98:15,631–15,642, doi: 10.1029/93JA00762

Huppert HE, Neufeld JA (2014) The fluid mechanics of carbon dioxide sequestration. Annu Rev Fluid Mech 46:255–272, doi: 10.1146/annurev-fluid-011212-140627

IDI-Chile (2011) Temas Prioritarios para una Política Nacional de Recursos Hídricos. Instituto de Ingenieros de Chile. http://www.iing.cl/images/iing/pdf/Informe_Tem_prior_rec_hid.pdf, Online accessed 14 March 2016

ING-Chile (2011) Principal fuente energética de Chile: Generación termoeléctrica. Revista Ingenieros n° 197. http://www.ingenieros.cl/2011-01-revista-ingenieros-enero-marzo/, Online accessed 14 March 2016

Ippolito I, Daccord G, Hinch E, Hulin J (1994) Echo tracer dispersion in model fractures with a rectangular geometry. J Contam Hydrol 16:87

Jenny P, Lee JS, Meyer DW, Tchelepi HA (2014) Scale analysis of miscible density-driven convection in porous media. J Fluid Mech 749:519–541, doi: 10.1017/jfm.2014.229

Jha B, Cueto-Felgueroso L, Juanes R (2011a) Fluid mixing from viscous fingering. Phys Rev Lett 106:194,502, doi: 10.1103/PhysRevLett.106.194502

Jha B, Cueto-Felgueroso L, Juanes R (2011b) Quantifying mixing in viscously unstable porous media flows. Phys Rev E 84:066,312, doi: 10.1103/PhysRevE.84.066312

Jha B, Cueto-Felgueroso L, Juanes R (2013) Synergetic fluid mixing from viscous fingering and alternating injection. Phys Rev Lett 111:144,501, doi: 10.1103/PhysRevLett.111.144501

Joseph D, Huang A, Hu H (1996) Non-solenoidal velocity effects and Korteweg stresses in simple mixtures of incompressible liquids. Physica D 97:104–125

Kass M, Witkin A, Terzopoulos D (1988) Snakes: Active Contour Models. Int J Comput 1:321–331, doi: 10.1007/BF00133570

Khattab IS, Bandarkar F, Khoubnasabjafari M, Jouyban A (2012) Density, viscosity, surface tension, and molar volume of propylene glycol + water mixtures from 293 to 323 K and correlations by the Jouyban?Acree model. Arabian Journal of Chemistry doi: 10.1016/j.arabjc.2012.07.012

Kirtman B, Power SB, Adedoyin JA, Boer GJ, Bojariu R, Camilloni I, Doblas Reyes FJ, Fiore AM, Kimoto M, Meehl GA, Prather M, Sarr A, Schar C, Sutton R, Van Oldenborgh GJ, Vecchi G, Wang HJ (2013) Near-term Climate Change: Projections and Predictability. In: Stocker TF, Qin D, Plattner GK, Tignor M, Allen S, Boschung J, Nauels A, Xia Y, Bex V, Midgley P (eds) Climate Change 2013: The Physical Science Basis. Contribution of Working Group I to the Fifth Assessment Report of the Intergovernmental Panel on Climate Change, Cambridge University Press, Cambridge, United Kingdom and New York, NY, USA, pp 953–1028, doi: 10.1017/CBO9781107415324.023

Kneafsey TJ, Pruess K (2009) Laboratory Flow Experiments for Visualizing Carbon Dioxide-Induced, Density-Driven Brine Convection. Transp Porous Med 82:123–139, doi: 10.1007/s11242-009-9482-2

Korteweg DJ (1901) Sur la forme que prennent les équations du mouvement des fluides si l'on tient compte des forces capillaires causées par des variations de densité considérables mais continues et sur la théorie de la capillarité dans l'hypothèse d'une variation de la densité. Arch Néer Sci Exactes et Nat Sér II 6:1–24

Koster JN (1983) Interferometric investigation of convection in plexiglass boxes. Exp Fluids 1:121–128, doi: 10.1007/BF00272010

Koster JN, Muller U (1982) Free convection in vertical gaps. J Fluid Mech 125:429–451, doi: 10.1017/S0022112082003425

Kumar P, Muralidhar K (2012) Schlieren and Shadowgraph Methods in Heat and Mass Transfer. SpringerBriefs in Applied Sciences and Technology, Springer New York, doi: 10.1007/978-1-4614-4535-7

Kvernvold O, Tyvand PA (1981) Dispersion effects on thermal convection in a hele-shaw cell. Int J Heat Mass Transfer 24:887–890

Lahssen A (1976) Geothermal exploration in northern Chile - Summary. In: Halbouty MT, Maher JC, , Lian HM (eds) Circum-Pacific Energy and Mineral Resource, American Association of Petroleum Geologists Memoir, chap 25, pp 169–175

Lahssen A (1986) Origen y potencial de energía geotérmica en los Andes de Chile. In: Frutos J, Oyarzún R, Pincheira M (eds) Geología y Recursos Minerales de Chile, Univ. de Concepción, Chile, p 423

Lahssen A, Trujillo P (1975) El tatio geothermal field, Chile. In: Proceedings 2nd U.N. Symposium on Development and Use of Geothermal Resources, San Francisco, CA, pp 157–178

Lahssen A, Sepúlveda F, Palacios C (2005) Present status of geothermal exploration in Chile. In: Proceedings, World Geothermal Congress 2005, Antalya, Turkey

Lahssen A, noz NM, Parada MA (2010) Geothermal development in Chile. In: Proceedings, World Geothermal Congress 2010, Bali, Indonesia

Lahssen A, Rojas J, Morata D, Aravena D (2015) Geothermal Exploration in Chile: Country Update. In: Proceedings, World Geothermal Congress 2015, Melbourne, Australia

Le Borgne T, Dentz M, Davy P, Bolster D, Carrera J, de Dreuzy JR, Bour O (2011) Persistence of incomplete mixing: A key to anomalous transport. Phys Rev E 84:015,301, doi: 10.1103/PhysRevE.84.015301, URL http://link.aps.org/doi/10.1103/PhysRevE.84.015301

Lee S, Kim S (2004) Application of holographic interferometry and 2D PIV for HSC convective flow diagnostics. Meas Sci Technol 15:664, doi: 10.1088/0957-0233/15/4/008

Lele SK (1992) Compact Finite Difference Schemes with Spectral-like Resolution. J Comput Phys 103:16–42

Letelier JA, Herrera P, Mujica N, Ortega JH (2016) Enhancement of synthetic schlieren image resolution using total variation optical flow: application to thermal experiments in a Hele-Shaw cell. Exp Fluids 57(2):1–14, doi: 10.1007/s00348-015-2109-1

Liberzon A, Gurka R, Taylor Z (2009) Openpiv home page. [Online], available: http://www.openpiv.net

Linderberg E, Wessel-Berg D (1997) Vertical convection in an aquifer column under a gas cap of CO_2. Energy Conserv Mgmt 38:229–234

Lucas B, Kanade T (1981) An iterative image registration technique with an application to stereo vision. In: Proc. Seventh International Joint Conference on Artificial Intelligence, Vancouver, pp 674–679

MacMinn CW, Juanes R (2013) Buoyant currents arrested by convective dissolution. Geophys Res Lett 40(10):2017–2022, doi: 10.1002/grl.50473

MacMinn CW, Neufeld JA, Hesse MA, Huppert HE (2012) Spreading and convective dissolution of carbon dioxide in vertically confined, horizontal aquifers. Water Resour Res 48, doi: 10.1029/2012WR012286

Magliocco M, Kneafsey T, Pruess K, Glaser S (2011) Laboratory experimental study of heat extraction from porous media by means of CO_2. In: Thirty Sixth Workshop on Geothermal Reservoir Engineering

Mainhagu J, Golfier F, Oltean C, Bues M (2012) Gravity-driven fingers in fractures: experimental study and dispersion analysis by moment method for a point-source injection. J Contam Hydrol 132:12–27, doi: 10.1016/j.jconhyd.2012.02.004

Marquez-Neila P, Baumela L, Alvarez L (2014) A Morphological Approach to Curvature-Based Evolution of Curves and Surfaces. IEEE T Pattern Anal 36:2–17, doi: 10.1109/TPAMI.2013.106

Martin J, Rakotomalala N, Salin D (2002) Gravitational instability of miscible fluids in a Hele-Shaw cell. Phys Fluids 14:902, doi: 10.1063/1.1431245

ME-Chile (2015) Energía 2050. Política Energética de Chile. Ministerio de Energía de Chile. http://www.energia2050.cl/uploads/libros/libro_energia_2050.pdf, Online accessed 14 March 2016

Van der Meer LGH (1992) Investigations regarding the storage of carbon dioxide in aquifers in the netherlands. Energ Convers Manage 33:611–618

Meinhardt-Llopis E, Sánchez J, Kondermann D (2013) Horn-Schunck Optical Flow with a Multi-Scale Strategy. Image Processing On Line 3:151–172, doi: 10.5201/ipol.2013.20

Emami Meybodi H, Hassanzadeh H, Green CP, Ennis King J (2015) Convective dissolution of CO_2 in saline aquifers: Progress in modeling and experiments. Int J Greenh Gas Con 40:238–266, doi: 10.1016/j.ijggc.2015.04.003

Meybodi HE, Hassanzadeh H (2011) Hydrodynamic dispersion in steady buoyancy-driven geological flows. Water Resour Res 47, doi: 10.1029/2011WR010949

MOP-Chile (2013) Estrategia Nacional de Recursos Hídricos 2012-2025. Ministerio de Obras Públicas. http://www.mop.cl/documents/ENRh_2013_OK.pdf, Online accessed 14 March 2016

MOP-DGA (2011) Estimación de Recarga en Cuencias Altiplánicas y Precordilleranas de Vertiente Pacífica. Ministerio de Obras Públicas, Dirección General de Aguas. http://documentos.dga.cl/SUB5347v1.pdf, Online accessed 14 March 2016

Mumford D, Shah J (1989) Optimal approximation by piecewise smooth functions and associated variational problems. Commun Pure Appl Math 42:577–685

Nagamo K, Mochida T, Ochifuji K (2002) Influence of natural convection on forced horizontal flow in saturated porous media for aquifer thermal energy storage. Appl Therm Eng 22:1299–1311, doi: 10.1016/S1359-4311(02)00056-X

Neufeld JA, Hesse MA, Riaz A, Hallworth MA, Tchelepi HA, Huppert HE (2010) Convective dissolution of carbon dioxide in saline aquifers. Geophys Res Lett 37:L22,404, doi: 10.1029/2010GL044728

Nield D, Bejan A (2006) Convection in Porous Media, 3rd edn. Springer-Verlag New York, doi: 10.1007/978-1-4614-5541-7

Nordbotten JM, Celia MA (2011) Geological Storage of CO_2: Modeling Approaches for Large-Scale Simulation. John Wiley & Sons

Oelkers EH, Gislason SR, Matter J (2008) Mineral Carbonation of CO_2. Elements 4:333–337

Oltean C, Felder C, Panfilov M, Bues M (2004) Transport with a Very Low Density Contrast in Hele-Shaw Cell and Porous Medium: Evolution of the Mixing Zone. Transport Porous Med 55:339–360, doi: 10.1023/B:TIPM.0000013332.08029.af

Oltean C, Golfier C, Bues M (2008) Experimental and numerical study of the validity of Hele-Shaw cell as analogue model for variable-density flow in homogeneous porous media. Adv Water Resour 31:82–95, doi: 10.1016/j.advwatres.2007.06.007

Orr FM (2009) Onshore Geologic Storage of CO_2. Science 325(5948):1656–1658, doi: 10.1126/science.1175677

Osher S, Sethian J (1988) Fronts propagating with curvature-dependent speed: Algorithms based on Hamilton-Jacobi formulations. J Comput Phy 79:12–49, doi: 10.1016/0021-9991(88)90002-2

Otero J, Dontcheva LA, Johnston H, Worthing RA, Kurganov A, Petrova G, Doering CR (2004) High Rayleigh number convection in a fluid-saturated porous layer. J Fluid Mech 500:263–281

Ozawa M, Muller U, Kimura I (1992) Flow and Temperature measurement of natural convection in a Hele-Shaw cell using a thermo-sensitive liquid-crystal tracer. Exp Fluids 12:213–222, doi: 10.1007/BF00187298

Palm E, Weber JE, Kvernvold O (1972) On steady convection in a porous medium. J Fluid Mech 54:153–161, doi: 10.1017/S002211207200059X

Pau GS, Bell JB, Pruess K, Almgren AS, Lijewski MJ, Zhang K (2010) High-resolution simulation and characterization of density-driven flow in CO_2 storage in saline aquifers. Adv Water Resour 33:443?455, doi: 10.1016/j.advwatres.2010.01.009

Pimentel (2009) Estudio Prospectivo de Emisiones de Gases de Efecto Invernadero de la Minería del Cobre en Chile. COCHILCO. Recopilación de estudios 2009 : Desarrollo Minero en Chile, Análisis y Desafíos, 42 − 79. http://www.cochilco.cl/descargas/estadisticas/recopilacion/2009.pdf, Online accessed 14 March 2016

Pollack H, Hurter S, Johnson J (1993) Heat flow from the Earth's interior: Analysis of the global data set. Rev Geophys 31:267–280, doi: 10.1029/93RG01249

Polubarinova-Kochina P (1952) Theory of Ground Water Movement (Translated from Russian by R. De Wiest (1962)). Princeton University Press, Princeton N.J.

Pope SB (2011) Turbulent Flows, 9th edn. Cambridge University Press

Pramanik S, Mishra M (2013) Linear stability analysis of Korteweg stresses effect on themiscible viscous fingering in porous media. Phys Fluids 25:074,104

Pramanik S, Mishra M (2015) Viscosity scaling of fingering instability in finite slices with Korteweg stress. EPL 109:64,001, doi: 10.1209/0295-5075/109/64001

Prasad A, Simmons C (2003) Unstable density-driven flow in heterogeneous porous media: A stochastic study of the *Elder* [1967b] short heater problem. Water Resour Res 39(1)

Press WH, Teukolsky SA, Vetterling WT, Flannery BP (2007) Numerical Recipes 3rd Edition: The Art of Scientific Computing, 3rd edn. Cambridge University Press, New York, NY, USA

Pruess K (1991) TOUGH2: A general-purpose numerical simulator for multiphase nonisothermal flows. Lawrence Berkeley Lab., CA (United States)

Pruess K (2006) Enhanced geothermal systems (EGS) using CO_2 as working fluid - a novel approach for generating renewable energy with simultaneous sequestration of carbon. Geothermics 35:351–367, doi: 10.1016/j.geothermics.2006.08.002

Pruess K, Garcia J (2002) Multiphase flow dynamics during CO_2 disposal into saline aquifers. Environ Geol 42:282–295, doi: 10.1007/s00254-001-0498-3

Raffel M (2015) Background-Oriented Schlieren (BOS) techniques. Exp Fluids 56:1–17, doi: 10.1007/s00348-015-1927-5

Raffel M, Willert C, Kompenhans J (1998) Particle Image Velocimetry. A Practical Guide, 2nd edn. Springer-Verlag Berlin Heidelberg, doi: 10.1007/978-3-540-72308-0

Randolph JB, Saar MO (2011a) Combining geothermal energy capture with geologic carbon dioxide sequestration. Geophys Res Lett 38:L10,401, doi: 10.1029/2011GL047265

Randolph JB, Saar MO (2011b) Coupling carbon dioxide sequestration with geothermal energy capture in naturally permeable, porous geologic formations: Implications for CO_2 sequestration. Energy Procedia 4:2206–2213, doi: 10.1016/j.egypro.2011.02.108

Rapaka S, Chen S, Pawar R, Stauffer P, Zhang D (2008) Non-modal growth of perturbations in density-driven convection in porous media. J Fluid Mech 609:285–303, doi: 10.1017/S0022112008002607

Reed A (2013) Energy Under the Andes: Benefits, Barriers to Development, and Relevant Policy Alternatives for Chile's Untapped Geothermal Resources. Master's thesis, University of Pittsburgh

Ress DAS (2002) The onset of Darcy-Brinkman convection in a porous layer: an asymptotic analysis. Int J Heat Mass Tran 45:2213–2220, doi: 10.1016/S0017-9310(01)00332-5

Riaz A, Meiburg E (2003) Three-dimensional miscible displacements simulations in homogeneous porous media with gravity override. J Fluid Mech 494(95)

Riaz A, Pankiewitz C, Meiburg E (2004) Linear stability of radial displacements in porous media: Influence of velocity-induced dispersion and concentration-dependent diffusion. Phys Fluids 16:3592, doi: 10.1063/1.1775431

Riaz A, Hesse M, Tchelepi HA, Orr FM (2006) Onset of convection in a gravitationally unstable diffusive boundary layer in porous media. J Fluid Mech 548:87–111, doi: 10.1017/S0022112005007494

Richard H, Raffel M (2001) Principle and applications of the background oriented schlieren BOS method. Meas Sci Technol 12:1576, doi: 10.1088/0957-0233/12/9/325

Robinson JL (1976) Theoretical analysis of convective instability of a growing horizontal thermal boundary layer. Phys Fluids 19:778, doi: 10.1063/1.861570

Rubinstein J, Torquato S (1989) Flow in random porous media: mathematical formulation, variational principles, and rigorous bounds. J Fluid Mech 206:25–46, doi: 10.1017/S0022112089002211

Rudin LI, Osher S, Fatemi E (1992) Nonlinear total variation based noise removal algorithms. Physica D 60:259–268, doi: 10.1016/0167-2789(92)90242-F

Ruhnau P, Schnorr C (2007) Optical Stokes flow estimation: an imaging-based control approach. Exp Fluids 42:61–78, doi: 10.1007/s00348-006-0220-z

Ruhnau P, Gutter C, Schnorr C (2005a) A variational approach for particle tracking velocimetry. Meas Sci Technol 16:1449–1458, doi: 10.1088/0957-0233/16/7/007

Ruhnau P, Kohlberger T, Schnorr C, Nobach H (2005b) Variational optical flow estimation for particle image velocimetry. Exp Fluids 38:21–32, doi: 10.1007/s00348-004-0880-5

Ruyer-Quil C (2001a) Inertial corrections to the Darcy law in a Hele-Shaw cell. CR Acad Sci Paris, Serie IIb 329:337, doi: 10.1016/S1620-7742(01)01309-5

Ruyer-Quil C (2001b) Inertial corrections to the Darcy law in a Hele?Shaw cell. CR Acad Sci Paris, Serie IIb 329:337, doi: 10.1016/S1620-7742(01)01309-5

Sanchez J, Meinhardt-Llopis E, Facciolo G (2013) TV-L_1 Optical Flow Estimation. Image Processing On Line 3:137–150, doi: 10.5201/ipol.2013.26

Scheidegger A (1974) The Physics of Flow through Porous Media. University of Toronto Press

Schincariol R, Schwartz F, Mendoza C (1997) Instabilities in variable density flows: Stability ans sensitivity analyses for homogeneous and hetereogeneous media. Water Resour Res 33(1):31–41

Schmid PJ (2007) Nonmodal Stability Theory. Annu Rev Fluid Mech 39:129–162, doi: 10.1146/annurev.fluid.38.050304.092139

Schoofs S, Spera F, Hansen U (1999) Chaotic thermohaline convection in low-porosity hydrothermal systems. Earth Planet Sc Lett 174:213–229

Sharp DH (1984) An overview of Rayleigh-Taylor instability. Physica D : Nonlinear Phenomena 12:3–10, doi: 10.1016/0167-2789(84)90510-4

Sheu L, Tam L, Chen J, Chen H, Lin K, Kang Y (2008) Chaotic convection of viscoelastic fluids in porous media. Chaos Soliton Fract 37:113–124

Simmons C, Narayan K (1997) Mixed convection processes below a saline disposal basin. J Hydrol 194:263–285

Simms MA, Garven G (2004) Thermal convection in faulted extensional sedimentary basins: theoretical results from finite-element modeling. Geofluids 4:109–130, doi: 10.1111/j.1468-8115.2004.00069.x

Slim AC, Bandi MM, Miller JC, Mahadevan L (2013) Dissolution-driven convection in a Hele-Shaw cell. Phys Fluids 25:024,101, doi: 10.1063/1.4790511

Stark M (2013) Optical Flow PIV: Improving the Accuracy and Applicability of Particle Image Velocimetry. ETH, Department of Mechanical and Process Engineering, URL https://books.google.cl/books?id=p92MnQEACAAJ

Strong DM, Chan TF (2003) Edge-preserving and scale-dependent properties of total variation regularization. Inverse Probl 19:165–187, doi: 10.1088/0266-5611/19/6/059

Sun T, Teja A (2004) Density, Viscosity and Thermal Conductivity of Aqueous Solutions of Propylene Glycol, Dipropylene Glycol, and Tripropylene Glycol between 290 K and 460 K. J Chem Engng Data 49:1311–1317, doi: 10.1021/je049960h

Suter D (1994) Vector splines in computer vision. In: Proc. Australasian Workshop Thin Plates, Sydney

Sutherland BR, Dalziel SB, Hughes GO, Linden PF (1999) Visualization and measurement of intertial waves by synthetic schlieren: part 1. vertically oscillating cylinder. J Fluid Mech 390:93–126, doi: 10.1017/S0022112099005017

Szulczewski ML, Juanes R (2013) The evolution of miscible gravity currents in horizontal porous layers. J Fluid Mech 719:82–96, doi: 10.1017/jfm.2012.631

Szulczewski ML, Hesse MA, Juanes R (2013) Carbon dioxide dissolution in structural and stratigraphic traps. J Fluid Mech 736:287–315, doi: 10.1017/jfm.2013.511

Taylor GI (1953) Dispersion of solute matter in solvant flowing slowly through a tube. Proc R Soc London, Ser A 219:186

Teng H, Yamasaki A, Chun M, Lee H (1997) Why does CO_2 hydrate disposed of in the ocean in the hydrate formation region dissolve in seawater? Energy

Thomas C, Lemaigre L, Zalts A, D'Onofrio A, De Wit A (2015) Experimental study of CO_2 convective dissolution: The effect of color indicators. Int J Greenh Gas Con 42:525–533, doi: 10.1016/j.ijggc.2015.09.002

Tokgoz S, Geisler R, van Bokhoven LJA, Wieneke B (2012) Temperature and velocity measurements in a fluid layer using background-oriented schlieren and PIV methods. Meas Sci Technol 23:115,302, doi: 10.1088/0957-0233/23/11/115302

Turan J, Ovsenik L, Benca M (2002) Laboratory Equipment Type Fiber Optic Refractometer. Radioengineering 11:27–32

Ueda A, Kato K, Ohsumi T, Yajima T, Iteo H, Kaieda H, Metcalfe R, Takase H (2005) Experimental studies of CO_2-rock interaction at elevated temperatures under hydrothermal conditions. Geochem J 39:417–425

Vafai K, Tien C (1981) Boundary and inertia effects on flow and heat transfer in porous media. Int J Heat Mass Transfer 24:195–203, doi: 10.1016/0017-9310(81)90027-2

Vaughan DG, Comiso JC, Allison I, Carrasco J, Kaser G, Kwok R, Mote P, Murray T, Paul F, Ren J, Rignot E, Solomina O, Steffen K, Zhang T (2013) Observations: Cryosphere. In: Stocker TF, Qin D, Plattner GK, Tignor M, Allen S, Boschung J, Nauels A, Xia Y, Bex V, Midgley P (eds) Climate Change 2013: The Physical Science Basis. Contribution of Working Group I to the Fifth Assessment Report of the Intergovernmental Panel on Climate Change, Cambridge University Press, Cambridge, United Kingdom and New York, NY, USA, pp 317–382, doi: 10.1017/CBO9781107415324.012

Wang Z, Bovik AC (2009) Mean Squared Error: Love It or Leave It? a new look at signal fidelity measures. IEEE Signal Proc Mag 26:98–117, doi: 10.1109/MSP.2008.930649

Wang Z, Bovik AC, Sheikh HR, Simoncelli EP (2004) Image quality assessment: From error visibility to structural similarity. IEEE T Image Process 13:600–612, doi: 10.1109/TIP.2003.819861

Wedel A, Cremers D (2011) Stereo Scene Flow for 3D Motion Analysis, 1st edn. Springer London, doi: 10.1007/978-0-85729-965-9

Wedel A, Pock T, Zach C, Cremers D, Bischof H (2008) An improved algorithm for TV-l^1 optical flow. In: Proc. of the Dagstuhl motion workshop, Dagstuhl Castle

Weir GJ, White SP, Kissling WM (1996) Reservoir Storage and Containment of Greenhouse Gases. Transp Porous Med 23:37–60

Whitaker S (1986) Flow in porous media I: a theoretical derivation of darcy's law. Transp Porous Med 1:3–25, doi: 10.1007/BF01036523

Wildeman S, Lhuissier H, Sun C, Lohse D (2012) Inside a kettle. arXiv:12103693

Winters KB, de la Fuente A (2012) Modelling rotating stratified flows at laboratory-scale using spectrally-based DNS. Ocean Modelling 49-50:47–59, doi: 10.1016/j.ocemod.2012.04.001

Winters KB, MacKinnon JA, Mills B (2004) A spectral model for process studies of rotating, density-stratified flows. J Atmos Ocean Tech 21:69–94, doi: 10.1175/1520-0426(2004)021<0069:asmfps>2.0.co;2

Yang C, Gu T (2006) Accelerated mass transfer of CO_2 in reservoir brine due to density-driven convection at high pressures and elevated temperatures. Ind Eng Chem Res 45:2430–2436

Zach C, Pock T, Bischof H (2007) A duality based approach for realtime TV-L_1 Optical Flow. In: Hamprecht A, Schnorr C, Jahne B (eds) Pattern Recognition, Springer Berlin Heidelberg, chap 22, pp 214–223

Zhao HK, Osher S, Merriman B, Kang M (1996) A variational level set approach to multiphase solution. J Comput Phy 127:179–195, doi: 10.1006/jcph.1996.0167

Zingale M, Woosley SE, Rendleman CA, Day MS, Bell JB (2005) Three-dimensional numerical simulations of Rayleigh-Taylor unstable flames in type Ia supernovae. Astrophys J 632:1021–1034, doi: 10.1086/433164

Appendices

Appendix A

Hele-Shaw models

In the following, we show some Hele-Shaw models used in the literature

- Equation 1 : Ruyer-Quil model (Ruyer-Quil, 2001b)

$$\frac{6}{5}\,\rho_a\left[\frac{\partial \mathbf{u}}{\partial t}+\frac{9}{7}\,(\mathbf{u}\cdot\nabla)\mathbf{u}\right]=-\nabla p-\rho\,g\,\hat{z}-\mu\,K^{-1}\mathbf{u}+\frac{6}{5}\,\mu\nabla^2\mathbf{u}$$

- Equation 2 : Gondret model (Gondret and Rabaud, 1997). Gap averaged equation

$$\rho_a\left[\frac{\partial \mathbf{u}}{\partial t}+\frac{6}{5}\,(\mathbf{u}\cdot\nabla)\mathbf{u}\right]=-\nabla p-\rho\,g\,\hat{z}-\mu\,K^{-1}\mathbf{u}+\mu\nabla^2\mathbf{u}$$

- Equation 3 : Bizon model with scalar transport in the Boussinesq limit (Bizon et al, 1997b). Non-dimensional gap averaged equations, with $\omega_y = (\nabla\times\mathbf{u})_y$, $\sigma=\nu/D$, $\alpha=12(L/b)^2$ and $Ra=g\Delta\rho L^3/\nu D$. Here the subscript $\perp$ refers to a two dimensional projection.

$$\frac{\partial \mathbf{u}}{\partial t}+\frac{4}{5}\,\omega_y\,\hat{y}\times\mathbf{u}=-\nabla p+\sigma\left[\nabla_\perp^2-\alpha\right]\mathbf{u}-\frac{3}{2}\,\sigma\,Ra\,S\,\hat{z}$$

$$\frac{\partial S}{\partial t}+\frac{2}{3}\,\mathbf{u}\cdot\nabla_\perp S=\nabla_\perp^2 S$$

$$\nabla_\perp\cdot\mathbf{u}=0$$

- Equation 4 : Oltean model including Taylor dispersion (Oltean et al, 2004). Depth-averaged two dimensional equations, governing flow and transport of a density-variable pollutant into a plane fracture with permeability $K=b^2/12$.

$$\mu K^{-1}\mathbf{u} = -\nabla p - \rho\, g\, \hat{z}$$

$$\frac{\partial \rho}{\partial t} + \nabla \cdot (\rho\, \mathbf{u}) = 0$$

$$\frac{\partial (\rho S)}{\partial t} + \nabla \cdot (\rho S \mathbf{u}) = \frac{\partial}{\partial x_p}\left[\rho\, D_{pk}\, \frac{\partial S}{\partial x_k}\right]$$

$$D_{pk} = D_m\, \delta_{pk} + \frac{2}{35}\frac{K}{D_m}\left[1 + \frac{S}{\rho}\,\frac{\partial \rho}{\partial S}\right] u_p u_k$$

Appendix B

Gâteaux functional derivative

Let $f : \mathbf{R}^n \to \mathbf{R}$ be a scalar-valued function. In $\mathbf{R}^n$, the directional derivative along a vector $\mathbf{u}$ at the point $\mathbf{x}$ is defined as

$$\mathcal{D}_{\mathbf{u}} f = \frac{d}{d\epsilon} f(\mathbf{x} + \epsilon \mathbf{u})\Big|_{\epsilon=0} = \lim_{\epsilon \to 0} \frac{f(\mathbf{x} + \epsilon \mathbf{u}) - f(\mathbf{x})}{\epsilon}\,, \tag{B.0.1}$$

where the physical interpretation of Eqn. (B.0.1) is the rate of change of f with the time ϵ when moving past $\mathbf{x}$ at velocity $\mathbf{u}$. Now, we can generalize Eqn. (B.0.1) to functional derivatives from a Banach space $\mathcal{B}$ to $\mathbf{R}$. Banach space is a complete normed vector space. Two known examples of Banach spaces are $\mathbf{R}^n$ and the set of continuous functions on closed interval of $\mathbf{R}$ with the norm $\| f \| = \sup |f(x)|$ with $x \in \mathbf{R}$.

The Gâteaux derivative of a functional $J : \mathcal{B} \to \mathbf{R}$ is defined as

$$\mathcal{D}_{\psi} J = \frac{d}{d\epsilon} J[f + \epsilon \psi]\Big|_{\epsilon=0} = \lim_{\epsilon \to 0} \frac{J[f + \epsilon \psi] - J[f]}{\epsilon}\,. \tag{B.0.2}$$

Then, when $\mathcal{B}$ is $\mathbf{R}^n$, we recover Eqn. (B.0.1). Like the Fréchet functional derivative defined on a Banach space, the Gâteaux derivative defined in Eqn. (B.0.1) is often used to formalize the computation of functional derivatives in calculus of variations and mathematical physics, so its application is fundamental to derive the differential equations that solves the segmentation problem that arises in Chan-Vese and Chan-Tai models.

Appendix C

Isodata algorithm

The main goal of Isodata algorithm is that allow us to initialize the level set functions close to the minimum of the functional defined in Eqn. (9.1.12) on page 119.

The Isodata algorithm for two regions is the following

1. Compute the mean value $\bar{f}$ of the image f .
2. Compute the mean value $\bar{f}_1$ and $\bar{f}_2$ of each region of the image f divided by $\bar{f}$.
3. Recompute the new mean value $\bar{f} = (1/2)(\bar{f}_1 + \bar{f}_2)$.
4. Repeat from step 2 iteratively until $\bar{f}$ converges.

For four regions, the algorithm is the following

1. Compute the mean value $\bar{f}$ of the image f .
2. Denote the two subimages divided by $\bar{f}$, f_1 and f_2 .
3. Apply the Isodata algorithm for two regions to the subimage f_1 , in order to find $\bar{f}_1$.
4. Apply the Isodata algorithm for two regions to the subimage f_2 , in order to find $\bar{f}_2$.
5. Recompute the new mean value $\bar{f} = (1/2)(\bar{f}_1 + \bar{f}_2)$.
6. Repeat from step 2 iteratively until $\bar{f}$ converges.

Appendix D

The split-Bregman iteration

Let f and u be two-dimensional arrays, where f is given. The discrete setting of Eqn. (11.1.1) is

$$\min_u \left\{ \frac{\lambda}{2} ||f-u||_2^2 + \frac{\mu}{2} ||\nabla u||_2^2 + ||\nabla u||_1 \right\}, \tag{D.0.1}$$

where $||u||_1 = \sum_{i,j} \sqrt{(u_{ij})^2}$ is the classical discrete TV seminorm and $||\cdot||_2$ is the L^2 norm. In the work of Cai et al, the approximation of the discrete gradient operator for the ith row is given by the backward finite difference with periodic boundary conditions

$$(\nabla_x u)_{ij} = \begin{cases} u_{i,1} - u_{i,n}\,, & j = 1 \\ u_{i,j} - u_{i,j-1}\,, & j = 2, \ldots, n \end{cases}$$

where n is the number of pixels in the j-direction and $u_{i,j}$ is the jth pixel in the ith row of u. Similiarly, we can discretize ∇_y as

$$(\nabla_y u)_{ij} = \begin{cases} u_{1,j} - u_{n,j}\,, & i = 1 \\ u_{i,j} - u_{i-1,j}\,, & i = 2, \ldots, n \end{cases}$$

These discretizations can be modified using compact finite differences (Lele, 1992) without add more computational costs. To solve Eqn. (D.0.1), we set $d_x = \nabla_x u$ and $d_y = \nabla_y u$, so this yields to the weakly enforced minimization problem

$$\min_u \left\{ \frac{\lambda}{2} ||f-u||_2^2 + \frac{\mu}{2} ||\nabla u||_2^2 + ||(d_x, d_y)||_1 + \frac{\sigma}{2} ||d_x - \nabla_x u||_2^2 + \frac{\sigma}{2} ||d_y - \nabla_y u||_2^2 \right\}. \tag{D.0.2}$$

The application of the split-Bregman iteration to strictly enforce the constrains yields to the iterative equations

$$u^{(k+1)} = \arg\min_{g} \left\{ \frac{\lambda}{2} ||f - u^{(k)}||_2^2 + \frac{\mu}{2} ||\nabla u^{(k)}||_2^2 \right.$$
$$\left. + \frac{\sigma}{2} ||d_x^{(k)} - \nabla_x u^{(k)} - b_x^{(k)}||_2^2 + \frac{\sigma}{2} ||d_y^{(k)} - \nabla_y u^{(k)} - b_y^{(k)}||_2^2 \right\} \quad \text{(D.0.3)}$$

$$(d_x^{(k+1)}, d_y^{(k+1)}) = \arg\min_{d_x, d_y} \left\{ ||(d_x^{(k)}, d_y^{(k)})||_1 + \frac{\sigma}{2} ||d_x^{(k)} - \nabla_x u^{(k)} - b_x^{(k)}||_2^2 \right.$$
$$\left. + \frac{\sigma}{2} ||d_y^{(k)} - \nabla_y u^{(k)} - b_y^{(k)}||_2^2 \right\} \quad \text{(D.0.4)}$$

$$b_x^{(k+1)} = b_x^{(k)} + (\nabla_x u^{(k+1)} - d_x^{(k+1)}) \quad ; \quad b_y^{(k+1)} = b_y^{(k)} + (\nabla_y u^{(k+1)} - d_y^{(k+1)}) \quad \text{(D.0.5)}$$